Laboratory Investigation of the Dynamics of Shear Flows in a Plasma Boundary Layer

by

Ami Marie DuBois

A dissertation submitted to the Graduate Faculty of
Auburn University
in partial fulfillment of the
requirements for the Degree of
Doctor of Philosophy

Auburn, Alabama
December 14, 2013

Approved by

Edward Thomas, Jr., Chair, Professor of Physics
William Amatucci, Staff Scientist at Naval Research Laboratory
Uwe Konopka, Professor of Physics
David Maurer, Professor of Physics

Abstract

The laboratory experiments presented in this dissertation investigate a regime of instabilities that occur when a highly localized, radial electric field oriented perpendicular to a uniform background magnetic field gives rise to an azimuthal velocity shear profile at the boundary between two interpenetrating plasmas. This investigation is motivated by theoretical predictions which state that plasmas are unstable to transverse and parallel inhomogeneous sheared flows over a very broad frequency range.

Shear driven instabilities are commonly observed in the near-Earth space environment when boundary layers, such as the magnetopause and the plasma sheet boundary layer, are compressed by intense solar storms. When the shear scale length is much less than the ion gyro-radius, but greater than the electron gyro-radius, the electrons are magnetized in the shear layer, but the ions are effectively un-magnetized. The resulting shear driven instability, the electron-ion hybrid instability, is investigated in a new interpenetrating plasma configuration in the Auburn Linear EXperiment for Instability Studied (ALEXIS) in the absence of a magnetic field aligned current. In order to truly understand the dynamics at magnetospheric boundary layers, the EIH instability is studied in the presence of a density gradient located at the boundary layer between two plasmas. Theoretical models are used to show that the EIH instability in a uniform density plasma cannot be supported by the parameters that are accessible to ALEXIS.

As plasma boundary layers begin to relax from a compressed state, the ratio of the ion gyro-radius to the shear scale length decreases, and observations of broadband electrostatic noise, which extend from well below the ion cyclotron frequency to the electron plasma frequency, have been reported. By decreasing the magnetic field strength in the ALEXIS device, a continuous variation of the ratio of the ion gyro-radius to the shear scale length is observed. As a result, a transition of the shear flow driven instability regime is also observed, which is reminiscent of the satellite observations of broadband electrostatic noise. For the first time, a laboratory experiment has reproduced the actual space observation of broadband emission, which is a characteristic signature of boundary layer crossings by a satellite.

Acknowledgments

I would like to start by thanking my advisor Dr. Edward Thomas, for all of his support throughout my time here at Auburn. Without his advice and guidance, none of this would have been possible. I am so thankful for the opportunities he has granted me, from working on ALEXIS, collaborating with so many wonderful people, and traveling to so many wonderful new places across the country and around the world to attend conferences.

I am also greatly appreciative of the advice and direction provided by Dr. Bill Amatucci and Dr. Guru Ganguli at the Naval Research Laboratory. Parts of this research would have been nearly impossible without their involvement. Additionally, I am very grateful for all of the support that the physics department faculty members have provided over the years. It was a privilege to be able to learn from and work with everyone in this department.

My time in Auburn would not have been as productive or enjoyable without the company of my fellow graduate students Ashley Eadon, Ross Fisher, Jeff Herfindal, Aaron Modic, Mihir Pandaya and Ivan Arnold. Thank you for all of the invaluable advice and encouragement you have given over the years. From studying for qualifying exams to struggling with experiments, each one of you made the journey through graduate school easier, and at many times entertaining. I definitely would not have made it out in one piece without the company of you guys.

Finally, I would like to dedicate this dissertation to my family who has always encouraged my curiosity of science. I would like to thank my parents for all of the support and advice throughout the years, and for believing in me even when I didn't. Without you guys, my larger than life dreams would have never come true. Thank you to my grandparents, who helped me in any and every way they could throughout the last 10 years of school and always had a room open for me when I needed a few days just to get away and go to the beach. It would have been impossible to make it this far without all of your support and encouragement!

Table of Contents

List of Figures

List of Tables

Chapter 1: Introduction

Plasma, known as the fourth state of matter, is the most prevalent state of matter in the universe[1,2] – making up the stars in the night sky, including our own sun, and filling the empty space in our solar system in the form of the solar wind. When a gas is heated, the atoms or molecules that make up the gas can be stripped of one or more electrons, resulting in an ionized gas consisting of free electrons and positively charged particles known as ions.[1,2] Plasma is naturally occurring on earth in the form of lightning[1–3], aurora[1–3] and high temperature flames. Artificially, it is used to make the components that are found in computers and cell phones[3], fluorescent light bulbs[1–3], neon signs[1–3], and plasma televisions[3]. The work presented in this dissertation uses a laboratory experiment, the Auburn Linear EXperiment for Instability Studies (ALEXIS), to investigate boundary layer processes in the near-Earth space environment. Specifically, this work is focused on the generation of plasma instabilities by localized flows in a plasma.

1.1 Sheared plasma flows

Most plasmas, whether man-made or naturally occurring, are inhomogeneous by nature. Spatial variations can occur in plasma parameters such as the density, temperature, and plasma potential. In particular, spatial variations in the plasma potential lead to inhomogeneous electric fields ($\boldsymbol{E}$). If the electric field is oriented perpendicular to a uniform background magnetic ($\boldsymbol{B}$) field, a transverse sheared $\boldsymbol{E} \times \boldsymbol{B}$ velocity profile (i.e., $\boldsymbol{v}_{flow} = \boldsymbol{E} \times \boldsymbol{B}$) can arise in the plasma.

However, if the inhomogeneous electric field is established by a current that is parallel to the magnetic field (i.e., a field aligned current), a sheared velocity flow parallel to the background magnetic field can form. The importance of sheared flows arises from their ubiquity in fusion, space, and laboratory plasmas. In the presence of sheared plasma flows, a range of phenomena, such as increased confinement in fusion plasmas[4–13] and ion heating in space plasmas[14–16] have been observed. Shear flows in plasmas can also lead to either the suppression or enhancement of electrostatic and electromagnetic fluctuations[17–22].

In magnetically confined fusion plasmas, the presence of sheared flows can lead to an increase in confinement of plasmas due to the formation of transport barriers at the plasma edge.[4–8] This is a signature of the transition from a "low" to a "high" confinement mode, or "H"-mode. H-mode was first discovered in the Axisymmetric Divertor Experiment (ASDEX) tokamak device.[4] However, H-mode was not immediately linked to sheared plasma flows. Itoh and Itoh[23] theorized the role of edge electric fields in the evolution of transport barriers, after which Burrell and Groebner[5,24,25] were able to experimentally link radial electric fields at the edge of the DIII-D tokamak to transport barriers and turbulence suppression. They were the first to recognize that the reduction in transport was due to an increase in the sheared flows in the plasma.[24,25] Experiments in other tokamak devices, such as the Continuous Current Tokamak (CCT)[6] at UCLA and the Mega-Amp Spherical Tokamak (MAST)[26], have also observed that sheared flows in the edge regions resulted in a reduction in the turbulence and an improvement in the confinement of the plasma.

Sheared flows have also been observed in other fusion device configurations such as stellarators[9–11,27,28] and reversed field pinch (RFP) experiments[12,13]. In the TJ-II stellarator[9,10] it was observed that as the plasma density increased, a shear flow layer developed in the edge

region of the plasma. As a result, there was a decrease in the overall electrostatic fluctuations and in the particle transport. These broadband electrostatic fluctuations are believed to drive particle and energy transport away from the plasma core.[13] Experiments performed in the Compact Auburn Torsatron (CAT)[27] used a biasing electrode to modify electric fields and drive poloidal plasma rotation. The induced rotation resulted in an increase in the plasma density and temperature, and indications of improved particle confinement for radially inward electric fields were observed. A similar observation was made in experiments in the Compact Toroidal Hybrid (CTH)[28], which studied the plasma response to sheared flows. Electrostatic fluctuations were suppressed when the direction of the edge electric field was switched from radially outward to radially inward. RFP experiments such as the Reversed Field Pinch Experiment (RFX)[12] and the Madison Symmetric Torus (MST)[13] also observed that $\boldsymbol{E} \times \boldsymbol{B}$ flows led to a reduction of electrostatic fluctuations in the shear region, and an overall reduction in the particle flux and transport in the plasma.

A number of fusion related laboratory experiments have been performed on spatially inhomogeneous flows, notably zonal flows, which are a phenomenon that are closely related to $\boldsymbol{E} \times \boldsymbol{B}$ flows.[29] Zonal flows emerge from a turbulent state in the plasma and act to regulate and suppress turbulence and transport via shearing.[29] Experiments in the H-1 Heliac[30] at the Australian National University were the first to provide evidence that zonal flows are spatially correlated with transport barrier regions in an H-mode plasma. Extensive work on the generation of zonal flows and the induced energy transfer has been done on the linear Controlled Shear Decorrelation Experiment (CSDX)[31–33] at the University of California at San Diego. Shear flow is not only a mechanism that occurs in fusion plasmas, but also in space and laboratory plasmas.

Plasma flows, both along and across Earth's magnetic field lines, are common in the space environment. Observations show that Earth's magnetopause[34,35] and the plasma sheet boundary layer (PSBL)[36–38] can exhibit strong shear flows caused by localized electric fields. Velocity shear is also generated in active experiments in space. For example, a region of electron depletion is created in the local plasma in the ionosphere by the release of electron capturing agents such as SF_6, $Ni(CO)_4$, etc. At the boundary of the depletion, highly sheared electron flows can develop and shear driven instabilities are excited.[39–41] Sheared plasma flows have also been observed in the magnetoshere of Mars by the Mars Express Spacecraft[42], in the ionosphere of Venus by the Pioneer Venus Orbiter[42], and at the comet Halley by the Giotto and VEGA spacecrafts[43].

Plasma flows have been suggested as a source of free energy to drive instabilities in the ion acoustic, ion cyclotron, and lower hybrid frequency regimes.[15] The instabilities that can arise from shear flows are considered to be an important mechanism in ion heating[14–16,44,45], acceleration[46,47], and transport[48–50]. However, interpreting the *in-situ* measurements made with satellites or sounding rockets can be challenging because the motion of these measurement platforms makes separating temporal and spatial effects difficult. As a result, a number of laboratory experiments have been built in order to gain a better understanding of shear flows and the resulting instabilities.

A number of groups have done laboratory experiments on shear driven instabilities that are found in the space environment. For example, at the University of Iowa, Merlino and co-workers[51–56] have studied parallel shear driven instabilities in Cesium ion plasmas in a Q-machine. Agrimson *et al.*[51,52,54] and Kim *et al.*[55,56] excited both the current driven ion-acoustic and the current driven electrostatic ion cyclotron (CDEIC) instabilities by forming a magnetic

field aligned ion flow and biasing concentric ring electrodes to drive a parallel velocity shear. Merlino *et al*.[53] also showed that parallel shear velocity can lead to the excitement of ion cyclotron-like modes in the presence of a density gradient. At West Virginia University (WVU), Teodorescu *et al*.[57] also used a Q-machine to excite multi-harmonic ion cyclotron waves driven by a parallel velocity shear, and showed that this was related to the observations of strong in-homogeneities in the Earth's auroral region. Also at WVU, Scime *et al*.[58] and Spangler *et al*.[59] showed that parallel shear and ion temperature anisotropy are required for the growth of shear-modified ion acoustic waves.

Instabilities driven by both parallel and perpendicular shear has also been studied in laboratory experiments. Koepke and co-workers[60] were the first to provide experimental verification of an instability driven by the inhomogeneity in the wave energy density. This inhomogeneity is caused by velocity shear oriented transverse to the background magnetic field. The resulting instability is called the Inhomogeneous Energy Density Driven (IEDD) Instability and was theoretically predicted by Ganguli *et al*.[61,62] The transverse shear was driven by applying a voltage to a segmented electrode, which produced dc electric fields localized to the region of a field aligned current. Other experiments involved studying the transition between the CDEIC instability and the IEDD instability.[63–65] The co-location of parallel and perpendicular velocity shear has also been shown to suppress low frequency instabilities, such as drift waves.[66]

Finally, transverse shear driven instabilities have been studied with negligible field aligned current. For example, Kent *et al*.[67] and Jassby *et al*.[68] both showed that a large transverse shear in a Q-machine can excite a low frequency instability known as the Kelvin-Helmholtz instability. At the Naval Research Laboratory (NRL), Amatucci *et al*.[69] reported the first observation of the IEDD instability driven exclusively by a transverse sheared flow (no field

aligned current). Amatucci and co-workers[44,45] later showed that significant perpendicular ion heating can result from transverse shear driven waves in the ion cyclotron frequency range. At Tohoku University, Hatakeyama *et al.*[70] used a potassium ion plasma in a Q-machine to show that transverse sheared flows stabilize ion cyclotron instabilities. Finally, Tejero *et al.*[21] used localized transverse dc electric fields with minimal magnetic field aligned current to spontaneously generate electromagnetic ion cyclotron (EMIC) waves. This showed that transverse electric fields can behave as a radiation source for electromagnetic waves, which can transport energy away from the region of wave generation. This phenomenon suggests that not all energy reaching the ionosphere is dissipated as local heating, but rather can be radiated back into the magnetosphere, which would be consistent with satellite observations.[21]

1.2 Experiment motivation

Previous work on the Auburn Linear EXperiment for Instability Studies (ALEXIS) has focused on studying shear driven instabilities in the ion cyclotron frequency range. ALEXIS is a 170 cm long, 10 cm diameter linear magnetized plasma column. The early ALEXIS configuration[71] made use of three filaments to produce helium plasmas. The plasma potential profile was modified using electrode rings in order to drive transverse sheared flows. Thomas *et al.*[17,19] showed that a radially inward electric field produced a transverse sheared flow that resulted in a shear driven instability, which was later shown to be consistent with the IEDD mechanism[72] modified by the presence of a small field aligned current. It was also shown that when the direction of the electric field was changed to radially outward, the sheared flow had a stabilizing influence on the plasma, and the observed instability was suppressed. The ALEXIS device was upgraded to replace the filament source with an rf plasma source[73] and studies then focused on the CDEIC instability[72]. It was found that when a negative voltage was applied to

electrode rings, low frequency waves that were identified as drift waves were supported in the plasma.[18] However, with a positive voltage, a significant field aligned current was established in the plasma which led to the suppression of the drift waves[18] and excited the CDEIC instability[72].

All of the previous experiments performed in the ALEXIS device studied shear driven ion cyclotron-like instabilities. In this regime, the shear scale length (L_E) is considered to be comparable to the ion gyro-radius (ρ_i). It was desired to study a different mechanism that can occur when the electric field becomes extremely localized so that the shear scale length is less than the ion gyro-radius; a regime in which electrons are magnetized in the shear layer, but the ions are effectively un-magnetized. The resulting transverse shear driven instability occurs at a frequency well above the ion cyclotron frequency and closer to the lower hybrid frequency. This mode is known as the electron-ion hybrid (EIH) instability, which was first proposed by Ganguli *et al*.[74] and Romero *et al*.[48,75,76]

Several laboratory experiments have studied the EIH instability. For example, in the String Plasma Device (SPD)[77] at Tokai University, the effect of transverse velocity shear on plasma transport was studied in a steady state, filamentary plasma where the plasma radius was smaller than the ion gyro-radius, but larger than the electron gyro-radius so that the electrons are magnetized in the shear layer, but the ions are effectively un-magnetized. In this experiment, an electric field oriented perpendicular to a uniform background magnetic field was created by applying a large voltage to a disk electrode, which resulted in a transverse shear driven instability in the lower hybrid frequency range. While the instability characteristics were indicative of the EIH mechanism, the setup contained a significant field aligned current that increased with increasing transverse shear, which makes it difficult to determine the true source of the fluctuations. Kumar *et al*.[78] studied plasma diffusion across inhomogeneous magnetic fields and

observed large electrostatic fluctuations in the lower hybrid frequency range in the greatest region of $\boldsymbol{E} \times \boldsymbol{B}$ shear. The fluctuations were proposed to be the EIH instability, but were never fully characterized and compared to theoretical models. Amatucci *et al*.[50] was the first to experimentally verify the EIH instability in a transverse sheared plasma flow with negligible field aligned current. The experimental configuration made use of two plasma sources, which allowed for the independent control of the plasma potential and the density profile at the plasma boundary. The instability was fully characterized in a uniform density configuration in order to uniquely determine the source of the oscillations. The experiment showed that by adding a density gradient between the plasmas, the frequency of the instability dropped below the lower hybrid frequency, but the density gradient effects were not fully explored in this work. Because lower hybrid instabilities like the EIH instability are commonly observed at space plasma boundary layers in the presence of density gradients, it is important to study such instabilities with density gradients in the plasma in order to truly understand the dynamics of highly localized magnetospheric boundary layers.

Lower hybrid instabilities like the EIH instability are commonly observed in the near-Earth space environment at boundaries such as the magnetopause, the plasma sheet boundary layer[35] and in chemical release experiments in the ionosphere[39–41]. Figure 1-1 shows an example of such an observation by the four Cluster satellites at the dusk-side crossing of the magnetopause. The spacecraft potential (V_{ps}) shown in Figure 1-1(a) is directly correlated to the plasma density, so that a high potential corresponds to a high density, and a low potential corresponds to a low plasma density. Panels (b) through (e) display electrostatic fluctuations (0 to 10 Hz) observed from all four satellites, and panel (f) shows the wave activity for higher frequencies (10 to 50 Hz). The electromagnetic wave activity is shown in panel (g). Panels (h)

and (i) show the magnitude and the elevation angle of the magnetic field respectively, where 90 degrees corresponds to a northward field. Note that in panel (i), the abrupt change in the elevation angle is indicative of the spacecraft crossing the magnetopause and entering (decreasing angle)/leaving (increasing angle) the magnetosheath.

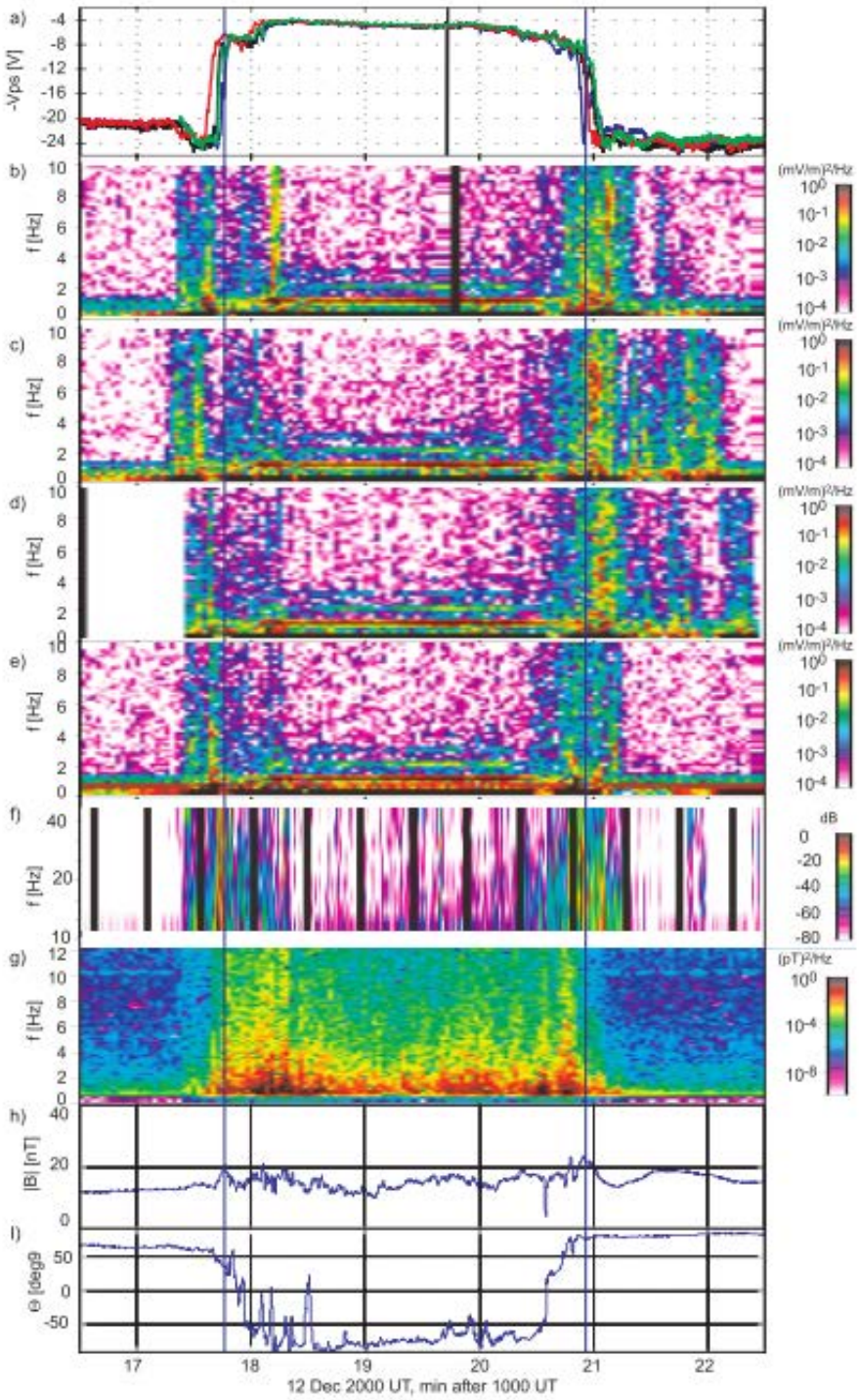

Figure 1-1: Observations of heavy electrostatic wave emission at the dusk-side crossing of the magnetopause from the four Cluster satellites. The spacecraft potential (a) is directly correlated to the plasma density. Panels (b) to (e) show the electrostatic wave activity from 0 to 10 Hz and panel (f) shows the electrostatic wave activity from 10 to 50 Hz. The electromagnetic wave activity is shown in panel (g). Panels (h) and (i) show the magnitude and the elevation angle of the magnetic field, respectively. An elevation angle of 90 degrees corresponds to a northward magnetic field [Figure 3 from reference [35].]

The Cluster satellite data presented in Figure 1-1 shows that at roughly the same time as the decrease in the elevation angle (vertical blue line), there is a sharp increase in the spacecraft potential. This indicates that the spacecraft has crossed the magnetopause and enters the magnetosheath. There is a large density gradient across this boundary, and the electric field scale length is said to be less than or equal to the ion gyro-radius.[35] Panels (b) through (f) show that there are broadband waves observed by each spacecraft at the boundary crossing. For reference, the ion cyclotron frequency is 0.3 Hz and the lower hybrid frequency is 10 Hz.[35] The broadband electrostatic fluctuations occur near the lower hybrid frequency, indicating that the observed spectra are lower hybrid waves.

Intense solar storms can compress and steepen boundary layers like the one discussed above. As such boundary layers begin to relax from a compressed state and the ratio of the ion gyro-radius to the shear scale length decreases, observations of broadband electrostatic noise have been reported[48,49,75,79–81] in which the frequency range extends from below the ion cyclotron frequency up to the electron plasma frequency. Simulations performed by Romero *et al*.[48] have confirmed that the free energy available in sheared electron flows can give rise to broadband wave spectra and can excite Kelvin-Helmholtz, ion cyclotron-like, and lower hybrid modes[22,62,74] at magnetospheric boundary layers.

Kinetic theory described by Ganguli *et al*.[15,62,74] discusses the three distinct instability regimes in the context of the ion gyro-radius and the shear scale length, as is shown in Figure 1-2. The ratio of the ion gyro-radius to the shear scale length acts as a surrogate for the magnitude of stress that a plasma layer is subjected to[80] and determines which mode is dominant. For example, when $\rho_i / L_E << 1$, the Kelvin-Helmholtz instability appears in the plasma with a characteristic frequency that is below the ion cyclotron frequency. As the shear scale length

becomes comparable to the ion gyro-radius, the IEDD instability, which is distinct from the Kelvin-Helmholtz instability, arises in the plasma. The EIH instability, as was discussed above, is excited when the ion gyro-radius becomes much larger than the shear scale length so that the ions are considered to be un-magnetized and the electrons remain magnetized. All of these instability regimes have a single free energy source, a transverse shear flow, but the physics of the energy extraction to support wave growth are different. The ratio of the ion gyro-radius to the shear scale length is a convenient tunable experimental parameter that can be exploited in order to transition between the modes. As discussed in detail above, each of these modes has been studied separately in a variety of plasma configurations. However, no single experiment has shown the continuous transition from one mode to another to test how these different modes are linked with one another, which is the basis of the relaxation process.[15]

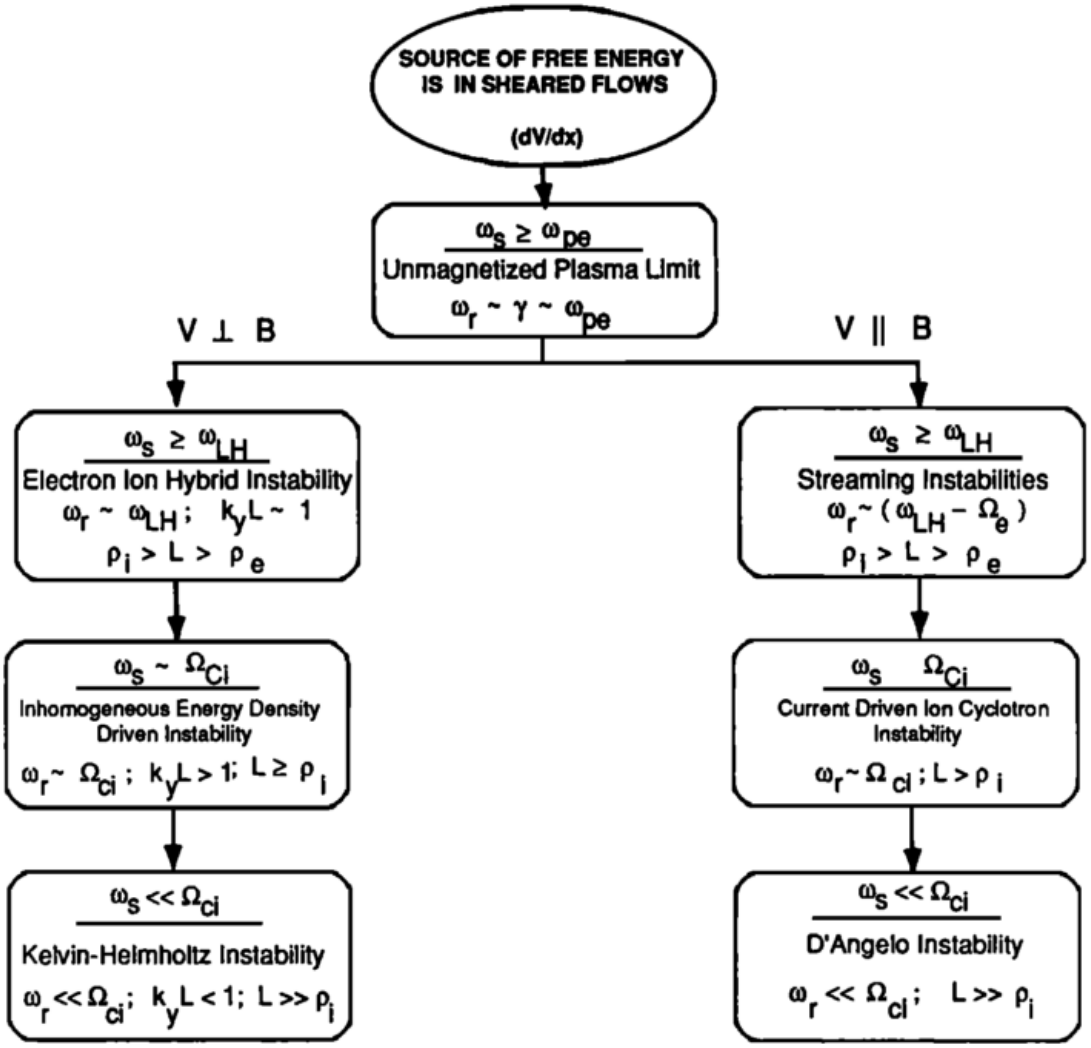

Figure 1-2: A hierarchy of microinstabilities that can be triggered by velocity shear. [Figure 2 from reference [15].]

The experiments presented in this dissertation focus on instabilities in the lower hybrid frequency range. Specifically, the results discussed in the following chapters will show that a localized transverse sheared plasma flow has been successfully produced in a new dual plasma configuration in the ALEXIS device. This transverse shear flow excites the EIH instability in the absence of a field aligned current in the plasma. In order to truly understand the dynamics at magnetospheric boundary layers, the goal of the experiment is to drive the EIH instability in the presence of a density gradient that is co-located with the region of greatest shear. It was also

desired to study the transition of the EIH instability characteristics going from a uniform density configuration to a plasma with a density gradient. However, it will be shown that the EIH instability wavelength in a uniform density plasma is larger than the axial length of the experimental device, and therefore cannot be supported by the parameters that are accessible to ALEXIS. The second part of the experiment will, for the first time, show a continuous variation of the ratio of the ion gyro-radius to the shear scale length – and the associated transition of the instability regimes driven by the shear flow mechanism – in a single laboratory experiment. This final experiment is a demonstration of the relaxation mechanism of compressed plasma layers in a collisionless plasma.

1.3 Dissertation outline

This dissertation is organized into 5 chapters and 2 appendices. Chapter 2 begins by discussing lower hybrid instabilities and illustrates how the EIH instability is related to this class of instabilities. Section 2.2 presents the theoretical framework for the EIH instability dispersion relation. The dispersion relation is derived for both a uniform and a non-uniform density profile. The shooting code that is used to numerically solve the dispersion relation is presented in Section 2.2.4. Finally, the whistler wave, which is the electromagnetic branch of the electron-ion hybrid instability, is briefly discussed in Section 2.3.

In Chapter 3, a description of the experimental setup is presented. The vacuum vessel, electromagnet configuration, vacuum system and gas regulation system are discussed in Sections 3.1 through 3.4. A description of the plasma sources and the plasma modification hardware is given in Section 3.5. Finally, the *in situ* diagnostics used in the experiment are presented in Section 3.6.

Chapter 4 is divided into three experiments. Section 4.1 discusses the plasma parameters measured for each plasma source to illustrate that the addition of the secondary source was necessary in order to drive lower hybrid waves. The second section discusses the characterization of the EIH instability in a plasma with density gradient. The results of the EIH instability in a plasma with a uniform density are also discussed. Finally, Section 4.3 presents the results of an ion gyro-radius modification experiment.

A summary of the theoretical framework and experiments is given in Chapter 5. The implications of the experiments and future work are also presented in this chapter.

Finally, the appendix is comprised of two parts. Appendix A discusses a project on the identification and suppression of drift waves that was performed using the initial configuration of ALEXIS. Appendix B lists the *Mathematica* shooting codes used to generate the theoretical models, as well as the LabVIEW VI's used to acquire and analyze data.

Chapter 2: Theory

In Chapter 1, it was shown that a broad range of sheared flow driven plasma instabilities can arise in both space and laboratory plasma environments. These instabilities exist in frequency regimes that extend from well below the ion cyclotron frequency up to the lower hybrid frequency. In particular, a central goal of this work has been to investigate the physical properties of the electron-ion hybrid (EIH) instability. This chapter introduces the dispersion relation derivations for the EIH instability, presented in slab geometry. It is appropriate to briefly discuss the EIH instability in the context of lower hybrid instabilities because the EIH instability is so closely related (Section 2.1). The theory presented in Section 2.2 focuses on the derivation of the EIH instability with and without a density gradient in the plasma. The shooting code used to numerically solve the dispersion relation is also discussed. Finally, in the interest of completeness, a brief discussion of the electromagnetic component of the EIH instability, the whistler wave, is presented in Section 2.3.

2.1 Lower hybrid instabilities

A lower hybrid instability is described as an electrostatic wave with a frequency near the lower hybrid frequency (Equation 2-1) that travels nearly transverse to a background magnetic field[1,82],

$$\omega_{LH}^2 = \frac{1}{(\Omega_{ci}\,\Omega_{ce})^{-1} + \omega_{pi}^{-2}} = \frac{\omega_{pi}^2 \Omega_{ce}^2}{\omega_{pe}^2 + \Omega_{ce}^2} \tag{2-1}$$

where Ω_{ci} is the ion cyclotron frequency, Ω_{ce} is the electron cyclotron frequency, ω_{pi} is the ion plasma frequency and ω_{pe} is the electron plasma frequency which are defined as,

$$\begin{aligned} \Omega_{ci} &= \frac{eB}{m_i} \\ \Omega_{ce} &= \frac{eB}{m_e} \\ \omega_{pi} &= \sqrt{\frac{n_i e^2}{\epsilon_o m_i}} \\ \omega_{pe} &= \sqrt{\frac{n_e e^2}{\epsilon_o m_e}}. \end{aligned} \tag{2-2}$$

An equally important characteristic of lower hybrid waves is the difference between the ion and electron motion. Since the lower hybrid frequency is between the ion cyclotron and electron cyclotron resonances[2,83], the mass difference governs the motion of the ions and electrons around the magnetic field. Consider a background magnetic field ($\vec{\boldsymbol{B}}$) in the z-direction with a transverse dc electric field ($\vec{\boldsymbol{E}}$). The electrons experience a drift in the direction of $\vec{\boldsymbol{E}} \times \vec{\boldsymbol{B}}$. The ions however, are much more massive than the electrons so the motion is not seriously affected by the magnetic field and will move principally in the direction of the electric field.[83] For lower hybrid instabilities, the ions are effectively un-magnetized compared to the electrons.

For cold plasmas, the lower hybrid dispersion relation (Equation 2-3) is derived from the electrostatic dispersion relation (ESDR)[2,82]. Instead of obeying the Boltzmann relation, the

electrons are governed by the full equation of motion.[1] This derivation has been discussed in detail by Gurnett and Bhattacharjee[2] and Swanson[82].

$$\omega^2 = \omega_{LH}^2 + \frac{\omega_{pe}^2 \Omega_{ce}^2}{\left(\Omega_{ce}^2 + \omega_{pe}^2\right)} \frac{k_\parallel^2}{k_\perp^2} = \omega_{LH}^2 \left(1 + \frac{m_i}{m_e} \cot^2 \theta\right) \qquad (2\text{-}3)$$

In the lower hybrid dispersion relation, $k_\parallel$ is the parallel wavenumber, $k_\perp$ is the perpendicular wavenumber, and θ is the angle of propagation with respect to the magnetic field (i.e., θ = 0 corresponds to propagation parallel to the magnetic field).

Equation 2-3 shows that the frequency of the lower hybrid instability is not explicitly dependent on the wavenumber[82], but instead on the angle of propagation. Figure 2-1 shows the lower hybrid dispersion relation as a function of (a) the ratio of $k_\parallel$ to $k_\perp$and (b) the angle of propagation with respect to the magnetic field. In the limit where the propagation angle becomes more oblique (i.e., the instability begins to propagate along the magnetic field line), the ratio of the wavenumbers increases, the second term in the dispersion relation becomes more dominant and the frequency becomes much larger than the lower hybrid frequency. However, in the limit where the propagation angle approaches π/2 and the instability begins to propagate nearly perpendicular to the magnetic field line, the wavenumber ratio approaches zero and the second term in the dispersion relation is finite so that the lower hybrid frequency dominates the expression. Therefore, lower hybrid oscillations are observed only when $k_\perp >> k_\parallel$ and $\theta \sim \pi/2$.

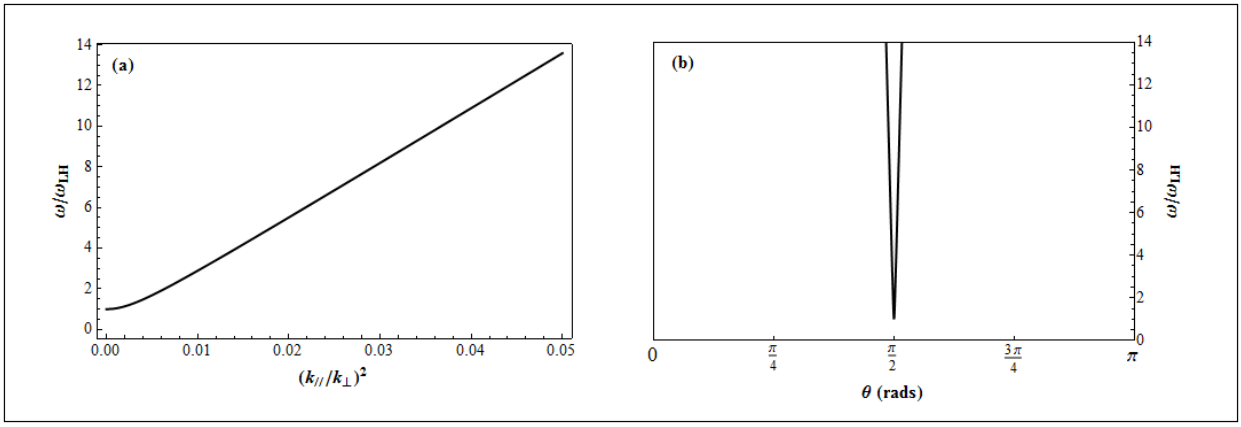

Figure 2-1: The lower hybrid frequency is plotted as a function of (a) the ratio of the parallel wavenumber to the perpendicular wavenumber squared, and (b) the angle of propagation with respect to the magnetic field line. When θ = 0, the instability propagates along the magnetic field line and θ = π/2 corresponds to a motion that is perpendicular to the magnetic field line. Lower hybrid oscillations are only observed for small values of the wavenumber ratio and when the instability motion is nearly perpendicular to the magnetic field line.

Lower hybrid waves are commonly studied in the terrestrial space environment, such as the auroral region[46,84–86], magnetosphere[87], magnetotail[38,88,89], the plasma sheet boundary layer[90], the neutral sheet boundary layer[37,91] and chemical release experiments[39–41,92]. These instabilities have also been observed at comets[43], in the magnetospheres of other planets[42] such as Venus and Mars and in laboratory experiments[16,50,77,78,93,94]. Lower hybrid waves in a magnetized plasma can be driven by a number of free energy sources such as electron or ion beams and diamagnetic drifts that are associated with density gradients.[95] Examples of lower hybrid waves include the electron-ion hybrid (EIH) instability, lower hybrid drift (LHD) instabilities and the Farley-Buneman streaming instability. The EIH instability has a frequency in the lower hybrid frequency range and is driven by strong sheared plasma flows when the shear frequency is less than the electron cyclotron frequency, but larger than the ion cyclotron frequency. Since the shear frequency is inversely proportional to the shear scale length, it can also be said that the EIH instability arises when the shear scale length is much larger than the electron gyro-radius, but less than the ion gyro-radius. This mechanism is responsible for magnetized electrons and un-magnetized ions.[41,74,75] The LHD instability, much like the EIH instability, has a frequency near

the lower hybrid frequency and has been observed in both the space plasma environment[37,87–90] and in laboratory experiments[16,93]. However, unlike the EIH instability, the LHD instability is driven by the diamagnetic drift[93,95,96], or a large density gradient. The LHD instability prefers perpendicular wavelengths that are of the same order as the electron gyro-radius so that $k_y\rho_e \sim 1$.[89,93] Finally, additional instabilities in the lower hybrid frequency range with transverse motion include a collisional streaming instability called the Farley-Buneman instability. Amateur radio operators first observed the strong echoes associated with this instability,[85,97] while Farley[85] and Buneman[86] were the first to explain the origin of these echoes. In the *E* region of the ionosphere, charged particles mirror bounce back and forth on magnetic field lines. In this region, the ion-neutral collision rate substantially exceeds the ion cyclotron frequency, causing the ions to de-magnetize relative to the electrons.[84–86,97] When the electron velocity exceeds a critical amplitude relative to the un-magnetized ions, the Farley-Buneman streaming instability develops.[94,97] The electrons are essentially streaming along the magnetic field lines through the un-magnetized ions. The common relation between all of the instabilities described, and all lower hybrid instabilities in general, is having un-magnetized ions relative to magnetized electrons, as well as propagating at frequencies near the lower hybrid frequency. The EIH instability mechanism is discussed in detail in Section 2.2. In Chapter 4 the EIH mechanism will be discussed in the context of experimental data, and the difference between the EIH instability and other lower hybrid instabilities, such as the LHD instability and Farley-Buneman streaming instability, will be examined.

2.2 Electron-ion hybrid instability

The main focus of this work is to understand the properties of the EIH mechanism. Because of the sensitivity of this instability to the plasma density, the following derivation will

consider cases where the plasma density is uniform and where there is a density gradient. Both of these regimes will be investigated in the experimental studies that will be described in Chapter 4. Consider a dc electric field ($\vec{\boldsymbol{E}} = E\hat{\boldsymbol{x}}$) in a plasma that is oriented transverse to a background magnetic field ($\vec{\boldsymbol{B}} = B_0\hat{\boldsymbol{z}}$). The combination of these crossed electric and magnetic fields give rise to a plasma flow in the direction $\vec{\boldsymbol{V}}_E = \vec{\boldsymbol{E}} \times \vec{\boldsymbol{B}}$. If this electric field is allowed to have a spatial variation, e.g., $\vec{\boldsymbol{E}} = E(x)\hat{\boldsymbol{x}}$, then the resulting flow will be spatially non-uniform and the resulting velocity shear can excite a variety of plasma instabilities – notably in the ion cyclotron range of frequencies[74]. However, if the dc electric field is localized over a distance such that the half width-half maximum (HWHM) of the electric field region, or the shear scale length ($L_E \sim E(x)[dE(x)/dx]^{-1}$), is much greater than the electron gyro-radius, but less than the ion gyro-radius, the electrons will be magnetized and the ions will be effectively un-magnetized. This gives rise to conditions that are favorable for the generation of instabilities that are in the lower hybrid range of frequency[74]. This mode is called the electron-ion hybrid (EIH) instability.

The EIH dispersion relation is derived using kinetic theory in slab geometry and follows the formalism of Ganguli, Lee, and Palmadesso[74]. As described above, we consider a plasma with a uniform background magnetic field in the z-direction and with a localized dc electric field in the x-direction. This creates an $\vec{\boldsymbol{E}} \times \vec{\boldsymbol{B}}$ drift in the y-direction. Starting with the generalized perturbed density given in Ganguli *et al.*[62] (see Equation 26 of Ref. 4),

$$n_{1\alpha}(x) = -\frac{q_\alpha \beta_\alpha}{m_\alpha} \int_{-\infty}^{+\infty} dk_x e^{ik_x x} \int_{-\infty}^{+\infty} d\xi \int_0^{+\infty} d\omega_\perp \omega_\perp \int_{-\infty}^{+\infty} dv_z$$

$$\times \int_{-\infty}^{+\infty} dk_x' \phi_k(k_x') N_\alpha(\xi)\, e^{i(k_x' - k_x)\xi}\, e^{\frac{-\beta_\alpha}{2}(\omega_\perp^2 + v_z^2)} \tag{2-4}$$

$$\times \left[1 - \sum\nolimits_{n=-\infty}^{n=\infty} \frac{(\omega_1 + \omega_{2\alpha} - \omega_\alpha^*)\, J_n^2(\sigma_\alpha)}{\omega_1 - \omega_{2\alpha} - n\Omega_\alpha - k_z v_z}\right]$$

where,

$$\beta_\alpha = \frac{1}{V_\alpha^2}$$

$$\omega_\perp^2 = v_x^2 + \eta(\xi) u_y^2 + [V_E''(\xi)/\Omega_\alpha^2]\left(u_y \langle u_y^2 \rangle - u_y^3/3\right)$$

$$u_y = v_y - \langle v_y \rangle$$

$$N_\alpha(\xi) = n_{o\alpha} y(\xi/L_E) \left(\frac{\beta_\alpha}{2\pi}\right)^{3/2}$$

$$\omega_1 = \omega - k_y V_E(\xi)$$

$$V_E(\xi) = -\frac{cE_o(\xi)}{B_o} \tag{2-5}$$

$$\omega_{2\alpha} = \frac{k_y V_E''(\xi) \rho_\alpha^2}{2}$$

$$\omega_\alpha^* = k_y \epsilon_{n\alpha} \rho_\alpha \Omega_\alpha$$

$$\epsilon_{n\alpha} = \frac{\rho_\alpha}{L_n}$$

$$\sigma = \frac{k_\perp \omega_\perp}{\Omega_\alpha}$$

and α denotes the species, k is the wavenumber, ξ is the guiding center position[62], v_x, v_y, and v_z are the equilibrium drift velocities in the x, y, and z-directions respectively, $J_n(\sigma)$ is a Bessel

function of the first kind, V_α is the thermal velocity, η is a parameterization of the magnitude of the velocity shear[62], < > represents a time average[62], $n_{0\alpha}$ is a constant density y(ξ/L_E) is a generalized radial density profile, L_E is the velocity shear scale length, ω_1 is the Doppler shifted frequency, ρ_α is the gyro-radius, and L_n is the density gradient scale length. Since the electric field is a function of position, both $V_E'(\xi)$ and $V_E''(\xi)$ are non-zero. The second derivative of the velocity shear, $V_E''(\xi)$, controls the key physics in this derivation.

To proceed, consider only the case of perpendicular propagation ($k_z = 0$). Equation 2-4 is integrated over v_z and $\omega_\perp$, which reduces the generalized perturbed density equation to

$$n_{1\alpha}(x) = -\frac{q_\alpha n_{0\alpha}}{m_\alpha}\left(\frac{\beta_\alpha}{2\pi}\right)\int_{-\infty}^{+\infty} dk_x e^{ik_x x}\int_{-\infty}^{+\infty} d\xi\, y(\xi/L_E)$$

$$\times \int_{-\infty}^{+\infty} dk_x' \phi_k(k_x') e^{i(k_x'-k_x)\xi} \qquad (2\text{-}6)$$

$$\times\left[1 - \sum_{n=-\infty}^{+\infty} \frac{(\omega_1 + \omega_{2\alpha} - \omega_\alpha^*)}{\omega_1 - \omega_{2\alpha} - n\Omega_\alpha}\Gamma_n(b_\alpha)\right]$$

where,

$$b_\alpha = k_\perp^2 \rho_\alpha^2$$

$$\Gamma_n(b_\alpha) = I_n(b_\alpha) e^{-b_\alpha} \qquad (2\text{-}7)$$

and $I_n(b_\alpha)$ is a modified Bessel function.

The following sections derive the perturbed density for the ions (2.2.1) and the electrons (2.2.2) starting with Equation 2-6. The resulting equations from Sections 2.2.1 and 2.2.2 are used in conjunction with Poisson's equation to derive a dispersion relation in Section 2.2.3. The

shooting code that is used to numerically solve the dispersion relation is then discussed in Section 2.2.4.

2.2.1 Perturbed ion density

In order to derive the dispersion relation, the perturbed ion density term is solved for starting with Equation 2-6 where $\alpha \rightarrow i$. Consider a localized electric field so that the shear scale length is much smaller than the ion gyro-radius. Since the electric field is localized over a short distance, the ions will experience the electric field over a short region during a single gyro-orbit. The influence of the dc electric field is then assumed to be negligible and $V_E(\xi) = 0$ for ions. The influence of the density gradient is also assumed to be negligible for ions ($\omega_i^* = 0$) because any density gradient present in the plasma will have a scale length much smaller than the ion gyro-radius. However, assuming that the plasma is quasi-neutral, the ions and electrons have the same zero-order density profile and $y(\xi/LE)$ remains in Equation 2-6. Equation 2-6 is reduced to a new form that is given by

$$n_{1i}(x) = -\frac{q_i n_{0i}}{m_i}\left(\frac{\beta_i}{2\pi}\right)\int_{-\infty}^{+\infty} dk_x e^{ik_x x}\int_{-\infty}^{+\infty} d\xi\, y(\xi/L_E)$$

$$\times \int_{-\infty}^{+\infty} dk_x' \phi_k(k_x') e^{i(k_x'-k_x)\xi} \qquad (2\text{-}8)$$

$$\times \left[1 - \sum_{n=-\infty}^{+\infty} \frac{\omega}{\omega - n\Omega_i}\Gamma_n(b_i)\right].$$

The variable b_i is the product of the perpendicular wavenumber and the ion-gyro-radius. In the limit where the ions are effectively un-magnetized (i.e., for a large ion gyro-radius compared to a shear scale length) and considering a short perpendicular wavelength so that $k_y >> 1$, it is reasonable to assume $b_i >> 1$. The modified Bessel function, $I_n(b_i)$ (Equation 2-7), can be simplified using an asymptotic expansion[98] so that

$$I_n(b_i) \approx \frac{1}{\sqrt{2\pi n}} \frac{e^{qn}}{\sqrt{b_i/n}\,[1+(n/b_i)^2]^{1/4}} \tag{2-9}$$

where,

$$q = \sqrt{1+\left(\frac{b_i}{n}\right)^2} + \ln\left[\frac{b_i/n}{1+\sqrt{1+(b_i/n)^2}}\right]. \tag{2-10}$$

Then $\Gamma_n(b_i)$ reduces to

$$\Gamma_n(b_i) = \frac{e^{-b_i}}{\sqrt{2\pi b_i}} \frac{e^{qn}}{[1+(n/b_i)^2]^{1/4}}. \tag{2-11}$$

For $b_i >> n$, a Taylor Series Expansion is used and Equation 2-11 can be simplified to

$$\Gamma_n(b_i) = \frac{e^{-n^2/2b_i}}{\sqrt{2\pi b_i}} \tag{2-12}$$

where higher order terms are assumed to be negligible.

For an instability where the growth rate is greater than or equal to the ion cyclotron frequency, the resonances of the perturbed density are smoothed out and the summation over n in Equation 2-8 is replaced by an integral[74],

$$\begin{aligned} n_{1i}(x) = -\frac{q_i n_{0i}}{m_i}\left(\frac{\beta_i}{2\pi}\right) \int_{-\infty}^{+\infty} dk_x e^{ik_x x} \int_{-\infty}^{+\infty} d\xi\, y(\xi/L_E) \\ \times \int_{-\infty}^{+\infty} dk_x' \phi_k(k_x') e^{i(k_x'-k_x)\xi} \left[1 - \int_{-\infty}^{+\infty} dn\, \frac{\omega}{\omega - n\Omega_i} \Gamma_n(b_i)\right]. \end{aligned} \tag{2-13}$$

The assumption that the growth rate is greater than or equal to the ion cyclotron frequency will be examined in the context of experimental results in Chapter 4. Focusing on the integral over n

in Equation 2-13, a new term is defined, $\tilde{t} = \frac{n\Omega_i}{\sqrt{2}k_\perp V_i}$. Substituting $\tilde{t}$ and $\Gamma_n(b_i)$ (Equation 2-12) into the integral gives us

$$\int_{-\infty}^{\infty} dn \frac{\omega}{\omega - n\Omega_i} \Gamma_n(b_i) = \frac{\zeta}{\sqrt{\pi}} \int_{-\infty}^{+\infty} d\tilde{t} \frac{e^{-\tilde{t}^2}}{\zeta - \tilde{t}} \tag{2-14}$$

where $\zeta = \frac{\omega}{\sqrt{2}k_\perp V_i}$. Equation 2-14 is related to the plasma dispersion function, $Z(\zeta)$[82]:

$$Z(\zeta) = -\frac{1}{\sqrt{\pi}} \int_{-\infty}^{+\infty} d\tilde{t} \, \frac{e^{-\tilde{t}^2}}{\zeta - \tilde{t}}. \tag{2-15}$$

The integral in Equation 2-15 is then reduced to

$$\frac{\zeta}{\sqrt{\pi}} \int_{-\infty}^{+\infty} d\tilde{t} \frac{e^{-\tilde{t}^2}}{\zeta - \tilde{t}} = -\zeta Z(\zeta) \tag{2-16}$$

and the perturbed ion density in Equation 2-13 becomes

$$\begin{aligned} n_{1i}(x) = -\frac{q_i n_{0i}}{m_i} \left(\frac{\beta_i}{2\pi}\right) \int_{-\infty}^{+\infty} dk_x e^{ik_x x} \int_{-\infty}^{+\infty} d\xi \, y(\xi/L_E) \\ \times \int_{-\infty}^{+\infty} dk_x' \phi_k(k_x') e^{i(k_x' - k_x)\xi} \, [1 + \zeta Z(\zeta)]. \end{aligned} \tag{2-17}$$

The final term in Equation 2-17 is dependent on the plasma dispersion function, and can be reduced using the derivative of the plasma dispersion function, where Swanson[82] shows that

$$Z'(\zeta) = -2[1 + \zeta \, Z(\zeta)]. \tag{2-18}$$

Assuming that $\zeta >> 1$, the asymptotic expansion for the plasma dispersion function derivative (Equation 2-18) is[82],

$$Z'(\zeta) \sim -2i\sqrt{\pi}\sigma\zeta\, e^{-\zeta^2} + \frac{1}{\zeta^2} \tag{2-19}$$

where,

$$\sigma = \begin{Bmatrix} 0 \\ 1 \\ 2 \end{Bmatrix} for\ Im(\zeta) \begin{Bmatrix} > 0 \\ = 0 \\ < 0 \end{Bmatrix}. \tag{2-20}$$

As previously stated above, the growth rate of the instability is greater than or equal to the ion cyclotron frequency, which is greater than zero. Since ζ is proportional to the mode frequency, ω, it can be said that *Im(ζ)* is proportional to the growth rate. As previously assumed, the growth rate is greater than or equal to the ion cyclotron frequency, and $\Omega_{ci} \neq 0$. Therefore *Im(ζ)* > 0 and *σ = 0*. As a result, only the second term in Equation 2-19 remains so that

$$[1 + \zeta Z(\zeta)] \sim -1/(2\zeta^2). \tag{2-21}$$

The perturbed ion density in Equation 2-17 then becomes

$$\begin{aligned} n_{1i}(x) = \frac{q_i n_{0i}}{2\pi m_i \omega^2} \int_{-\infty}^{+\infty} dk_x e^{ik_x x}\, k_\perp^2 \int_{-\infty}^{+\infty} d\xi\, y(\xi/L_E) \\ \times \int_{-\infty}^{+\infty} dk_x' \phi_k(k_x') e^{i(k_x' - k_x)\xi} \end{aligned} \tag{2-22}$$

where $k_\perp^2 = -\frac{\partial^2}{\partial x^2} + k_y^2$.

The remaining integrals in Equation 2-22 are carried out using the following Fourier Transformation identity[99],

$$\int_{-\infty}^{+\infty} dx e^{ixy} Z(y) = 2\pi Z(x). \tag{2-23}$$

The second derivative of the density profile [n″(x)] is negligible and assumed to be zero so that the perturbed ion density becomes,

$$n_{1i}(x) = \frac{\omega_{pi}^2(x)}{4\pi q_i \omega^2}\left(k_y^2 - \frac{\partial^2}{\partial x^2}\right)\phi_1(x) \tag{2-24}$$

where $\omega_{pi}^2(x) = \frac{4\pi n_{oi} y(x/L_E) q_i^2}{m_i}$ is the ion plasma frequency. Equation 2-24 is the perturbed ion density, which will be used in Poisson's equation to derive the dispersion relation (Section 2.2.3). In the next section, the perturbed electron density will be derived, which will also be used in Section 2.2.3.

2.2.2 Perturbed electron density

Following a similar procedure as in the previous section, Equation 2-6 is used to calculate the perturbed electron density term (α → e),

$$n_{1e}(x) = -\frac{q_e n_{0e}}{m_e}\left(\frac{\beta_e}{2\pi}\right)\int_{-\infty}^{+\infty} dk_x e^{ik_x x}\int_{-\infty}^{+\infty} d\xi\, y(\xi/L_E)$$

$$\times \int_{-\infty}^{+\infty} dk_x' \phi_k(k_x') e^{i(k_x' - k_x)\xi} \tag{2-25}$$

$$\times \left[1 - \sum_{n=-\infty}^{+\infty} \frac{(\omega_1 + \omega_{2e} - \omega_e^*)}{\omega_1 - \omega_{2e} - n\Omega_e}\Gamma_n(b_e)\right].$$

Since the instability frequency is much less than the electron cyclotron frequency, only the *n = 0* harmonic is kept, and $\Gamma_n(b_e) \to \Gamma_0(b_e)$. The modified Bessel function, $I_n(b_e)$, in Equation 2-7 becomes[100],

$$I_n(b_e) \to \frac{1}{\Gamma(n+1)}\left(\frac{b_e}{2}\right)^n = \frac{1}{\Gamma(1)} \tag{2-26}$$

where,

$$\Gamma(1) = \lim_{n\to\infty} \frac{1}{(n+1)^n} \sim 1. \tag{2-27}$$

Recalling the definition of $\Gamma_n(b_e)$ in Equation 2-7 and using Equations 2-26 and 2-27, $\Gamma_0(b_e)$ reduces to e^{-b_e}, and assuming small gyro-orbits for electrons ($b_e \ll 1$) a Taylor series expansion is performed, keeping only small order terms,

$$\Gamma_0(b_e) = e^{-be} \sim (1+b_e)^{-1} \sim 1 - b_e. \tag{2-28}$$

With this result, Equation 2-28 then simplifies to

$$\begin{aligned} n_{1e}(x) = -\frac{q_e n_{0e}}{m_e}\left(\frac{\beta_e}{2\pi}\right)\int_{-\infty}^{+\infty} dk_x e^{ik_x x}\int_{-\infty}^{+\infty} d\xi\, y(\xi/L_E) \\ \times \int_{-\infty}^{+\infty} dk_x' \phi_k(k_x') e^{i(k_x'-k_x)\xi}\left[1 - \frac{\omega_1 + \omega_{2e} - \omega_e^*}{\omega_1 - \omega_{2e}}(1 - k_\perp^2 \rho_e^2)\right]. \end{aligned} \tag{2-29}$$

The final term in brackets in Equation 2-29 is written as,

$$1 - \frac{\omega_1 + \omega_{2e} - \omega_e^*}{\omega_1 - \omega_{2e}}(1 - k_\perp^2 \rho_e^2) = \frac{-2\omega_{2e} + \omega_e^* + b_e(\omega_1 + \omega_{2e} - \omega_e^*)}{\omega_1 - \omega_{2e}}. \tag{2-30}$$

Since the ratio of the electron gyro-radius to the shear scale length is much less than 1, it is assumed that ω_{2e} and ω_e* are small compared to ω_1 (see Equation 2-5) and Equation 2-30 becomes,

$$1 - \frac{\omega_1 + \omega_{2e} - \omega_e^*}{\omega_1 - \omega_{2e}}(1 - k_\perp^2 \rho_e^2) = \frac{-2\omega_{2e} + \omega_e^*}{\omega_1} + b_e. \tag{2-31}$$

Substituting Equation 2-31 back into Equation 2-29 and using variables defined in Equation 2-5, Equation 2-29 is reduced to,

$$n_{1e}(x) = -\frac{q_e n_{0e}}{m_e}\left(\frac{\beta_e}{2\pi}\right)\int_{-\infty}^{+\infty} dk_x e^{ik_x x}\int_{-\infty}^{+\infty} d\xi\, y(\xi/L_E)$$

$$\times \int_{-\infty}^{+\infty} dk_x' \phi_k(k_x') e^{i(k_x'-k_x)\xi}\, \rho_e \qquad (2\text{-}32)$$

$$\times \left[\frac{-k_y V_E''(\xi) + \left(k_y \Omega_{ce}\right)/L_n}{\omega - k_y V_E(\xi)} + \frac{\partial^2}{\partial x^2} + k_y^2\right].$$

The remaining integrals are evaluated using Equation 2-23 in the same way they were for the ion perturbed density, and the electron perturbed density is,

$$n_{1e}(x) = -\frac{\omega_{pe}^2(x)}{4\pi\, q_e \Omega_{ce}^2}\left[{k_y}^2 - k_y \frac{{V_E}''(x) - \Omega_{ce}/L_n}{\omega - k_y V_E(x)} - \frac{\partial^2}{\partial x^2}\right]\phi_1(x) \qquad (2\text{-}33)$$

where, again, it is assumed that the second derivative of the density profile is small so that *n″(x)* is zero and $\omega_{pe}^2(x) = \frac{4\pi n_{oe} y(x/L_E) q_e^2}{m_e}$ is the electron plasma frequency. In the following section, the perturbed ion and electron densities will be used in conjunction with Poisson's equation to calculate the EIH instability dispersion relation.

2.2.3 Dispersion relation

Given the perturbed ion (Equation 2-24) and electron (Equation 2-33) densities derived above, the EIH instability dispersion relation is calculated using Poisson's equation (Equation 2-34a) and the gradient of the electrostatic potential (Equation 2-34b).

$$\nabla \cdot \vec{\boldsymbol{E}}_1(x) = 4\pi \sum_{\alpha} q_\alpha n_{1\alpha} \qquad (2\text{-}34a)$$

$$\vec{\boldsymbol{E}}_{\boldsymbol{1}}(x) = -\nabla \Phi_1(x). \qquad (2\text{-}34b)$$

The gradient of the electrostatic potential (Equation 2-34b) is substituted into Poisson's equation (Equation 2-34a) and, after summation over the species, this becomes,

$$-\nabla^2\Phi_1(x) = 4\pi(q_e n_{1e} + q_i n_{1i}) \tag{2-35}$$

where $-\nabla^2 \rightarrow -\frac{\partial^2}{\partial x^2} - \frac{\partial^2}{\partial y^2} = -\frac{\partial^2}{\partial x^2} + k_y^2$. Substituting the perturbed ion (Equation 2-24) and electron (Equation 2-33) densities into Equation 2-35 leads to the dispersion relation for the EIH instability,

$$\left(-{k_y}^2 + \frac{\partial^2}{\partial x^2} + F(\omega, x)\frac{k_y[V_E''(x) - \Omega_{ce}/L_n]}{\omega - k_y V_E(x)}\right)\phi_1(x) = 0 \tag{2-36}$$

where,

$$F(\omega, x) = \frac{\delta^2(x)}{\left[(\delta^2(x)+1)\left(1 - \frac{{\omega_{LH}}^2(x)}{\omega^2}\right)\right]}$$
$$\delta^2(x) = \frac{{\omega_{pe}}^2(x)}{{\Omega_{ce}}^2}. \tag{2-37}$$

The dispersion relation in Equation 2-36 is generalized such that a specific plasma frequency has not been defined. In the limit where a localized density gradient is present in the plasma, then the plasma frequency corresponding to the region of higher density is used[48,76] because this is where the bulk of the plasma resides and hence the instability will be more prevalent here. The dispersion relation for the EIH instability present in a plasma with a density gradient then becomes,

$$\left(-{k_y}^2 + \frac{\partial^2}{\partial x^2} + F(\omega)\frac{k_y[V_E''(x) - \Omega_{ce}/L_n]}{\omega - k_y V_E(x)}\right)\phi_1(x) = 0 \tag{2-38}$$

where $F(\omega)$ and δ (Equation 2-37) are no longer dependent on position (x). For a plasma with a uniform density (in the limit where L_n becomes large), then the plasma frequency is no longer dependent on position (x) because $y(x/L_E) \rightarrow 1$, and the dispersion relation is simplified to,

$$\left[-{k_y}^2 + \frac{\partial^2}{\partial x^2} + F(\omega)\frac{k_y V_E''(x)}{\omega - k_y V_E(x)}\right]\phi_1(x) = 0. \tag{2-39}$$

Equation 2-39 is the dispersion relation for the EIH instability in a plasma with a uniform density. Equations 2-38 and 2-39 show that the second derivative of the drift velocity is essential for driving the instability, so in order for the EIH instability to be observed experimentally, there must be a large potential gradient in the plasma (assuming a uniform magnetic field).

In order to use the shooting code that is described in Section 2.2.4 to numerically solve the EIH instability dispersion relation, the parameters in Equations 2-38 and 2-39 are normalized using the following definitions,

$$\begin{aligned} \tilde{k}_y &= k_y L_E \\ \tilde{x} &= \frac{x}{L_E} \\ \tilde{\omega} &= \frac{\omega}{k_y V_{Eo}} \\ V_E(x) &= V_{Eo} f(\tilde{x}) \end{aligned} \tag{2-40}$$

where the "twiddle" represents the normalized quantity, V_{Eo} is the equilibrium velocity in the y-direction due to the $\vec{\boldsymbol{E}} \times \vec{\boldsymbol{B}}$ drift, and $f(\tilde{x})$ is the velocity shear profile. Using these normalized quantities, $\partial^2/\partial x^2$ becomes $(1/L_E^2)(\partial^2/\partial \tilde{x}^2)$ and k_y^2 becomes $\tilde{k}_y^2/L_E^2$, and Equations 2-38 and 2-39 reduce to,

$$\left(\frac{1}{L_E^2}\frac{\partial^2}{\partial \tilde{x}^2} - \frac{\tilde{k}_y^2}{L_E^2} + F(\omega)\frac{k_y[V_E''(x) - \Omega_{ce}/L_n]}{\omega - k_y V_E(x)}\right)\phi_1(x) = 0 \tag{2-41a}$$

$$\left[\frac{1}{L_E^2}\frac{\partial^2}{\partial \tilde{x}^2} - \frac{\tilde{k}_y^2}{L_E^2} + F(\omega)\frac{k_y V_E''(x)}{\omega - k_y V_E(x)}\right]\phi_1(x) = 0. \tag{2-41b}$$

Concentrating on the lower hybrid frequency term in *F(ω)* in Equations 2-41a and 2-41b, the ratio of the ion plasma frequency to the electron plasma frequency squared can be reduced to approximately the ratio of the electron mass to the ion mass (assuming quasi-neutrality), or 1/μ, where μ is the mass ratio. Using the normalized quantities in Equation 2-40 and the mass ratio, the normalized equation for *F(ω)* is,

$$F(\tilde{\omega}) = \frac{\delta^2}{\delta^2 + 1}\frac{1}{\left(1 - \frac{\beta^2}{\tilde{\omega}^2}\right)} \tag{2-42}$$

where,

$$\beta^2 = \frac{1}{\mu\alpha^2\tilde{k}_y^2\left(1 + \frac{1}{\delta^2}\right)}$$
$$\alpha^2 = \frac{V_{Eo}^2}{\Omega_{ce}^2 L_E^2}. \tag{2-43}$$

Substituting Equation 2-42 and the normalized quantities defined in Equation 2-40 into Equations 2-41a and 2-41b gives the normalized dispersions relations for the EIH instability in the presence of a density gradient (Equation 2-44a) and for a uniform density (Equation 2-44b),

$$\left[\frac{\partial^2}{\partial \tilde{x}^2} - \tilde{k}_y^2 + F(\tilde{\omega})\frac{f''(\tilde{x}) - R_L/\alpha}{\tilde{\omega} - f(\tilde{x})}\right]\phi_1(\tilde{x}) = 0 \tag{2-44a}$$

$$\left[\frac{\partial^2}{\partial \tilde{x}^2} - \tilde{k}_y^2 + F(\tilde{\omega})\frac{f''(\tilde{x})}{\tilde{\omega} - f(\tilde{x})}\right]\phi_1(\tilde{x}) = 0 \tag{2-44b}$$

where $R_L = L_E/L_n$. These normalized equations will be used in a shooting code to solve for the real and imaginary components of the dispersion relation. The shooting code and theoretical model results will be discussed in Section 2.2.4.

2.2.4 Shooting code

To solve the normalized dispersion relations derived in Section 2.2.3 above (Equations 2-44a and 2-44b) for the real and imaginary parts of the frequency, it was necessary to use a shooting code[74], which can be found in Appendix B. The shooting code numerically solves the differential equation by guessing a solution at large values of $\tilde{x}$ (s) and integrating from $-s$ to $+s$ for given parameters and boundary conditions of the differential equation, where the boundary conditions are assumed to be $\phi(-s) = 0.1$ and $\phi'(-s) = 0.1 * k_y$. Assuming that as x approaches infinity, the solution follows WKB theory so that the solution is required to asymptotically approach zero at the boundaries ($\pm s$).[62] Given the solution of the differential equation, the dispersion relation can be obtained by solving for different values of ω given various values of normalized quantities (such as $\tilde{k}_y$, α, δ, or R_L) or experimental parameters (such as electron density, density gradient scale length, magnetic field strength, electric field or shear scale length).

Table 2-1: Typical parameters measured in ALEXIS used to calculate the real and imaginary parts of the frequency as a function of k_y for a uniform density.

Experimental Parameter	**Value**
Gas	Argon
Magnetic field strength (Gauss)	100
Electron density (m^{-3})	1×10^{15}
Electric field (V/cm)	20
Shear scale length (cm)	0.40
Ion gyro-radius (cm)	1.0
Shooting Code Parameter	**Value**
$\delta = \omega_{pe}/\Omega_{ce}$	1.0
$\alpha = V_{Eo}/(\Omega_{ce}L_E)$	0.028

In the following figures, the theoretical dispersion and growth rates are plotted using the values in Table 2-1 and a velocity shear profile of $Sech^2(x)$. The parameter values listed in Table 2-1 are typical values that have been measured in the interpenetrating plasma configuration in ALEXIS. The figures presented in this section are meant to show that the theoretical model provides us with solutions that exist for typical measurements of electron density and electric field strengths and to illustrate that it is important to consider the effect of a density gradient on the dispersion relation by showing that the frequency shifts with the addition of a localized density gradient.

Figure 2-2 shows frequency and growth rate for the EIH instability in a plasma with a uniform density. There exists an instability whose frequency is close to the lower hybrid frequency and increases with increasing wavenumber. The growth rate is non-zero for the range of wavenumbers, and peaks for perpendicular wavenumbers near 100 m^{-1}. This suggests that there is positive growth in the range of the plasma parameters that can be measured in ALEXIS.

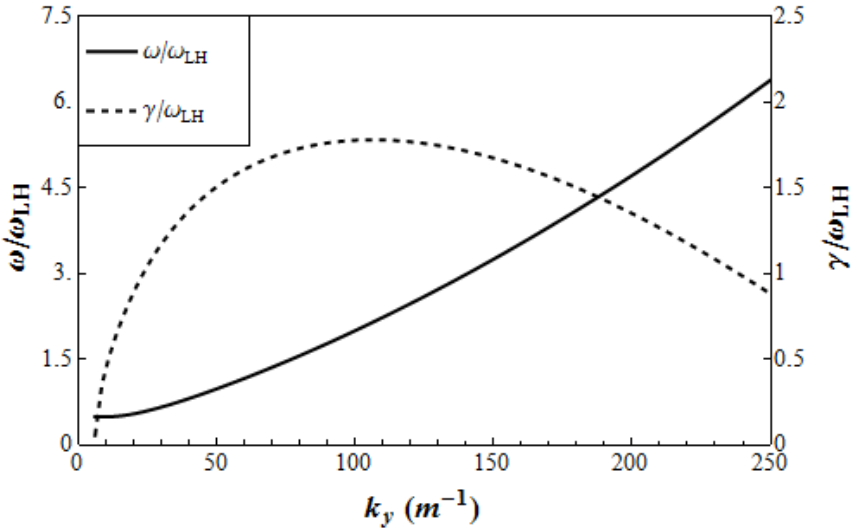

Figure 2-2: The real (solid line) and imaginary (dashed line) parts of the electron-ion hybrid frequency as a function of the perpendicular wavenumber. The frequency and growth rate are normalized to the lower hybrid frequency. This dispersion relation was calculated assuming a uniform density.

It was found that as the ratio of the electron plasma frequency to the electron cyclotron frequency *(δ)* increases, the frequency decreases exponentially closer to the lower hybrid frequency. The growth rate was found to be constant for large values of δ, but when the ratio grows small (less than 0.3) the growth rate is zero. The EIH instability is not supported for small values of δ, i.e., when the electron cyclotron frequency becomes much larger than the electron plasma frequency. The velocity shear was also found to vary the dispersion relation. Assuming a constant magnetic field strength, it was found that as the electric field increases, both the frequency and the growth rate increase linearly. For small electric field strengths, both the frequency and growth rate drop below the lower hybrid frequency and approach zero. This

suggests that the dc electric field is essential for driving the EIH instability in a uniform density. The next figure will show how the effects of the density gradient change the dispersion relation, and will compare how the frequency and growth rate differ from the uniform density model.

Using the values listed in Table 2-1 and a perpendicular wavenumber of 70 m^{-1}, the frequency and growth rate as a function of the ratio of the shear scale length to the density gradient scale length are shown in Figure 2-3. It is assumed that L_E remains constant and L_n is varied. As L_n becomes large (i.e., the density becomes more uniform), the ratio of the two scale lengths (L_E/L_n) becomes small and the predicted frequency and growth rate approach that of a uniform density. The growth rate is highest for $L_E/L_n \sim 0.4$. It will be shown in Chapter 4 that this is a typically measured value in ALEXIS, and so there exists a regime where there is a stable solution for the EIH instability in a density gradient when the shear profile is more localized than the density gradient profile. As the density gradient becomes more localized than the velocity shear, the values for the frequency and the growth rate asymptotically approach zero. The frequency decreases well below the lower hybrid frequency as a density gradient is introduced, and it is shown that the growth rate is non-zero, so the EIH instability can be supported.

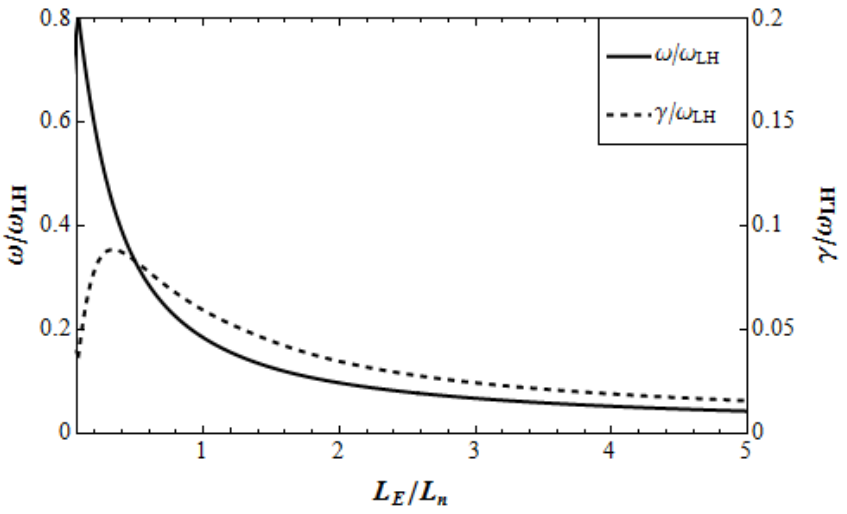

Figure 2-3: The EIH frequency (solid line) and growth rate (dashed line) as a function of the ratio of the shear scale length to the density gradient scale length (R_L) for k_y = 70 m^{-1}. When the ratio is zero, there is a uniform density present in the plasma. As the ratio grows, a sharp density gradient appears in the plasma and the frequency and growth rate both decrease below the lower hybrid frequency.

Figure 2-3 showed that the addition of a density gradient term decreased the mode frequency and growth rate significantly. The dispersion relation as a function of the perpendicular wavenumber for a plasma with a density gradient is shown in Figure 2-4. The dispersion relation is calculated using the parameters listed in Table 2-1 and with $L_E/L_n = 0.33$ so that the velocity shear profile is more localized than the density gradient. The mode frequency decreases asymptotically to $0.1\omega_{LH}$ for an increasing perpendicular wavenumber. The growth rate is positive, but much less than the lower hybrid frequency, and also decreases for increasing perpendicular wavenumbers. This suggests that the instability can be supported for a wide range of perpendicular wavelengths in a plasma with a density gradient in the ALEXIS device. In Chapter 4, the experimental data will be compared to the theoretical dispersion relation using the shooting code results.

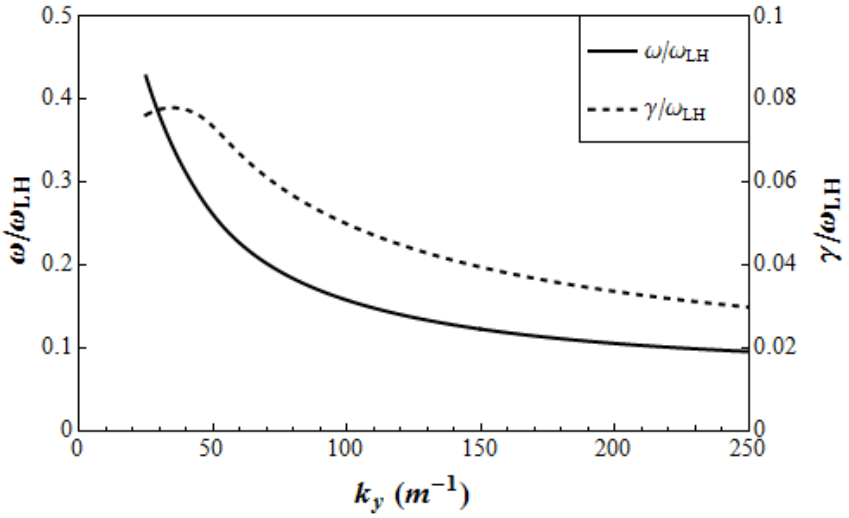

Figure 2-4: The frequency (solid line) and growth rate (dashed line) are plotted as a function of the perpendicular wave number when there is a density gradient present in the plasma (R_L = 0.33). Notice that the density gradient significantly lowers the frequency and growth rate values compared to the uniform density dispersion relation.

2.3 Whistler wave

In 1918, Heinrich Barkhausen heard whistling tones while listening to signals from an antenna.[2] In World War II, German troops that were using radios to intercept allied radio transmissions reported hearing the same kinds of tones.[82] In 1953, 35 years after the whistling tones were first reportedly heard, L.R.O. Storey explained that when lightning occurs in one of Earth's hemispheres, audio frequency waves are generated in the ionosphere[1,2,82]. These waves, which are highly dispersed, travel along the magnetic field lines to the opposite hemisphere with the highest frequencies arriving first.[1] This results in a distinct whistling tone.

The whistler wave is the electromagnetic branch of the electron-ion hybrid instability. Although the whistler wave is not the focus of this dissertation, a brief explanation of the dispersion relation is included for completeness. For a wave propagating along a magnetic field line, the dispersion relation, which is discussed in detail in Swanson[82], Chen[1], and Gurnett and

Bhattacharjee[2], is equal to n^2 (the index of refraction), which is calculated from the elements of the cold plasma dielectric tensor[82], where $\Omega_{ci} << \omega << \Omega_{ce}$, so that,

$$n^2 = K_1 + iK_2 = 1 - \frac{\omega_{pi}^2}{\omega(\omega + \Omega_{ci})} - \frac{\omega_{pe}^2}{\omega(\omega - \Omega_{ce})} \sim \frac{\omega_{pe}^2}{\omega\Omega_{ce}}. \quad (2\text{-}45)$$

The index of refraction is related to the frequency and wavenumber,

$$k = \frac{\omega\, n}{c}. \quad (2\text{-}46)$$

Substituting Equation 2-45 into Equation 2-46 and solving for the frequency, ω, gives the Whistler wave dispersion relation,

$$\omega = \frac{c^2 k^2 \Omega_{ce}}{\omega_{pe}^2}. \quad (2\text{-}47)$$

The dispersion relation can be used to calculate the phase and group velocities, which are both dependent on ω. This leads to the high frequencies traveling faster than the lower frequencies along the magnetic field lines, causing the distinct whistling tone. Because of the close relationship between the EIH mode and the Whistler wave, it may be possible for future researchers to investigate the electromagnetic branch of the EIH instability in a future ALEXIS experiment.

2.4 Summary

To summarize, this chapter introduces the theoretical dispersion relation for the electron-ion hybrid instability. Because of the close relationship between the EIH instability and other lower hybrid instabilities, the shared mechanism was discussed in Section 2.1. Examples of electrostatic lower hybrid instabilities were also briefly examined in this section. In Section 2.2,

the derivation of the EIH instability dispersion relation for a plasma with a density gradient (Equation 2-44a) and a uniform density (Equation 2-44b), as well as the shooting code that is used to numerically solve the dispersion relations are discussed in depth. In Chapter 4, experimental data will be compared to the theoretical dispersion relations that are numerically solved using this shooting code. Finally, the electromagnetic branch of the EIH instability, the whistler wave, is briefly described in Section 2.3. In future works, the electrostatic to electromagnetic branch transition can be studied.

Chapter 3: Experimental Design and Hardware

The experiments described in this dissertation were performed in the Auburn Linear EXperiment for Instability Studies (ALEXIS). ALEXIS is a magnetized cylindrical plasma column designed to study different types of instabilities that are caused by sheared plasma flows. Both electrostatic[17–19,72] and electromagnetic[101] instabilities are studied in the device using a variety of *in-situ* diagnostics. This chapter describes the experimental hardware used in this study, including the vacuum vessel, plasma generation and modification, and plasma diagnostics.

3.1. Vacuum vessel

ALEXIS is a 170 cm long, stainless steel vacuum vessel which is based on the ISO-100 (100 mm diameter) flange configuration. Figure 3-1 shows the five components of the device consisting of: (A) the antenna, (B) a standard 6-way cross, (C) the main chamber, (D) a custom box used for optical access, and (E) the double-walled, water-cooled section. The ports are labeled using numbers 1 through 7 and the electromagnets are labeled a through i.

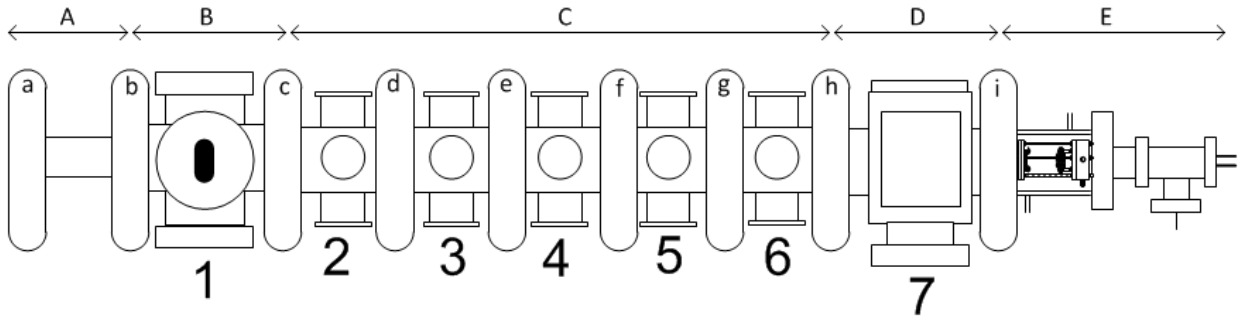

Figure 3-1: The Auburn Linear Experiment for Instability Studies has 5 main components – The antenna (A), a standard 6-way cross (B), the main chamber (C), a custom box that can be used for optical access (D), and a double-walled water-cooled section with a tee attached (E). The ports are numbered 1 (closest to the antenna) to 7 (farthest from the antenna). The magnets are lettered a through i.

Section A is the primary plasma generation region. The rf antenna is a single turn loop made of copper and fitted to the outside of a 5 cm diameter, 25 cm long glass dome. The glass dome is fitted to an ISO-100 glass to metal flange that connects it to the rest of the vacuum chamber. Plasmas are generated using a radio frequency (f = 13.56 MHz) generator that is discussed in detail within Section 3.5. A faraday cage surrounds the antenna in order to reduce the RF noise in the room.

The antenna section is connected to a standard 6-way cross (section B in Figure 3-1), which has a 10 cm inner diameter and a length of 26 cm. The side ports can be fitted with ISO-100 windows, for viewing the plasma, or ISO-100 flanges for *in situ* diagnostics. The 6-way cross is then connected to the main chamber.

The main chamber (section C in Figure 3-1) is 91 cm long with a diameter of 10 cm. The cylindrical sides are fitted with QF40 (40 mm diameter) ports separated by 18.3 cm axially and located every 90 degrees azimuthally. There are 20 ports located on the main chamber that can be used to attach gas inlets, vacuum equipment, or *in situ* diagnostics. The ends of the main chamber are fitted with ISO-100 flanges which are used to connect sections B and D.

A custom box, section D in Figure 3-1, is used for optical access. The custom box has three polycarbonate windows with dimensions of 30 by 50 cm, or a viewing area of 150 cm^2. This large viewing area allows for excellent optical access over the entire cross sectional area of the plasma. The other three sides of the custom box are fitted with ISO-100 flanges in order to connect it to the main chamber (D), the water-cooled section (E), and a high-speed diffusion pump, which attaches to the bottom port.

Finally, section E consists of an ISO-100 double-walled water-cooled section. This section houses the thermionically emitting filaments that are used as a secondary plasma source. Water lines are attached to this section to prevent overheating while the filaments are in use. The filament source is discussed in detail in Section 3.5. An ISO-100 to KF50 adaptor is connected to the water cooled section so that a KF50 tee could be added. The tee is needed to connect two feed-throughs: a high current electrical feed-through, which provides the heating source to the filament and a high voltage electrical feed-through to provide a biasing voltage to a grid that is in front of the filament.

The high current feed-through has two copper leads that are 0.375 inches in diameter and 0.625 inches apart. The leads were initially 4 inches long, but were cut down to 1 inch so they could be fit into the KF-50 tee. Because the feed-through leads are so thick, custom-made fittings are required to attach a 12 AWG cable. The fittings are made of 1.5 inch long, 0.5 inch diameter (outside) copper. Set screws are used to secure the fittings in place. The feed-through with the custom fittings attached is seen in Figure 3-2.

Figure 3-2: High current feed-through used to power the filament source. Copper fittings were made for each lead to connect cables.

3.2. Electromagnet configuration

ALEXIS uses nine electromagnet coils (Figure 3-1) to produce the axial magnetic field that confines the plasma column. The electromagnets were designed and manufactured by Everson Electric Company, which is now Everson Tesla Incorporated. In order to compensate for the uneven spacing of some magnets, and to reduce the "ripple" of the magnetic field, three coil configurations are used. Table 3-1 lists the coil configuration type and the axial locations of all nine electromagnets. Coil type 1 has 48 turns, type 2 has 50 turns, and type 3 has 59 turns.[73]

Table 3-1: The axial locations of each magnet with respect to the antenna, and the different configurations of each coil.

Magnet	**a**	**b**	**c**	**d**	**e**	**f**	**g**	**h**	**i**
Axial Location (m)	0	0.183	0.443	0.626	0.809	0.992	1.175	1.358	1.618
Configuration Type	1	1	3	1	2	2	1	3	1

Each coil is wound using hollow copper tubing with an inner diameter of 0.36 cm and an outer diameter of 0.71 cm. It is necessary to use copper tubing so the electromagnets can be water-cooled. Fiberglass tape insulates the copper, and then the magnet is potted in epoxy resin. This leaves all magnets with an inner diameter of 20 cm, an outer diameter of 33 cm, and an axial length of 6.4 cm.[73]

There are two power supplies that provide current to the magnet coils. The two coils surrounding the antenna region ("a" and "b" in Figure 3-1), or the source magnets, are controlled using a Power Ten model P63C-10330, 6.6 kW power supply. The remaining seven coils ("c" through "i") that surround the 6-way cross, main chamber, and custom box, are controlled using a Power Ten model P66C-40330, 13 kW power supply. Each power supply can provide a dc current up to 330 A.

3.3. Vacuum pumps

The ALEXIS device uses a two-stage, vacuum pumping system to maintain a base pressure in the 10^{-5} Torr range. Figure 3-3 shows a diagram of the ALEXIS vacuum and gas regulation systems. The first stage uses an Axiden model 2010SD, 2.8 liter per second roughing pump (P1 in Figure 3-3). Using the roughing pump, pressures of about 10 mTorr can be maintained. The second stage uses an Edwards 100/300c Diffstak, 300 liters per second diffusion pump (P2 in Figure 3-3), which lowers the pressure from the mTorr range to the working base pressure. The diffusion pump is also backed by the roughing pump.

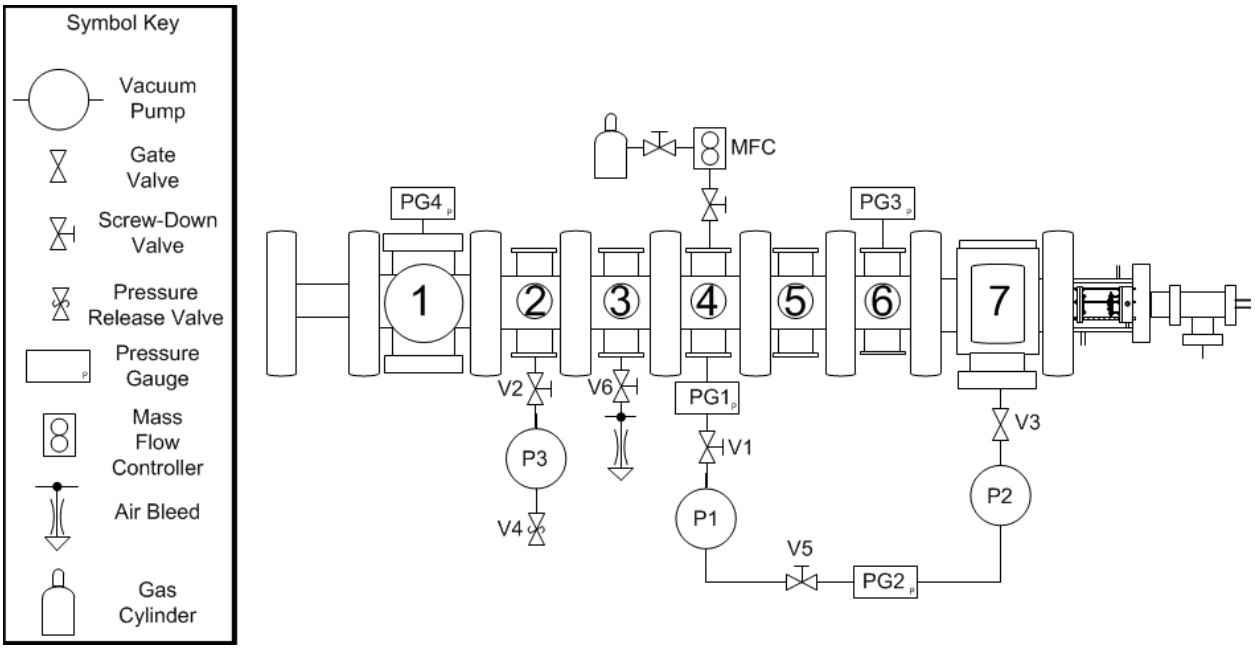

Figure 3-3: A schematic diagram of the ALEXIS vacuum and gas regulation system. P1 is the roughing pump, P2 is the diffusion pump and P3 is the adsorption pump. V1 is the roughing valve between the roughing pump and vacuum vessel, V2 is the valve between the adsorption pump and main chamber, V3 is the gate valve between the diffusion pump and the main chamber, V4 is the pressure release valve on the adsorption pump, V5 is the backing valve between the roughing and diffusion pumps and V6 is the up to air valve on the chamber. PG1 and PG2 are the two thermocouple gauges, PG3 is the B-A ionization gauge and PG4 is the cold cathode pressure gauge.

An additional vacuum component is a Varian VPS-630 adsorption pump (P3 in Figure 3-3). The adsorption pump is not necessary for creating vacuum in the ALEXIS device, but it allows for good vacuum conditions to be established in as little as six hours. Instead of mechanical parts, the adsorption pump has a high surface area material (zeolite), which is cooled to liquid nitrogen temperatures. When the chamber is at roughing pressure, the roughing valve (V1 in Figure 3-3) between the roughing pump and the main chamber is shut, and the valve between the main chamber and adsorption pump is opened (V2 in Figure 3-3). Gas molecules that still remain in the chamber are then drawn into the adsorption pump and collect on the zeolite surface, decreasing the pressure in the chamber.[73] When the chamber pressure reaches approximately 10^{-4} Torr, the adsorption pump valve is then shut, and the gate valve (V3 in Figure 3-3) between the diffusion pump and chamber is opened. A pressure release valve (V4 in Figure

3-3) keeps the adsorption pump from over pressurizing as the temperature rises from liquid nitrogen temperatures.

After repeated uses, the zeolite will eventually become saturated with water vapor, which will greatly reduce the efficiency of the adsorption pump. To remove the water vapor and regenerate the zeolite, the pump must be baked out at 250 degrees Celsius for 1 to 2 hours. This is done while the chamber is under roughing vacuum, and the valve to the adsorption pump is opened to the chamber.

3.4. Gas regulation

Another important part of the ALEXIS plasma device is the gas regulation system. This allows for multiple gas species to be used independently or mixed in different ratios. The two components of the gas regulation system are gas flow control and several kinds of gauges to measure gas pressures within the vacuum chamber.

Gas flow into the vacuum chamber is maintained using a MKS instrument model 1179A mass flow controllers (MFC in Figure 3-3). The mass flow controllers regulate flows up to 10 sccm (standard cubic centimeters per minute). The advantage of having multiple mass flow controllers is this allows for multiple gas species to be mixed at different ratios, or to switch to different gas species without having to switch out gas lines. The mass flow controllers are connected to an MKS instrument type 247 controller which is integrated into a data acquisition (DAQ) system. This allows for computer control of the system and enables reproducible operating conditions to be achieved in ALEXIS.

The neutral pressure within the vacuum chamber is monitored using several different gauges. There are two thermocouple gauges as well as a Bayerd-Alpert (B-A) ionization gauge

that are integrated into a Kurt J. Lesker KJL 4500 ionization gauge controller. The first of the thermocouple gauges (PG1 in Figure 3-3) is connected to the main chamber at port 4 where the roughing pump is connected to the main chamber and is used to monitor the base pressure of the vacuum vessel. The second thermocouple (PG2 in Figure 3-3) is mounted between the roughing pump and the diffusion pump and is used to monitor the backing pressure between the two pumps. The B-A gauge (PG3 in Figure 3-3), which can read pressures as low as 10^{-8} Torr, is mounted on a 61 cm long QF40 nipple that connects to the top of the main chamber at port 6. The use of the nipple allows the gauge to be kept out of the magnetic field, which could damage the gauge. A Kurt J. Lesker 943 cold cathode pressure gauge (PG4 in Figure 3-3) also allows for the reading of pressures down to 10^{-6} Torr. This gauge is connected to the top of the 6-way cross (port 1) and is held out of the magnetic field using a 13 cm long QF40 nipple. The thermocouple gauges can only read pressures as low as 10^{-2} Torr, so the use of the B-A gauge and cold cathode gauge are essential.

3.5. Plasma generation and modification

In its present configuration, the ALEXIS device uses two plasma sources – one at each end of the vacuum chamber. Each of these sources is described in this section. The primary plasma source for ALEXIS is a radio frequency (rf) plasma source. The first component of the rf plasma source is a Kurt J. Lesker model R601, 600 W power supply that has a fixed frequency of 13.56 MHz. The rf power supply is a combination of a frequency generator and amplifier and is integrated into the DAQ system in order to control and monitor the forward and reflected powers. The power is coupled into the plasma using a matching network and an antenna, which was described in Section 3.1.

The matching network is based on a modified L network[73]. A schematic of the matching network is shown in Figure 3-4. There are two load capacitors connected in parallel and a tune capacitor. The load capacitors used are a Comet CV1C-500 UINN (15-500 pF, 15kV, 79A) capacitor (labeled C1 in Figure 3-4) and a Jennings (25-2500 MMFD, 6kV) radio capacitor (labeled C2 in Figure 3-4). The tune capacitor is a Comet CV05C-1500 LON/5, 10-1500 pF, 5kV/3kV capacitor (labeled C3 in Figure 3-4). A Byrd model 4391A power meter is placed between the RF power supply and the load capacitors and allows the matching network to be tuned so that most of the power is coupled into the plasma rather than being reflected.

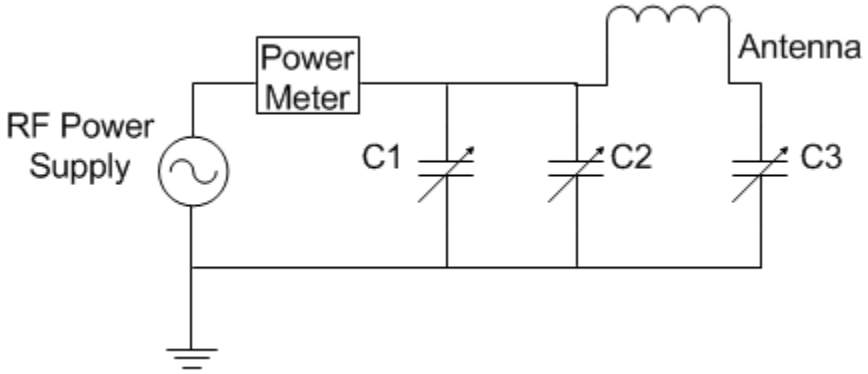

Figure 3-4: The matching network consists of an RF power supply, Byrd power meter, two load capacitors (C1 and C2), a tune capacitor (C3), and an antenna. The load capacitors are in parallel with each other, and the power meter is connected in series between the RF power supply and the load capacitors.

The second plasma source is located in the water cooled section (section E in Figure 3-1) and is designed to have a much smaller diameter than the main rf generated plasma. It is a "hot filament" plasma source; i.e., it uses thermionic emission from a heated wire to produce a plasma. The hot filament source (Figure 3-5 and "a" in Figure 3-7) has three separate, parallel filaments that are made from 4 inch long, 0.25 mm diameter tungsten. A Sorensen Model XG 1500 W, 20V-76A DC power supply (PS-3 in Figure 3-6) is used to resistively heat the filaments. The filaments are attached to a 3 inch diameter, 0.25 inch thick Macor block. The Macor block is then screwed onto a ¾ inch long aluminum ring ("b" in Figure 3-7) with a 3 inch

outer diameter and a 2.5 inch inner diameter, which has four set screws that are used to hold the assembly in place in the water-cooled section.

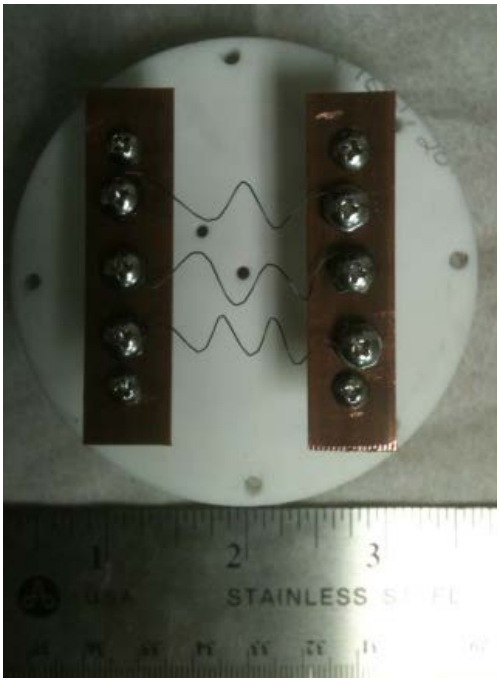

Figure 3-5: The filament source in the back of the chamber is shown above. Each filament is made from 4 inch long, 0.25 mm diameter tungsten.

In order to perform the wave experiments, it is necessary to create a highly localized radial electric field at the boundary between the rf and filament plasmas (Figure 3-6). It is possible to control this electric field by changing the plasma potential of the filament plasma using a 1.5 inch x 1.5 inch square, stainless steel mesh (100 lines/inch) placed 3.5 inches in front of the filament source (Figure 3-6 and "c" in Figure 3-7). A Xantrex XHR 600-1.7 (i.e., 0 to 600 V, 0 to 1.7 A) DC power supply (PS-2 in Figure 3-6) is used to bias the filament source with respect to the mesh, causing the electrons to accelerate away from the filament. The power supply is operated in constant current mode to maintain a constant emission current in the range of 10 to 100 mA. This ensures a constant flux of electrons into the plasma which helps control the density of the plasma. The mesh bias is controlled using a four-quadrant Kepco BOP100-1M

(i.e., 0 to +/- 100 V, 0 to +/- 1 A) bipolar operational power supply/amplifier (PS-1 in Figure 3-6). This Kepco power supply is also integrated into the DAQ system to allow for computer control. Figure 3-6 shows the circuit schematic of the hot filament source, the biasing mesh, the blocking disk, grounding mesh, rf antenna and matching network, and the different power supplies used to control this portion of the experiment.

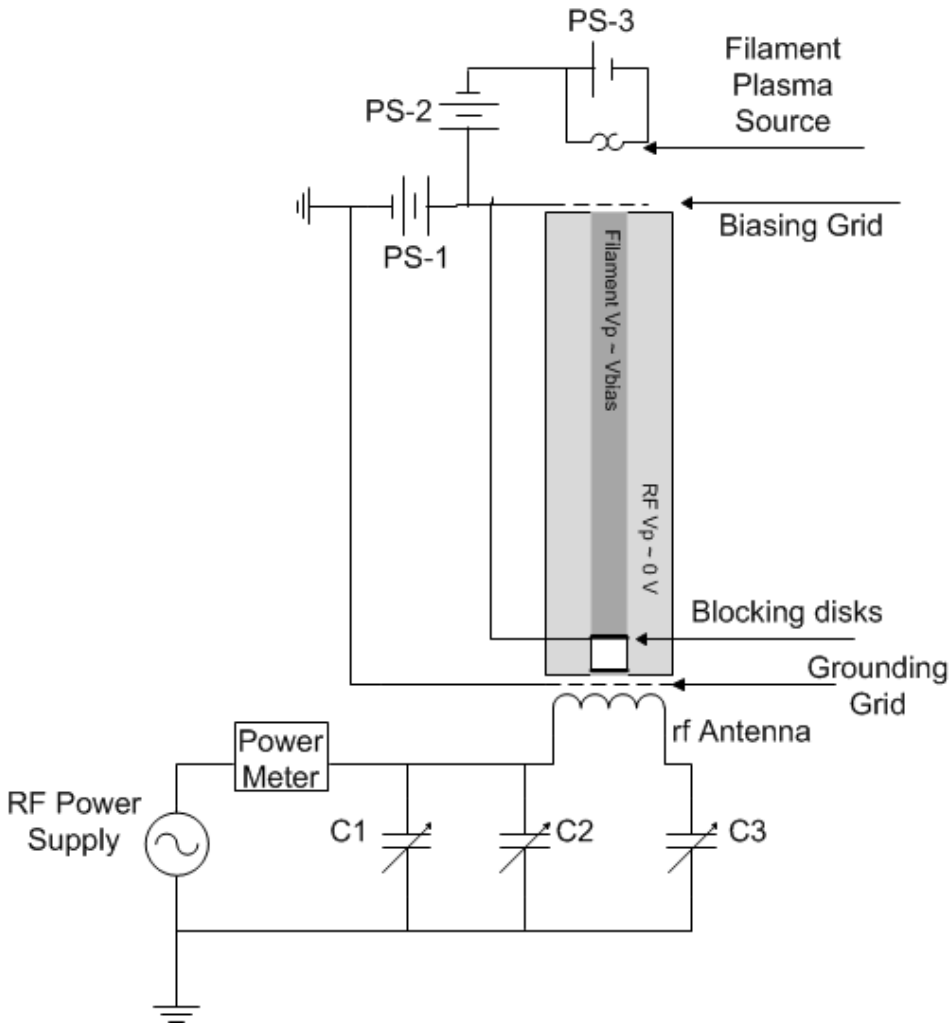

Figure 3-6: Schematic interpenetrating plasma experiment. The rf antenna and matching network are shown at the bottom of the schematic and the hot filament source circuit is shown at the top, where PS-1 controls the bias on the mesh, PS-2 controls the bias voltage on the filament source relative to the biasing mesh, and PS-3 resistively heats the filament source. The biasing grid allows the plasma potential of the filament plasma to be controlled independently from the rf plasma potential. This allows a localized radial electric field to form near the boundary between the plasmas. The blocking disk is electrically connected to the biasing grid, which limits the amount of parallel current in the experiment.

The mesh attaches to the back of a 0.25 inch thick Macor disk that has a 3 inch outer diameter. The disk has a 0.94 inch diameter hole at the center to allow the filament plasma to pass through into the main chamber. The Macor disk, also keeps the rf plasma electrically isolated from the biasing mesh. A 0.25 inch thick aluminum disk (with the same dimensions as the Macor) attaches to the front of the Macor in order to terminate the rf plasma ("d" in Figure 3-7). Threaded rod is used to keep the filament aligned with the hole in the Macor, and ensures that the aluminum disk is electrically connected to the aluminum ring stand (and chamber ground).

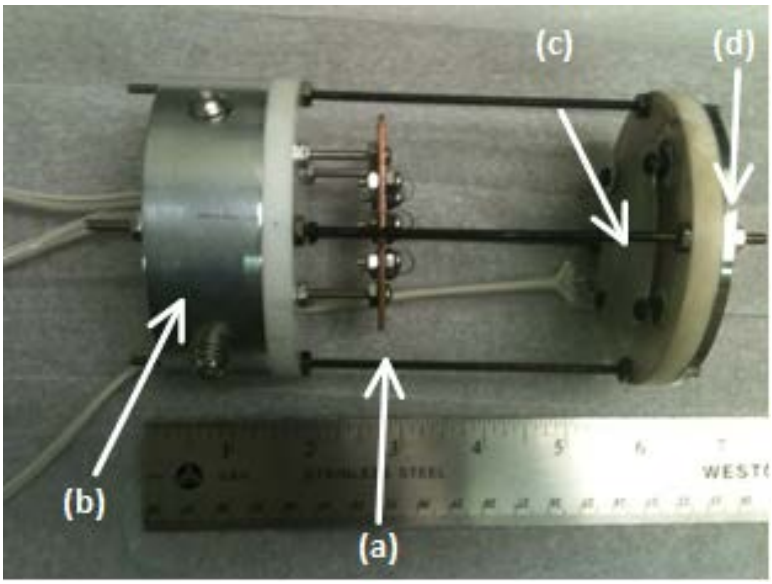

Figure 3-7: The filament assembly includes: (a) the tungsten filament, (b) the aluminum ring used to hold the assembly in place in the water-cooled section, (c) a stainless steel mesh that is used to bias the filament plasma, and (d) an aluminum disk to insure the rf plasma remains grounded.

A blocking disk (Figure 3-6 and Figure 3-8) is used to isolate the center of the rf plasma and to terminate the filament plasma. The disk is made from 1 inch diameter, 0.5 inch thick Macor, with 1 inch diameter, 0.063 inch thick stainless steel disks attached to either side. The Macor is needed between the stainless steel disks to electrically isolate the plasmas from each other. The side facing the filament plasma can be biased to the same potential as the stainless steel mesh, as is shown in the experimental schematic in Figure 3-6. By biasing the blocking

disk, the entire filament plasma can be maintained at a single potential that can be set independently of the outer, rf plasma. This helps to avoid drawing any field aligned current in the plasma. A threaded rod screws into the side of the Macor and covered in single-bore ceramic tubing to keep the blocking disk upright. The blocking disk is inserted into the vacuum vessel from the Port 1, bottom flange.

Figure 3-8: A blocking disk is used block out the center of the rf plasma, and to terminate the filament plasma. One side of the disk is biased to the same potential as the stainless steel mesh, so that a uniform plasma potential can be set on the filament plasma.

A high transparency stainless steel mesh is also added to the six-way cross (just behind the antenna) to keep the rf plasma electrically connected to chamber ground and ensure that a constant electric field between the rf and filament plasmas could be reproduced. The mesh also completes the Faraday cage around the rf antenna, thus reducing the amount of rf noise that is picked up by the various instruments and diagnostics used in the lab.

3.6. Diagnostics

There are several different types of *in-situ* diagnostics used on ALEXIS. This wide variety of diagnostics allows the measurements of plasma potential (3.6.1), electron density and

temperature (3.6.2), electrostatic fluctuations and wavenumbers (3.6.3), and electromagnetic fluctuations (3.6.4).

3.6.1. Emissive probe

In 1923, Irving Langmuir described two ways to measure plasma potential.[102] The first method uses a cold Langmuir probe (which will be described in 3.6.2) and the second using an emissive probe. While both techniques have been proven to give an accurate measurement of the plasma potential, it can be more challenging to determine the plasma potential from a Langmuir probe trace. Using an emissive probe can overcome many of the difficulties that often accompany the Langmuir probe.[103] When a probe is inserted into a typical laboratory plasma, the probe collects more electrons than ions because of the higher mobility of the electrons. This causes the probe to acquire a potential lower than the plasma potential, called the floating potential. The floating potential allows the probe to collect additional ions in order to maintain a zero net current.[103] The purpose of the emissive probe is to heat the tip until the floating potential reaches the plasma potential. To achieve this, the tip is heated to a temperature where electrons are emitted (thermionic temperature) and this current dominates the ion current.[104] When the electron emission exceeds the electron saturation current, the probe will float to a potential that is approximately the plasma potential.[102,103]

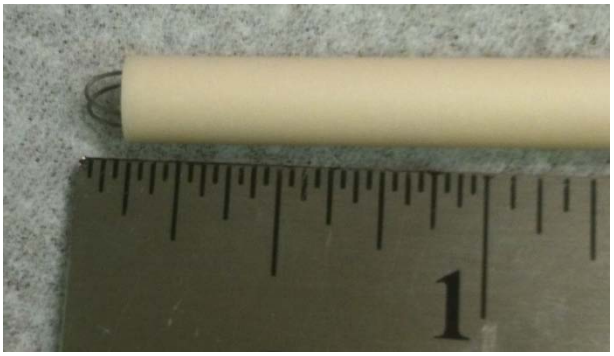

Figure 3-9: Example of the double emissive probe that is used on ALEXIS. Both loops are made from 0.1 mm diameter tungsten wire that has been set in a 3 mm diameter loop.

An electrically floating double emissive probe is used in ALEXIS (Figure 3-9). The probe tips are made from 0.1 mm diameter tungsten wire set in a 3 mm diameter loop. The emissive probe only has tungsten at the tip, with 18 AWG copper running through the ceramic in order to reduce the power requirements. Only one tip on the probe is used at a time, with the other tip serving as a backup. Using a GW Instek model GPR-3060D (30 A, 6 V) dc power supply, the tips are heated to thermionic temperatures ($T > 2000$ K).[105] This probe setup is mounted on a linear probe drives so that the probe position can be controlled via computer.

The emissive probe is calibrated to find the correct heating current that must be applied to get an accurate reading of the plasma potential. When the probe is inserted into the plasma column, a bias voltage applied to the tip is swept from -60 V to +60 V using a Keithley 2400 source meter. The current collected by the probe tip is recorded for different applied voltages (called an I-V characteristic trace). This was repeated for several different heating currents. Figure 3-10 shows the floating potential as a function of the heating current. As the heating current is increased, the floating potential increases asymptotically to the plasma potential. The calibration process is performed in the rf plasma (black curve) and filament plasma (red curve) independently, and again when both plasmas are on (blue curve). The vertical dashed lines show the appropriate heating currents to use in order to measure the plasma potential accurately in

each case. For the rf plasma, an appropriate heating current is 1.73 A (black dashed line), and 1.60 A (red dashed line) for the filament plasma heating current. When both plasmas are on, a heating current of 1.65 A (blue dashed line) is used.

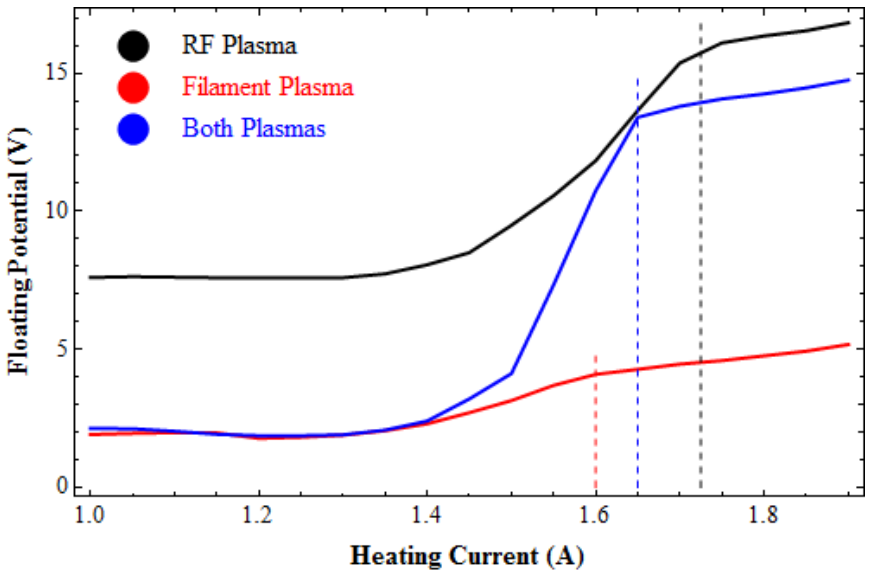

Figure 3-10: The floating potential measured using an emissive probe as a function of the applied heating current for just an rf plasma (black), just a filament plasma (red) and both plasmas (blue). The dashed curves indicate the appropriate heating currents used to measure the plasma potential.

The emissive probe measures the floating potential (when cold) or the plasma potential (when heated). As the probe moves radially across the plasma column, 10 voltage measurements are recorded at each radial position by an Agilent 34401A digital multimeter (DMM). The potential is calculated by taking the average of the measurements at each radial position. The potential profile is differentiated using the 2nd order central method to calculate the electric field,

$$E_i = \frac{1}{2\,dx}\left(V_{p\,i+1} - V_{p\,i-1}\right) for\ i = 0,1,2,\ldots,n-1 \qquad (3\text{-}1)$$

where V_p is the plasma potential at a given position, dx is the distance between positions of the measurements and n is the number of measurements taken.

3.6.2. Langmuir probes: single and double probe

Langmuir probes were one of the earliest diagnostics used to measure basic plasma parameters such as the floating and plasma potential, electron density, and the electron temperature.[106] A Langmuir probe can be as simple as a small wire that is placed into the plasma. The plasma parameters can be determined from the current-voltage (I-V) characteristic trace, which is a plot of the current flowing through the probe as a function of the bias voltage (measured relative to ground) that is applied to the probe. The most common interpretation of the Langmuir probe I-V trace is based upon the assumption of a quasi-neutral, Maxwellian plasma at infinity that has warm electrons with an electron temperature, T_e, and cold ions with an ion temperature, $T_i \approx 0$. An example of a typical Langmuir probe characteristic trace is shown in Figure 3-11. It is noted that a typical Langmuir probe I-V trace is oriented such that a net ion current is negative and a net electron current is positive.

As noted above, the Langmuir probe trace represents the current collected by the probe as a function of the applied bias voltage. The total current collected at any bias voltage (V) is the sum of ion and electron currents to the probe. This result is well established in plasma physics and is discussed widely in the literature.[107–109] The total current is given by[103,108]:

$$I = I_i + I_e(V) = en_o A\sqrt{\frac{T_e}{m_i}}\left[-e^{-\frac{1}{2}} + \frac{1}{2}\sqrt{\frac{2m_i}{\pi m_e}}exp\left(\frac{e(V - V_p)}{T_e}\right)\right] \qquad (3\text{-}2)$$

where m_i is the ion mass, m_e is the electron mass, A is the surface area of the probe, n_0 is the plasma density, V_p is the plasma potential, and e is the fundamental electron charge (1.6×10^{-19} C). The first term (I_i), which is independent of the bias voltage, represents the ion saturation current. The second term (I_e), which is dependent on the bias voltage, represents the electron current.

When plotted, there are several important features to note on the Langmuir probe I-V trace (Figure 3-11). First, the ion saturation current (lower dashed line) is the maximum negative current the probe can draw and is independent of voltage, as indicated in Equation 3-2. The electron saturation current (upper dashed line) is the maximum positive current the probe can draw. The blue dot represents the floating potential, which occurs where there is no net current. The dashed green lines in Figure 3-11 show the linear fits to the electron saturation and transition regions. The plasma potential, represented by the red dot, is taken as the point where the two fits cross. The single tipped Langmuir probe traces are often difficult to interpret in rf-generated plasmas due to the rapid oscillations of the plasma potential. An alternative method is the double probe.

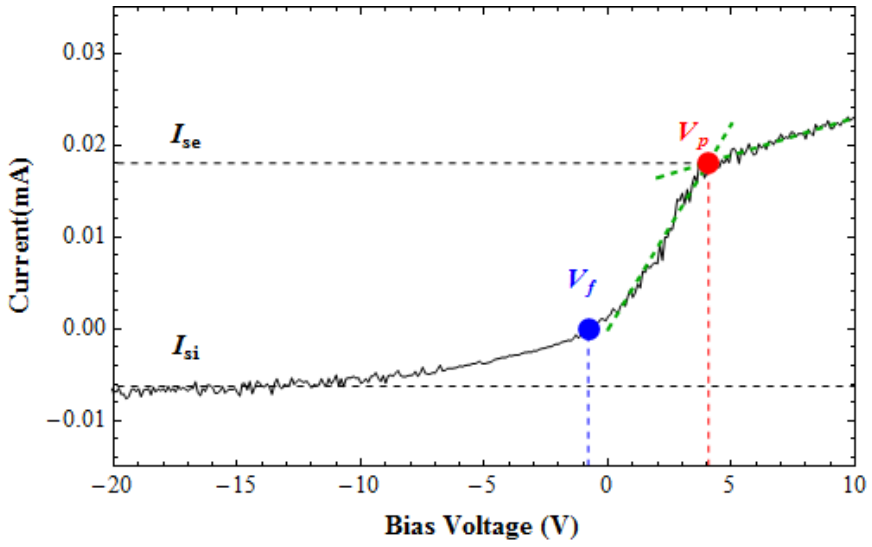

Figure 3-11: A typical I-V characteristic trace taken with a single tipped Langmuir probe. The horizontal dashed lines represent the electron saturation current (upper) and the ion saturation current (lower). The blue dot shows the location of the floating potential, where the net current is zero. The green dashed lines represent the linear fits to the electron saturation and transition regions. The point where the linear fits meet is the plasma potential, which is represented by the red dot.

A double probe, as seen in Figure 3-12, has two identical Langmuir probe tips. The pair of probes are configured to electrically float so that there is no net current collected by the two probes.[109] Instead, as the two probe tips are biased relative to each other, current flows from one

tip to the other. As a result, the largest double probe current is limited to the ion saturation current.

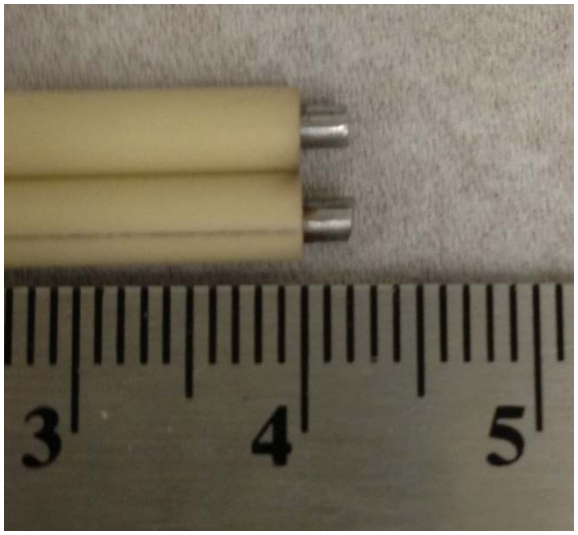

Figure 3-12: An example of a double probe used in ALEXIS. The probe tips are made of 2 mm diameter stainless steel and are inserted into ceramic tubing. The probe tips protrude 2 mm out of the ceramic tubing, and are separated by 2.5 mm. The surface area of each probe tip is 0.157 cm^2.

For the experiments on ALEXIS, the double probe has 2 mm diameter stainless steel tips. The tips protrude 2 mm out of ceramic tubing (4 mm outer diameter, 2.4 mm inner diameter) into the plasma. The probe tips are separated by 2.5 mm and each tip has a surface area of 0.157 cm^2. The probe tips are biased relative to each other using a Keithley 2400 Sourcemeter.

The electron density and temperature can be derived from the characteristic current-voltage (I-V) trace of the double probe. A typical double probe characteristic trace for the ALEXS double probe is shown in Figure 3-12. Assuming two identical probe tips, then the trace can be fitted using

$$I = I_{si} \tanh\left(\frac{eV}{2T_e}\right) \tag{3-3}$$

where I is the current collected, I_{si} is the ion saturation current, e is the electron charge, V is the voltage difference between the two tips, and T_e is the electron temperature.[103] Modifications to Equation 3-3 are made to account for geometric and plasma sheath effects[110] so that,

$$I(V) = a_0(V - a_1) + a_2 \tanh\left(\frac{V - a_1}{a_3}\right) + a_4 \tag{3-4}$$

where a_o is the slope of the ion saturation region (due to sheath effects), a_1 is the current offset, a_2 is the ion saturation current, a_3 is the slope of the transition region about zero volts ($dI/dV_{V=0}$) and a_4 is the voltage offset. The current and voltage offsets are due to differences between the tips of the double probe. Figure 3-13 shows typical double probe data (black) and the modified hyperbolic tangent fit in Equation 3-4 (green). The electron temperature (T_e) and electron density (n_e) are calculated using,

$$T_e = \frac{I_{si}}{2\, dI/dV_{V=0}} = \frac{a_2}{2a_3} \tag{3-5}$$

$$n_e = \frac{I_{si}}{eA}\sqrt{\frac{m_i}{T_e}} = \frac{a_2}{eA}\sqrt{\frac{m_i}{T_e}} \tag{3-6}$$

where the electron temperature is in electron volts (eV), A is the surface area of the probe tips and m_i is the ion mass.[109]

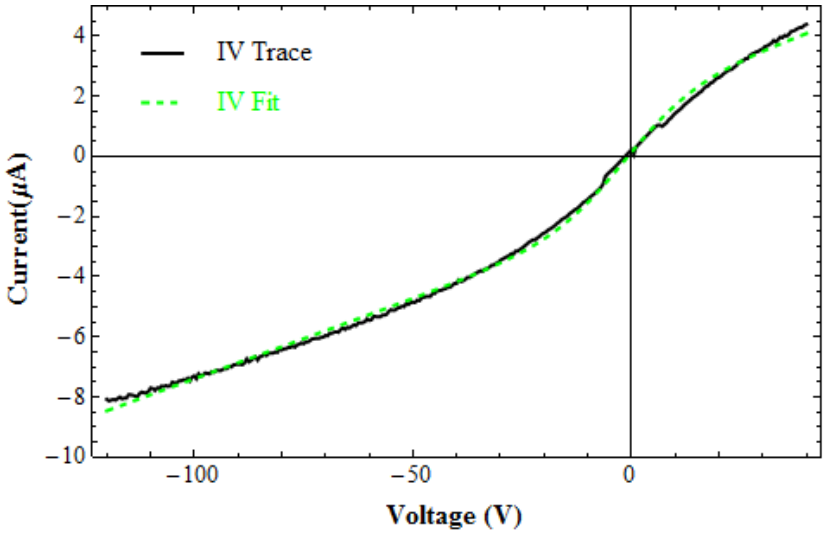

Figure 3-13: An example of a typical characteristic trace from a double probe (black) and the hyperbolic tangent fit (green). The electron temperature can be calculated using the slope when there is zero bias between the probe tips. The electron density can be calculated using the electron temperature and the ion saturation current.

3.6.3. "k" – probe

A "k" - probe, which is shown in Figure 3-14, is an electrically floating pair of single tipped Langmuir probes that is used to determine the wavenumber (i.e., "k") of electrostatic fluctuations in the plasma. This is accomplished by simultaneously recording the potential fluctuations in the plasma from each tip. By measuring potential fluctuations, it is possible to calculate the frequency and relative amplitude of instabilities in the plasma, as well as determining the wavelength and wavenumbers of the fluctuations. The probe tips are made from 2.7 mm diameter tungsten that protrude 2 mm out of double bore ceramic and have a separation distance of 3 mm. The probe, which is rotated to different angles by hand, is mounted on a linear probe drive which is computer controlled.

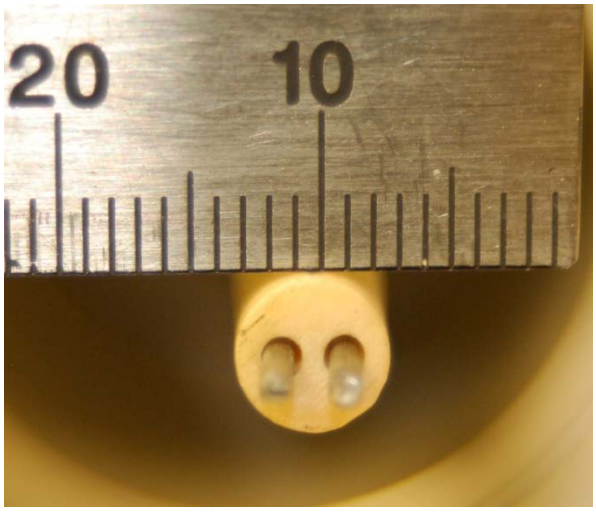

Figure 3-14: An example of a "k"-probe that is used in ALEXIS to calculate the wave number and wavelength of electrostatic fluctuations. It is made from 2.7 mm diameter tungsten that extends 2 mm from 2-bore ceramic tubing. The probe tips are separated by 3 mm.

To calculate the frequency and relative amplitude of the instability, the potential fluctuations are measured on one probe tip at different radial positions in the plasma. In order to minimize noise in the signal, 5 data sets are taken at each radial position and are averaged

together. A Fast Fourier Transform (FFT) is performed on the signal which yields a frequency spectrum like the one shown in Figure 3-15.

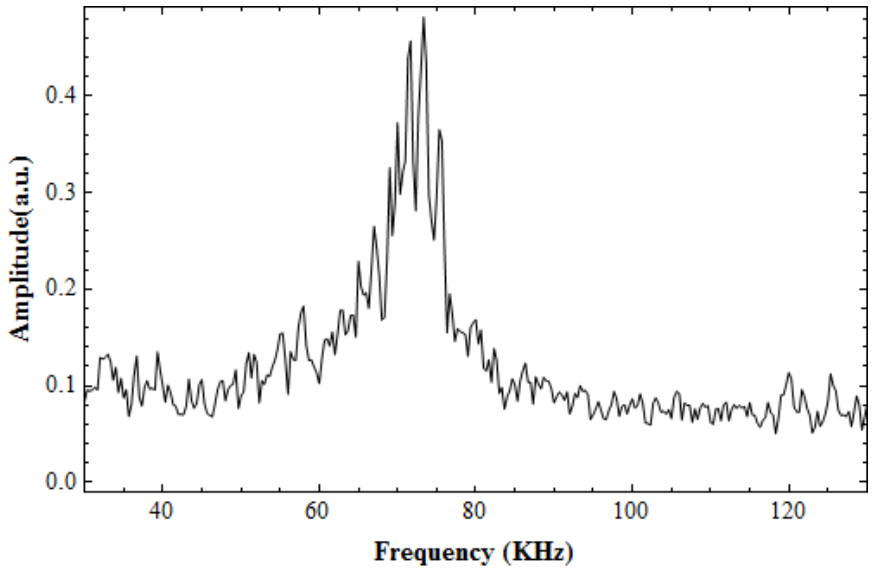

Figure 3-15: Example of a frequency spectrum. The frequency of the instability is 73.31 KHz.

The frequency of the instability (73.31 KHz in the example spectrum) is calculated at the same radial position as the largest amplitude fluctuations occur. The peak wave power is calculated at each radial position for a given frequency range around the peak amplitude of the instability and is then plotted as a function of the radial position, as is shown in Figure 3-16. In this example, the largest amplitude fluctuations occur at roughly 0.4 cm. This becomes important when measuring the wavenumber and wavelength of the instability.

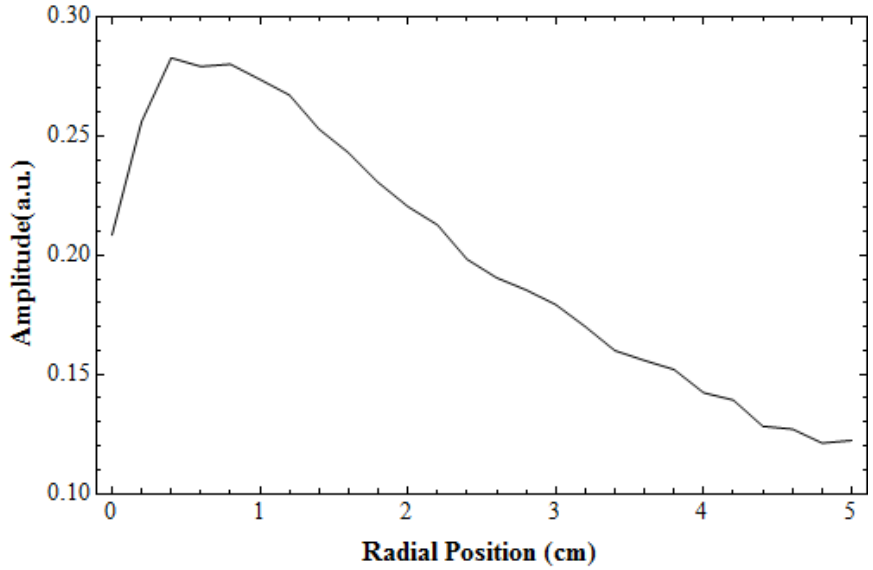

Figure 3-16: Example of the peak wave power plotted as a function of the radial position. This shows that the largest amplitude fluctuation occurs near 0.4 cm.

The magnitude and phase difference of the signal between the two probe tips are needed to calculate the wavenumber and wavelength of the wave. If the phase difference between the two probe tips is zero, then the wave reaches the tips at the same time. However, if the wave reaches them at different times, then there is a phase difference between the time signals recorded by the probe tips. An example of this is shown in Figure 3-17.

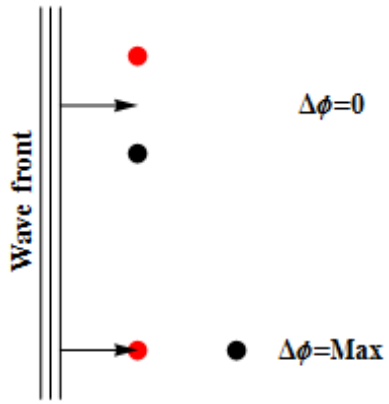

Figure 3-17: The red and black circles represent the probe tips of the "k"-probe. When a wave front hits the probe tips simultaneously (top) there is no phase difference in the recorded time signals. However, when the wave hits the tips at different times (bottom), the phase difference between the signals is maximum.

The "k"-probe is set to the same radial location as the peak wave power (where the largest amplitude fluctuations occur). The probe is then rotated through different angles, which changes the orientation of the probe tips with respect to the background magnetic field. At each angle, the voltage fluctuations are measured simultaneously from each probe tip. A cross power spectrum is used to calculate the magnitude and phase difference between the two time domain signals.[111] The cross power spectrum is calculated using,

$$CPS = \frac{FFT(2) \times FFT^{*}(1)}{N^2} \tag{3-7}$$

where N is the common number of data points between the two signals, *FFT(2)* is the Fast Fourier Transform of the signal from one probe tip, and $FFT^{*}(1)$ is the complex conjugate of the fast Fourier transform of the signal from the other probe tip. The magnitude yielded by the cross power spectrum is fit with a Lorentzian curve,

$$y = \frac{a \times h^2}{h^2 + (x - f)^2} + c \tag{3-8}$$

where a is the maximum amplitude, h is the frequency value at the half-width and half-maximum, f is the frequency at which the maximum amplitude occurs, and c is the background noise of the signal. Figure 3-18 shows the cross power spectrum and the corresponding Lorentzian curve fit.

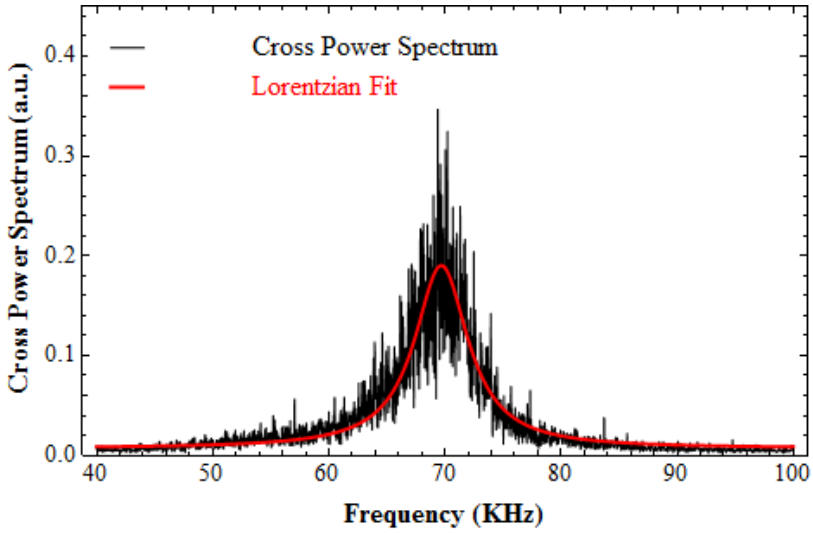

Figure 3-18: Example of the Lorentzian curve (red) fit to the cross power spectrum (black).

The half-maximum is calculated on both sides of the curve, and the average phase difference[110] between those two points is calculated for each angular position, as shown in Figure 3-18.

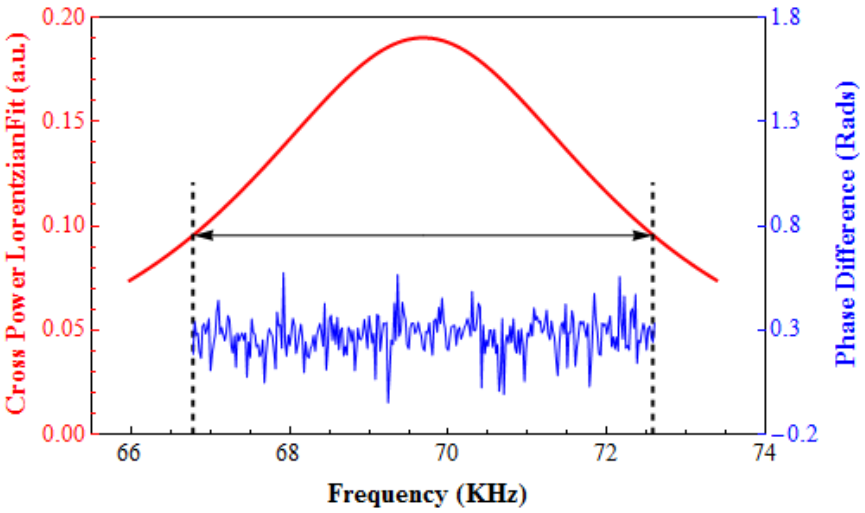

Figure 3-19: The average phase difference is calculated from the phase difference array (blue) between the half maximum points (black dashed lines) on the Lorentzian fit (red) of the cross power spectrum.

The phase difference is plotted as a function of probe rotation angle and fit with a sinusoidal curve. If several wavelengths fit between the probe tips, then a sinusoidal curve would not fit the data and the phase could not be accurately measured. On the other hand, if the wavelength of the instability is much larger than the probe tip separation, it can also become

difficult to make an accurate measurement of the phase difference. Figure 3-20 shows a typical data set that has been fit with a sinusoidal curve, where at zero degrees, the probe tips are parallel to the background magnetic field, and at 90 degrees they are perpendicular to the magnetic field.

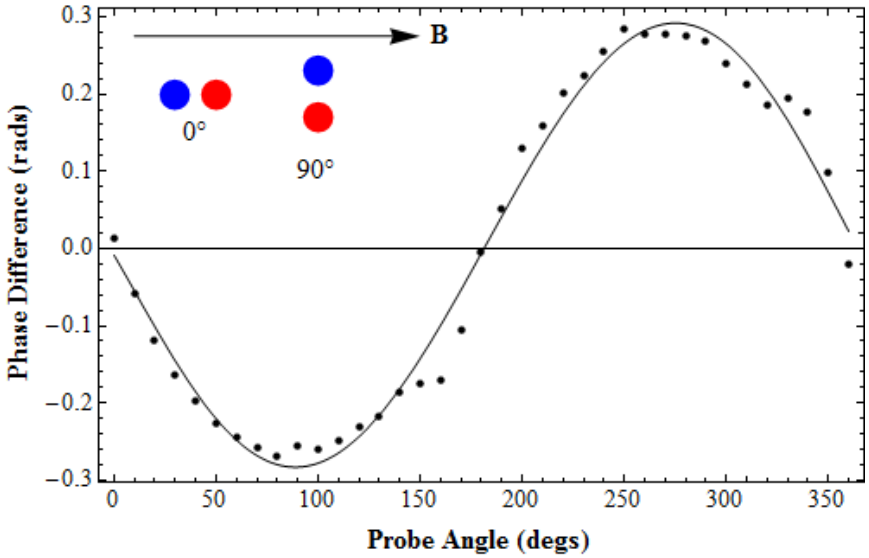

Figure 3-20: Example of phase data plotted as a function of angle with respect to the magnetic field. The data (circles) is fit with a sinusoidal curve (solid line) which indicates that the probe tip separation is an appropriate distance. The maximum phase occurs at the angle of propagation.

The maximum phase difference occurs at the propagation angle of the instability, and can be used to calculate the magnitudes of the wavenumber and wavelength of the instability,

$$k = \frac{\Delta\phi}{\Delta x} \tag{3-9a}$$

$$\lambda = \frac{2\pi}{k} \tag{3-9b}$$

where k is the wavenumber, $\Delta\phi$ is the phase difference, Δx is the probe tip separation, and λ is the wavelength.

To extract out the parallel and perpendicular components of the wavenumber, the wavenumber is calculated from the phase difference at each probe angle and this data is also fit with a sinusoidal curve. The parallel wavenumber is calculated from the averages of the

wavenumbers at 0, 180 and 360 degrees. The perpendicular wavenumber is calculated from the average of the wavenumber at 90 and 270 degrees. This is assuming that k_x is small so that the perpendicular wavenumber can be approximated as k_y.

3.6.4. Magnetic Loop (B-dot) probe

The original intent of this research was to study the transition between electrostatic and electromagnetic modes. A magnetic loop probe, or a "B-dot" probe, is a diagnostic probe that is used to measure electromagnetic fluctuations. The operating principle of a magnetic loop probe is relatively straight-forward. According to Faraday's law, a time-changing magnetic field will induce a voltage in a coil. The integral form of Faraday's law can be written as:

$$\int_{\boldsymbol{Coil}} \vec{\boldsymbol{E}} \cdot \vec{d\boldsymbol{l}} = \int_{\boldsymbol{s}} \frac{d\vec{\boldsymbol{B}}}{dt} \cdot d\vec{\boldsymbol{s}} \tag{3-10}$$

On the left hand side of Equation 3-10, the voltage induced is determined by integrating the electric field around the coil. If the magnetic fluctuations can be represented by the harmonic form[103], $\vec{\boldsymbol{B}} \sim \vec{\boldsymbol{B}} e^{-i\omega t}$, then the derivative, $\frac{d\vec{\boldsymbol{B}}}{dt} \rightarrow -i\omega\vec{\boldsymbol{B}}$. Therefore, Faraday's law can then be re-written as:

$$V = i\omega A\vec{B} \cdot \hat{n} \tag{3-11}$$

where A is the area of the coil and $\hat{n}$ is the unit vector perpendicular to the plane of the coil. So if the area of the coil is known, and the frequency and voltage across the coil are measured, then the amplitude of the fluctuating magnetic field can be calculated.

The magnetic loop probe uses a three-axis configuration to make simultaneous measurements of the magnetic field fluctuations both parallel and perpendicular to the magnetic

field. The probe is made of three 8.2 μH inductor coils that have a loop cross sectional area of 2.54 x 3.05 mm^2 and are made from 50 turns of wire. An example of one of these inductors can be seen in Figure 3-21a. A twisted pair of wires is soldered to each end of the inductor to reduce the noise seen in the signal and inserted into a single bore ceramic tube. The inductors are then coated with Ceramabond 569 to electrically insulate and hold them in place at the end of the ceramic tubing, which is placed in stainless steel tubing for shielding purposes. To eliminate any capacitive pickup, tin foil is placed over the probe tips and is coated with another layer of Ceramabond 569 to ensure that the probe is insulated from electrostatic fluctuations in the plasma and to keep it securely connected to the stainless steel tubing. The stainless steel tubing is then covered with heat shrink tubing to keep the probe shaft electrically isolated from the plasma, and grounded to the ALEXIS chamber to create an electrostatic shield. The probe assembly is mounted on a motor driven linear feed-through and is controlled via computer. The designs for the magnetic loop probe shown in Figure 3-21b are based on designs from the Naval Research Laboratory (NRL).

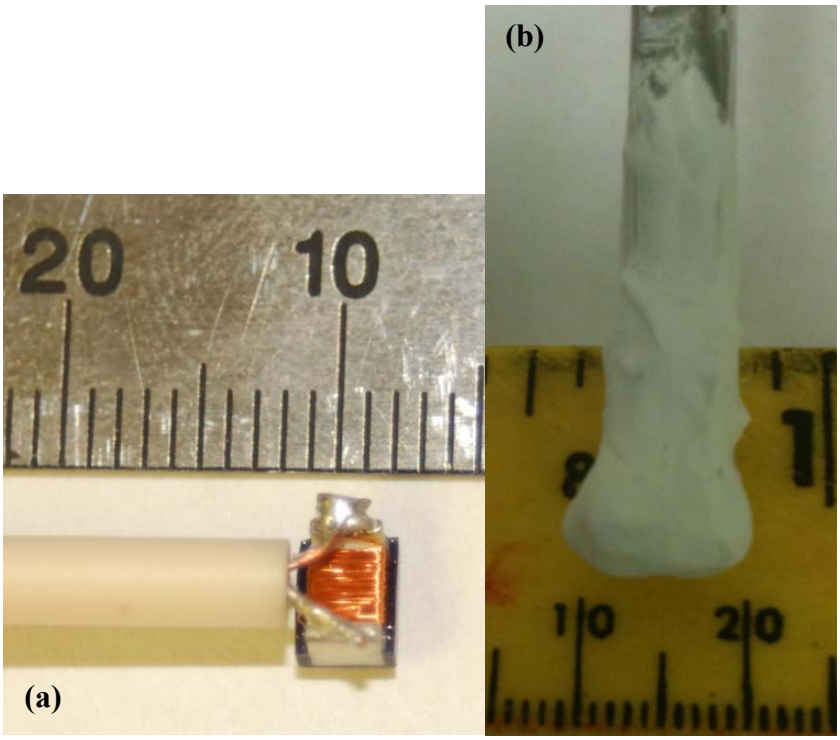

Figure 3-21: a) An example of an 8.2 µH inductor used for the magnetic loop probes prior to being insulated (left) and b) a three axis magnetic loop probe after being insulated with Ceramabond 569 (right).

A differential amplifying circuit is used to subtract out the common mode noise to reduce capacitive pickup and amplify the remaining signal from the magnetic loop probe. The inverting branch of the circuit makes use of an NE5534P operational amplifier and has a gain of 33 with a common mode rejection ratio of 33. The non-inverting branch of the circuit makes use of a LT1028 low noise operational amplifier that further amplifies the signal by 34. Various capacitors were included to decrease the rf noise in the circuit.[112] Table 3-2 lists the values of the capacitors and resistors, and the operational amplifiers used in the circuit.

Table 3-2: Component list for the differential amplifying circuit.

Printed Circuit Board code	Component
R1, R2	10 Ω
R3, R4	330 Ω
R5	3.3 kΩ
R6	100 Ω
R7	50 Ω
C1, C2	10 μF Tantalum
C5 – C8	10 μF ceramic
U1	NE5534P
U2	LT1028

Figure 3-22 shows (a) a schematic of the amplifying circuit used and (b) the layout of the printed circuit board used in the experiment.

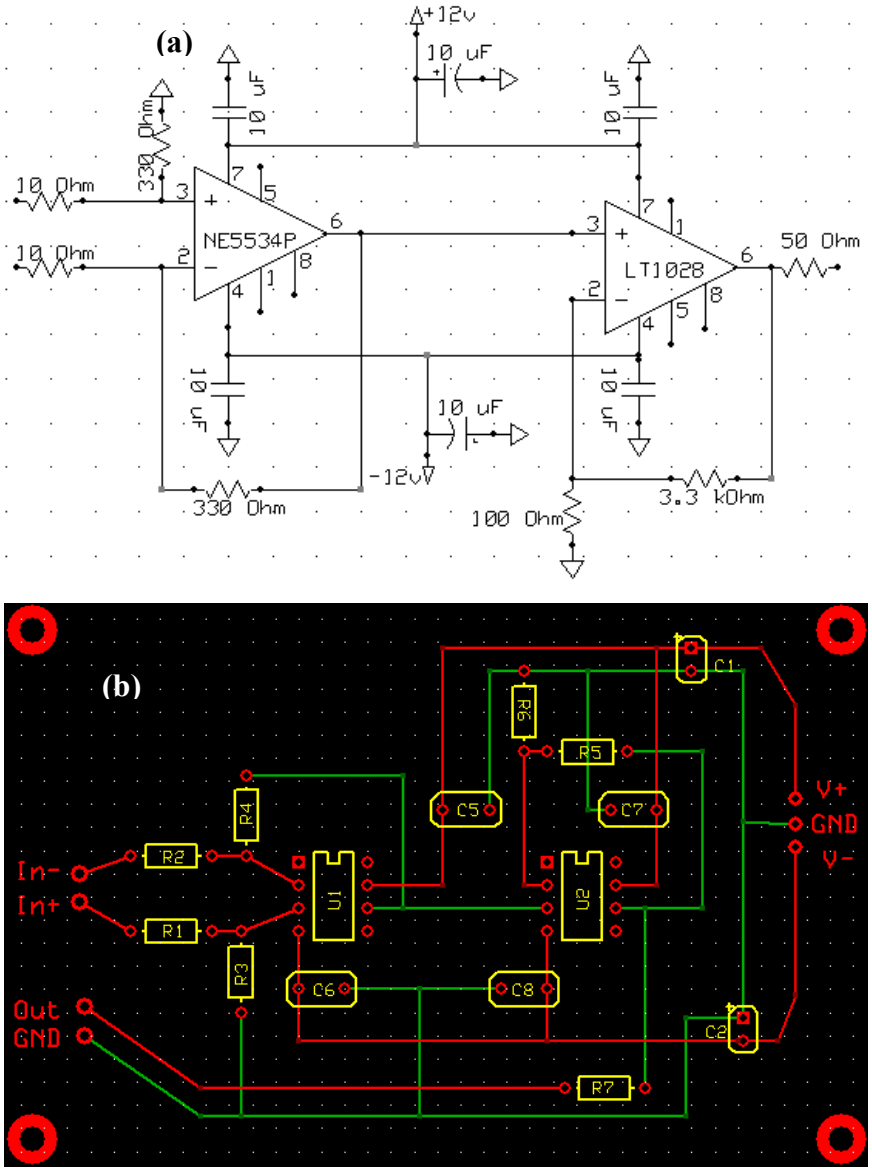

Figure 3-22: (a) The inverting to non-inverting differential amplifying circuit used to amplify the signal from the magnetic loop probe. The inverting circuit is the first stage (the first op-amp) and the non-inverting circuit is the second stage (the second op-amp). (b) The printed circuit board, where the traces on the bottom layer are shown in green. The traces on the top layer are shown in red. The component outlines are shown in yellow. The circuit has an overall gain of 1000.

In order to calculate the amplitude of the fluctuating magnetic field in the plasma, the effective inductor area must be calculated as a function of frequency. To calibrate the probe tips, a HP33120A, 15MHz function/arbitrary waveform generator was used to put a 10 volt amplitude sinusoidal wave on a 9 cm diameter Helmholtz coil with 10 turns. The current in the Helmholtz coil creates a fluctuating magnetic field that is calculated by[110],

$$B = \left(\frac{4}{5}\right)^{3/2} \frac{\mu_o N\, I}{R} \tag{3-12}$$

where N is the number of turns on the Helmholtz coil, R is the radius of the coil, and I is the current. A 0.1 V/A Pearson coil was used to read the current in the Helmholtz coil. A HP54600B 100 MHz oscilloscope was used to display the current from the Pearson coil, and the signal from the magnetic loop probe. Using Equations 3-11 and 3-12, the effective area of each inductor is calculated while each inductor was both parallel and perpendicular to the magnetic field of the Helmholtz coil. In Figure 3-23, the solid lines represent the effective area when the inductors were parallel to the field, and the signal was at a maximum, and the dashed lines represent the area when the signal was at a minimum (inductors being perpendicular to the field). Each color represents a different inductor. A resonant frequency is seen near 500 kHz. The "B-dot" probe that was built for use in the ALEXIS device was not used in the research presented in the chapters that proceed. However, it is important to discuss this diagnostic, as future experiments in ALEXIS can make use of it.

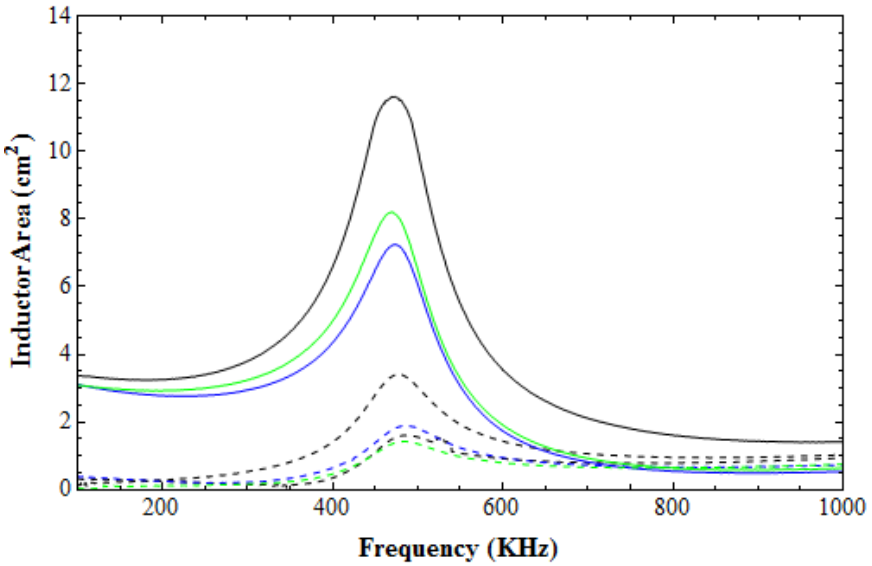

Figure 3-23: Magnetic loop probe inductor area as a function of frequency. The solid lines show the area when the inductor was parallel to the magnetic field, and the dashed lines show the area when the inductor was perpendicular to the field. Each color corresponds to an individual inductor.

Chapter 4: Experimental Results

As discussed in Chapter 1, previous experiments performed in the ALEXIS device focused on electrostatic instabilities driven by sheared flows when the ion gyro-radius was of the same order as the shear scale length.[17–19,72] These instabilities are found in the ion cyclotron frequency range and can be driven by both perpendicular and parallel velocity shear. The goal of this project was to study a different regime of transverse shear driven instabilities that can arise when the ion gyro-radius (ρ_i) is larger than the shear scale length (L_E). In this regime, the electrons are magnetized in the shear layer, but the ions are effectively un-magnetized. The resulting shear driven instability occurs at a frequency well above the ion cyclotron frequency (Ω_{ci}) and closer to the lower hybrid frequency (ω_{LH}). This mode is known as the electron-ion hybrid (EIH) instability.[74]

The EIH instability has been studied both theoretically and experimentally, as was discussed in Chapter 1. To better simulate the conditions of magnetospheric boundary layers where the EIH instability occurs naturally, this experiment investigates the EIH instability in the presence of a density gradient. In order to the create highly localized electric fields and density gradients that are often observed at plasma boundary layers, ALEXIS was redesigned to include a secondary plasma source.[113] Section 4.1 will discuss the plasma parameters of each, and show that the addition of the secondary plasma source was necessary in order to drive an instability in

the lower hybrid frequency range. The impact of having two different plasma sources on the cylindrical symmetry of the experiment will also be discussed.

Section 4.2 of this chapter is divided into two parts. The first part begins by presenting an electrostatic instability observed in the interpenetrating plasma configuration of ALEXIS. The instability driving mechanism and experimental results will be discussed in the context of the theoretical models presented in Section 2.2. An original goal of this experiment was to not only study the effect of a density gradient on the EIH instability, but to also study the instability as the plasma density is varied from a spatially uniform profile to a profile with a density gradient. However, in the presence of a uniform density profile, the EIH instability was not observed. This result will be explained as a theoretically consistent consequence of the finite length of ALEXIS.

Finally, Section 4.3 presents the results of an ion gyro-radius modification experiment performed by varying the magnetic field strength. This experiment will show the transition between three transverse shear driven modes in a single experiment for the first time. The mechanism responsible for the mode transition will be discussed.

4.1 Dual plasma parameter measurements

As discussed in Chapter 3, ALEXIS was completely reconfigured for these experiments. With the addition of the filament plasma source, ALEXIS now has three possible experimental configurations when the blocking disk is in place; the rf plasma with a void in the center, the filament plasma only, and the interpenetrating plasma (both the rf plasma and the filament plasma). The difference in the plasma parameters in the three configurations will be examined and it will be shown that in order to excite electrostatic instabilities in a region of intense sheared plasma flow, the interpenetrating plasma configuration is essential to the experiment. In the

figures presented in this section, the rf plasma data is shown in black (circles) and the filament plasma data is shown in red (squares). The interpenetrating plasma configuration measurements are represented by blue (diamonds). The experimental operating conditions for the data presented in this section are listed in Table 4-1. The radial profiles for the (a) plasma potential, (b) electric field, (c) electron density and (d) electron temperature are shown in Figure 4-1, where the shaded region marks the radial location of the blocking disk. The edge of the shaded region represents the approximate location of the boundary between the rf and filament plasmas. In these plots, r = 0 cm denotes the center of the plasma column and r = 5 cm corresponds to the vacuum vessel wall. These experiments were all performed using argon plasmas.

Table 4-1: The operating conditions used for the plasma parameter comparison experiment.

	rf Plasma	Filament Plasma	Dual Plasma
Neutral Gas	Argon	Argon	Argon
Magnetic Field (Gauss)	146	146	146
Neutral Pressure (mTorr)	0.26	0.26	0.26
rf Power (W)	30	Off	30
Emission Current (mA)	Off	60	60
Grid Bias (V)	85	85	85
Filament Bias (V)	Off	-15	-15
Electron Cyclotron Frequency (GHz)	2.57	2.57	2.57
Ion Cyclotron Frequency (kHz)	35	35	35
Electron Plasma Frequency (MHz)	284.7	900.2	636.6
Ion Plasma Frequency (MHz)	1.05	3.32	2.34
Lower Hybrid Frequency (MHz)	1.04	3.13	2.28

The plasma potential profiles shown in Figure 4-1(a) are generated using an emissive probe mounted at Port 3 that is scanned radially across the plasma starting from the outermost edge (r = 5 cm) to the center of the column (r = 0 cm) in 2 mm steps. When the rf plasma is on and the blocking disk is biased to 85 V, the spatial structure of the plasma potential varies little, indicating that the bias voltage applied to the blocking disk and biasing grid do not modify the

spatial structure of plasma potential. As discussed in Section 3.5, the potential of the filament plasma is controlled by varying the bias applied to the mesh and blocking disk. In the case of the filament plasma, the magnitude of the plasma potential is approximately equal to the bias applied to the biasing mesh. The spatial structure of the plasma potential is significantly modified, decreasing sharply in the center of the plasma. In the interpenetrating plasma configuration, the magnitude of the plasma potential (~ 60 V) is less than the bias voltage applied to the mesh (85 V), and the spatial structure is again significantly modified near the boundary between the plasmas, indicating that a transverse electric field is generated in this region.

The electric field profiles shown in Figure 4-1(b) are calculated from the negative gradient of the plasma potential profiles. Note that a positive electric field indicates that a radially outward electric field is present, while a negative electric field corresponds to a radially inward electric field in the plasma. With a large bias voltage applied to the blocking disk, a small radially outward electric field (~ 4 V/cm) is generated in the rf plasma void configuration. There is a large electric field with a peak strength of approximately 45 V/cm produced near the center of the filament plasma. In this configuration, the shear scale length, which is calculated from the half-width at half-maximum of the radial electric field profile, is approximately 0.3 cm. An electric field with L_E = 0.45 cm and a peak magnitude between 20 and 30 V/cm is observed at r = 0.4 cm in the interpenetrating plasma configuration. Note that with a magnetic field strength of 146 Gauss and assuming an ion temperature of 0.02 eV, the ion gyro-radius is calculated to be 0.88 cm. Therefore, the electric fields generated in both the filament and dual plasma configurations have shear scale lengths that are 2 to 3 times smaller than the ion gyro-

radius, creating conditions that are favorable for the generation of shear driven instabilities in the lower hybrid frequency range.

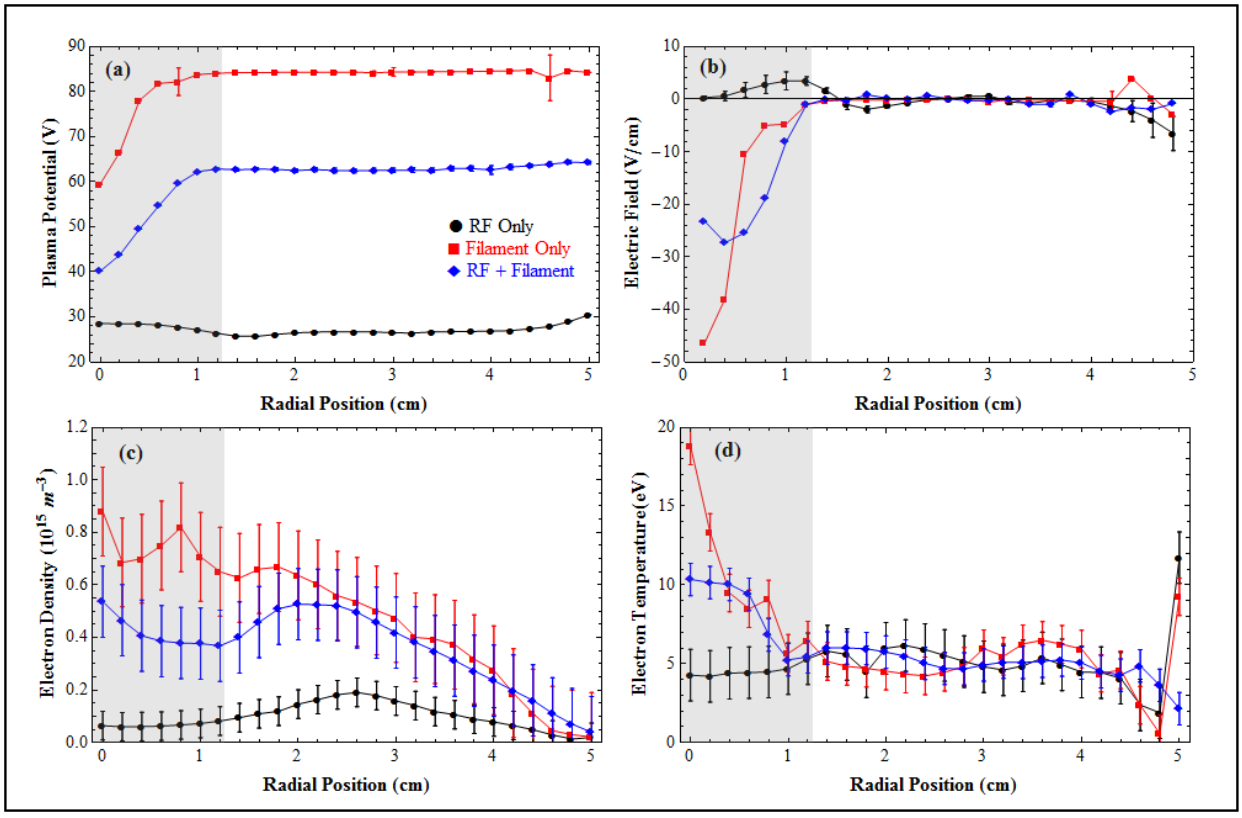

Figure 4-1: The measured plasma parameters for the rf plasma with the blocking disk in the center (circles, black), the filament plasma only (squares, red), and the interpenetrating plasma configuration (diamonds, blue). The radial profiles for (a) plasma potential, (b) electric field, (c) electron density, and (d) electron temperature are shown for each configuration.

To measure electron density profiles, a double tipped Langmuir probe at Port 4 is scanned radially across the plasma column from r = 5 cm to r = 0 cm in 0.2 cm steps. At each radial position, the voltage across the probe tips is swept from -120 V to +40 V, creating a current-voltage characteristic trace similar to the one shown in Figure 3-12. Using the methods discussed in Section 3.6.2, the electron density is then calculated at each radial position. Figure 4-1(c) shows the resulting electron density profiles. The maximum rf plasma density is approximately 0.2×10^{15} m^{-3} and is observed to near r = 2.6 cm. The electron density decreases

in the central region of the blocking disk, creating a density depletion region in the center of the plasma. The rf antenna edge is located at r = 2.5 cm, which accounts for the peak in density near this location. The peak filament plasma density is approximately 0.9×10^{15} m^{-3} and is almost an order of magnitude greater than the rf plasma density in the center of the plasma column. In the dual plasma configuration, there is an increase in the density near the rf antenna edge, after which the density decreases. However, instead of a region of density depletion, the electron density is observed to increase again in the filament plasma region. It appears that the plasmas are coupled to each other, in that their individual densities do not combine to create a higher density plasma, but instead appear to create a plasma with a density greater than the rf plasma, but less than the filament plasma density. By adjusting the emission current, the filament plasma density can be increased or decreased to create a uniform density plasma or a plasma with a large density gradient. This will be illustrated in Section 4.2.

Finally, Figure 4-1(d) shows the radial electron temperature profiles, which are measured in the same manner as described for the electron density profiles. For all configurations, the electron temperatures outside of the blocking disk edge are relatively constant between 4 and 7 eV. Note that large temperatures are often calculated at radial positions outside of 4.5 cm. These measurements are somewhat unreliable due to the low plasma densities ($n_e < 10^{13}$ m^{-3}) measured at the edge of the chamber. However, inside the perimeter of the blocking disk, the temperatures differ greatly between the three configurations. The rf plasma has an electron temperature that remains constant across the plasma column (~ 5 eV), but the filament electron temperature increases to approximately 20 eV in the center of the chamber. The large increase in the filament

electron temperature is believed to be from primary electrons that are accelerated away from the filaments.

It is noted that in earlier configurations of ALEXIS, a filament source was the primary plasma source.[71] In this configuration, a secondary grid was placed in front of the filaments in order to decelerate electrons and to reduce the number of primary electrons entering the main experimental section. Typical electron temperatures were measured using double tipped Langmuir probes to be between 3 and 8 eV. However, for these experiments, there is no grid in place to decelerate the electrons, which may lead to a larger population of the primary electrons.

To measure floating potential fluctuations that may be driven by the radial electric field generated in the plasma, a single tipped Langmuir probe located at Port 5 was placed in the same region as the radial electric field (r = 0.8 cm). Figure 4-2(a) shows the fluctuations in the floating potential for the three different configurations. The frequency spectra shown in Figure 4-2(b) are calculated by taking a Fast Fourier Transform (FFT) of the floating potential fluctuations. The spectra plot shows that there are no instability signatures in the rf or the filament plasma configurations, in spite of a large radial electric field that was measured in the filament plasma. However, in the interpenetrating plasma configuration, an instability with a harmonic is observed at a frequency of approximately 42 kHz, or $0.12 f_{LH}$. There were no instabilities observed in any of the configurations below 20 kHz or above 100 kHz. In order to excite a high frequency instability in the region of a large transverse electric field, the dual plasma configuration is crucial.

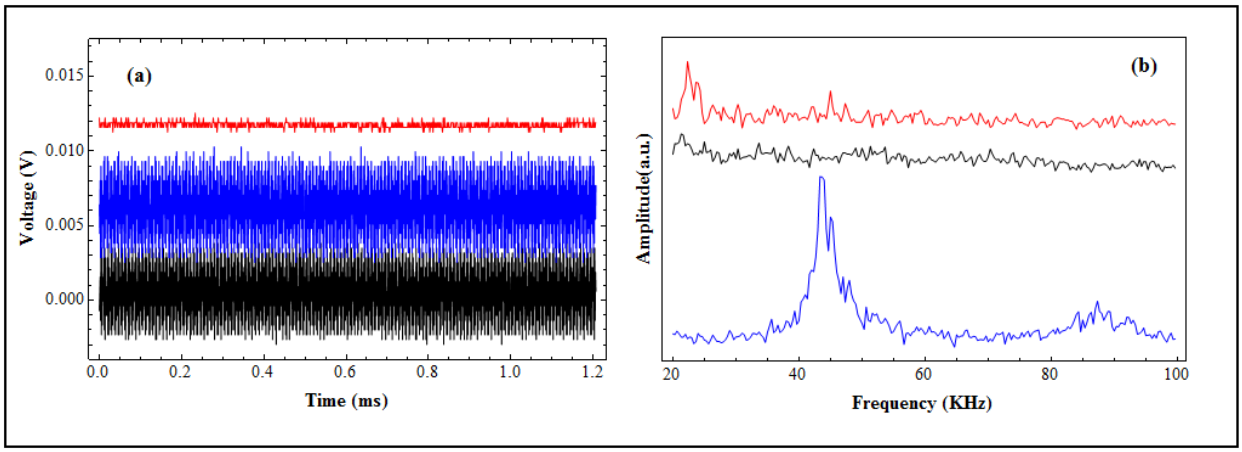

Figure 4-2: The (a) floating potential fluctuations and (b) the corresponding FFT spectra are shown for the rf plasma with the blocking disk in the plasma (black), the filament plasma (red), and for the interpenetrating plasma configuration (blue).

There was a concern about the impact of the addition of the secondary plasma source on the cylindrical symmetry of the experiment. The following data was taken under the same conditions listed in Table 4-1 in the interpenetrating plasma configuration. The floating potential was measured from both sides of the vacuum vessel using two different probes at two different axial port locations. Each probe was moved radially into the chamber in 0.2 cm steps from 5 cm to the center of the plasma column (0 cm). In Figure 4-3, the data plotted from -5 to 0 cm was measured using a Langmuir probe tip located on the left side of the vacuum vessel at Port 5. The data plotted from 0 to +5 cm was measured using a cold emissive probe located on the right side of the vacuum vessel at Port 3. This figure shows that there is cylindrical symmetry in the dual plasma configuration. As a result, radial profiles for the experiments discussed in the following sections are only taken from one side of the chamber.

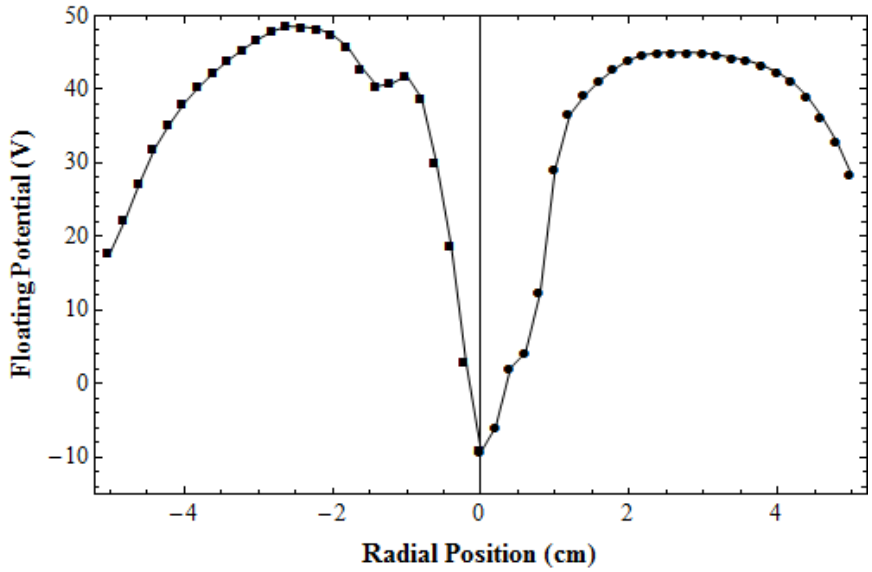

Figure 4-3: This plot shows the floating potential measured from both sides of the vacuum vessel. The data from -5 cm to 0 cm was measured using an electrically floating Langmuir probe on the left side of ALEXIS at port 5. The data from 0 cm to 5 cm was measured using the emissive probe located on the right side of ALEXIS at port 3.

In summary, it has been established that a void was successfully created in the primary rf plasma by placing a blocking disk in the center, and by doing so, the blocking disk did not significantly modify the spatial structure of the plasma potential. The filament plasma was observed to fill in the density depletion region, creating conditions where the density gradient between the plasmas can be controlled by varying the parameters of the filament plasma. A localized electric field with typical shear scale length measured of approximately 0.45 cm, was successfully created by biasing the filament plasma to a high voltage relative to the rf plasma, and it was shown that this double plasma configuration is necessary in order to drive an instability in the same region as the peak electric field. Finally, the azimuthal symmetry of the experiment was shown to hold, permitting the measurement of radial profiles from one side of the experiment.

4.2 Electron-ion hybrid instability experiments

A previous study using the Naval Research Laboratory's Space Physics Simulation Chamber (SPSC) was conducted to simulate the dynamics of highly localized magnetospheric boundary layers and study the EIH instability for the case of a uniform density profile in order to isolate the effects of the localized electric field.[50] In these experiments, it was shown that if a density gradient was introduced into the plasma, the characteristic frequency of the EIH instability dropped well below the lower hybrid frequency. However, the EIH instability was never fully characterized and studied in the density gradient configuration.

This experiment serves to study the EIH instability in the case of a density gradient and as the spatial structure of the density is transitioned from a large density gradient to no density gradient (uniform density). In this section, the discovery of a high frequency electrostatic instability and the associated plasma parameters is discussed. The identification of the instability driving mechanism is studied, and the experimental results will show the instability is the EIH instability, albeit modified by a density gradient. Finally, the results of EIH instability in a plasma with no density gradient are presented.

4.2.1 Density gradient modified electron-ion hybrid instability

The previous section showed that a localized region of highly sheared plasma flow could be created near the boundary of two interpenetrating plasmas. From measurements of radial electric field profiles, a typical shear scale length was calculated to be approximately 0.45 cm. To excite the EIH instability, the ion gyro-radius, which can be controlled via the magnetic field strength, must be larger than the shear scale length. Figure 4-4 shows the calculated electron (red) and ion (black) gyro-radii as a function of magnetic field strength. The average calculated

shear scale length is indicated by the horizontal dashed line (blue), and the vertical dashed line (blue) represents the magnetic field strength where the ion gyro-radius becomes larger than the shear scale length. Therefore, in order to run the experiment in the correct regime, the magnetic field strength must be less than 300 Gauss.

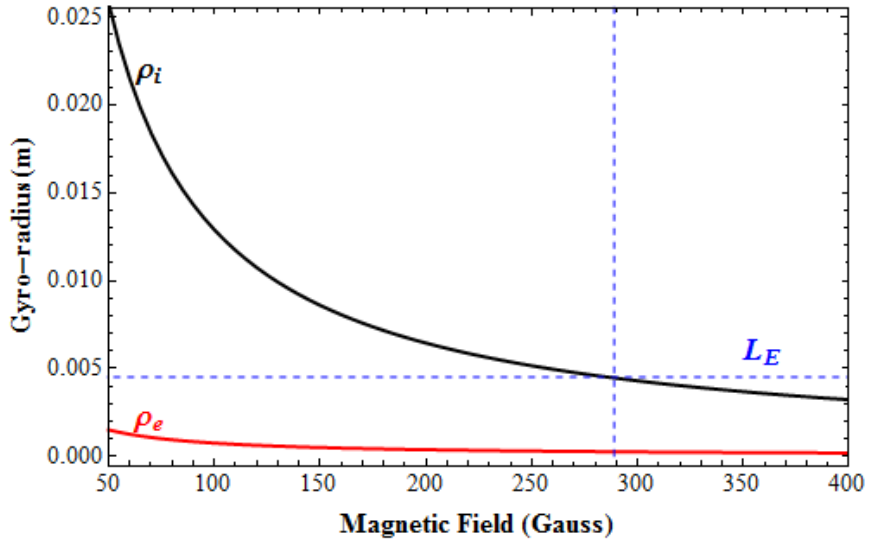

Figure 4-4: The calculated ion (black) and electron (red) gyro-radii are shown as a function of the magnetic field. The horizontal dashed line (blue) indicates a typical measurement of the shear scale length, L_E. The vertical dashed line (blue) indicates that the ion gyro-radius becomes larger than the shear scale length for magnetic field strengths less than 290 G.

The EIH instability is found in the lower hybrid frequency range, where the lower hybrid frequency, $\omega_{LH}^2 = 1/\left[(\Omega_{ci}\Omega_{ce})^{-1} + \omega_{pe}^{-2}\right]$, is dependent on the magnetic field strength and the electron density. To pinpoint the correct frequency range in which to find the EIH instability, the lower hybrid frequency can be calculated for different magnetic field strengths and electron densities. Figure 4-5(a) shows the calculated lower hybrid frequency as a function of the magnetic field strength for densities of approximately 4×10^{14} m^{-3}. Under conditions when the ion gyro-radius is larger than the shear scale length, the lower hybrid frequency is less than 400 kHz, and is constant until very low field strengths are reached.

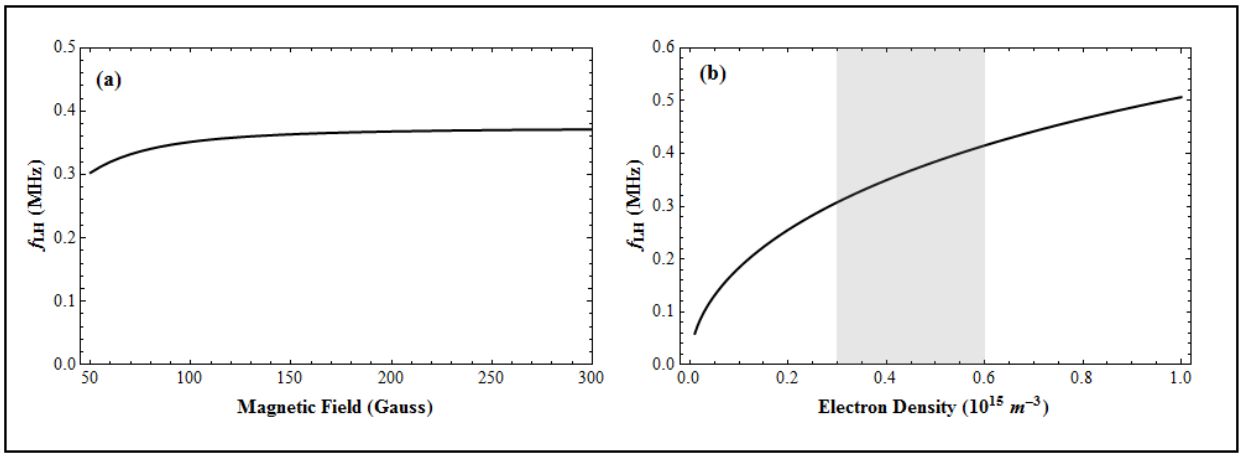

Figure 4-5: The calculated lower hybrid frequency (f_{ci}) is plotted as a function of (a) the magnetic field strength and (b) the electron density. The shaded region in (b) highlights typical electron densities measured in ALEXIS.

Figure 4-5(b) shows the lower hybrid frequency as a function of the electron density for a magnetic field strength of 95 Gauss. From Equation 2-1, the lower hybrid frequency is dependent on the density through the ion plasma frequency. The sensitivity of the lower hybrid frequency as a function of density is explained by the difference in the values of the plasma and cyclotron frequencies from which the lower hybrid frequency is derived. In the high density limit, because the inverse of the ion plasma frequency (ω_{pi}) approaches zero, the lower hybrid frequency is proportional to $\sqrt{\Omega_{ci}\Omega_{ce}}$, where Ω_{ce} and Ω_{ci} are the electron and ion cyclotron frequencies, respectively.[2,83] By contrast, in the low density limit, $\omega_{LH} \sim \omega_{pi}$.[2,83] The lower hybrid frequency decreases with decreasing density because the electron cyclotron frequency (high density limit) is much larger than the ion plasma frequency (low density limit). The shaded region highlights the lower hybrid frequency for the range of densities that can be achieved in ALEXIS. For typical conditions in ALEXIS with a low magnetic field strength, the lower hybrid frequency (and thus the EIH instability frequency) will be less than 400 KHz.

Table 4-2: Operating Conditions for the EIH experiment in ALEXIS.

Parameter	Value
Neutral Gas	Argon
Magnetic Field (B)	95 Gauss
Neutral Gas Pressure	0.29 mTorr
rf Power	40 W
Filament Emission Current (I_e)	60 mA
Filament Bias (V_{fil})	-20 V
Grid Bias (V_{grid})	80 V
Ion Temperature (T_i)	0.02 eV
Ion cyclotron frequency (f_{ci})	3.6 kHz
Lower hybrid frequency (f_{LH})	350 kHz

The experiments discussed in this section were performed using the operating conditions listed in Table 4-2. The first evidence of a high frequency instability in ALEXIS is shown in Figure 4-6. The 3D plot shows the wave power profile and frequency spectrum as a function of the radial position for a highly localized electrostatic instability observed in ALEXIS. The FFT amplitude is shown on the vertical axis (z-axis), the frequency on the left axis (y-axis), and the radial position on the right axis (x-axis), where r = 5 cm represents the edge of the vacuum vessel and 0 cm denotes center of the chamber. The colors indicate the FFT amplitude, where red corresponds to a large amplitude (3×10^{-5}) while dark blue indicates the noise floor of the spectrum (5×10^{-6}), plotted on a logarithmic scale. On the x-z panel, the wave power profile (radial profile of the peak FFT amplitude) shows that the instability amplitude peaks close to r = 0.6 cm, near the approximate boundary of the rf and filament plasmas. The y-z panel shows that the instability is localized in frequency space near 70 kHz ($f \sim 0.2 f_{LH}$). The x-y panel shows the FFT amplitude in both frequency space and as a function of the radial position.

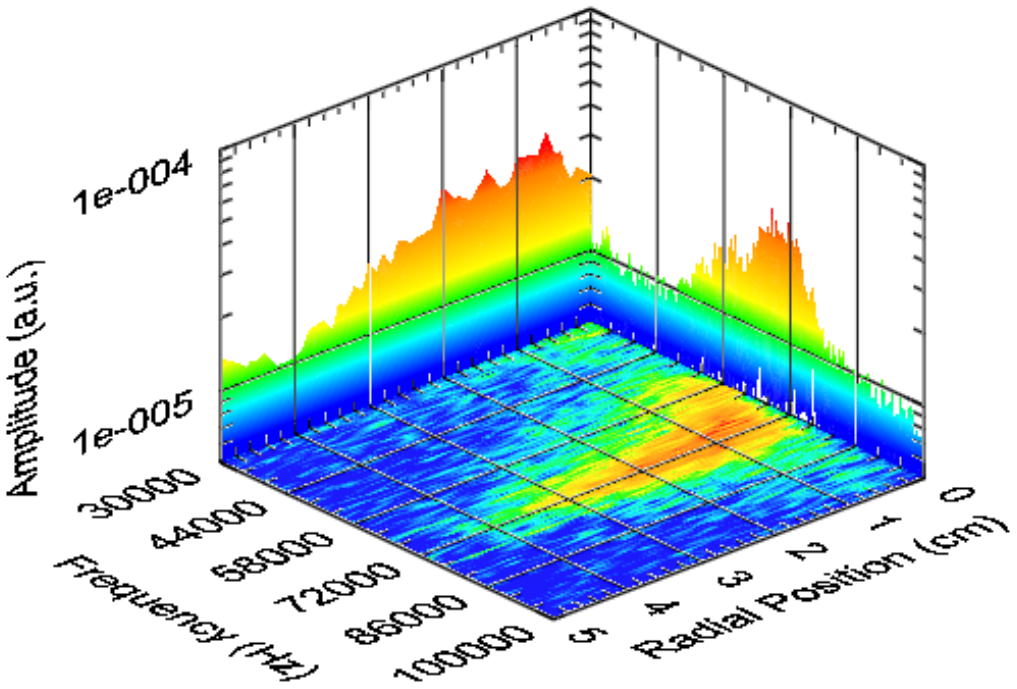

Figure 4-6: A 3D plot showing the Fourier spectrum of floating potential fluctuations in the presence of a localized electric field. The vertical axis and color represent the amplitude of the signal (a.u.), where red indicates a large amplitude and blue indicates a small amplitude. The left axis (y-axis) is the frequency (in Hz) and the right axis (x-axis) is the radial position (cm).

The measured plasma parameters are shown in Figure 4-7, where the shaded region in each figure represents the blocking disk region. The boundary between the interpenetrating plasmas is approximated as the edge of the shaded region. The plasma potential profile is shown in Figure 4-7(a). Outside of the blocking disk region, the plasma potential is measured to be approximately 60 V and the spatial structure is constant. However, at the blocking disk boundary, the plasma potential decreases. The radial electric field profile in Figure 4-7(b) shows that outside of the blocking disk region, the electric field is approximately zero and a peak electric field of 40 V/cm is located at r = 0.6 cm. As before, a negative electric field indicates there is a radially inward electric field in the plasma. The shear scale length is calculated to be approximately 0.4 cm and, with a magnetic field strength of 95 Gauss, the ion gyro-radius is calculated to be 1.4 cm, so the ion gyro-radius is about 3 times larger than the shear scale length.

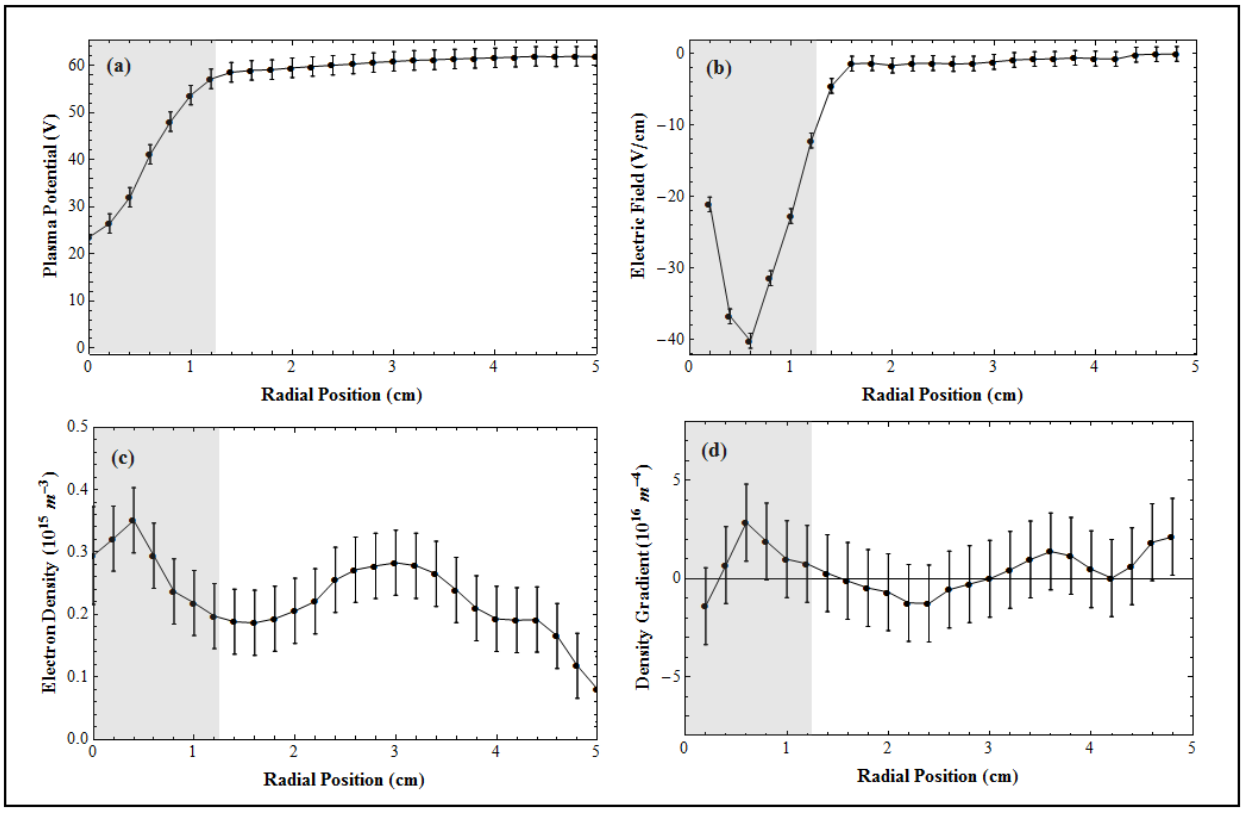

Figure 4-7: The measured plasma parameters for the observed instability. (a) shows the radial plasma potential profile and (b) shows the radial electric field profile as calculated from the plasma potential. (c) shows the electron density and (d) shows the electron density gradient profile as calculated from the electron density profile.

The electron density profile in Figure 4-7(c) shows that there is an increase in the density in the shaded region. The corresponding density gradient profile, shown in Figure 4-7(d), shows that there is a non-zero density gradient ($\nabla n(x) \sim 3 \times 10^{16}$ m^{-4}) at the same radial location as the peak electric field. Figure 4-6 showed that the peak amplitude of the instability is located at 0.6 cm, in the same region as both the electric field and the density gradient.

Since there is both an electric field and a density gradient in the same proximity as the observed instability, the driving mechanism of the instability must be identified. This is an important point because there are many instabilities than can exist in the presence of both a density gradient and a transverse electric field. Instabilities in the lower hybrid frequency range

can also be excited by parallel shear in the presence of density gradients. So, it is also important to rule out a parallel current as the driving mechanism.

4.2.1.1 Modification of the electric field profile

Many known instabilities are found in the lower hybrid frequency range in the presence of sheared plasma flows and density gradients. For instance, the lower hybrid drift (LHD) instability, which is driven by a large density gradient, has often been observed in plasmas with large parallel and perpendicular sheared flows.[89,114–116] Shear driven instabilities, such as streaming instabilities[15,50] and the EIH instability[39–41,49,80,92] can exist at magnetospheric boundaries where large density gradients are known to exist. These gradients are not the driving mechanism of the instabilities, but can substantially modify their properties. Additionally, the Farley-Buneman[84–86,97] streaming instability, which is often found in the ionosphere, is driven by electron beams and can be found in the presence of large electric fields. In this section, the mechanism responsible for exciting the electrostatic instability observed in the interpenetrating plasma configuration in ALEXIS is determined.

To determine the driving mechanism, the plasma potential of the filament plasma is varied by changing the bias on the grid and blocking disk. A large, positive grid bias corresponds to an electric field with a magnitude greater than 15 V/cm. A small positive grid bias corresponds to an electric field with a magnitude that is close to zero. In this experiment, the grid bias is varied from 100 V to 0 V in 5 V steps. The objective is to find conditions where either the density gradient profile or the electric field profile remains constant, and the other parameter changes. If the properties of the instability (such as frequency, amplitude, and wave power profile) respond to the changing parameter, we can infer that to be the driving mechanism.

Figure 4-8 shows the (a) density and (b) density gradient profiles for grid bias voltages of 75 V (circles, orange), 65 V (squares, green), 55 V (diamonds, blue) and 45 V (triangles, purple) as a function of the radial position. As the bias voltage is decreased, the density is observed to increase but the spatial structure remains constant and the location of the peak density is always localized to r = 0.4 cm. The spatial structure of the density gradient is consistent for each bias voltage and the peak density gradient (in the region of interest) is located at r = 0.6 cm for each case. The density gradient does not change significantly as the bias voltage applied to the plasma is varied.

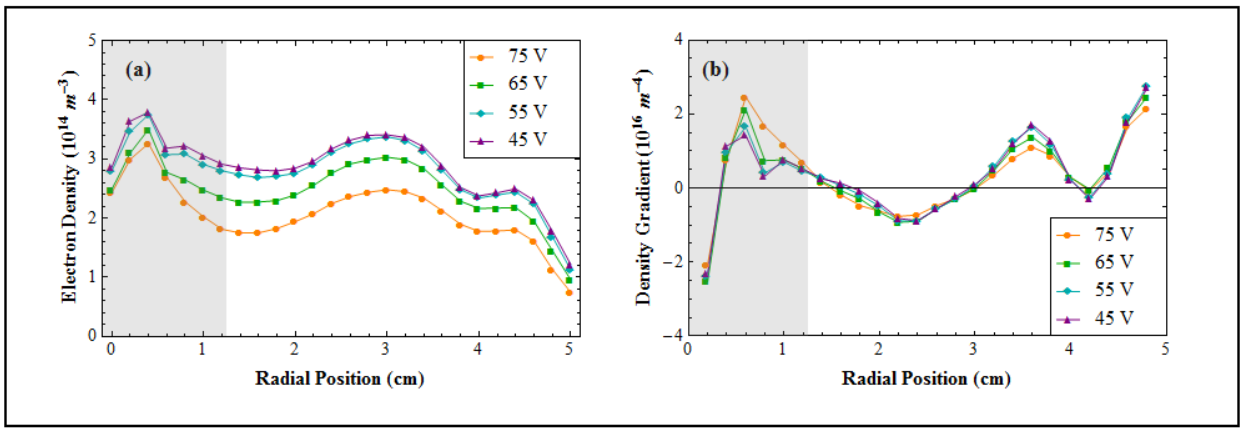

Figure 4-8: The (a) electron density profiles and (b) electron density gradient profiles as a function of the radial position for four grid bias values.

Since the bias voltage does not appear to modify the density gradient, it is necessary to determine if varying the grid bias has an influence on the electric field and instability amplitude. Figure 4-9 and Figure 4-10 show the instability amplitude and spectra, respectively, for different bias voltages. The spectra are measured at the same radial location as the peak wave power for each bias voltage. Figure 4-9 shows the evolution of the instability wave power (blue) and the electric field (red) as the grid bias is decreased. The wave power is calculated from the sum of the spectrum amplitude between 50 kHz and 100 kHz for each radial position. With a bias

voltage of 75 V applied to the grid bias, the filament plasma generates an electric field that is localized around 0.8 cm, with a peak electric field strength of 30 V/cm. There is a large amplitude wave that is localized to the same region as the electric field.

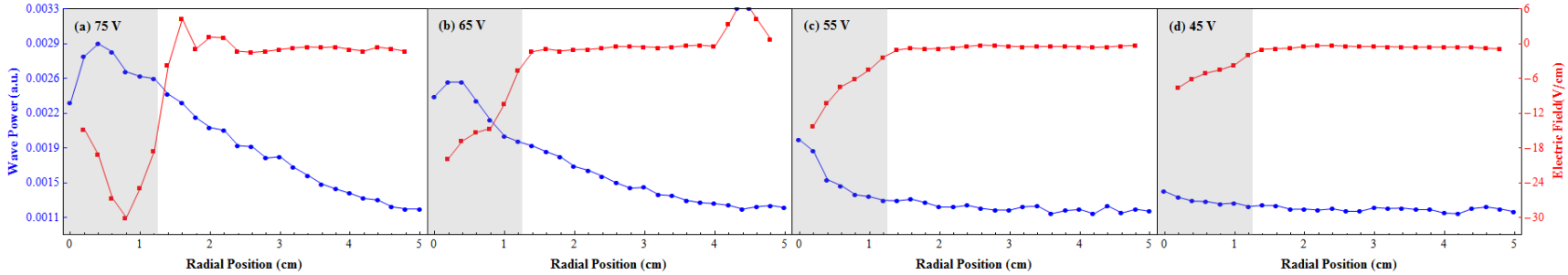

Figure 4-9: The wave power profile (blue) and radial electric field profile (red) are shown for different grid bias values. The profiles are shown for grid bias values of (a) 75 V, (b) 65 V, (c) 55 V and (d) 45 V (decreasing from left to right). The shaded regions represents where the blocking disk and filament plasma are approximately located. The boundary between the rf and filament plasmas is located at the edge of the shaded region.

As the grid bias is decreased to 65 V (b), the magnitude of the electric field decreases to near 20 V/cm, and as a result, the wave amplitude also decreases. The peak electric field moves toward the center of the chamber, and the wave packet follows the electric field, also moving inward. With the grid bias decreasing further to 55 V in frame (c), the peak electric field decreases and is now localized to the center of the plasma column. The peak wave power also moves to 0 cm, with the amplitude dropping significantly. Finally, as the grid bias reaches 45 V (d), the electric field drops below 10 V/cm and the peak wave power has now reached the level of the noise and there is no longer an instability in the plasma.

The variation of the bias voltage also has a large impact on the spectra of the instability. In Figure 4-10, the spectra acquired at the same radial location as the peak wave power are shown, where the spectra for a grid bias of 75 V and 65 V were acquired at r = 0.4 cm, and at r = 0 cm for grid biases of 55 V and 45 V. The spectra are arranged so that the magnitude of the electric field decreases going from the top of the plot to the bottom. The top spectrum (orange) corresponds to Figure 4-9(a) when a bias of 75 V is applied to the filament plasma. The bottom spectrum (purple) corresponds to Figure 4-9(d), when there was a bias of 45 V applied to the plasma. At the 75 V bias, when there is a peak electric field of approximately 30 V/cm, there is a large peak in the Fourier spectrum localized in frequency space near 70 kHz. As the electric field decreases, the peak amplitude of the spectra also decreases. For a 45 V grid bias, where the peak electric field is less than 10 V/cm and the wave power profile reaches the noise level, the spectrum shows that there is no instability present.

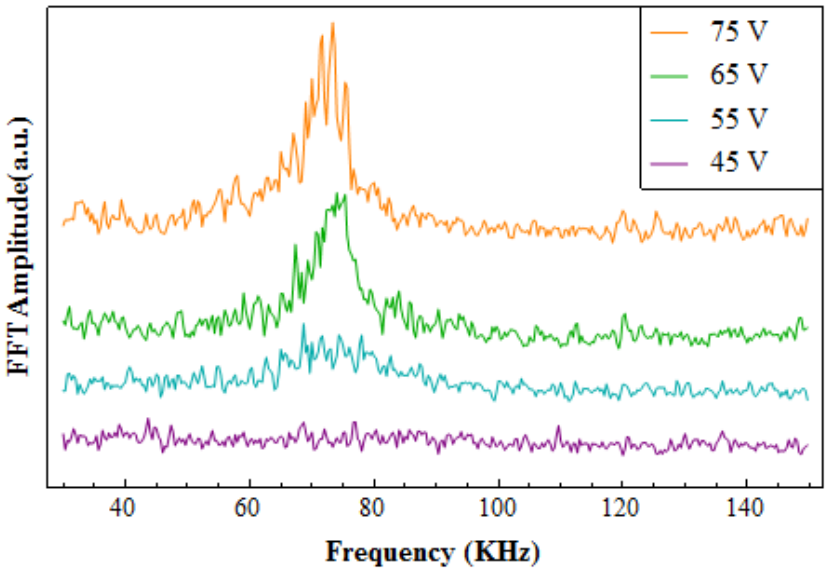

Figure 4-10: The Fourier spectra for grid bias values of 75 V (orange), 65 V (green), 55 V (blue) and 45 V (purple). The spectra were measured at r = 0.4 cm, 0.4 cm, 0 cm and 0 cm respectively.

Given that the density gradient remains constant and the amplitude of both the wave power and the spectra react to the changing electric field, it appears that the instability is driven by a sheared flow in the plasma. If the instability were driven by a density gradient instead of the electric field, the diamagnetic drift frequency (ω*) would be much larger than the shear frequency (ω_s) where,

$$\omega^* = -\frac{k_y T_e}{B n_e}\frac{\partial n_e}{\partial x} \tag{4-1}$$

$$\omega_s = {}^{E}/_{B L_E}. \tag{4-2}$$

The ratio of the diamagnetic drift frequency to the shear frequency is plotted in Figure 4-11 as a function of the radial position. To calculate this ratio, the electric field, density, and density gradient profiles when a 75 V grid bias is applied to the filament plasma are used.

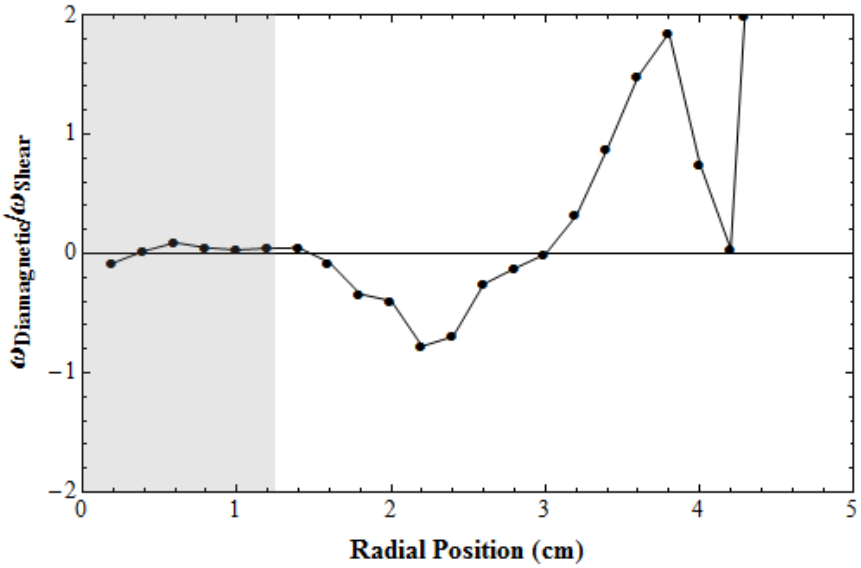

Figure 4-11: The radial profile of the diamagnetic drift frequency divided by the shear frequency. The shaded region indicates where the blocking disk and filament plasma are approximately located. The boundary between the rf and filament plasmas is located at the edge of the shaded region.

The electric field and the density gradient are both localized to the shaded region where the peak wave power is collocated. Figure 4-11 shows that outside of the region of interest, the diamagnetic drift frequency dominates and any instabilities localized to this region would be driven by a density gradient. However, in the region of greatest shear, the diamagnetic drift frequency is much less than the shear frequency, and the shear mechanism dominates. Since the instability is localized to this region, it is concluded that the observed instability is driven by the transverse velocity shear that is induced by the radial electric field, and not the density gradient.

In Figure 4-12, scatter plots of the diamagnetic drift frequency divided by the shear frequency as a function of the (a) peak electric field and (b) peak density gradient are shown. It must be noted that the data presented in the plots is for bias voltages where there was an instability observed in the plasma. For large magnitude electric fields, the ratio of the two frequencies is very small. But as the peak electric field decreases (which also corresponds to the wave amplitude decreasing), the ratio of the frequencies begins to rise. The ratio of the

frequencies is also very small for low density gradients, but as the density gradient increases, the frequency ratio also increases. For both plots, the shear frequency is always much greater than the diamagnetic drift frequency.

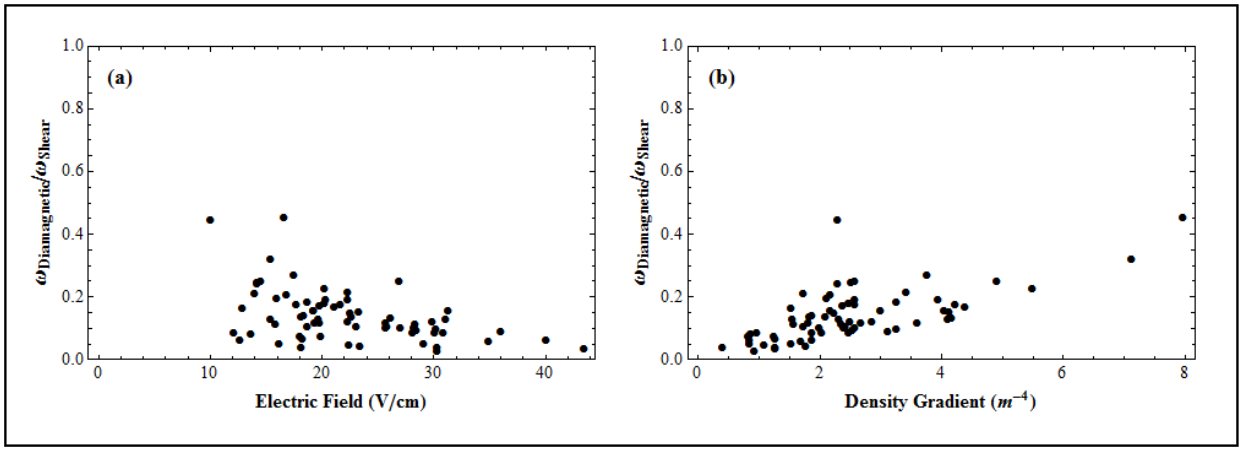

Figure 4-12: The ratio of the diamagnetic drift frequency to the shear frequency as a function of (a) the peak radial electric field and (b) the electron density gradient measured at the same location as the peak wave power.

As was discussed in Section 2-1, the Farley-Buneman streaming instability is also found near the lower hybrid frequency with un-magnetized ions and magnetized electrons. Because of the similarity between this streaming instability and the EIH instability, it is appropriate to rule out the mechanism that is responsible for driving the Farley-Buneman instability. In the *E* region of the ionosphere, charged particles mirror bounce back and forth along magnetic field lines. When the ion-neutral collision frequency (ν_{in}) substantially exceeds the ion cyclotron frequency, the ions can become un-magnetized relative to the electrons and the Farley-Buneman instability can develop. The ion-neutral collision frequency is,

$$\nu_{in} = \sigma \, n_{neutral} \sqrt{\frac{k_B T_i}{m_i}} \tag{4-3}$$

where σ is the cross sectional area, which for weakly ionized plasmas like those in ALEXIS is considered to be[117] ~ 5×10^{-19} m^2, k_B is the Boltzmann constant, T_i is the ion temperature (K), m_i is the ion mass, and $n_{neutral}$ is the neutral density where,

$$n_{neutral} = \frac{Pressure}{k_B T_i}. \tag{4-4}$$

For the observed instability, the ion-neutral collision frequency is 1.16 kHz compared to an ion cyclotron frequency of 22.75 kHz. For reference, the electron cyclotron frequency is 167 MHz and the shear frequency is 80 MHz. Ions are usually considered to be de-magnetized by collisions have a ratio of $\nu_{in} / \Omega_{ci} >> 1$. In this case, $\nu_{in} / \Omega_{ci} << 1$, so collisions with neutrals do not de-magnetize the ions, reducing the likelihood of the Farley-Buneman mechanism. However, within the shear layer, the ions can be considered to be un-magnetized if two criteria are satisfied: $\omega_s / \Omega_{ce} << 1$ and $\omega_s / \Omega_{ci} >> 1$. It is this second case that is satisfied by the experimental conditions. Therefore, it can again be concluded that it is the shear flow characteristics that are responsible for the observed instability.

The data presented thus far demonstrates that the instability driving mechanism is related to the transverse electric field as opposed to a density gradient or streaming electrons. To further prove this point, the parallel current was measured on the filament side of the blocking disk (r = 1.27 cm). The biasing grid is electrically connected to the blocking disk in order to prevent any parallel current from arising in the system[113] (and thus preventing parallel shear driven instabilities). It is essential that a parallel current be ruled out for the driving mechanism. The parallel current is measured to be near zero (~ -3 mA), and is nearly constant for all grid bias

values. The parallel drift velocity ($V_{\parallel drift}$) is calculated from the parallel current in the system and is compared to the electron thermal speed (V_{the}),

$$V_{\parallel drift} = \frac{I}{en_e A} \tag{4-5a}$$

$$V_{the} = \sqrt{\frac{2eT_e}{m_e}} \tag{4-5b}$$

where e is the electron charge, n_e is the electron density, A is the area of the blocking disk face, T_e is the electron temperature in electron-volts, and m_e is the electron mass. Figure 4-13 shows the parallel drift velocity normalized to the electron thermal speed, where $V_{\parallel drift} \sim 0.1 V_{the}$ is the threshold for the onset of current driven ion cyclotron instabilities (red dashed line). The shaded region indicates the bias voltage range where the waves were observed in the plasma.

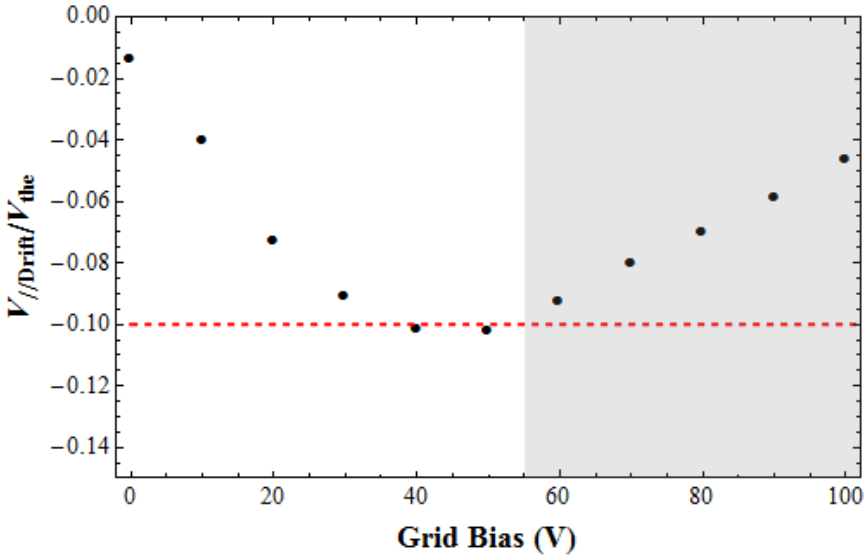

Figure 4-13: The current measured on the face of the blocking disk (facing the filament plasma) is used to calculate the parallel drift velocity in the experiment. The parallel drift velocity is normalized to the electron thermal speed for different grid bias values. For the bias voltages where a wave is observed (shaded region), the parallel drift velocity is below the threshold for the onset of parallel shear driven instabilities (horizontal dashed line).

Recall that as the bias voltage decreases, both the magnitude of the transverse electric field and the instability amplitude decrease. However, the parallel drift velocity increases as the bias voltage decreases, and $V_{\|drift} < 0.1V_{the}$ for conditions where the wave was observed in the plasma. The parallel drift velocity reaches the parallel shear driven instability threshold for bias voltages where no wave was observed in the plasma, which indicates that the instability is not a parallel shear driven instability. Thus, it can be concluded that parallel current is not the mechanism responsible for the observed instability. Having eliminated the density gradient, streaming electrons, and axial current, it is concluded that the transverse electric field is the primary driving mechanism of the instability.

4.2.1.2 Electrostatic instability characterization

In the previous section, the driving mechanism of the electrostatic instability observed in ALEXIS was determined to be the electric field. As the electric field decreases, the frequency of the instability should also decrease. A threshold should exist so that below a certain electric field magnitude, the wave amplitude goes to zero and the instability is no longer excited, as was shown in Amatucci *et al*.[50]. A series of spectra observed as the electric field is decreased (by varying the grid bias) is shown in Figure 4-14, where the magnitude of the electric field decreases from 31 V/cm to 8 V/cm from top to bottom. For large electric fields, there is a large amplitude instability at a frequency of approximately 70 kHz. As the peak electric field decreases, the peak FFT amplitude also decreases and the instability shifts to lower frequencies. The spectrum associated with the disappearance of the instability is indicated by the thick black line, which occurs for an electric field strength of approximately 10 V/cm. The maximum FFT

amplitude as a function of the transverse electric field strength is shown in Figure 4-15. As the electric field strength decreases, the instability amplitude also decreases, and below 10 V/cm, the instability amplitude reaches the noise level (indicated by the dashed horizontal line) and there is no longer an instability. The dashed vertical line indicates the threshold electric field, below which there is no instability present in the plasma.

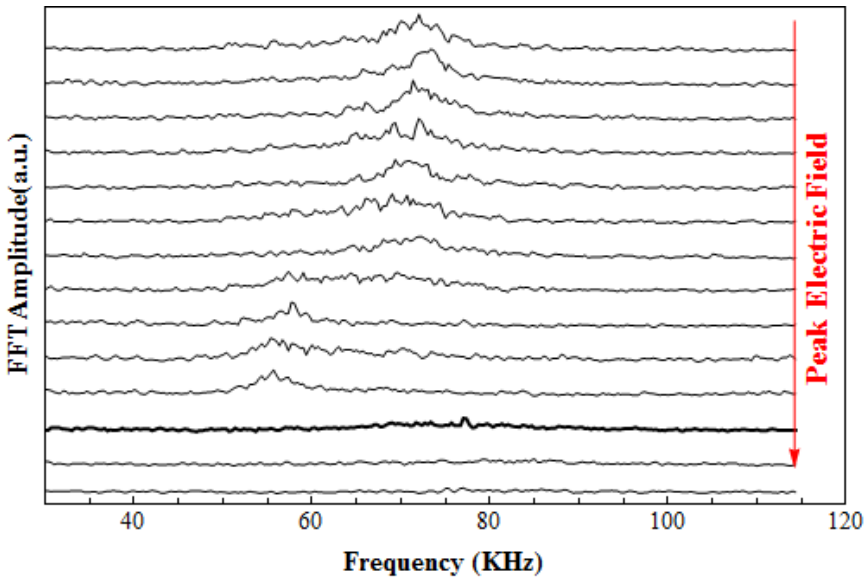

Figure 4-14: Fourier spectra for a varying radial electric field, where the electric field magnitude decreases from 31 V/cm to 8 V/cm from top to bottom. As the electric field magnitude decreases, the FFT frequency shifts down and the FFT amplitude decreases. The spectrum associated with the disappearance of the instability is indicated by the thick black line.

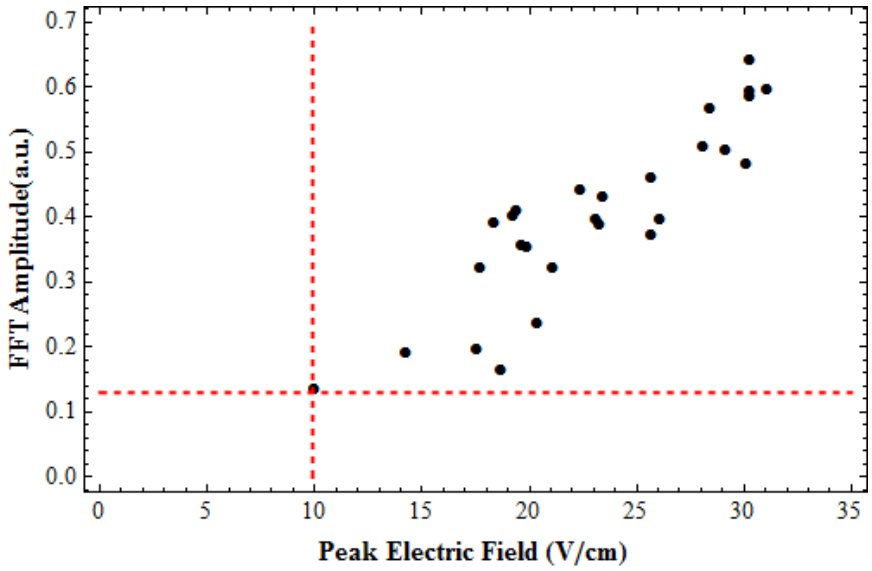

Figure 4-15: The maximum FFT amplitude is plotted as a function of the peak radial electric field. The dashed horizontal line (red) represents the noise floor of the FFT spectra and the dashed vertical line (red) represents the threshold of the electric field for which the instability disappears.

In addition to the correlation between the instability amplitude and the electric field strength, the components of the wavenumber vector, $\vec{k} = \vec{k}_{\parallel} + \vec{k}_{\perp}$, (where the parallel and perpendicular directions are defined with respect to the axial magnetic field direction) are used to reveal characteristics that are indicative of the EIH instability. In this experiment, the parallel and perpendicular wavenumbers are calculated using a double tipped Langmuir probe referred to as the "k"-probe. The "k"-probe is moved to the same radial position as the peak wave power and is rotated from 0 to 360 degrees in 10 degree steps. A phase difference measurement is taken at each rotated position and the wavenumber is calculated using $k = \Delta\phi/\Delta x$ (Equation 3-9(a)). The analysis for this diagnostic is discussed in Section 3.6.3.

The perpendicular wavenumber corresponds to the measurement acquired at 90 degrees, and the parallel wavenumber is computed from the average of the measurements at 0 and 360 degrees. In this experiment, the perpendicular wavenumber (k_y) was measured to be 87 m^{-1}, but can range anywhere from 60 m^{-1} to 100 m^{-1}. The parallel wavenumber (k_z) ranges from 1 m^{-1} to

29 m^{-1}, but was generally measured to be close to 10 m^{-1}. In spite of the experimentally observed variation of the parallel and perpendicular wavenumber values, the ratio k_z / k_y was consistently measured to be less than 0.2 with an average value of ~ 0.14 +/- 0.03. The EIH instability has perpendicular wavenumbers that are much larger than the parallel wavenumbers so that k_z / k_y is much less than 1. Simulations by Romero *et al.*[76] showed this ratio to be approximately 0.18 for the EIH mode. Amatucci *et al.*[50] showed that in a uniform density configuration, k_θ was typically measured to be 63 m^{-1} with very small k_z values.

The relationship between the wave packet and the Doppler shifted frequency is also a signature of the EIH instability. The wave packet should be localized around the position where the Doppler shifted frequency (ω_1) is at a minimum. The Doppler shifted frequency is defined as,

$$\omega_1 = \omega - k_y V_{Eo} \tag{4-6}$$

where ω is the EIH mode frequency and V_{Eo} is the magnitude of the velocity shear. Figure 4-16 shows the wave power (blue) and Doppler shifted frequency (red) as a function of the radial position. The shaded region represents the radius of the blocking disk. The wave packet (peak wave power) is localized to the region of the greatest Doppler shift, which is very indicative of the EIH instability.

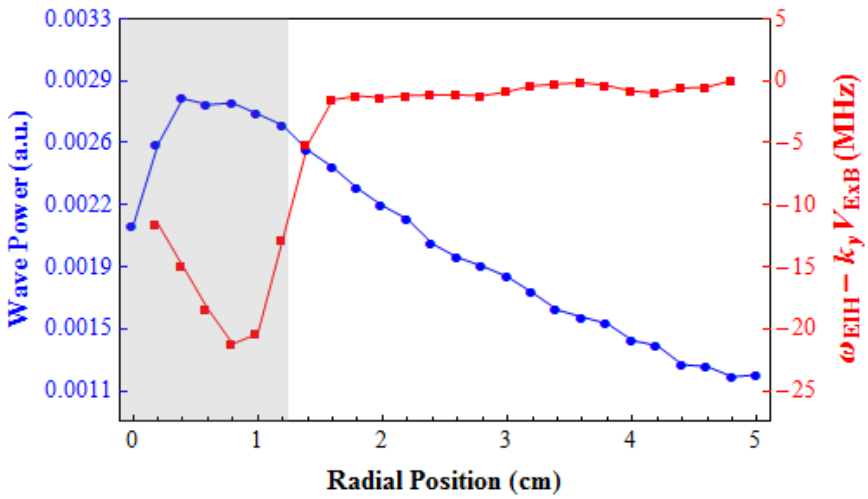

Figure 4-16: The wave power profile (blue) and Doppler shifted frequency profile (red) are plotted as a function of the radial position. The shaded region represents the filament plasma, with the edge of the shaded region indicating the approximate radial position of the boundary between the plasmas.

Kinetic theory described by Ganguli *et al.*[15,62,74] and Romero *et al.*[48,49,75,76] discuss the perpendicular wavelength with respect to both the electron gyro-radius and the shear scale length. For the EIH instability, the perpendicular wavelength is larger than ρ_e ($k_y \rho_e < 1$) and is of the same order as the shear scale length ($k_y L_E \sim 1$). For measurements in this experiment, Figure 4-17 shows $k_y \rho_e$ (x-axis) and $k_y L_E$ (y-axis). These measurements show that the wavelength is of the same order as the shear scale length ($k_y L_E \sim 0.39$) and not the electron gyro-radius ($k_y \rho_e \sim 0.093$). These results are consistent with the EIH instability and also help rule out instabilities such as the lower hybrid drift (LHD) instability[50,118] and the modified two-stream instability[50], which both prefer shorter wavelengths so that $k_y \rho_e \sim 1$.

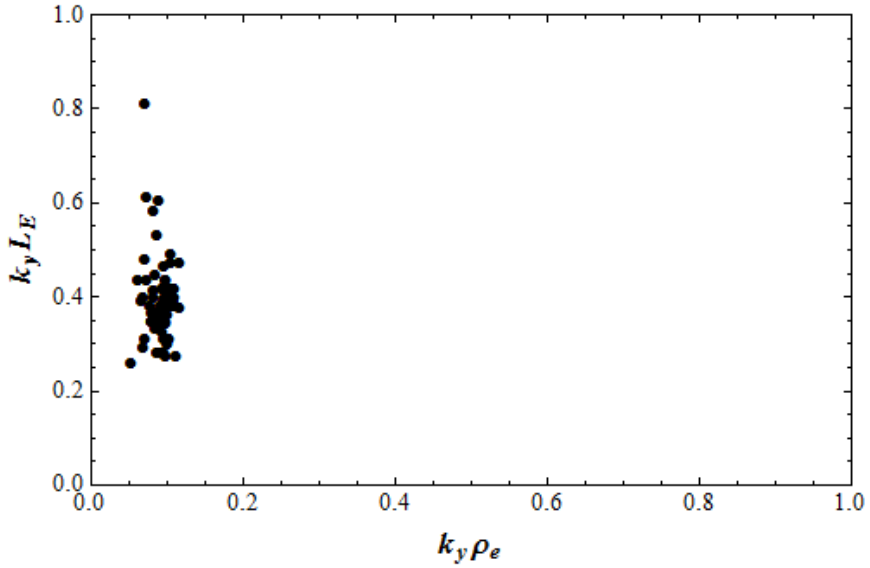

Figure 4-17: Measurements of $k_y L_E$ (y-axis) and $k_y \rho_e$ (x-axis) are shown. For all measurements, $k_y \rho_e$ was observed to be much less than 1 meaning the perpendicular wavelength is greater than the electron gyro-radius. $k_y L_E$ was measured to be of the same order as 1 meaning the perpendicular wavelength is of the same order as the shear scale length.

In the next series of plots, the experimental data is discussed in the context of the theoretical dispersion curves discussed in Section 2.2. The shooting code described in Section 2.2.4 is used to numerically solve the differential dispersion relations in Equation 2-44. The shooting code requires the normalized input parameters, $\alpha = V_{Eo}/(\Omega_{ce} L_E)$ (Equation 2-43), $\delta = \omega_{pe}/\Omega_{ce}$ (Equation 2-37) and $R_L = L_E/L_n$. The normalized parameters are calculated from average measurements in ALEXIS. For example, when computing a value of δ from a data set that includes 5 measurements of the electron density, δ is calculated from the mean electron density. To plot the dispersion relation against the electron density, the equation for δ is solved for the electron density to get,

$$n_e(\delta) = \frac{\epsilon_o m_e}{e^2} \Omega_e^2 \delta^2 \tag{4-7}$$

where ϵ_o is the constant of permittivity of free space, m_e is the electron mass, and e is the electron charge. Assuming that the magnetic field strength does not vary, $(\epsilon_o m_e \Omega_e^2)/e^2$ is constant and

the electron density is proportional to δ^2. The figures discussed below all show the theoretical dispersion relations as a function of measureable parameters. Table 4-3 lists the average values for the plasma parameters and the normalized parameters used in the shooting code.

Table 4-3: Average values for plasma and normalized theoretical parameters that are used in the shooting code to numerically solve the EIH dispersion relations and growth rates.

Parameter	Figure 4-19	Figure 4-20	Figure 4-21	Figure 4-22
B_o (Gauss)	95	95	95	95
E_x (V/cm)	40	20	22	25
L_E (cm)	N/A	0.52	0.44	Plotted
n_e (10^{14} m^{-3})	4.04	2.85	Plotted	3.58
L_n (cm)	N/A	Plotted	1.19	1.33
k_y (m^{-1})	71	80	87	79
$\boldsymbol{\alpha = V_{Eo}/(\Omega_{ce}L_E)}$	0.063	0.029	0.032	N/A
$\boldsymbol{\delta = \omega_{pe}/\Omega_{ce}}$	0.38	0.32	N/A	0.36
$\boldsymbol{R_L = L_E/L_n}$	Plotted	N/A	0.38	0.35
$\boldsymbol{\tilde{k}_y = k_y L_E}$	0.32	0.41	0.39	0.37

For typical ALEXIS parameters, Figure 2-3 showed that as the ratio of L_E / L_n increases (or as the density gradient becomes increasingly more localized) the mode frequency drops below the lower hybrid frequency. Figure 4-18 shows the ratios of the frequency (solid line) and growth rate (dashed line) to the lower hybrid frequency as a function of R_L. The experimentally measured frequencies and growth rates (as compared to the lower hybrid frequency) are shown in red and blue respectively. These data were taken as the current on the source magnets (magnets surrounding the rf antenna) was varied. By varying the source magnet current, the magnetic field is changed only slightly from 99 to 95 Gauss. The theoretical frequency curve shows that as the density gradient becomes more localized in the plasma, the frequency drops well below the lower hybrid frequency. In the limit where the density gradient is more localized than the electric field, the theoretical growth rate was observed to approach zero and the

frequency becomes increasingly smaller. The measured data shows that when the electric field is more localized than the density gradient ($L_E / L_n \sim 0.4$), the measured frequencies are in good experimental agreement with the theoretical predictions. The measured growth rates ($\gamma / 2\pi$) were between 8 kHz ($\gamma / \omega_{LH} \sim 0.027$) and 20 kHz ($\gamma / \omega_{LH} \sim 0.06$), but were typically closer to 12 kHz ($\gamma / \omega_{LH} \sim 0.036$). The theoretical model shows that ratio of the growth rate to the lower hybrid frequency is between 0.03 and 0.1. For reference, the ion cyclotron frequency (f_{ci}) corresponding to this data is ~ 3.6 kHz so that $\gamma / \Omega_{ci} \sim 3.75$ +/- 1.1. The growth rates presented here validate the assumption made in Section 2.2.1 that the instability growth rate is larger than or equal to the ion cyclotron frequency. Therefore, it is shown that the experimentally measured growth rates are in good agreement with the theoretically predicted values.

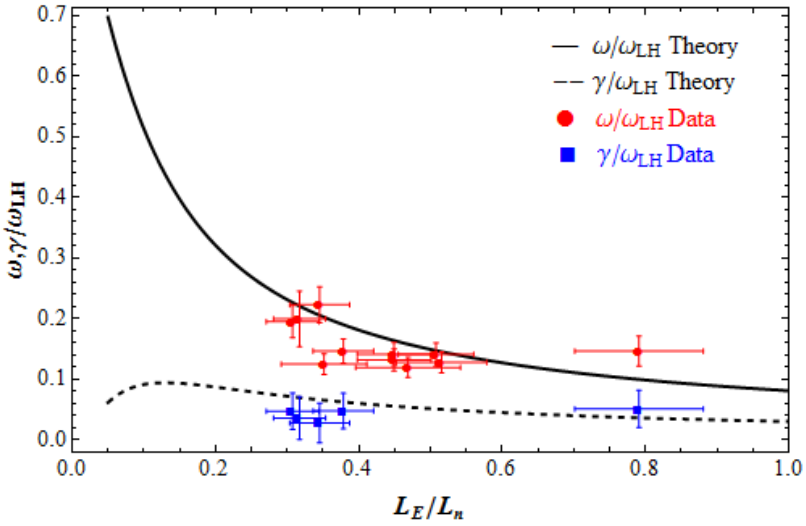

Figure 4-18: The theoretical curves for the frequency (solid line) and growth rate (dashed line) are plotted as a function of the ratio of the shear scale length to the density gradient scale length (L_E/L_n). The experimentally measured frequencies (red) and growth rates (blue) are plotted against the theoretical model.

An alternate approach to show the effect of the density gradient on the dispersion relation is to assume the shear scale length is constant and then plot the frequency as a function of the density gradient scale length. An experiment was performed to measure the frequency as the bias voltage on the grid was varied from 100 V to 55 V. In Figure 4-19, the ratios of the EIH

frequency to the lower hybrid frequency (solid line) and the growth rate to the lower hybrid frequency (dashed line) are plotted as a function of the density gradient scale length, assuming a constant shear scale length. For these conditions, L_E = 0.52 +/- 0.07 cm. The theoretical curves show that as the density gradient scale length, L_n, increases (i.e., the density gradient profile becomes broader), the plasma density profile becomes more uniform and the mode frequency increases towards the lower hybrid frequency. As the density gradient becomes more localized and the density gradient scale length approaches the shear scale length, the growth rate approaches zero. This indicates that once the density gradient becomes more localized than the electric field, the EIH instability cannot be supported. Typically, the density gradient scale length was measured to be greater than 0.9 cm, indicating that the electric field profile is twice as localized as the density gradient. The experimental measurements show that as L_n increases, the frequency also increases in a manner that is generally in good agreement with the theoretical predictions.

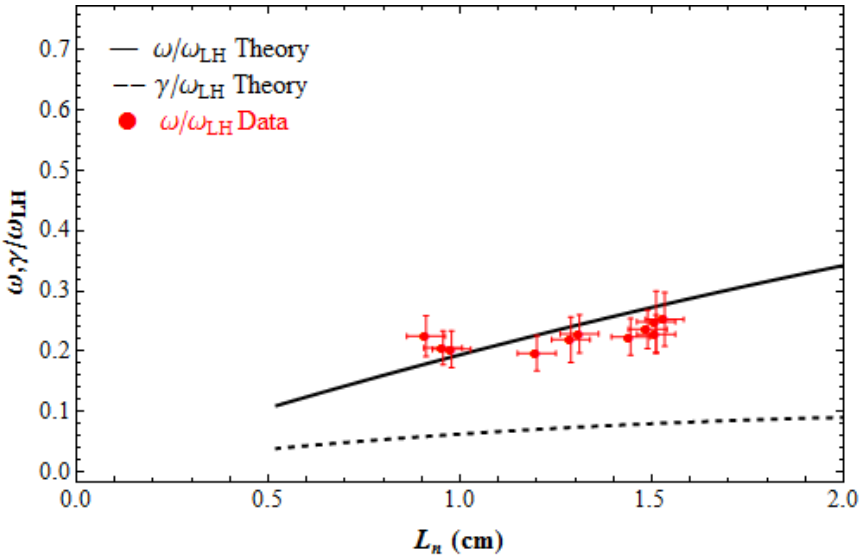

Figure 4-19: The theoretical curves for the frequency (solid line) and growth rate (dashed line) are plotted as a function of the density gradient scale length. The experimentally measured frequency values (red) are plotted against the theoretical dispersion curve.

The data shown in Figure 4-20 was taken as the filament emission current was varied from 120 to 30 mA. The emission current is directly correlated to the electron density of the filament plasma, so that as the emission current increases, there is a corresponding increase in the plasma density. The dispersion relation and experimental measurements of the instability frequency are plotted as a function of the electron density. For these experimental measurements, a radial electron density profile and a radial profile of the instability amplitude were measured for each emission current. From this data, the electron density and instability frequency at the location of the maximum instability amplitude is recorded. The theoretical model shows that as the electron density increases, the ratio of the mode frequency to the lower hybrid frequency should decrease exponentially. Figure 4-20 shows that the experimentally measured frequencies not only decrease as the measured density increases, but the measured values closely match the theoretically predicted values.

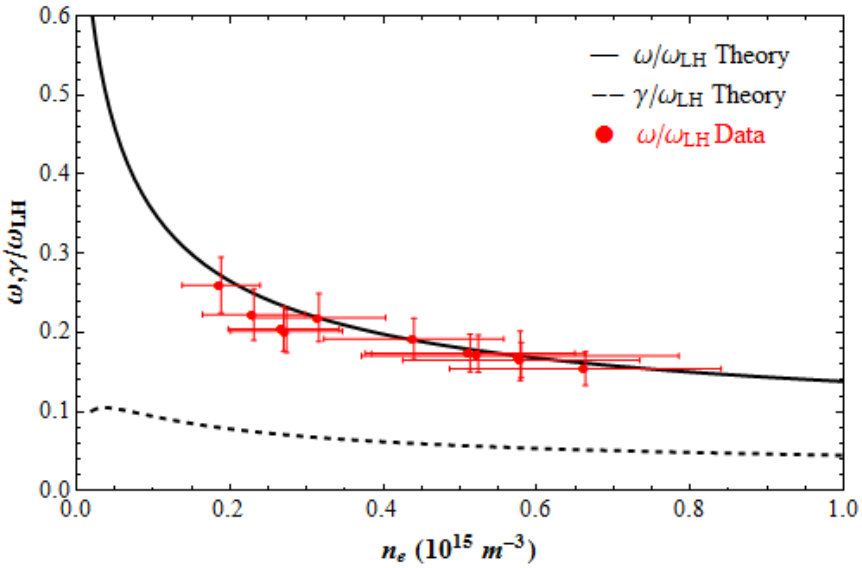

Figure 4-20: The frequency values are plotted as a function of the electron density. The experimentally measured data (red) shows excellent agreement with the computational frequency model (solid line). The theoretical growth rate curve is represented by the dashed line.

The final test performed on the instability characteristics is the scaling with the shear scale length, L_E. The measurements shown in Figure 4-21 were taken as the bias on the grid and the blocking disk was varied. The numerical solution for the frequency dispersion relation is plotted with the assumption that the density gradient scale length is fixed at L_n = 1.33 cm. As the shear scale length increases and the electric field profile broadens, the ratio of the EIH instability frequency to the lower hybrid frequency decreases from 0.26 to 0.22. The measured values of the instability frequency match the predicted EIH instability frequencies for localized electric field profiles.

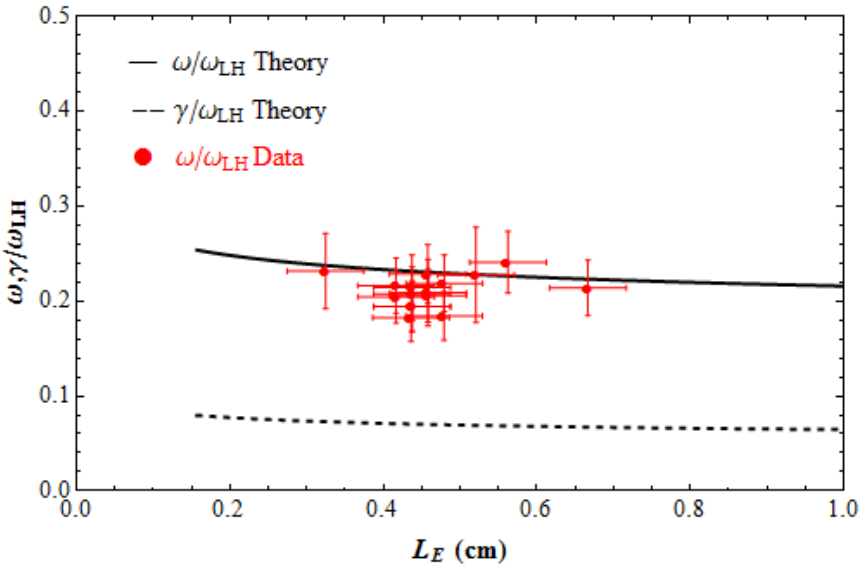

Figure 4-21: The measured mode frequencies (red) are plotted as a function of the shear scale length. The theoretical frequency curve is shown as the solid line and the computational growth rate is represented by the dashed line.

In summary, a series of experiments have been performed to characterize the observed instability in ALEXIS. The data presented here shows that the experimental measurements are consistent with the EIH instability in the presence of a density gradient. The ALEXIS measurements show that the instability shows the same characteristics and signatures that have previously been observed in experiments in the SPSC at the Naval Research Laboratory[50] and in

space plasmas[40,41,92] where density gradients in the presence of strong localized electric fields often occur. The instability behavior is also analogous to simulations performed by Romero *et al.*[49,75,80] and Peñano *et al.*[119].

4.2.2 Electron-ion hybrid instability in a uniform density

An important goal of this work was to study the EIH instability as the electron density is transitioned from a plasma with a uniform density to a non-uniform density. As was shown in Section 4.3.1, the EIH instability was successfully driven with a density gradient in the plasma. However, numerous attempts to drive the instability under uniform plasma conditions proved to be unsuccessful. This section will provide theoretical evidence that the EIH instability is not supported in a plasma with a uniform density in the ALEXIS device. Table 4-4 lists the parameters used for the theoretical models that are discussed in this section.

Table 4-4: The experimental (top) and theoretical (bottom) parameters for the uniform density configuration are listed.

Experimental Parameter	Value
B_o	127.5 Gauss
E_x	7 V/cm
L_E	0.4 cm
n_e	6×10^{14} m^{-3}
L_n	∞
Shooting Code Parameter	**Value**
$\alpha=V_{Eo}/(\Omega_{ce}\, L_E)$	0.006
$\delta=\omega_{pe}/\Omega_{ce}$	0.67
$R_L=L_E/L_n$	0

Both theory[74] and experimental measurements[50,77,78,120] have shown that the EIH instability frequency is very close to the lower hybrid frequency for a plasma with a uniform density. To find the correct EIH instability frequency range, the theoretical model in Equation 2-39, $\left[-k_y^2+\frac{\partial^2}{\partial x^2}+F(\omega)\frac{k_y V_E''(x)}{\omega-k_y V_E(x)}\right]\phi_1(x)=0$, provides the ratio of the mode frequency to the

lower hybrid frequency, where the lower hybrid frequency is calculated for typical plasma parameters measured in ALEXIS in the uniform density configuration (Table 4-4). The dispersion relation for the EIH instability in a uniform density is shown in Figure 4-22. The solid line shows the frequency ratio and the dashed line denotes the growth rate. The shaded region represents typical perpendicular wavenumber values that were measured in the density gradient case. The dispersion relation shows that in the region of possible k_y values, the mode frequency should be between $0.7\omega_{LH}$ and $0.9\omega_{LH}$. It is also important to note that in this region the growth rate is positive, indicating that the EIH instability should be supported in the conditions listed in Table 4-4.

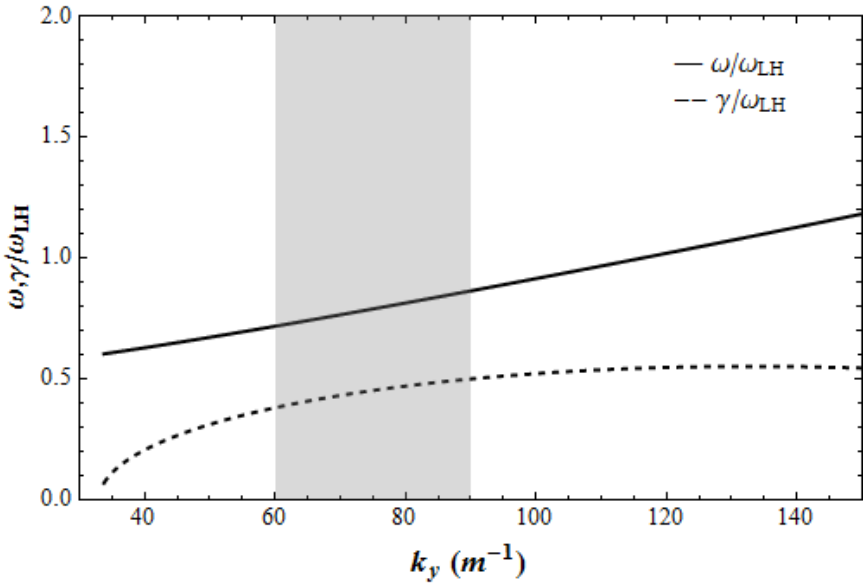

Figure 4-22: The theoretical dispersion relation as a function of the perpendicular wave number for a plasma with a uniform density. Typical values of ALEXIS were used in this computation. The frequency is shown as the solid line and the dashed line represents the theoretical growth rate. The shaded region highlights typical k_y values that were measured in the density gradient configuration.

The lower hybrid frequency (f_{LH}) was shown to not vary significantly as a function of the magnetic field strength in Figure 4-5(a). However, the lower hybrid frequency is highly dependent on the electron density. Figure 4-23 shows that the lower hybrid frequency decreases

for a decreasing electron density (for a magnetic field of 127.5 Gauss). The shaded region shows the range of typical electron densities that can be achieved in a plasma with a uniform density in ALEXIS. The lower hybrid frequency in this region ranges from 350 kHz for a density of 4×10^{14} m^{-3} to 450 kHz for a density of 7×10^{14} m^{-3}. It was shown above that the theoretical model predicted the ratio of the EIH instability frequency to the lower hybrid frequency to range anywhere between $0.7\omega_{LH}$ and $0.9\omega_{LH}$, so the EIH instability frequency (f_{EIH}) should be between 200 and 400 kHz.

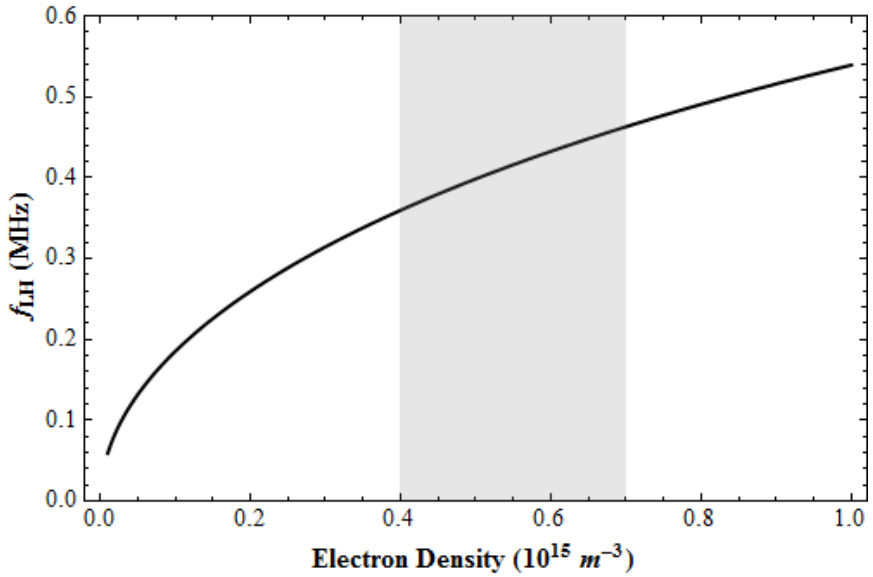

Figure 4-23: The lower hybrid frequency, f_{LH}, is plotted as a function of the electron density for a magnetic field of 127.5 Gauss. The shaded region highlights typical density values measured in ALEXIS, which indicates that the lower hybrid frequency will range from 350 kHz to 450 kHz.

For this experiment, the gas pressure was fixed to 0.26 mTorr, the grid bias was 85 V and the filament bias was -15 V. In order to make a uniform density profile, the densities of the rf and filament plasmas had to be matched. The rf power was increased to 100 W and the emission current was decreased to 40 mA. Figure 4-24 shows (a) the density profile and (b) the radial electric field profile where the shaded region represents the inner plasma and the edge of the shaded region indicates the approximate location of the boundary between the filament and rf

plasmas. Recall that in the previous section (see for example, Figure 4-7 or Figure 4-8), a density gradient was localized in the same region as the greatest sheared plasma flow occurred. In the region of the peak radial electric field strength, the density profile is significantly more uniform than in the density gradient case. There is a density gradient outside the greatest shear flow, but this region is of no interest to us since the wave packet will be localized around the peak electric field, as was shown in Section 4.3.1.

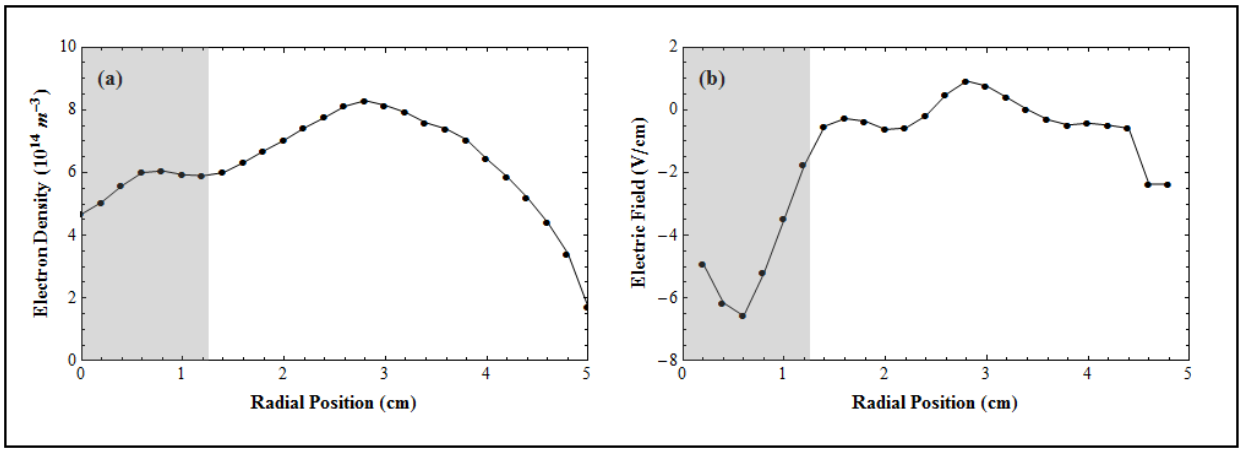

Figure 4-24: In (a) the electron density profile is shown and (b) shows the radial electric field profile. The electron density profile shows that a relatively uniform density has been achieved in the region of the peak electric field. The shaded region shows the blocking disk and filament plasma region, where the boundary between the rf and filament plasmas is represented by the edge of the shaded region.

A spectrum was measured at the same radial position as the peak electric field using the single tipped Langmuir probe located at Port 5. The theoretical model shown in Figure 4-22 predicts that the EIH instability will be located in frequency space between 200 kHz and 400 kHz. The spectrum in Figure 4-25 shows a very quiescent plasma, with no instabilities present in the stated frequency range. Note that the spikey peaks are due to electronic noise. These spikes are also observed in the signal in the absence of a plasma.

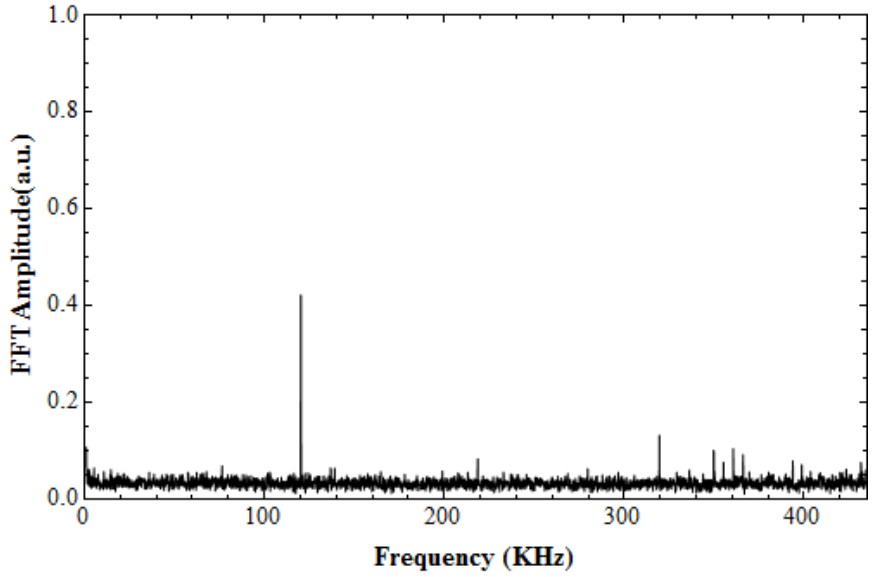

Figure 4-25: A typical Fourier spectrum for the uniform density case. The spikes are noise in the circuit. No instability is observed in the spectrum.

Parameter space was explored exhaustively to find the EIH instability in a uniform density plasma in ALEXIS. However, no instability was observed for frequencies greater than 100 kHz. So, it was asked why the EIH instability was not found in the uniform density configuration?

The answer to this question required a careful re-evaluation of the assumptions made to derive the EIH dispersion relation. Consider the theoretical model for the EIH instability in a uniform density. A key assumption in this derivation is that the instability has an infinitely long parallel wavelength such that $k_z = 0$. Obviously, the ALEXIS device, at a length of 1.7 m is somewhat less than "infinitely long", which limits k_z to a finite value. In the density gradient case, measured k_z values were typically between 1 and 29 m^{-1}, so clearly k_z is not zero; but the ratio k_z / k_y remained small. For the strong shear regime, Ganguli *et al.*[15] derived the EIH instability dispersion relation for a plasma with a uniform density with the k_z term included,

$$\left[\frac{\partial^2}{\partial x^2} - k_y^2 - k_z^2 + F(\omega)\left(\frac{k_y V_E''(x)}{\bar{\omega}} + \frac{k_z^2\Omega_e^2}{\bar{\omega}^2}\left\{1 - \frac{k_y V_d'(x)}{k_z\Omega_e}\right\}\right)\right]\phi_1(x) = 0 \qquad (4\text{-}8)$$

where $F(\omega)$ is defined in Equation 2-37, $V_E''(x)$ is the second derivative of the velocity shear, $V_d'(x)$ is the derivative of the magnetic field-aligned flow velocity, and

$$\bar{\omega} = \omega - k_y V_E(x) - k_z V_d(x). \qquad (4\text{-}9)$$

The magnetic field-aligned flow velocity is derived from a parallel current, and in Section 4.2.1.1 it was shown that the parallel drift velocity in the interpenetrating plasma configuration is below the threshold for the onset of parallel current driven instabilities, so $V_d(x)$ is neglected. If the dispersion relation in Equation 4-7 is simplified so that $k_z = 0$, the original dispersion relation for the EIH instability in a uniform density is recovered (Equation 2-39). The dispersion relation is normalized using the definitions in Equation 2-40 ($\tilde{k}_y = k_y L_E,\ \tilde{x} = x/L_E,\ \tilde{\omega} = \omega/\left(k_y V_{Eo}\right)$ and $V_E(x) = V_{Eo} f(\tilde{x})$), as well as the new normalization parameter,

$$\tilde{k}_z = k_z L_E. \qquad (4\text{-}10)$$

The normalized k_z dispersion relation is given as,

$$\left[\frac{\partial^2}{\partial \tilde{x}^2} - \tilde{k}_y^2 - \tilde{k}_z^2 + \frac{F(\tilde{\omega})}{\tilde{\omega} - f(\tilde{x})}\left(f''(\tilde{x}) + \frac{\left(\tilde{k}_z/\alpha\tilde{k}_y\right)^2}{\tilde{\omega} - f(\tilde{x})}\right)\right]\phi_1(\tilde{x}) = 0. \qquad (4\text{-}11)$$

The shooting code discussed in Section 2.2.4 was rewritten to include k_z so that the dispersion relation and growth rate could be plotted as a function of k_z and the axial wavelength.

Figure 4-26(a) shows the dispersion relation (solid line) and growth rate (dashed line) as a function of the parallel wavenumber. These results are for the same parameters listed in Table 4-4, and for a k_y = 87 m^{-1}. The addition of k_z into the dispersion relation significantly increases the instability frequency as much as five times greater than the lower hybrid frequency. More importantly, this shows that the growth rate for the EIH instability in a uniform density plasma maximizes as k_z approaches zero. The growth rate is zero for k_z values greater than 1.6 m^{-1}. In Figure 4-26(b), the dispersion relation (solid line) and growth rate (dashed line, black) are plotted as a function of the axial wavelength. The vertical dashed line (red) indicates the axial length of ALEXIS. This clearly shows that the growth rate is zero for wavelengths less than 4 meters. Therefore, it is concluded that under typical conditions in ALEXIS, the EIH instability cannot be supported in a uniform density because the required axial wavelengths (λ_z) are longer than the axial length of the experimental device.

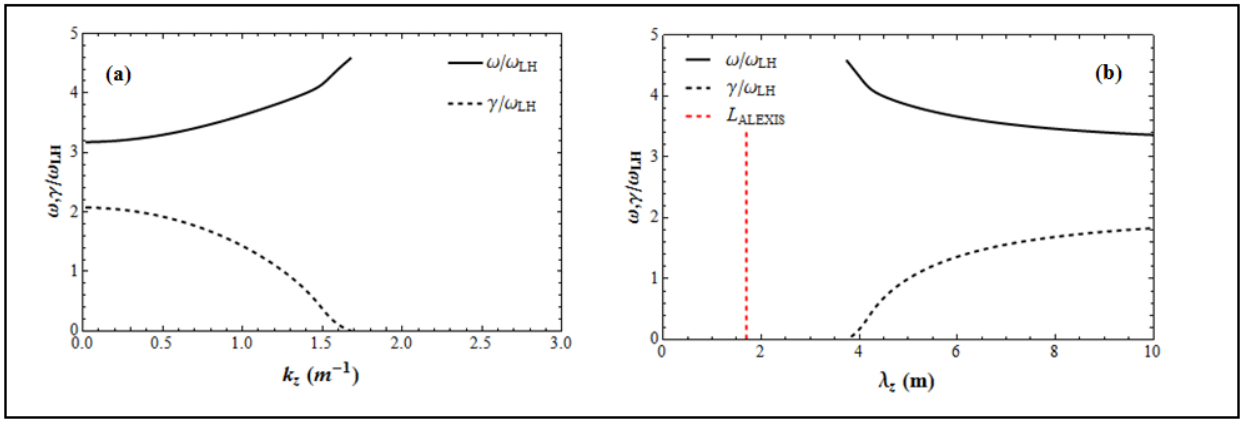

Figure 4-26: The theoretical model for a uniform density with k_z included shows (a) the frequency (solid line) and growth rate (black dashed line) as a function of the axial wavenumber and (b) the frequency (solid line) and growth rate (black dashed line) as a function of the axial wavelength. The red dashed line in (b) indicates the axial length of ALEXIS. The growth rate is zero for wavelengths less than 4 meters, which indicates that the EIH instability in a uniform density plasma cannot fit in the ALEXIS device in typical conditions.

The axial length of ALEXIS cannot be changed without effectively rebuilding the entire experiment. Therefore, an alternate question is: how could the operating conditions in ALEXIS

be modified to sustain the EIH instability? To address this question, the normalized shooting code parameters, δ and α, were varied individually to find a solution to the dispersion relation that could fit in ALEXIS. Figure 4-27 shows the dispersion relation and growth rate for α = 0.006 and a δ value of 0.20. Note that the maximum growth rate of the EIH instability in a uniform density plasma is predicted[74] to fall off sharply for value of $\delta < 0.5$. For $\delta < 0.20$, the EIH mode is not supported at all, and for $\delta > 0.20$, the growth rate is zero for axial wavelengths close to the axial length of ALEXIS.

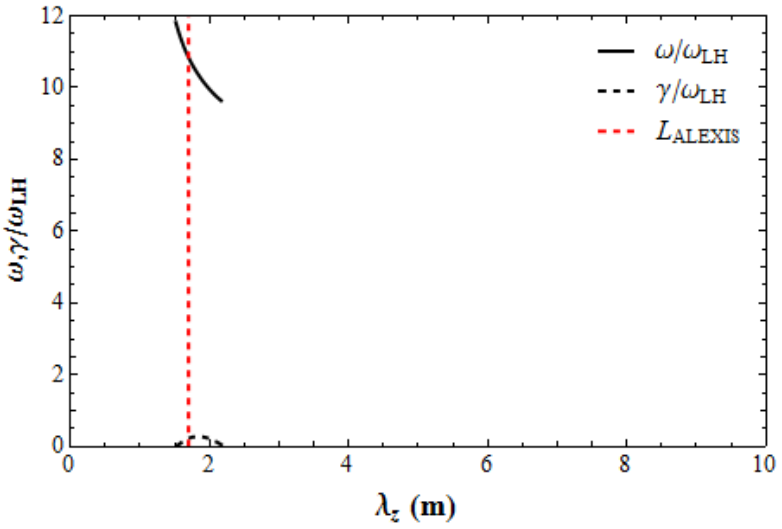

Figure 4-27: The computational data plotted here shows the frequency and growth rate as a function of the axial wavelength for δ = 0.20. The red dashed vertical line represents the axial length of ALEXIS. Here the growth rate is non-zero and the instability could be supported in ALEXIS. To achieve a value of δ this small, the density would have to be decreased to the mid 10^{13} m^{-3} range.

Since the normalized parameter δ is proportional to the square root of the electron density, decreasing the electron density while keeping the magnetic field strength constant will allow us to reach this value of δ. However, for this value of δ, the electron density would have to decrease by an order of magnitude to the mid 10^{13} m^{-3} range. Since the wavelengths are constrained to such a small window where the growth rate is positive in these conditions, it

would be impractical to strive to decrease the density in the hope that the EIH instability would be supported.

The other scenario that leads to a positive, non-zero growth rate for wavelengths that can fit in ALEXIS is to increase α to 0.09 while leaving $\delta = 0.67$. Since the shear scale length was observed to be more or less constant near 0.4 cm in these experiments, α is then exclusively proportional to the electric field strength. In order to reach such high values of α, the electric field must be increased to at least 100 V/cm. Figure 4-28 shows the dispersion relation (solid line) and growth rate (dashed line, black) as a function of the parallel wavelength for $\alpha = 0.09$, where the dashed vertical line (red) indicates the axial length of ALEXIS. The growth rate is clearly positive for wavelengths that can fit in ALEXIS. However, the largest value of the electric field that was measured in the dual plasma configuration was 42 V/cm (in the density gradient case), but were more typically between 20 and 30 V/cm. When there was a uniform density plasma, the measured values were usually near 10 – 15 V/cm. While this scenario is perhaps more attainable in ALEXIS, with the hardware available in the laboratory, these high electric fields were not able to be produced in the uniform density configuration.

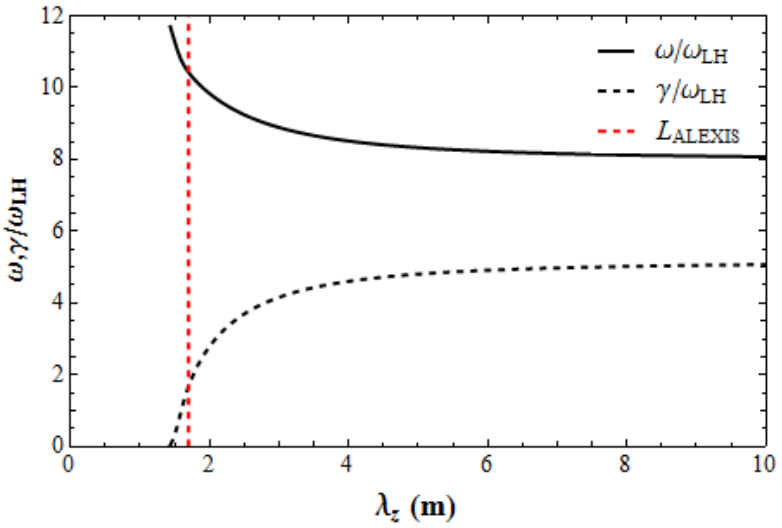

Figure 4-28: The computational data plotted here shows the frequency and growth rate as a function of the axial wavelength for $\alpha = 0.09$. The red dashed vertical line represents the axial length of ALEXIS. Here the growth rate is non-zero and the axial wavelength could fit in ALEXIS. To achieve a value of α this large, the electric field would have to be increased to 100 V/cm.

The data presented in this section shows that the EIH instability was not supported in ALEXIS with a uniform density plasma for the experimental conditions that are realistically attainable in the device. If the electron density was decreased by an order of magnitude, the growth rate would be non-zero for wavelengths that are close to the axial length of ALEXIS. Since δ is proportional to the square root of the electron density, lowering the density also decreases δ, which causes the maximum growth rate of the EIH mode to fall off sharply. Consequently, this limits the non-zero growth rate to a small range of wavelengths that barely fit in the experimental device. Alternatively, if the electric field strength was increased to 100 V/cm, the wavelength could also be decreased to fit in ALEXIS. However, achieving electric fields of that magnitude has proven to be inaccessible with the current configuration of ALEXIS.

4.3 Ion gyro-radius transition experiments

4.3.1 Introduction

For a wide variety of laboratory and space plasma environments, theoretical predictions[15,62,74] state that plasmas are unstable to transverse and parallel inhomogeneous flows over a very broad frequency and wavelength range. The kinetic theory described by Ganguli *et al*.[15,62,74] discusses three distinct instability regimes for transverse sheared plasma flows, where the instabilities may be characterized by a shear scale length compared to the ion gyro-radius. All of these instabilities have a single source of free energy, a transverse shear flow. The ratio of the ion gyro-radius to the shear scale length determines which mode is dominant, and is a convenient tunable parameter that can be used to induce the transition between the modes.

In the space plasma environment, sheared plasma flows have been observed by spacecraft at boundaries such as the Plasma Sheet Boundary Layer (PSBL)[36–38] and magnetopause[34,35]. Intense solar storms can compress and steepen the natural boundary layers. As boundary layers begin to relax from a compressed state and the ratio of the ion gyro-radius to the shear scale length decreases, observations of broadband electrostatic noise have also been reported[35,49,75,79–81], in which the frequency range extends from below the ion cyclotron frequency up to the electron plasma frequency. Simulations performed by Romero *et al*.[48] have confirmed that the free energy available in sheared electron flows can give rise to broadband wave spectra that can excite Kelvin-Helmholtz, ion cyclotron-like, and lower hybrid modes. As discussed in Chapter 1, a number of laboratory experiments have focused on studying these shear driven modes separately[19,28,50,60,67,69,77,78,121]. However, the continuous transition between the three modes has not been demonstrated using a single experimental setup, as would be the case in realistic

situations. In this section, the demonstration of the continuous variation of the ratio ρ_i / L_E, and the associated transition of the instability regimes driven by the shear flow mechanism is discussed.

4.3.2 Impact of the ion gyro-radius on velocity shear driven instabilities

The goal of this experiment is to create a localized radial electric field and then vary the ion gyro-radius with respect to the shear scale length by changing the magnetic field strength to access the different instability regimes defined by the magnitude of velocity shear. In this experiment, the magnetic field strength is varied from 90 Gauss to 590 Gauss and all other experimental parameters remain constant. Table 4-5 lists the operating parameters for this experiment.

Table 4-5: The operating parameters used in the ion gyro-radius transition experiment.

Parameter	Value
Neutral Gas	Argon
Magnetic Field (B)	90 to 590 Gauss
Neutral Gas Pressure	0.29 mTorr
rf Power	40 W
Filament Emission Current (I_e)	60 mA
Filament Bias (V_{fil})	-20 V
Grid Bias (V_{grid})	80 V
Ion Temperature (T_i)	0.02 eV
Ion cyclotron frequency (f_{ci})	3.6 to 22.5 kHz
Lower hybrid frequency (f_{LH})	~ 350 kHz

An electrically floating heated emissive probe located at Port 3 is used to measure the plasma potential as the probe is moved radially across the plasma column. The shear scale length is then calculated from the half-width at half-maximum of the radial electric field profile. Figure 4-29(a) shows the ion gyro-radius (circles, black) and the calculated shear scale lengths (squares, pink) as a function of the magnetic field strength. The red arrows indicate the EIH instability

data that was discussed in Section 4.2. The dashed horizontal lines (blue) show the minimum and maximum shear scale length values. The measured values range from 0.25 cm to 0.6 cm, with an average of 0.4 +/- 0.076 cm. For magnetic field strengths less than 160 Gauss, the ion gyro-radius is larger than the shear scale length. These are the same condition described in Section 4.3 when the EIH instability was observed. For magnetic field strengths greater than 520 Gauss, the ion gyro-radius is less than the shear scale length. Between 160 and 520 Gauss, the ion gyro-radius is comparable to the measured shear scale length values.

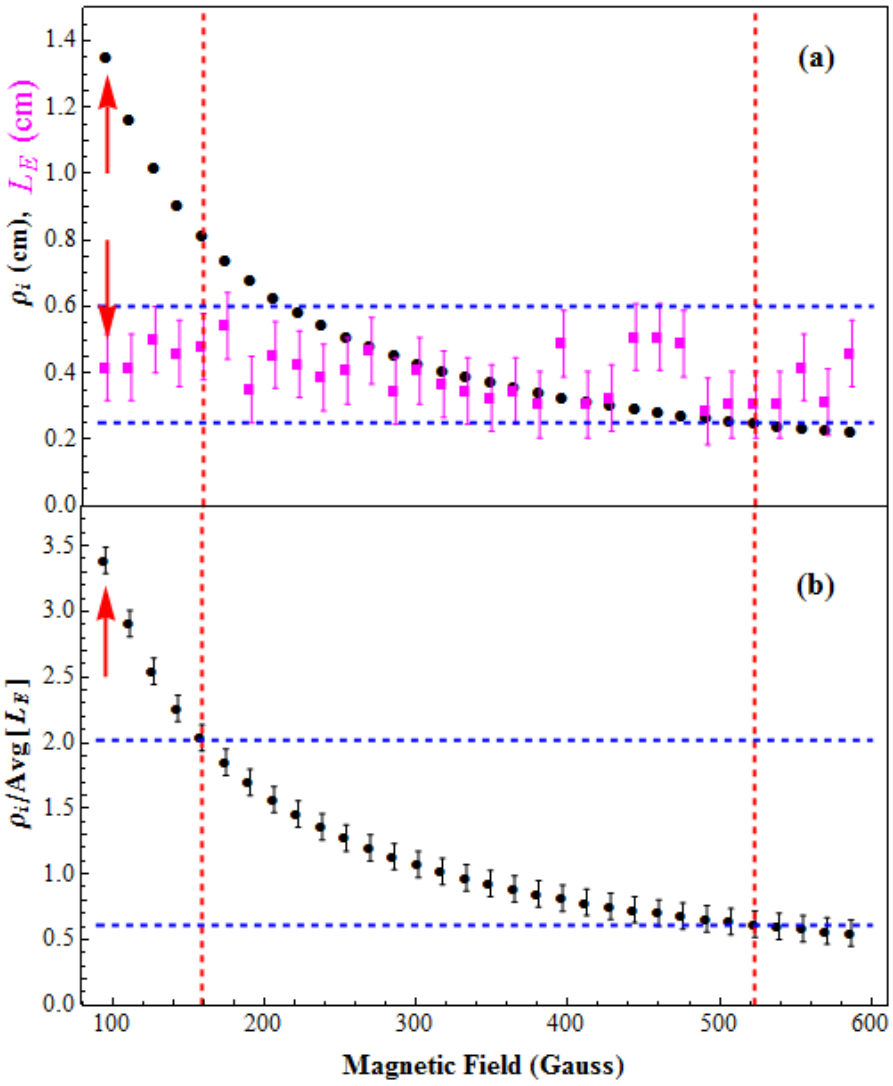

Figure 4-29: (a) The ion gyro-radius (circles, black) and the measured shear scale length (squares, pink) as a function of the magnetic field strength. The dashed horizontal lines (blue) show the minimum and maximum measured scale length. (b) The ratio of the ion gyro-radius to the average shear scale length as a function of the magnetic field strength. The vertical dashed lines (red) in both plots indicate the magnetic field strengths for which a transition in the mode frequency occurs. The horizontal dashed lines (blue) in (b) indicate the ratio value for which this transition occurs. The red arrows indicate the EIH instability data that was discussed in Section 4.2.

The response of the plasma was studied as the magnitude of the ratio ρ_i / L_E was varied from 0.55 to 3.39. The dashed lines (red) in Figure 4-29 indicate the magnetic field strengths for which a transition in the mode frequency occurs. Figure 4-29(b) shows the ratio of the ion gyro-radius to the average measured shear scale length (L_E = 0.4 cm). Here the horizontal dashed lines

(blue) show the ratio value for which the transition in the mode frequency occurs. The logarithm of the ratio of the mode frequency to the ion cyclotron frequency is plotted as a function of ρ_i / L_E in Figure 4-30 to show the three distinct frequency modes observed in the plasma. For reference, under these operating conditions, the ion cyclotron frequency (i.e., $f_{ci} = \Omega_{ci} / 2\pi$) ranges from 3.6 kHz to 22.5 kHz as a function of increasing magnetic field strength. When ρ_i / L_E is between 0.55 and 0.62 (corresponding to a high magnetic field strength), the mode frequency (~ 2 kHz) is much smaller than the ion cyclotron frequency ($\omega / \Omega_{ci} \sim 0.1$ +/- 0.0035), and when ρ_i / L_E is between 2.04 and 3.39 (corresponding to a low magnetic field strength), the mode frequency (> 50 kHz) is much higher than the ion cyclotron frequency ($\omega / \Omega_{ci} \sim 10.6$ +/- 2.8). If ρ_i / L_E is between 0.64 and 1.85, the mode frequency (~ 15 kHz) is comparable to the ion cyclotron frequency ($\omega / \Omega_{ci} \sim 1.2$ +/- 0.39).

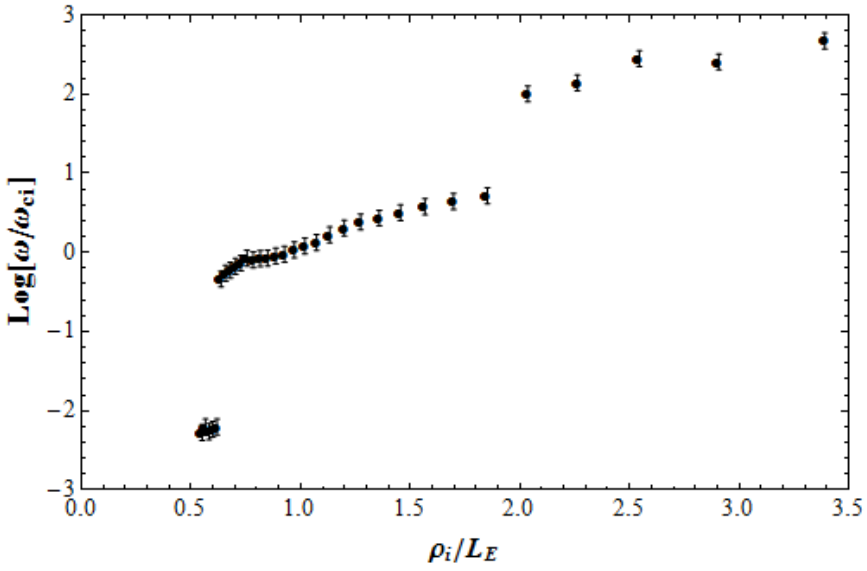

Figure 4-30: The ratio of the mode frequency to the ion cyclotron frequency is plotted on a Log scale as a function of the ratio of the ion gyro-radius to the shear scale length. For a large ρ_i / L_E (low magnetic field strength) there is an instability with a frequency less than the ion cyclotron frequency. For a small ρ_i / L_E (large magnetic field) the instability frequency is greater than the ion cyclotron frequency. When the ion gyro-radius is comparable to the shear scale length, the frequency was near the ion cyclotron frequency.

Figure 4-31 shows an example 3D plot for the three frequency ranges in the different ρ_i / L_E regimes. Each 3D plot shows the FFT spectrum amplitude (z-axis), frequency (y-axis), and the radial position (x-axis). For the radial position axis, 0 cm denotes the center of the plasma column and 5 cm corresponds to the edge of the vacuum vessel. In the x-z plane, the peak FFT spectrum amplitude is shown as a function of the radial position. The FFT amplitude is shown in frequency space in the y-z plane. In the x-y plane, the frequency is shown as a function of the radial position. The plot color corresponds to the FFT spectrum amplitude, where red indicates a large amplitude and blue indicates a low amplitude. Dark blue indicates the noise floor.

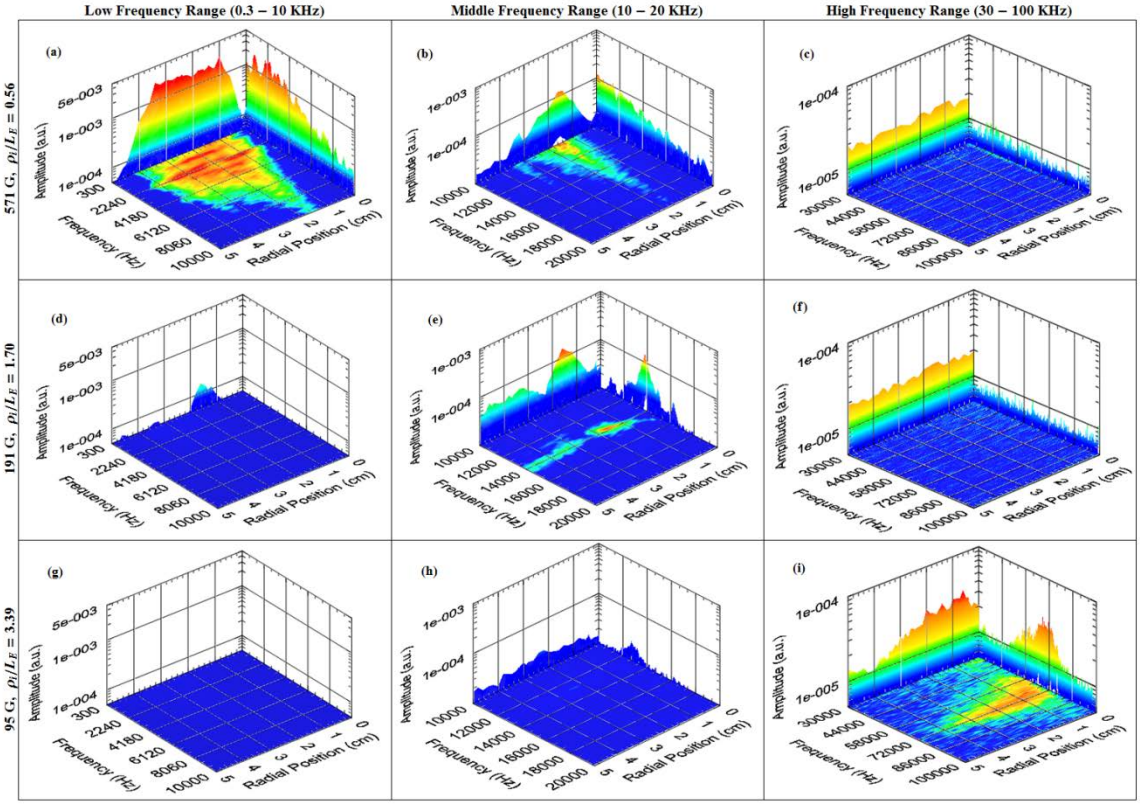

Figure 4-31: The 3D plots showing the FFT amplitude on the vertical axis, frequency on the left axis, and radial position on the right axis. The plots show different frequency ranges going from left to right, and show increasing values of ρ_i / L_E going from top to bottom. The color scale corresponds to the FFT amplitude where red indicates a high amplitude structure, and dark blue represents the noise floor of the FFT spectrum.

The first column (plots a, d, g) shows 3D plots for a low frequency range between 0.3 and 10 kHz. Plots b, e and h in the middle column show plots for the ion cyclotron frequency range (10 to 20 kHz), and the right most column (plots c, f, i) shows plots for a high frequency range between 30 and 100 kHz. It is important to note that the FFT spectrum amplitude scale in each plot is different. The first column has an amplitude that extends from 1×10^{-4} to 5×10^{-3}. The amplitude range in the second column extends from 1×10^{-5} to 1×10^{-3}. And the amplitude in the last column ranges from 1×10^{-5} to 1×10^{-4}. Each row shows 3D plots for a different ρ_i / L_E regime, where the ratio of ρ_i / L_E increases going from the top row to the bottom row. For example, Figure 4-31(a) shows the 3D plots for the low frequency range when the ion gyro-radius is smaller than the shear scale length, and Figure 4-31(g) shows the 3D plot for the low frequency range when the ion gyro-radius is larger than the shear scale length. The purpose of this plot is to show that for each ρ_i / L_E regime, an instability exists at only one frequency. No other instabilities exist in the plasma at the same time, and that only by changing the ρ_i / L_E ratio is an instability in a new frequency range introduced.

In the regime where $\rho_i < L_E$, there is an instability present below 10 kHz (in plot a), and at higher frequencies there are no high amplitude fluctuations present in the plasma (as shown in plots b and c). When the ion gyro-radius is comparable to the shear scale length, plot (d) shows that there is no longer an instability below 10 kHz, and (f) shows that no instability exists above 30 kHz in the high frequency range. Plot (e) shows that an instability is now supported only in the middle frequency range near the ion cyclotron frequency. Finally, in the regime where the ion gyro-radius is greater than the shear scale length ($\rho_i / L_E = 3.39$), no instabilities are excited at

low frequencies, and the EIH instability is observed near 70 kHz. This figure shows that the three distinct modes do not exist at the same point in time.

4.3.3 Transverse shear driven mode characterization

In the next series of plots, the distinct modes observed in the plasma are discussed. It will be shown that every aspect of the instability changes as the ratio ρ_i / L_E varies, not just the frequency of the instability. In the interest of completeness, the high frequency mode, which was characterized as the EIH instability modified by a density gradient, will also be described briefly.

4.3.3.1 Low frequency mode

The data discussed in this section is for the low frequency instability that is observed when ρ_i / L_E = 0.56. Figure 4-32 shows the Fourier spectrum of the low frequency instability, measured at the same radial location as the peak wave amplitude. The characteristic frequency is close to 1 kHz, with the three harmonics near 2 kHz, 3 kHz, and 4 kHz. This spectrum is a very typical case of what is observed when the ion gyro-radius is smaller than the shear scale length. The instability is located at a low frequency so that ω / Ω_{ci} = 0.11.

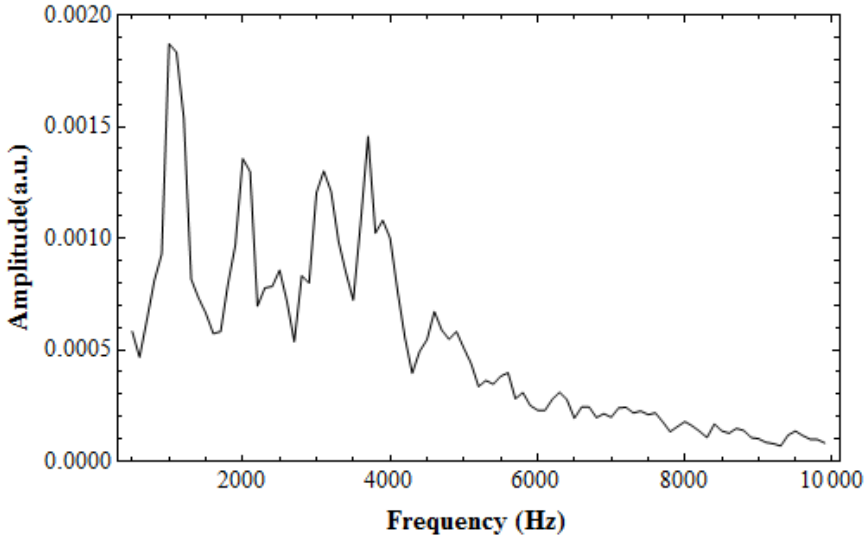

Figure 4-32: Fourier spectrum for when the ion gyro-radius is less than the shear scale length (corresponding to a high magnetic field strength). The characteristic frequency is approximately 1 kHz, with three harmonics at higher frequencies. For this case, $\rho_i / L_E = 0.56$.

Figure 4-33 shows (a) the wave power profile, (b) the radial electric field profile, and (c) the radial electron density profile for the low frequency instability. The wave power profile shows that the instability extends over the entire plasma column, peaking at r = 1.6 cm. There is a radially outward electric field with a peak value of 16 V/cm located at r = 1.8 cm. The electron density profile shows that the electron density peaks at r = 2 cm with a density of 5.5×10^{15} m^{-3}. This figure shows that the wave packet is localized in the same region as the peak electric field and the peak electron density. The parallel and perpendicular wavenumber components (relative to the background axial magnetic field), are measured to be 7.99 m^{-1} and 137.46 m^{-1} respectively, with a ratio of $k_z / k_y = 0.058$ and a mode number ($m = k_y r$) of 2.2. The mode characteristics are consistent with those exhibited by the Kelvin-Helmholtz instability.[76,122] In Romero *et al.*[76], simulations showed that for the Kelvin-Helmholtz instability, the ratio $k_z / k_y \sim 0.01$, and Peñano *et al.*[119] showed that the growth rate for this instability is non-zero for mode numbers greater than 1 in a cylindrical device such as ALEXIS.

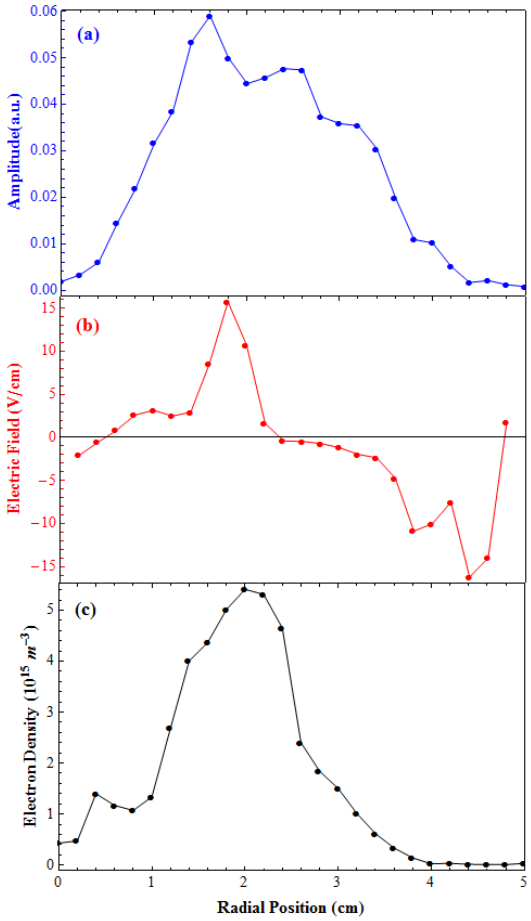

Figure 4-33: The (a) wave power, (b) electric field, and (c) electron density profiles that correspond to the low frequency instability are shown. For this case, $\rho_i / L_E = 0.56$.

4.3.3.2 Ion cyclotron frequency mode

A typical spectrum for the instability found in the regime when the ion gyro-radius is close to the shear scale length ($\rho_i / L_E = 1.70$) is shown in Figure 4-34. The spectrum in this case is extremely localized in frequency space and shows that the instability has a much higher frequency ($\omega / \Omega_{ci} = 1.9$) than in the previous case. This spectrum was measured at the same radial position as the peak wave amplitude.

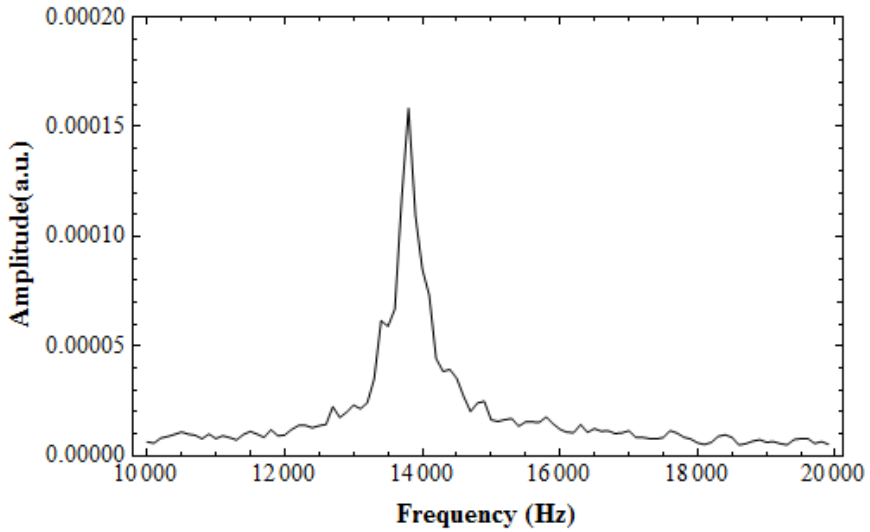

Figure 4-34: Fourier spectrum for when the ion gyro-radius close to the shear scale length. For this case, $\rho_i / L_E = 1.70$.

Figure 4-35 shows the plasma parameter profiles, (a) the wave power, (b) the radial electric field, and (c) the electron density, measured for this case. The wave power shows that the instability is much more localized in space, peaking at r = 1.6 cm. A radially inward electric field, with a peak strength of 10.5 V/cm is measured in the plasma. The electric field is now observed to peak in the center of the plasma column so that the peak wave power occurs just outside the radial location of the peak electric field. The electron density is an order of magnitude less than in the previous example, peaking at 5×10^{14} m^{-3}. The electron density profile shows that the density in the filament plasma region is much less than that of the rf plasma, creating a density hole in the plasma. The wave power peaks between the peak electric field and the peak electron density. The parallel and perpendicular components of the wavenumber are measured to be 15.55 m^{-1} and 112.76 m^{-1} respectively, with a ratio of k_z / k_y = 0.14 and a mode number ($m = k_y r$) of 2.2. These characteristics are indicative of the inhomogeneous energy density driven instability (IEDDI) mechanism, which is driven by a transverse velocity shear when the ion gyro-radius is comparable to the shear scale length and has a mode frequency comparable to the ion cyclotron frequency.[19,119] Analysis by Peñano *et*

al.[119] show that the growth rate for the IEDDI mode maximizes at m = 1. It is noted that in earlier studies of the IEDDI mechanism on ALEXIS gave parameters of $k_z \sim 8$ m^{-1} and $k_y \sim 70$ m^{-1}, or $k_z / k_y \sim 0.11$ with a mode number between 1 and 2.[19] Although using quite different plasma sources, the axial and radial dimensions of ALEXIS remain the same. Therefore, it is reassuring that the wave packet for the current ALEXIS configuration is quite similar to the past results.

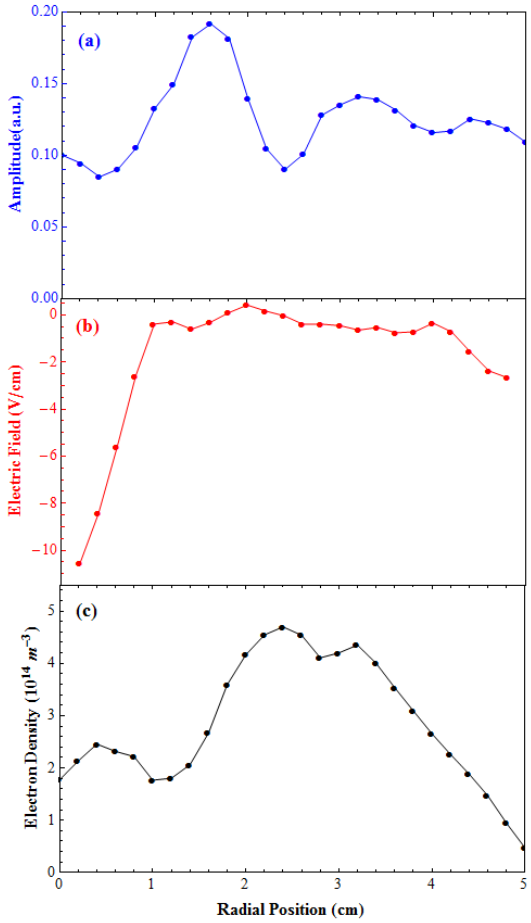

Figure 4-35: The (a) wave power, (b) electric field, and (c) electron density profiles that correspond to the ion cyclotron-like instability are shown. For this case, $\rho_i / L_E = 1.70$.

4.3.3.3 Electron-ion hybrid mode

The high frequency mode observed in this experiment has already been confirmed as the density gradient modified EIH instability, as was discussed in Section 4.2. Under these conditions, the ion gyro-radius is larger than the shear scale length (ρ_i / L_E = 3.39) and the instability is localized at a frequency much greater than the ion cyclotron frequency (ω / Ω_{ci} = 14.5) but close to the lower hybrid frequency (ω / ω_{LH} = 0.17). The data presented in Section 4.2 (Figure 4-7 and Figure 4-9) showed that the instability amplitude peaks at r = 0.4 cm and is localized near the boundary of the filament and rf plasmas where the velocity shear is localized with a peak electric field of 40 V/cm. The electron density is also observed to peak in the same region as the peak electric field, which creates a large density gradient at the same radial location as the peak wave power. The measured perpendicular and parallel wavenumber components are 87 m^{-1} and 10 m^{-1} respectively, with a ratio of k_z / k_y = 0.12. Simulations by Romero *et al.*[76] showed that for the EIH mode, k_z / k_y ~ 0.18. In this case, the mode number is not important, because the cylindrical effects are minimal.

In summary, this is the first experimental data that demonstrates that a stressed, collisionless plasma can relax through wave emission in a very broad frequency range. Three distinct modes spread over five orders of magnitude in frequency (normalized by Ω_{ci}) arise when the ratio of the ion gyro-radius to the shear scale length is varied by a factor of 7. As the ion gyro-radius transitions from a value less than the shear scale length to a value comparable to the shear scale length, the mode in the system goes from a frequency less than the ion cyclotron frequency to near the ion cyclotron frequency. As ρ_i / L_E increases more, the mode frequency rises further into the lower hybrid regime. In a small laboratory device like ALEXIS, it is difficult to access the ideal regimes defined by $1 << \rho_i / L_E$, $\rho_i / L_E \sim 1$, and $\rho_i / L_E << 1$ while

keeping other parameters nearly unchanged. But within the practical limitations, the transition between the modes is quite clear in this experiment.

Chapter 5: Conclusions

This work was performed using the Auburn Linear EXperiment for Instability Studies (ALEXIS) in an argon plasma. To conduct the experiments discussed in this dissertation, ALEXIS was upgraded to include a small, secondary plasma source for a dual plasma source configuration.[113] Biasing the two plasma sources to different potentials allows for highly localized electric fields to be generated at the boundary of the two plasmas, inducing a strong $\boldsymbol{E} \times \boldsymbol{B}$ velocity shear. The advantage of using such an interpenetrating plasma configuration is that independent control over both the density gradient and the electric field that appears at the boundary layer is possible. This experiment also has the versatility to be used in the dual plasma configuration, or the blocking disk can be moved out of the way so that the rf plasma source can be used independently from the filament source for basic plasma physics experiments, such as spectroscopy or the testing of new plasma diagnostics.

The work presented in this dissertation involved experimental studies of sheared plasma flows in a regime where the ion gyro-radius was larger than the shear scale length. The central goal of this work was to investigate the physical properties of the electron-ion hybrid (EIH) instability in the case where the plasma density is uniform and where there is a density gradient. The impact of varying the ratio of the ion gyro-radius to the shear scale length was also studied, which addressed several questions and outstanding theoretical predictions in regards to space

plasma physics and the plasma dynamics that occur at boundary layers in the space plasma environment. The experiments performed for this dissertation are briefly summarized in Section 5.1, and possible future experiments are presented in Section 5.2.

5.1 Summary of experiments

The theoretical framework discussed in Chapter 2 was a substantial undertaking for this project. The kinetic theory for the EIH instability was initially derived by Ganguli *et al*.[74] for a plasma with a uniform density. In the case of a density gradient, the differential dispersion relations had been discussed by Scales *et al*.[41] in context of chemical release experiments in the ionosphere in which electrons and two ion species (positive ions and heavy negative ions) were considered. Simulations by Romero *et al*.[75] discussed the effect of a density gradient on mode stability using a fluid description consisting of the mass conservation and momentum balance equations, in which pressure effects are ignored. The fluid model was generalized to include flows both parallel and perpendicular to the magnetic field vector, where the ion motion is considered in both the magnetized and un-magnetized limits. Since both of these formalisms were extremely generalized, the dispersion relation was re-derived using kinetic theory to include only electron and ion flow in a transverse direction in the limit where the ions are considered to be un-magnetized. The theoretical model discussed in Chapter 2 was used as a benchmark to compare experimental data to, as well as to characterize plasma instabilities and to provide evidence as to why the EIH instability was not observed in plasmas with a uniform density.

The interpretation of plasma parameters in the new experimental configuration was discussed in Section 4.1. In this experiment, it was established that a void was successfully created by placing a blocking disk in the center of the primary rf plasma. Data showed that the

blocking disk did not significantly modify the spatial structure of the rf plasma potential. The filament plasma was observed to fill the density depletion region, creating conditions where the density gradient between the plasmas could be controlled by varying the amount of filament plasma that was made. An electric field localized to the boundary between the plasmas was achieved by varying the potential of the filament plasma relative to the rf plasma potential. In a low magnetic field strength where the ion gyro-radius is greater than 1 cm, the shear scale length, which was measured to be approximately 0.45 cm, is less than the ion-gyro radius and it is possible to study a frequency regime that is new to the ALEXIS device. Despite having a large localized electric field in both the filament plasma configuration and the interpenetrating plasma configuration, it was shown that in order to drive an instability in the region of the greatest shear, the interpenetrating plasma configuration was essential. Finally, the azimuthal symmetry of the experiment was shown to hold for the dual plasma configuration. This preliminary experiment was essential to this work in order to show that the addition of the secondary plasma source was necessary in order to excite shear driven instabilities in the regime where $\rho_i / L_E > 1$.

The main focus of the second experiment was to understand the properties of the EIH instability with a uniform density and with a density gradient in the plasma in order to simulate the dynamics of plasma boundary layers in the magnetosphere. An instability in the lower hybrid frequency range was observed in the plasma in the region of the greatest sheared flow and a density gradient. Through varying the potential of the filament plasma and keeping the density gradient relatively constant, it was shown that the instability driving mechanism was the spatially inhomogeneous radial electric field. The instability was demonstrated to be the density gradient modified EIH instability through the comparison of experimental measurements and the

theoretical models derived in Chapter 2. The experimental results were shown to agree well with the EIH instability dispersion relation.

Despite exhaustive attempts at locating the EIH instability in a uniform density, no instability was observed in the lower hybrid frequency range. The theoretical framework for the EIH instability in a uniform density plasma was re-examined, and it was discovered that if the axial wavelength is considered to be finite and the axial wavenumber is included in the derivation of the dispersion relation, the EIH instability is not supported in a uniform density plasma in ALEXIS under the current operating conditions. The axial wavelength of the instability was shown to be greater than the length of ALEXIS. Nonetheless, the results of this work are unique in that the EIH instability had not previously been fully characterized in an experiment with a density gradient and a negligible field aligned current. In order to study the dynamics of plasma boundaries in the magnetosphere, the density gradient is an essential part of the experiment.

Finally, in the last experiment discussed in this dissertation, the ratio of the ion gyro-radius to the shear scale length was shown to be a convenient tunable experimental parameter to induce the transition between modes observed in the plasma. As the ratio of ρ_i / L_E is varied, a low frequency mode, ion cyclotron-like mode, and a lower hybrid mode were observed. The low frequency mode is predicted to be the Kelvin-Helmholtz instability, and the ion cyclotron-like mode is thought to be the Inhomogeneous Energy Density Driven Instability (IEDDI). The lower hybrid mode had previously been characterized as the EIH instability. Each of these modes has been studied individually in different laboratory devices and configurations, but the transition between the instabilities had never been studied in a single experiment under the continuous variation of the plasma conditions. The results of this work confirm the basic theory that plasma

is unstable to localized transverse velocity shear in a very broad frequency range, and also provides evidence for the theory described by Ganguli *et al*.[15,49] This theory, which was predicted two decades ago, proposes that as a compressed boundary layer relaxes in a collisionless plasma, it leads to a broadband electrostatic noise signature that satellites have often observed while crossing magnetospheric boundary layers. The results of this experiment are of particular interest to the space plasma community where the plasma boundary layer dynamics play a major role in the transport and distribution of mass, energy, and momentum into different regions of geo-space that affects near earth space weather. This experiment has significant practical importance as well, in that the accurate knowledge of space weather is vital for safeguarding satellites.

5.2 Future work

The work presented here opens up the possibility of several new experiments that can be performed in ALEXIS. However, due to the limitations of experimental hardware and operating conditions, not all of these opportunities can be explored at the moment. Initially, it was intended to study the EIH instability as well as the electromagnetic branch, the Whistler instability. Electromagnetic modes such as the electromagnetic ion cyclotron (EMIC) instability[123] have previously been studied on ALEXIS using a three axis magnetic loop, or a "B-Dot" probe which was described in Chapter 3. Under the current possible operating conditions, the densities in ALEXIS are not large enough to attain a high β parameter that would allow an electromagnetic mode to be supported in the plasma. The addition of the mesh near the rf antenna decreased the density by two orders of magnitude compared to previous ALEXIS configurations. To increase the plasma density, several designs are to be tested on ALEXIS in the near future, including the addition of a second high transparency mesh that can be biased to accelerate the rf plasma into

the chamber, and then use the existing mesh to set the plasma potential to ground. A second and more important concern with studying the Whistler wave is that the instability has extremely long axial wavelengths, and may not fit inside the ALEXIS device.

In Section 4.2.2, the theoretical framework for the EIH instability in a uniform density plasma was re-examined. A key assumption for the original uniform density theory was that the EIH instability has an infinitely long parallel wavelength, such that $k_z = 0$. When k_z is assumed to be finite, the dispersion relation shows that the EIH growth rate is zero for wavelengths that can fit inside the ALEXIS device when a uniform density is present in the plasma. For density gradient conditions, the theory was not re-derived to include a finite k_z because, chronologically, the density gradient experiment was performed before the uniform density experiment. Because the experimental data closely matched the existing theory for $k_z = 0$, it was not deemed necessary to go back and include k_z in the density gradient dispersion relation for this research. However, in future experiments, it would be of interest to re-derive the theory to investigate how the density gradient dispersion relation varies as k_z becomes finite.

It was predicted in Section 4.3 that the low frequency instability and the ion cyclotron-like instability are the Kelvin-Helmholtz and IEDDI instabilities respectively. In order to characterize these instabilities, the necessary theoretical framework has been derived by Ganguli *et al*.[62], so experimental measurements could be compared against the models. The results of such an experiment in conjunction with the results of the ion gyro-radius transition experiments presented in this dissertation, would be provide even more compelling evidence that this is the same broadband noise signature observed by satellites as compressed plasma boundary layers begin to relax.

Finally, Laser Induced Fluorescence (LIF) measurements would contribute greatly to experiments performed in ALEXIS. Ion flow and heating measurements using LIF in the ion gyro-radius transition experiment would be of particular interest in the space plasma community. It could be shown that when the EIH instability dominates, there is significant ion tail heating, and when the IEDDI mode dominates, the bulk ions are heated. However, there should be minimal ion heating for the Kelvin-Helmholtz mode. The energization process as these modes transition from one to another, as well as the transition of the magnitude of the ion flow velocity could also be studied using LIF. Ion flow velocity measurements have been performed in ALEXIS experiments previously.[72] However, in the current configuration, measurements are made at the same port as the diffusion pump. The diffusion pump has been observed to disrupt the plasma flow in the bottom half of the plasma column, leading to odd flow patterns and the breaking of the cylindrical symmetry of the plasma in this region. Also, low plasma densities make it difficult to resolve accurate and meaningful LIF measurements.

Bibliography

[1] F.F. Chen, *Introduction to Plasma Physics and Controlled Fusion, Volume 1: Plasma Physics*, 2nd Ed. (Springer, New York, 2006), pp. 131–135, 218.

[2] D.A. Gurnett and A. Bhattacharjee, *Introduction to Plasma Physics*, 1st ed. (Cambridge University Press, Cambridge, 2005), pp. 94–104.

[3] A. Piel, *Plasma Physics: An Introduction to Laboratory, Space, and Fusion Plasmas*, 1st ed. (Springer, Heidelberg, 2010).

[4] F. Wagner, G. Becker, K. Behringer, D. Campbell, A. Eberhagen, W. Engelhardt, and G. Fussmann, Phys. Rev. Lett. **49**, 1408–1412 (1982).

[5] F. Wagner, Plasma Phys. Control. Fusion **49**, B1–B33 (2007).

[6] R.J. Taylor, M.L. Brown, B.D. Fried, H. Grote, J.R. Liberati, G.J. Morales, P. Pribyl, D. Darrow, and M. Ono, Phys. Rev. Lett. **63**, 2365–2368 (1989).

[7] R.R. Weynants and G. Van Oost, Plasma Phys. Control. Fusion **35**, B177 – B189 (1993).

[8] K.H. Burrell, Phys. Plasmas **4**, 1499 (1997).

[9] B.A. Carreras, L. Garcia, M.A. Pedrosa, and C. Hidalgo, Phys. Plasmas **13**, 122509 (2006).

[10] M.A. Pedrosa, C. Hidalgo, E. Calderón, T. Estrada, A. Fernández, J. Herranz, and I. Pastor, Plasma Phys. Control. Fusion **47**, 777–788 (2005).

[11] T. Estrada, T. Happel, L. Eliseev, D. López-Bruna, E. Ascasíbar, E. Blanco, L. Cupido, J.M. Fontdecaba, C. Hidalgo, R. Jiménez-Gómez, L. Krupnik, M. Liniers, M.E. Manso, K.J. McCarthy, F. Medina, A. Melnikov, B. van Milligen, M.A. Ochando, I. Pastor, M.A. Pedrosa, F.L. Tabarés, and D. Tafalla, Plasma Phys. Control. Fusion **51**, 124015 (2009).

[12] V. Antoni, E. Martines, D. Desideri, L. Fattorini, G. Serianni, M. Spolaore, L. Tramontin, and N. Vianello, Plasma Phys. Control. Fusion **42**, 83 – 90 (2000).

[13] B.E. Chapman, C.-S. Chiang, S.C. Prager, J.S. Sarff, and M.R. Stoneking, Phys. Rev. Lett. **80**, 2137–2140 (1998).

[14] T.E. Moore, M.O. Chandler, C.J. Pollock, D.L. Reasoner, R.L. Amoldy, and B. Austin, J. Geophys. Res. **101**, 5279–5297 (1996).

[15] G. Ganguli, M.J. Keskinen, H. Romero, R. Heelis, T. Moore, and C. Pollock, J. Geophys. Res. **99**, 8873 (1994).

[16] M. Yamada and D.K. Owens, Phys. Rev. Lett. **38**, 1529–1532 (1977).

[17] E. Thomas, A.C. Eadon, and E.A. Wallace, Phys. Plasmas **12**, 042109 (2005).

[18] A.M. DuBois, A.C. Eadon, and E. Thomas, Phys. Plasmas **19**, 072102 (2012).

[19] E. Thomas, J.D. Jackson, E.A. Wallace, and G. Ganguli, Phys. Plasmas **10**, 1191 (2003).

[20] A.M. DuBois, E. Thomas, Jr., W.E. Amatucci, and G. Ganguli, Phys. Rev. Lett. **111**, 145002 (2013).

[21] E.M. Tejero, W.E. Amatucci, G. Ganguli, and C.D. Cothran, Phys. Rev. Lett. **106**, 185001 (2011).

[22] W.E. Amatucci, J. Geophys. Res. **104**, 14481–14503 (1999).

[23] S.-I. Itoh and K. Itoh, Phys. Rev. Lett. **60**, 2276–2279 (1988).

[24] K.H. Burrell, S.L. Allen, G. Bramson, N.H. Brooks, R.W. Callis, T.N. Carlstrom, M.S. Chu, A.P. Colleraine, D. Content, J.C. DeBoo, R.R. Dominguez, J.R. Ferron, and R.L. Freeman, Plasma Phys. Control. Fusion **31**, 1649–1664 (1989).

[25] R.J. Groebner, K.H. Burrell, and R.P. Seraydarian, Phys. Rev. Lett. **64**, 3015–3018 (1990).

[26] B. Lloyd, J.-W. Ahn, R.J. Akers, L.C. Appel, E.R. Arends, K.B. Axon, R.J. Buttery, C. Byrom, P.G. Carolan, C. Challis, D. Ciric, N.J. Conway, M. Cox, G.F. Counsell, G. Cunningham, A. Darke, A. Dnestrovskij, J. Dowling, M.R. Dunstan, A.R. Field, S.J. Fielding, S. Gee, M.P. Gryaznevich, P. Helander, M. Hole, M.B. Hood, P.A. Jones, A. Kirk, I.P. Lehane, G.P. Maddison, S.J. Manhood, R. Martin, G.J. McArdle, K.G. McClements, M.A. McGrath, H. Meyer, A.W. Morris, S.K. Nielsen, M. Nightingale, A. Patel, T. Pinfold, M.N. Price, J. Qin, C. Ribeiro, C.M. Roach, D.C. Robinson, O. Sauter, V. Shevchenko, S. Shibaev, K. Stammers, A. Sykes, A. Tabasso, D. Taylor, M.R. Tournianski, G. Turri, M. Valovic, G. Voss, M.J. Walsh, S. Warder, J.R. Watkins, H.R. Wilson, Y. Yang, and S. You, Nucl. Fusion **43**, 1665–1673 (2003).

[27] E. Thomas, S. Knowlton, R. Gandy, J. Cooney, D. Pritchard, and T. Pruitt, Phys. Plasmas **5**, 3991 (1998).

[28] M. Cianciosa, Ph.D. Dissertation, Auburn University, 2012.

[29] P.H. Diamond, S.-I. Itoh, K. Itoh, and T.S. Hahm, Plasma Phys. Control. Fusion **47**, R35–R161 (2005).

[30] H. Xia, M. Shats, and H. Punzmann, Phys. Rev. Lett. **97**, 255003 (2006).

[31] G.R. Tynan, R. a. Moyer, M.J. Burin, and C. Holland, Phys. Plasmas **8**, 2691 (2001).

[32] G.R. Tynan, P.H. Diamond, C. Holland, S.H. Muller, M. Xu, Z. Yan, and J.H. Yu, Plasma Phys. Control. Fusion **51**, 124055 (2009).

[33] Z. Yan, G.R. Tynan, C. Holland, M. Xu, S.H. Müller, J.H. Yu, and S.H. Muller, Phys. Plasmas **17**, 032302 (2010).

[34] D.A. Gurnett, R.R. Anderson, B.T. Tsurutani, E.J. Smith, G. Paschmann, G. Haerendel, S.J. Bame, and C.T. Russell, J. Geophys. Res. **84**, 7043 (1979).

[35] M. Andre, R. Behlke, J.E. Wahlund, A. Vaivads, A.I. Eriksson, A. Tjulin, T.D. Carozzi, C. Cully, G. Gustafsson, and D. Sundkvist, Ann. Geophys. **19**, 1471–1481 (2001).

[36] G.K. Parks, M. McCarthy, R.J. Fitzenreiter, J. Etcheto, K.A. Anderson, R.R. Anterson, T.E. Eastman, L.A. Frank, D.A. Gurnett, C. Huang, R.P. Lin, A.T.Y. Lui, K.W. Ogilvie, A. Pedersen, H. Reme, and D.J. Williams, J. Geophys. Res. **89**, 8885–8906 (1984).

[37] K. Sigsbee, C.A. Cattell, F.S. Mozer, K. Tsuruda, and S. Kokubun, J. Geophys. Res. **106**, 435–445 (2001).

[38] T. Streed, C. Cattell, F. Mozer, S. Kokubun, and K. Tsuruda, J. Geophys. Res. **106**, 6275–6289 (2001).

[39] P.A. Bernhardt, P. Rodriguez, C.L. Siefring, and C.S. Lin, J. Geophys. Res. **96**, 13887–13900 (1991).

[40] G. Ganguli, P.A. Bernhardt, W.A. Scales, P. Rodriguez, C.L. Siefring, and H. Romero, in *Phys. Sp. Plasmas (SPI Conf. Proc. Repr. Ser.* (Scientific Publishers Inc., Cambridge, MA, 1992), p. 161.

[41] W.A. Scales, P.A. Bernhardt, and G. Ganguli, J. Geophys. Res. **100**, 269 (1995).

[42] H. Gunell, U. V Amerstorfer, H. Nilsson, C. Grima, M. Koepke, M. Fränz, J.D. Winningham, R. a Frahm, J. Sauvaud, a Fedorov, N. V Erkaev, H.K. Biernat, M. Holmström, R. Lundin, and S. Barabash, Plasma Phys. Control. Fusion **50**, 074018 (2008).

[43] V.D. Shapiro, V. Shevchenko, A.S. Sharma, K. Papadopoulos, R.Z. Sadgeev, and V.B. Lebedev, J. Geophys. Res. **98**, 1325–1331 (1993).

[44] D.N. Walker, W.E. Amatucci, G. Ganguli, J.A. Antoniades, J.H. Bowles, and M.E. Koepke, Geophys. Res. Lett. **24**, 1187–1190 (1997).

[45] W.E. Amatucci, D.N. Walker, G. Ganguli, D. Duncan, J.A. Antoniades, J.H. Bowles, V. Gavrishchaka, and M.E. Koepke, J. Geophys. Res. **103**, 11711 (1998).

[46] P.M. Kintner, J. Vago, S. Chesney, R.L. Arnoldy, K.A. Lynch, C.J. Pollock, and T.E. Moore, Phys. Rev. Lett. **68**, 2448–2452 (1992).

[47] M.E. Koepke, Phys. Plasmas **9**, 2420 (2002).

[48] H. Romero, G. Ganguli, and Y.C. Lee, Phys. Rev. Lett. **69**, 3503 (1992).

[49] H. Romero and G. Ganguli, Geophys. Res. Lett. **21**, 645 (1994).

[50] W.E. Amatucci, G. Ganguli, D.N. Walker, G. Gatling, M.M. Balkey, and T. McCulloch, Phys. Plasmas **10**, 1963 (2003).

[51] E. Agrimson, N. D'Angelo, and R.L. Merlino, Phys. Rev. Lett. **86**, 5282–5285 (2001).

[52] E.P. Agrimson, N.D. Angelo, and R.L. Merlino, Phys. Lett. A **293**, 260–265 (2002).

[53] R.L. Merlino, Phys. Plasmas **9**, 1824 (2002).

[54] E. Agrimson, S.-H. Kim, N. D'Angelo, and R.L. Merlino, Phys. Plasmas **10**, 3850 (2003).

[55] S.-H. Kim, E. Agrimson, M.J. Miller, N. D'Angelo, R.L. Merlino, and G.I. Ganguli, Phys. Plasmas **11**, 4501 (2004).

[56] S.-H. Kim, R.L. Merlino, and G.I. Ganguli, Phys. Plasmas **13**, 012901 (2006).

[57] C. Teodorescu, E. Reynolds, and M.E. Koepke, Phys. Rev. Lett. **89**, 105001 (2002).

[58] E.E. Scime, a. M. Keesee, R.S. Spangler, M.E. Koepke, C. Teodorescu, and E.W. Reynolds, Phys. Plasmas **9**, 4399 (2002).

[59] R.S. Spangler, E.E. Scime, and G.I. Ganguli, Phys. Plasmas **9**, 2526 (2002).

[60] M.E. Koepke, W.E. Amatucci, J.J. Carroll, and T.E. Sheridan, Phys. Rev. Lett. **72**, 3355–3358 (1994).

[61] G. Ganguli, Y.C. Lee, and P.J. Palmadesso, Phys. Fluids **28**, 761 (1985).

[62] G. Ganguli, Y.C. Lee, and P.J. Palmadesso, Phys. Fluids **31**, 823 (1988).

[63] W.E. Amatucci, M.E. Koepke, J.J. Carroll, and T.E. Sheridan, Geophys. Res. Lett. **21**, 1595 (1994).

[64] M.E. Koepke, J.J. Carroll, and M.W. Zintl, Phys. Plasmas **5**, 1671 (1998).

[65] M.E. Koepke and E.W. Reynolds, Plasma Phys. Control. Fusion **49**, A145–A157 (2007).

[66] R. Hatakeyama, T. Kaneko, and W. Oohara, J. Plasma Phys. **76**, 513 – 523 (2010).

[67] G.I. Kent, N.C. Jen, and F.F. Chen, Phys. Fluids **12**, 2140 (1969).

[68] D.L. Jassby, Phys. Rev. Lett. **25**, 1567 (1970).

[69] W.E. Amatucci, D.N. Walker, G. Ganguli, J.A. Antoniades, D. Duncan, J.H. Bowles, V. Gavrishchaka, and M.E. Koepke, Phys. Rev. Lett. **77**, 1978 (1996).

[70] R. Hatakeyama and T. Kaneko, Phys. Scr. **T107**, 200 – 203 (2004).

[71] E.A. Wallace, E. Thomas, A.C. Eadon, and J.D. Jackson, Rev. Sci. Instrum. **75**, 5160 (2004).

[72] A.C. Eadon, Ph.D. Dissertation, Auburn University, 2011.

[73] A.C. Eadon, E.M. Tejero, A.M. DuBois, and E. Thomas, Rev. Sci. Instrum. **82**, 063511 (2011).

[74] G. Ganguli, Y.C. Lee, and P.J. Palmadesso, Phys. Fluids **31**, 2753 (1988).

[75] H. Romero, G. Ganguli, Y.C. Lee, and P.J. Palmadesso, Phys. Fluids B **4**, 1708 (1992).

[76] H. Romero and G. Ganguli, Phys. Fluids B **5**, 3163 (1993).

[77] A. Matsubara and T. Tanikawa, Jpn. J. Appl. Phys. **39**, 4920–4932 (2000).

[78] T.A. Santhosh Kumar, S.K. Mattoo, and R. Jha, Phys. Plasmas **9**, 2946 (2002).

[79] C.S. Lakhina, J. Geophys. Res. **92**, 12161–12170 (1987).

[80] H. Romero, G. Ganguli, P.J. Palmadesso, and P.B. Dusenbery, Geophys. Res. Lett. **17**, 2313 (1990).

[81] P.M. Kintner, J. Bonnell, R. Arnoldy, K. Lynch, M. Hall, C. Pollock, T. Moore, J. Holtet, C. Deehr, H. Stenbaek-nielsen, R. Smith, and J. Olson, Geophys. Res. Lett. **23**, 1865–1868 (1996).

[82] D.G. Swanson, *Plasma Waves*, 2nd. Ed. (IOP Publishing, New York, 2003), pp. 54–62, 71, 133–134.

[83] T.H. Stix, *Waves in Plasmas* (American Institute of Physics, New York, NY, 1992).

[84] Y.S. Dimant, J. Geophys. Res. **100**, 14605–14623 (1995).

[85] D.T. Farley, Phys. Rev. Lett. **10**, 279 – 282 (1965).

[86] O. Buneman, Phys. Rev. Lett. **10**, 285–287 (1963).

[87] S.D. Bale, F.S. Mozer, and T. Phan, Geophys. Res. Lett. **29**, 2–5 (2002).

[88] J.D. Huba, N.T. Gladd, and J.F. Drake, J. Geophys. Res. **86**, 5881–5884 (1981).

[89] C. Norgren, Uppsala University, Sweden, 2011.

[90] T. Okada, K. Tsuruda, H. Hayakawa, M. Nakamura, T. Mukai, T. Yamamoto, A. Matsuoka, T. Terasawa, F.S. Mozer, S. Kokybun, and H. Matsumoto, Geophys. Res. Lett. **21**, 2931–2934 (1994).

[91] I. Shinohara, T. Nagai, M. Fujimoto, T. Terasawa, T. Mukai, and T. Yamamoto, J. Geophys. Res. **103**, 365–388 (1998).

[92] P.A. Bernhardt, R.A. Roussel-Dupre, M.B. Pongratz, G. Haerendel, A. Valenzuela, D.A. Gurnett, and R.R. Anderson, J. Geophys. Res. **92**, 5777–5794 (1987).

[93] T.A. Carter, H. Ji, F. Trintchouk, M. Yamada, and R.M. Kulsrud, Phys. Rev. Lett. **88**, 1–4 (2002).

[94] P.I. John and Y.C. Saxena, Geophys. Res. Lett. **2**, 2–5 (1975).

[95] D. Winske and W. Daughton, Phys. Plasmas **19**, 072109 (2012).

[96] W. Daughton, G. Lapenta, and P. Ricci, Phys. Rev. Lett. **93**, 1–4 (2004).

[97] M. Oppenheim, N. Otani, and C. Ronchi, J. Geophys. Res. **101**, 17273–17286 (1996).

[98] M. Abramowitz and I. Stegun, *Handbook of Mathematical Functions*, 10th Ed. (Dover Publications, Washington, D.C., 1972), p. 378.

[99] B. Arfken, George and H.J. Weber, *Mathematical Methods for Physicists*, 6th Ed. (Elsevier Academic Press, Burlington, MA, 2005), pp. 87, 90, 931.

[100] J.D. Jackson, in *Class. Electrodyn.*, 3rd Ed. (John Wiley & Sons, Inc., New York, NY, 1999).

[101] A.M. DuBois, E. Thomas, E.M. Tejero, and W.E. Amatucci, Bull. Am. Phys. Soc. **55**, PP9 131 (2010).

[102] R.F. Kemp and J.M. Sellen, Rev. Sci. Instrum. **37**, 455 (1966).

[103] I.H. Hutchinson, *Principles of Plasma Diagnostics*, 2nd Ed. (Cambridge University Press, Cambridge, 2002).

[104] F.F. Chen, in *Princ. Plasma Process.* (n.d.), p. 75.

[105] W.B. Nottingham, Phys. Rev. Lett. **49**, 78 – 97 (1936).

[106] H.M. Mott-Smith and I. Langmuir, Phys. Rev. Lett. **28**, 727 – 763 (1926).

[107] F.F. Chen, Phys. Fluids **11**, 811 (1968).

[108] B. Lipschultz, I.H.H. Hutchinson, B. Labombard, and A. Wan, J. Vac. Sci. Technol. A **4**, 1810 (1986).

[109] N. Hershkowitz, *Plasma Diagnostics* (Academic Press, Inc, Boston, 1989).

[110] E.M. Tejero, Ph.D. Dissertation, Auburn University, 2011.

[111] J.M. Beall, Y.C. Kim, and E.J. Powers, J. Appl. Phys. **53**, 3933 (1982).

[112] P. Horowitz and W. Hill, *The Art of Electronics*, 2nd Editio (Cambridge University Press, New York, NY, 1989), p. 457.

[113] A.M. DuBois, I. Arnold, E. Thomas, E.M. Tejero, and W.E. Amatucci, Rev. Sci. Instrum. **84**, 1–6 (2013).

[114] R.C. Davidson, N.T. Gladd, C.S. Wu, and J.D. Huba, Phys. Fluids **20**, 301 (1977).

[115] R.C. Davidson and N.T. Gladd, Phys. Fluids **18**, 1327 (1975).

[116] J.D. Huba, N.T. Gladd, and K. Papadopoulos, Geophys. Res. Lett. **4**, 125–128 (1977).

[117]*Plasma Formulary* (Naval Research Laboratory, Washington, D.C., 2006).

[118] N.A. Krall and P.C. Liewer, Phys. Lett. A **4**, 2094–2103 (1971).

[119] J.R. Peñano, G. Ganguli, W.E. Amatucci, D.N. Walker, V. Gavrishchaka, and J.R. Peñano, Phys. Plasmas **5**, 4377 (1998).

[120] T.A. Peyser, C.K. Manka, B.H. Ripin, and G. Gangui, Phys. Fluids B **4**, 2448–2458 (1992).

[121] D.L. Jassby, Phys. Fluids **15**, 1590 (1972).

[122] H. Hojo, Y. Kishimoto, and J.W. Van Dam, J. Phys. Soc. Jpn. **64**, 4073–4076 (1995).

[123] A.M. DuBois, E.M. Tejero, A.C. Eadon, E. Thomas, and W.E. Amatucci, in *Bull. Am. Phys. Soc.* (2011).

[124] H.W. Hendel, T.K. Chu, and P.A. Politzer, Phys. Fluids **11**, 2426 (1968).

[125] T.C. Simonen, T.K. Chu, and H.W. Hendel, Phys. Rev. Lett. **23**, 568 (1969).

[126] M.J. Burin, G.R. Tynan, G.Y. Antar, N.A. Crocker, and C. Holland, Phys. Plasmas **12**, 052320 (2005).

[127] O. Grulke, S. Ullrich, T. Windisch, and T. Klinger, Plasma Phys. Control. Fusion **49**, B247 (2007).

[128] B.D. Scott, Phys. Plasmas **12**, 102307 (2005).

[129] B.D. Scott, New J. Phys. **4**, 52 (2002).

[130] R.F. Ellis, E. Marden-Marshall, and R. Majeski, Phys. Plasmas **22**, 113 (1980).

[131] F.F. Chen, Phys. Fluids **8**, 912 (1965).

[132] M. Ramisch, E. Häberle, N. Mahdizadeh, and U. Stroth, Plasma Sources Sci. Technol. **17**, 024007 (2008).

[133] T. Kaneko, H. Tsunoyama, and R. Hatakeyama, Phys. Rev. Lett. **90**, 125001 (2003).

[134] H. Tsuchiya, S. Itoh, A. Fujisawa, K. Kamataki, and S. Shinohara, Plasma Phys. Control. Fusion **50**, 055005 (2008).

[135] A. Mase, A. Itakura, M. Inutake, K. Ishii, J.H. Jeong, K. Hattori, and S. Miyoshi, Nucl. Fusion **31**, 1725 (1991).

[136] A.M. DuBois, A.C. Eadon, and E. Thomas, Bull. Am. Phys. Soc. **54**, GP8 119 (2009).

[137] D.B. Ilic, Phys. Rev. Lett. **34**, 464 (1975).

[138] A.K. Sen, V. Sokolov, and X. Wei, Phys. Plasmas **13**, 055905 (2006).

[139] S. Shinohara, N. Matsuoka, and S. Matsuyama, Phys. Plasmas **8**, 1154 (2001).

[140] A. Latten, T. Klinger, and A. Piel, Rev. Sci. Instrum. **66**, 3254 (1995).

[141] R.J. Goldston and P.H. Rutherford, *Introduction to Plasma Physics*, 1st ed. (IOP, London, 1997), pp. 465–468.

Appendix A – Suppression of Drift Waves

The following paper[18] describes an experiment performed in a previous configuration of ALEXIS where concentric electrode rings, located at the opposite end of the vacuum vessel from the rf plasma source, were used to modify the plasma potential. The initial objective for this configuration was to excite shear driven instabilities in the ion cyclotron frequency range when the shear scale length is comparable to the ion gyro-radius.[72] However, it was also discovered that a low frequency instability (identified as a drift wave) could be suppressed by inducing a large parallel current in the plasma.

A.1 Introduction

Drift instabilities are among the most studied phenomena in plasma physics. Driven by gradients in the plasma pressure, they are one of the "universal" instabilities that can arise in a plasma[1]. From early studies in the 1960's by Hendel, *et al.*[124], it has been shown that the generation of drift waves in collisional plasmas can lead to enhanced plasma transport. Similar work by Simonen *et al.*[125] (also using a Q-machine) showed that by using a modulated electron current along the magnetic field lines, it was possible to stabilize the drift waves and, in turn, improve plasma confinement.

While early studies of drift instabilities were performed in linear plasma devices, the physical mechanism of drift instabilities is pervasive across all plasma experimental geometries. As a result, these instabilities also play an important role in toroidal fusion experiments. In particular, the edge region of fusion devices, where large density gradients are often established, is believed to be dominated by drift wave driven turbulence.[126–129] In periods when the drift wave instability amplitude is large, there can be significant cross-field transport and enhanced plasma losses.[124,130,131] However, when large flows exist in the edge region – whether established by self-consistent zonal flows or driven by external electrodes – there can be a significant reduction in drift wave turbulence.

Studies in both toroidal and linear devices provide evidence for this connection between flows and turbulence. For example, studies on the TJ-K stellarator device demonstrated that a strong shear flow could change the structure of drift wave turbulence.[132] Similarly, studies by Kaneko *et al.*[133] on the Q_T-upgrade machine showed that in a modified plasma synthesis source, parallel shear could destabilize a drift wave. It was observed that as the shear length increased, the amplitude of the drift wave increased, but was eventually stabilized as the shear length reached a critical value.[133] Tsuchiya *et al.*[134] showed that by inducing a zonal flow due to $\boldsymbol{E} \times \boldsymbol{B}$ shearing in a cylindrical mirror device, the characteristics of the low frequency mode in the plasma could be changed. In a tandem mirror plasma device, drift wave fluctuation levels were observed to depend on the radial electric field created by applying a bias voltage to end plates.[135] These studies show that ongoing work on basic plasma devices can provide new insights into the fundamental physics that is of relevance to the broader plasma community. This paper reports on recent observations of the suppression of drift instabilities by plasma flows parallel to the magnetic field.

Experiments in the Auburn Linear EXperiment for Instability Studies (ALEXIS) have observed non-localized, low frequency instabilities in argon that extended radially over the entire column[136], and vary with magnetic field strength and radial electric field. These instabilities are identified as drift waves that are driven by a radial density gradient. This paper is presented in two parts. First, the characterization of the instability as a drift wave as a function of the applied electric and magnetic fields will be discussed. Second, efforts to suppress the drift wave by modifying the radial and axial plasma flow using a series of "ring electrodes" that are located at one end of the plasma column will be discussed.

A.2 Experimental setup

All of the experiments described in this paper are performed using the ALEXIS device. The configuration of the ALEXIS device has been described in detail in earlier works[71,73] so only a brief summary of the device is given here. ALEXIS is a 170 cm long, 10 cm diameter, magnetized linear plasma experiment. In its current configuration, there are four sections that make up the chamber, which can be seen in Figure A-1: (A) the antenna, (B) an ISO-100 six-way cross, (C) a 100 cm long experimental chamber, and (D) a custom designed vacuum box with large windows for optical access.

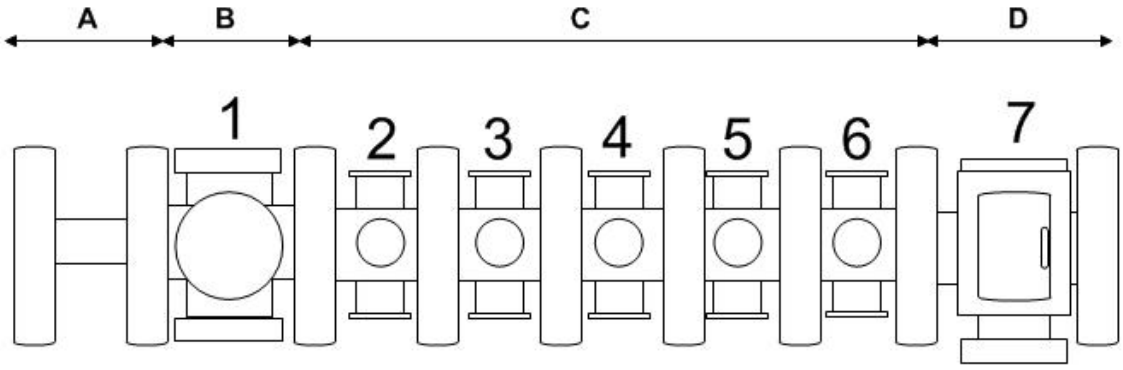

Figure A-1: A schematic drawing of the Auburn Linear EXperiment for Instability Studies (ALEXIS) where the numbers indicate port locations.

Plasmas in ALEXIS are generated using a 600 W radio frequency (rf) power supply – although plasmas are typically generated at rf powers from 30 to 200 W. A manually tuned matching network is used to couple the rf power into the plasma. Nine water-cooled electromagnets produce an axial magnetic field with a maximum strength of up to 1000 G. The two magnetic field coils that surround the antenna are operated separately from remaining seven and are used to optimize the plasma generation. For the experiments described in this paper, plasmas are generated using argon gas. Typical operating conditions are listed in Table A-1.

Table A-1: Typical Operating Parameters in ALEXIS.

Gas species	Argon
Magnetic field	300 – 800 G
Electron density	$0.5 – 5 \times 10^{16}$ m^{-3}
Electron temperature	1 – 5 eV
Ion temperature	< 0.05 eV
Gas pressure	0.25 – 0.75 mTorr
Ion cyclotron frequency	10 – 25 kHz

A range of *in-situ* diagnostic probes were used in this experiment to measure plasma parameters, including single tip Langmuir probes (floating potential fluctuations), emissive probes (plasma potential and radial electric field), and double probes (electron density and

electron temperature).[103,109] Additionally, a double tipped probe (described here as a "k"-probe) is used to make measurements of the wavenumber of observed electrostatic fluctuations.[50,110,137,138] The "k"-probe, which was specifically developed for this study, can be rotated to different angles with respect to the background magnetic field to measure electrostatic fluctuations. The phase difference between the probe tips is used to calculate the wavenumber and wavelength of the electrostatic fluctuation.

Two concentric electrode rings in the back of the chamber are mounted on a Macor (ceramic) block, and placed perpendicular to the magnetic field. The two rings are electrically isolated from each other and can be biased independently to modify the radial potential structure of the plasma. This is a variation on experimental configurations that have been used previously on ALEXIS[17,19,72] and similar linear experiments[21,63,69,139]. Here, ring 1 (inner ring) has an inner radius of 0.42 cm and an outer radius of 1.11 cm. Ring 2 (outer ring) has an inner radius of 1.27 cm and an outer radius of 1.91 cm. For the first part of this experiment, both rings were left floating. In the second part, ring 1 was electrically grounded to chamber ground, and ring 2 was biased.

A.3 Experimental results

Non-localized instabilities have been observed at or below the ion cyclotron frequency ($\omega \leq \omega_{ci}$) in ALEXIS. Two experiments are described below. In the first experiment, the objective is to clearly identify the physical mechanism responsible for driving the waves. In the second experiment, the plasma conditions are modified to control the properties of, and eventually suppress, the instability. Results from both experiments are discussed below.

A.3.1 Driving mechanism and characterization

The first part of the experiment was performed in order to identify the driving mechanism of the low frequency instability observed in ALEXIS, and to characterize the instability as a drift wave. To do this, the magnetic field strength and rf power were varied to investigate the scaling of the amplitude and frequency of the instability. Changing the magnetic field and the rf power modify the plasma parameters (specifically the electron density profile), which make them useful experimental controls for studying the properties of the observed instabilities. Table A-2 gives the baseline configuration for this portion of the experiment.

Table A-2: Experiment 1 configuration.

rf power	50 W
Magnetic field	240 - 720 G
Gas pressure	0.26 mTorr
Ring 1	Floating
Ring 2	Floating

The electron density, electron temperature, and plasma potential were carefully monitored in order to characterize how the underlying plasma parameters changed as a function of the magnetic field. Figure A-2 shows typical radial profiles of the: (a) electron density, (b) electron temperature, (c) plasma potential and, (d) the electric field for different magnetic field strengths. Notice that the electron temperature, plasma potential, and electric field remain constant across the plasma column as the magnetic field strength is varied. The electron density profile, however, is modified as a function of the magnetic field strength.

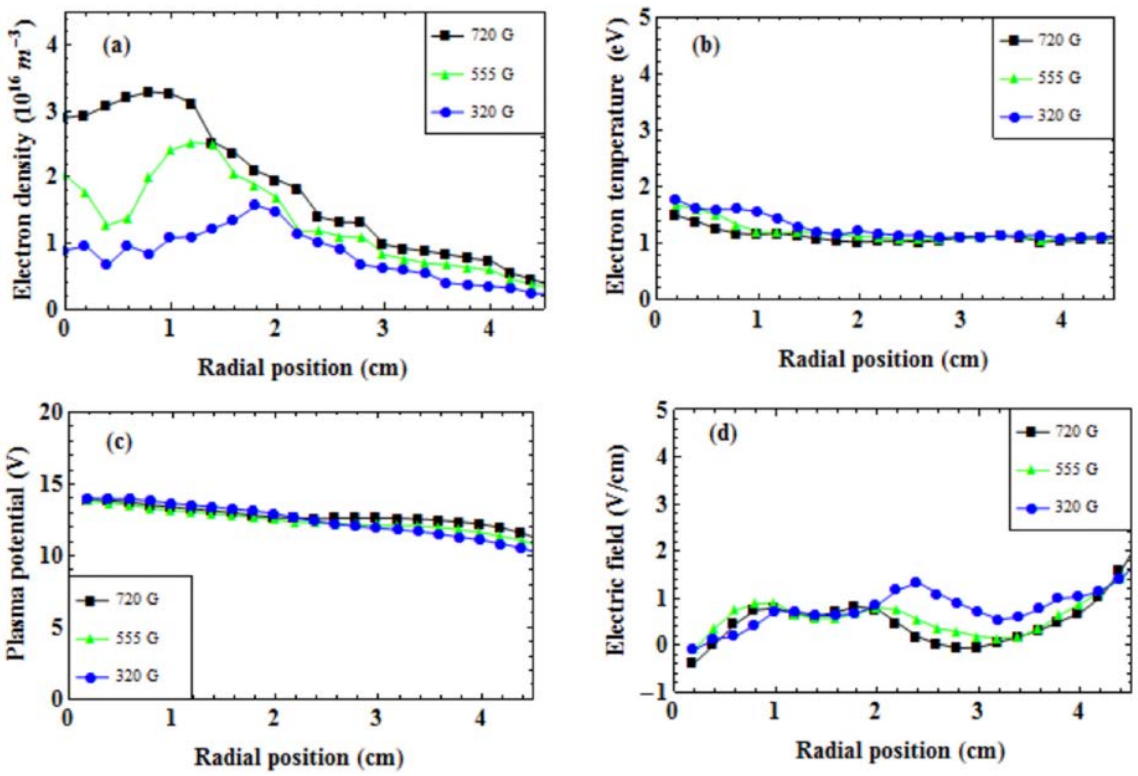

Figure A-2: (a) The radial profile of the electron density at different magnetic field strengths. (b) The radial profile of the electron temperature at different magnetic field strengths. (c) The radial profile of the plasma potential at different magnetic field strengths. (d) The radial electric field at different magnetic field strengths. The black squares represent the data at a magnetic field strength of 720 G, the green triangles represent data at a magnetic field of 555 G, and the blue circles represent data at 320 G. Note that the electron temperature, plasma potential, and electric field all remain constant, both across the plasma column and as the magnetic field strength is varied.

Using a single tip Langmuir probe, a frequency spectrum of the instability was measured at each point in space. As the probe is moved radially across the plasma column, a profile of the peak amplitude of the instability and the wave frequency was determined. An example of the peak amplitude as a function of radial position is shown in Figure A-3, where the inset plot is an example of the frequency spectrum. The instability was shown to extend over the entire plasma column. The radial location of the peak amplitude was observed to move radially outward as the magnetic field decreased. This was expected because as the magnetic field strength decreases, the cross sectional area of the plasma column expands. Figure A-4(a) shows that the frequency of the instability increased and Figure A-4(b) shows that the peak amplitude decreased as the magnetic field strength was lowered.

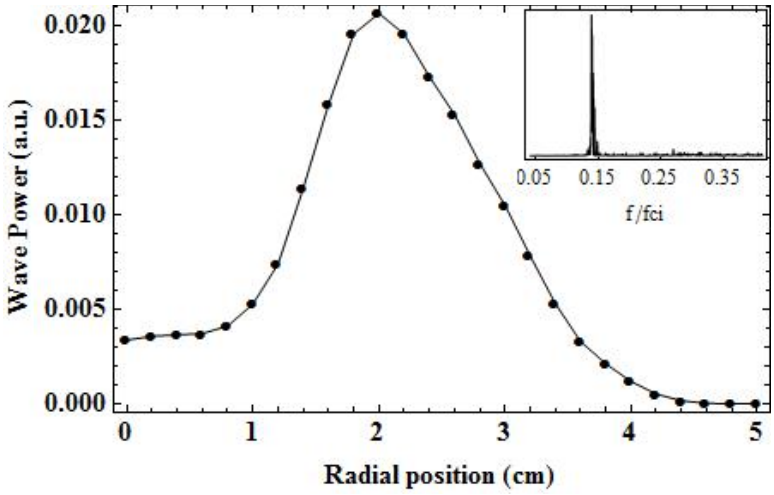

Figure A-3: The peak amplitude of the instability at each radial position where 0 cm coincides with the geometric center of the plasma column. The inset plot is an example of the frequency spectrum.

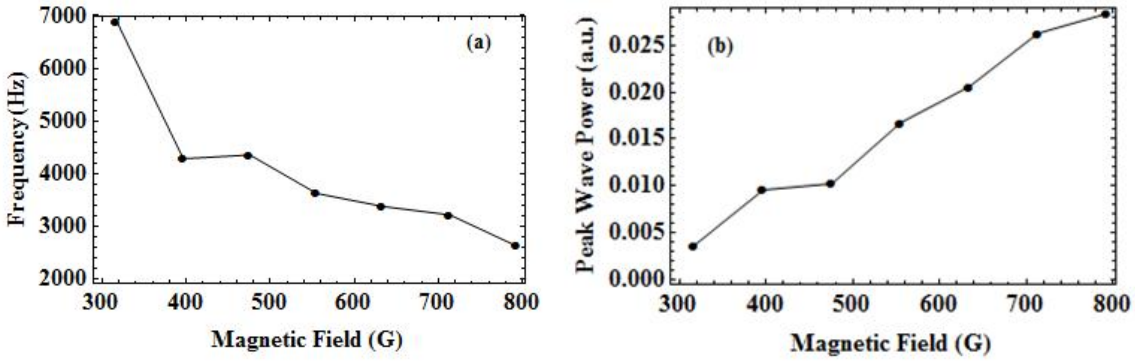

Figure A-4: (a) The frequency of the instability was observed to increase and (b) the peak amplitude of the instability was seen to decrease with a decreasing magnetic field strength.

The electron density and temperature were measured using a double probe. It was noted that the peak electron density occurs between 1 and 2.5 cm from the center of the column, and the temperature profile remained constant across the plasma column (between 1 and 2 eV) and as the magnetic field strength was varied, which is illustrated in Figure A-2(b). It was observed that the maximum electron density decreased as the magnetic field decreased in Figure A-2(a), which caused the density gradient near the center of the plasma column to decrease. Figure A-5 shows that as the magnetic field is decreased, the maximum electron density gradient also decreases.

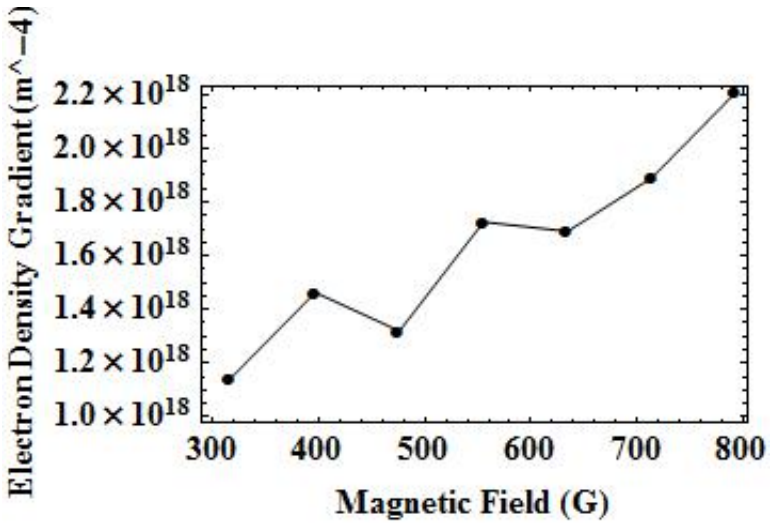

Figure A-5: The maximum electron density gradient as a function of magnetic field strength.

Electric fields present in plasmas can drive certain instabilities[21,50], so it was important to determine whether varying the magnetic field strength had an effect on the plasma electric field. To do this, the plasma potential was measured across the plasma column, which showed there was only a slight variation radially and as a function of magnetic field [Figure A-2(c)]. From the plasma potential, the radial electric field profile was calculated. This showed a constant radial electric field inside the plasma column near 0 V/cm [Figure A-2(d)]. A constant radial electric field that is approximately equal to zero indicates that the rotation due to the $\boldsymbol{E} \times \boldsymbol{B}$ drift can be ignored.[140] It was also seen that the electric field remained constant, even as the magnetic field decreased. This indicates that there is no observable correlation between the instability and the radial electric fields.

Since the electron temperature and the radial electric field profiles remain uniform across the plasma column (as was shown in Figure A-2), it is reasonable to eliminate these as the driving mechanism of the instability. The effect of the electron density on the instability was examined in more detail. The electron density was measured as the magnetic field strength was varied, and the peak density was calculated for each case. The maximum density measured from

all of the cases was then used to normalize the plots in Figure A-6. The same technique was also used to normalize the amplitude of the instability. Both the maximum density and maximum amplitude occurred at a magnetic field strength of 800 Gauss. In the case of a large magnetic field [Figure A-6(a)], the electron density changes by an order of magnitude across the plasma column, which created a sharp density gradient in the region of the peak instability amplitude. In the case of a small magnetic field [Figure A-6(c)], the density profile was observed to flatten out and the density gradient was greatly reduced. This corresponded to a small amplitude instability. This data suggests that the density gradient was the dominant mechanism for driving the instability observed in ALEXIS.

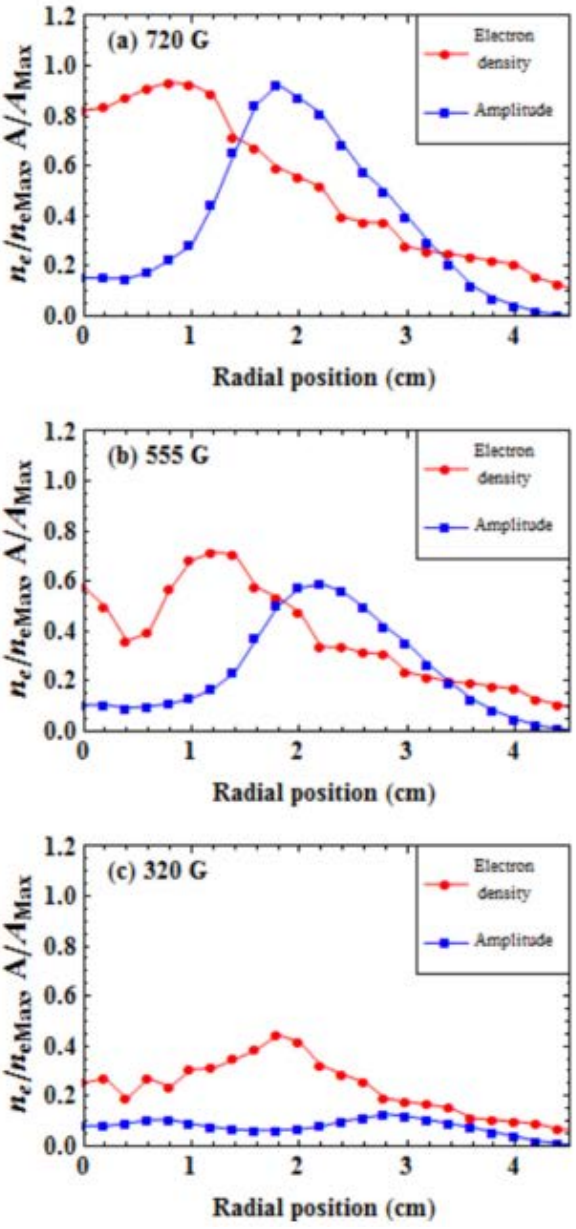

Figure A-6: The electron density (circle, red) and peak amplitude (squares, blue) as a function of the radial position at magnetic field strengths of (a) 720 G, (b) 555 G, and (c) 320 G.

Although there are several possible instabilities that can be driven by a density gradient, it was suspected that the low frequency instability observed in ALEXIS was a drift wave. To confirm this, experiments were performed in two different magnetic field configurations where the applied rf power was varied. Changing the rf power modifies the density gradient, but not the location of the maximum electron density, unlike varying the magnetic field strength. In this

configuration, the wave number of the instability was measured by setting the "k"-probe to the same radial location as the peak wave power. The phase difference was calculated between the probe tips when the probe was oriented parallel and perpendicular to the magnetic field.

Table A-3: Measured wavenumber values and corresponding density gradients as a function of the rf (heating) power at a magnetic field strength of 635 Gauss.

rf Power (W)	k// (m^{-1})	$k_\perp$ (m^{-1})	Density gradient (10^{18} m^{-4})
70	28.135	94.986	1.916
60	29.697	84.476	1.562
50	35.983	115.848	1.238
40	18.015	105.982	0.733
30	11.045	101.369	0.305

It was observed that the perpendicular component of the wavenumber ($k_\perp$) was much larger than the parallel component, which is consistent with the properties of a drift wave. However, for a fixed magnetic field strength the parallel and perpendicular components of the wavenumber remained relatively unchanged, even as the rf power was varied (see Table A-3 and Table A-4). Because of the relatively small size of the ALEXIS vacuum chamber, it is possible that a broad spectrum of wavenumbers were not supported by the plasma column.

Table A-4: Measured wavenumber values and corresponding density gradients as a function of the rf (heating) power at a magnetic field strength of 500 Gauss.

rf Power (W)	k// (m^{-1})	$k_\perp$ (m^{-1})	Density gradient (10^{18} m^{-4})
70	73.368	169.490	0.796
60	31.484	94.743	0.650
50	31.784	96.394	0.685
40	25.454	65.919	0.498

In order to confirm the observed instabilities as drift waves, it was necessary to perform a more definitive test of the drift dispersion relation. Assuming cold ions and a quasi-neutral

plasma, the drift wave dispersion relation was derived using slab geometry for instabilities in ALEXIS (Equation A-1):

$$\omega^2\left(1 + k_y^2\,\rho_{ci}^2\right) - \omega\,\omega_e^* - C_s^2\,k_z^2 = 0 \qquad \text{(A-1)}$$

where ρ_{ci} is the ion gyro-radius, ω_e is the electron diamagnetic frequency and C_s is the ion sound speed. In this derivation, since the probe tip separation distance (3 mm) is much smaller than the mean free collisional path (~11.4 cm), collisions were assumed to be negligible.

To further establish the importance of the contributions of collisions, consider the following comparison between the electron/ion-neutral collision frequencies, the coulomb collision frequencies, the electron/ion cyclotron frequencies, and the electron/ion plasma frequencies. In this hierarchy, for collisions to play an important role, it would be necessary to have the collision rate between a charged species (i.e., ion or electron) and neutral atoms significantly larger than the other characteristic plasma frequencies. The electron-neutral collision frequency (4.48 MHz) was calculated to be much less than both the electron cyclotron (11.17 GHz) and electron plasma (7.98 GHz) frequencies. The ion-neutral collision frequency (2.17 kHz) also proved to be trivial compared to the ion cyclotron (152.05 kHz) and ion plasma (29.44 MHz) frequencies. Finally, it was determined that the coulomb collision frequency (29.76 kHz) was an order of magnitude less than the ion cyclotron frequency. Given these comparisons, it is appropriate to assume that collisions are in fact negligible.

In order to draw a comparison between experimental measurements and the drift wave dispersion relation, the experimentally measured values of the parallel and perpendicular wavenumbers and the plasma parameters are combined in the positive root of Equation A-1 and used to estimate the drift wave frequency. This calculated result is then compared to the

frequency measured in the experiment. This comparison is shown in Figure A-7, where the calculated frequencies compare well with the frequencies measured with the Langmuir probe, which suggests the low-frequency instability observed in ALEXIS is a drift wave.

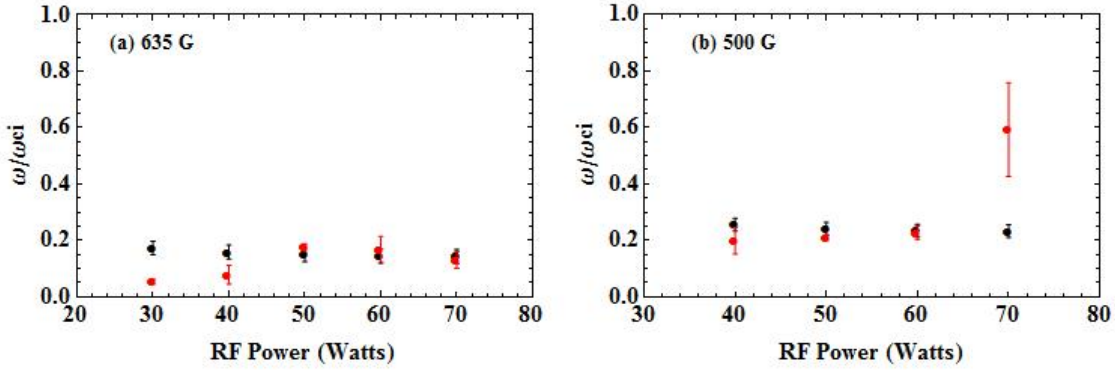

Figure A-7: The instability frequency measured using a Langmuir probe (black) compared with the frequency calculated using the drift wave dispersion relation (red) as a function of the rf power for magnetic field strengths of (a) 635 Gauss and (b) 500 Gauss.

A.3.2 Drift wave suppression

The second part of this experiment was performed to determine if it was possible to suppress the drift wave instability. To do this, the inner electrode ring (ring 1) was grounded while the outer ring (ring 2) was biased to different potentials. The negative bias configuration is equivalent to the previous experiment where the rings were allowed to electrically float at -15 V The magnetic field, gas pressure, and rf power were all kept constant. Data was taken to observe how the wave amplitude, frequency, electron density and plasma potential responded. Table A-5 shows the baseline configuration for this part of the experiment.

Table A-5: Experiment 2 configuration.

rf power	130 W
Magnetic field	320 G
Gas pressure	0.5 mTorr
Ring 1	0 V
Ring 2	40 to -40 V
Ion cyclotron frequency	12.2 kHz

When the outer electrode ring was set to a negative voltage, data taken with the single tip Langmuir probe showed a drift wave instability with a frequency of 5 - 6 kHz (approximately half that of the ion cyclotron frequency). Figure A-8(a) shows an example of the spectra observed at a negative bias. With a positive bias on the outer ring, a small amplitude instability was observed near the ion cyclotron frequency, but there was no instability observed below the ion cyclotron frequency. Figure A-8(b) shows the spectra at a positive bias in the frequency range of the drift wave (3 – 9 kHz). The colors represent the fluctuation amplitude, where red indicates a large amplitude fluctuation and blue indicates very small amplitude fluctuations [Figure A-8(c)]. Notice that at a positive bias, the noise floor drops into the 10^{-9} range, whereas at a negative bias, the noise floor is three orders of magnitude larger. Figure A-9 shows the peak wave amplitude measured between 3 and 9 kHz as a function of the bias voltage applied to the outer ring. The plot was normalized to the maximum amplitude, which occurred at -30 V. When there is no instability present in the drift wave frequency range, the normalized amplitude is approximately zero (at a positive ring bias). When there is a drift wave present, the normalized amplitude is one (as can be seen at the negative ring bias).

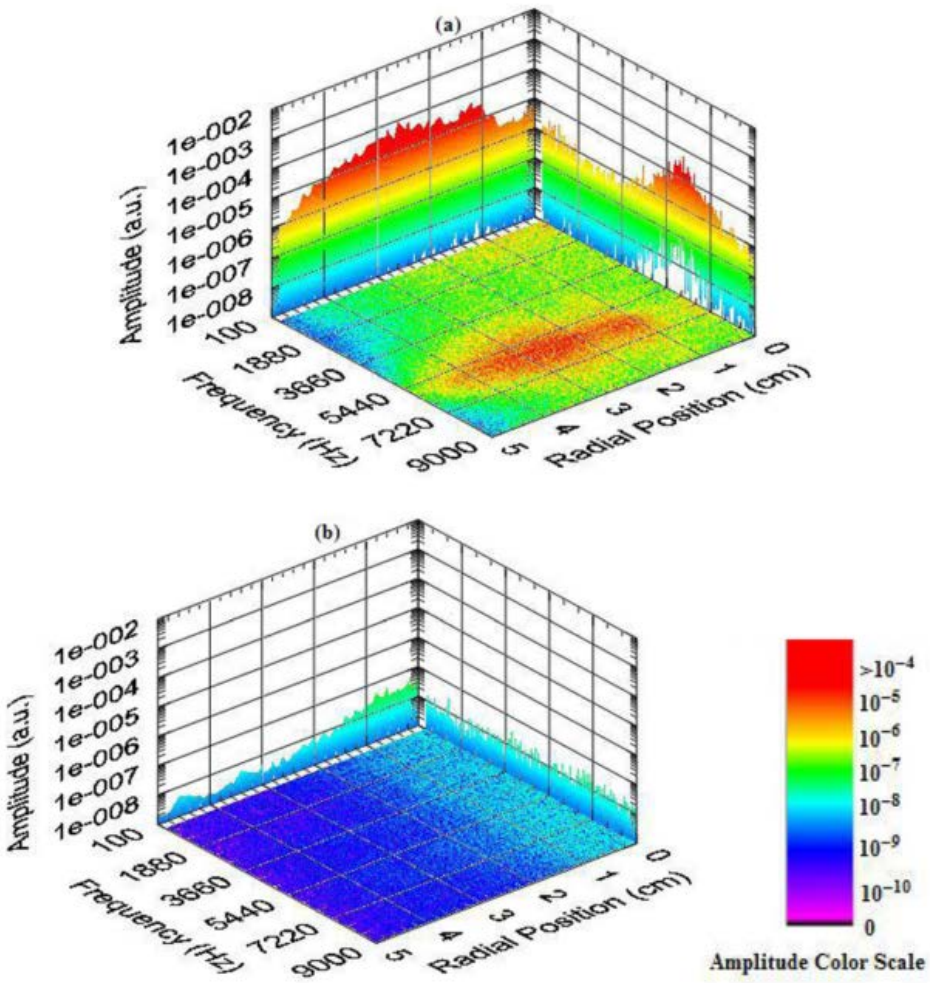

Figure A-8: Wave spectra at (a) a negative bias and (b) a positive bias. The color scale denotes the scaling of the instability amplitude (a.u.). On the radial position axis, 0 cm represents the center of the plasma column and 5 cm represents the edge of the vacuum vessel.

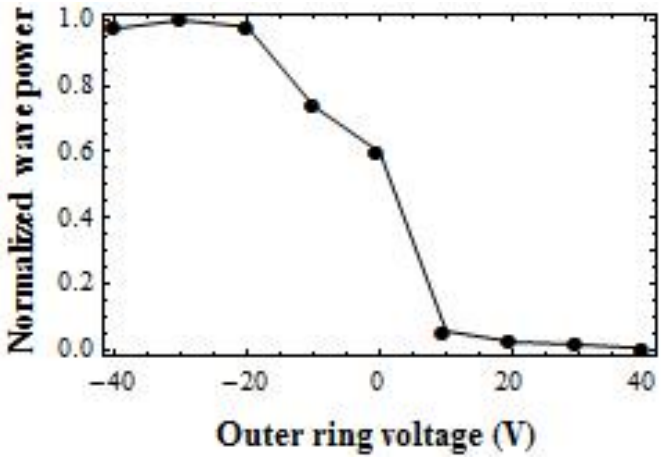

Figure A-9: The peak amplitude calculated in the drift wave frequency range (3 – 9 kHz) is plotted as a function of the bias voltage applied to the outer ring. The plot is normalized to the maximum amplitude (at -30 V). 0 indicates no instability was present and 1 indicates a large amplitude drift wave is present.

It was important to see how the other parameters were modified as the voltage on the outer ring changed. Data taken from the double probe showed that the maximum electron density occurred when a negative voltage was applied to ring 2, and decreased as the applied voltage became positive. The electron temperature was observed to remain constant across the plasma column and as the voltage on ring 2 was varied. Data from the emissive probe showed that the plasma potential remained constant (~ 17 V), even as the negative bias on the outer ring was varied. However, once the voltage applied to the outer ring was changed to a positive bias, the plasma potential increased, and continued to increase each time the positive bias was raised. The radial electric field was calculated, and showed that the electric field varied more for a positive ring bias than for a negative bias.

Data from the "k"-probe was used to calculate the parallel wavenumber as a function of the voltage on the outer ring. At negative voltages, the parallel wavenumber was finite (~20 m^{-1}), and the drift wave propagated towards the rings at end of the chamber. At positive voltages, the parallel wavenumber for the instability observed near the ion cyclotron frequency increased

(~100 m^{-1}) and the direction of propagation changed; i.e., this new instability was propagating away from the rings at the end of the chamber.

Finally, the density and the density gradient were measured for both positive and negative bias voltages. The measurements indicated that the density gradient at a negative bias (~ 7.5 × 10^{17} m^{-4}) was not significantly larger than the density gradient observed at a positive bias (~ 4.5 × 10^{17} m^{-4}). We interpret this to mean that the driving mechanism for the drift wave, the density gradient, remains in the plasma for both positive and negative bias voltages. Therefore, the data indicates that as the bias applied to the ring changes from negative to positive, the drift wave is suppressed and a different instability with a frequency near the ion cyclotron frequency arises in the plasma.

Now, consider what is occurring in the plasma column as the bias voltage on the rings is changed. Not only is there a change in the potential profile of the plasma – especially for the positive bias voltages – but there is also a parallel current that is collected by the rings. This is illustrated in Figure A-10, which shows the current collected by the outer ring as a function of the ring bias. Notice that as the voltage approaches a positive bias, the ring begins to draw electrons, giving rise to an increase in the parallel current. Recall, that under these positive bias conditions, an instability with a frequency near the ion cyclotron frequency was observed. Recent studies on ALEXIS[72] have shown that this instability is a current driven electrostatic ion cyclotron instability.

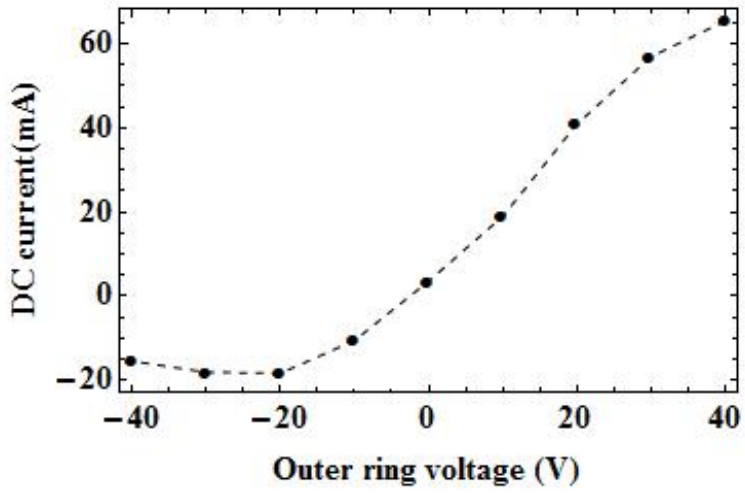

Figure A-10: The dc current collected by ring 2 (the outer ring) as a function of the bias voltage.

It was desired to see what effect the presence of this large parallel current had on the growth rate of the drift wave. Following the kinetic model presented in Goldston and Rutherford[141], it is shown that adding an electron drift velocity due to a parallel electron current, the drift wave dispersion relation is modified (Equation A-2a). In Equation A-2, U_{eo} is the electron drift speed due to a current parallel to the magnetic field and V_{the} is the electron thermal speed.

$$\omega\left(1 + k_y^2\,\rho_{ci}^2\right) - \omega_e^* - \frac{C_s^2\,k_z^2}{\omega} = -i\sqrt{\frac{\pi}{2}}\frac{\omega(\omega-\omega_e^*-k_z\,U_{eo})}{|k_z|\,V_{the}} \tag{A-2a}$$

$$\omega = \omega_e^* + \frac{C_s^2\,k_z^2}{\omega_e^*} \tag{A-2b}$$

$$\gamma = \sqrt{\frac{\pi}{2}}\,\frac{(\omega_e^*\,k_z\,U_{eo}-C_s^2\,k_z^2)}{|k_z|\,V_{the}} \tag{A-2c}$$

Now, assuming that $k_y\,\rho_{ci} \ll 1$ and $C_s\,k_z \ll \omega$ (where the first order correction is kept), the real part of the frequency is given by Equation A-2b, and the imaginary part of the frequency gives the growth rate (Equation A-2c). Using typical parameter values for drift waves in ALEXIS, the growth rate is plotted in Figure A-11 as a function of (a) the parallel wave number, k_z, and (b) the

perpendicular wave number, k_y, for three different parallel currents. When the outer electrode ring was biased negatively and drift waves were present in the plasma, a small negative parallel current was measured (approximately -10 to -20 mA). The thin blue line shows that the growth rate under these conditions is positive and the drift wave is able to propagate through the plasma. However, when there was a large positive parallel current (thick solid black line), the growth rate is negative and the drift wave is not supported under these conditions. The same is also true when there is zero current (red dashed line). The shaded region in both plots represents experimental values of the wavenumber associated with drift waves in ALEXIS. This suggests that the presence of this parallel current is responsible for modifying the dispersion relation so that the drift wave can no longer be supported by the ALEXIS plasma. This is also consistent with observations made in studies by Simonen *et al.*[125]

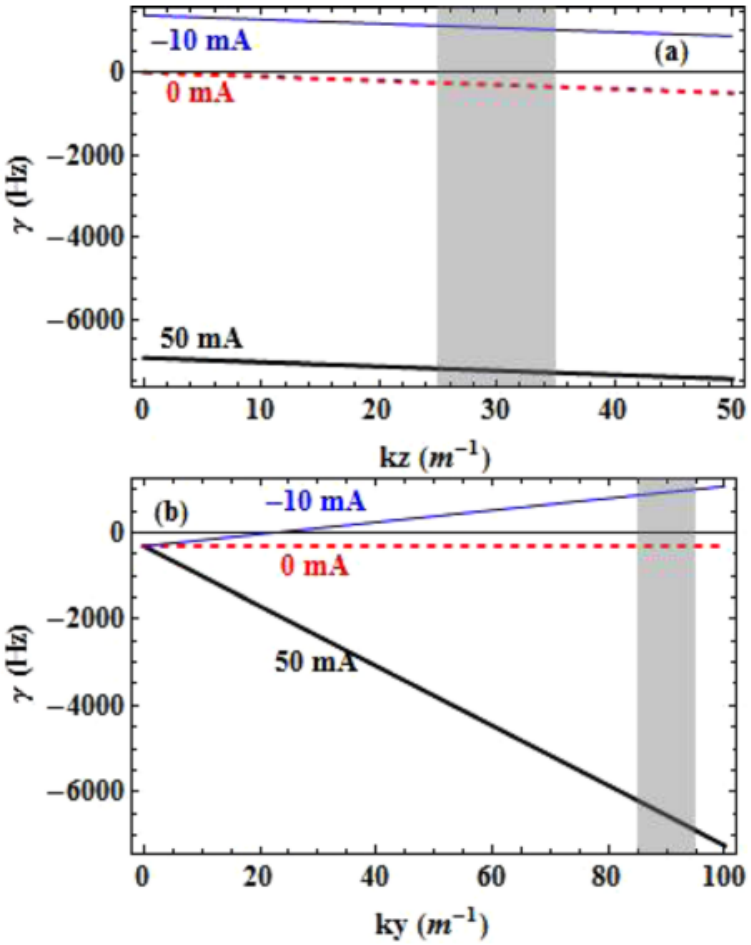

Figure A-11: The growth rate is plotted as a function of (a) the parallel wavenumber (at a fixed k_y = 100 m^{-1}) and (b) the perpendicular wavenumber (at a fixed k_z = 30 m^{-1}) for three different parallel currents. When there is a large positive parallel current (50 mA) present in the plasma, the growth rate is negative and the drift wave cannot be supported. When there is a small negative parallel current (-10 mA), the growth rate is positive and the drift wave is allowed to propagate within the plasma. The shaded region represents the measured wave numbers associated with drift waves. It is noted that $\omega_{ci} = 2\pi * 12$ kHz.

A.4 Conclusions

Non-localized, low frequency instabilities have been observed in the Auburn Linear EXperiment for Instability studies (ALEXIS). It was determined that the driving mechanism for the instability was a density gradient, and the instabilities were characterized as drift waves. A new experiment was performed to determine if the drift wave instability could be suppressed in ALEXIS.

Concentric electrode rings were used to change the radial potential structure of the plasma by varying the voltage applied to the rings. When a negative bias was applied to the rings, a large amplitude drift wave was observed at $0.5\omega_{ci}$. The plasma potential remained constant for different negative voltages, and there was a uniform electric field present in the plasma. Data from a "k"-probe showed that the wave-number was finite and the wave propagated toward the end of the chamber. As the voltage went from negative to positive, there was no longer a drift wave present and the peak density decreased. The plasma potential was observed to increase as the positive bias increased and a non-uniform radial electric field arose in the plasma. It was discovered that at a positive bias, the rings were collecting a large amount of current, and at a negative bias, the rings were giving off electrons.

It appears that the driving mechanism at a positive bias is the current drawn by the outer ring. This drives a wave in the ion-cyclotron regime that has a small electrostatic amplitude, but there was no wave present in the drift wave frequency range. The density gradient present at a negative bias was the driving mechanism for the drift wave. By biasing the ring electrodes positive, and creating a large parallel current in the plasma, drift waves were successfully suppressed in the ALEXIS device.

Appendix B – Computer Codes

B.1 Mathematica shooting codes

Shooting Code - Electron-Ion Hybrid Theory (Density Gradient)

ALEXIS Parameters

```
Needs["ErrorBarPlots`"]
Needs["PlotLegends`"]

e = 1.602 * 10^-19;
me = 9.109 * 10^-31;
εo = 8.85 * 10^-12;
ne = 10 * 10^14;
B = 100 / 10000;
Eo = 20 * 100;
LE = 0.40 / 100;
Ln = 1.2 / 100;
k = 70;
ωce = e * B / me;
ωpe = Sqrt[e^2 * ne / (me * εo)];
Veo = Eo / B;
δ = ωpe / ωce
α1 = Veo / (ωce * LE)
RL = LE / Ln
kLE = k * LE
```

Shooting Code

```
(* First Define a function that integrates from the left defined by -
 L to the right +L, for a given frequency and parameters *)
VE[x_] := Module[{}, Sech[x]^2]
shoot[ω_?NumericQ, k_?NumericQ, δ_?NumericQ, α1_?NumericQ, RL_?NumericQ] :=
 Module[{μ = 1837, s = 10, β},
  β = 1 / Sqrt[40 * μ * (1 + 1 / δ^2)] / k / α1;
  NDSolve[{y''[x] ==
      (k^2 - δ^2 / (δ^2 + 1) / (1 - (β / ω)^2) (D[D[VE[x], x], x] - RL / α1) / (ω - VE[x]))
       y[x], y[-s] == 0.1, y'[-s] == k 0.1}, y, {x, -s, s}][[1]]]

(* Then define a function that numerically evaluates the integrated
 differential equation at the end point and compares it to the
 growing asymptotic solution, this number should be zeroed out *)
F[ω_?NumericQ, k_?NumericQ, δ_?NumericQ, α1_?NumericQ, RL_?NumericQ] :=
 Module[{s = 10}, y[s] / Exp[k s] /. shoot[ω, k, δ, α1, RL]]
```

Eigenfunction

```
(*This module finds a single eigenvalue and plots the eigenfunction *)
Module[{ωFig3, solFig3, μ = 1837, α1 = 0.04, k = 1, δ = 2, RL = 0, β},
 (* This is how you would find a single root of F,
 i.e. eigenvalue of the boundary value problem *)
 ωFig3 = ω /. FindRoot[F[ω, k, δ, α1, RL] == 0, {ω, 0.3 + 0.2 i}];
 β = 1 / Sqrt[40 * μ * (1 + 1 / δ^2)] / k / α1;
 wwlh = ωFig3 / β;
 Print[
  StringJoin["Eigen value: ", ToString[Re[wwlh]], "+", ToString[Im[wwlh]], "i"]];
 (* And then to get the eigenfunction you call the
  shoot routine again with the root *)
 solFig3 = shoot[ωFig3, k, δ, α1, RL];
 Plot[{Re[(y[x] / y[0])] /. solFig3, Im[(y[x] / y[0])] /. solFig3}, {x, -10, 10},
  PlotStyle → {Black, Directive[Dashed, Black]}, Frame → True,
  FrameLabel → {"x/L", "ϕ(x)"}, FrameStyle → {Bold, 14}, PlotRange → All]]
```

```
Eigen value: 0.40915+0.697445i
```

InterpolatingFunction::dmval :

Input value {−4.9998} lies outside the range of data in the interpolating function. Extrapolation will be used. »

InterpolatingFunction::dmval :

Input value {−4.9998} lies outside the range of data in the interpolating function. Extrapolation will be used. »

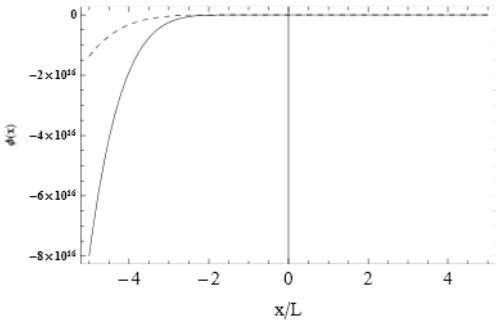

Frequency and Growth Rates

- **As a function of ky $* L_E$**

```
(* This module calculates the growth rate as a function of kyL_E *)
Module[{μ = 1837, α1 = 0.028, ks, ev, δ = 1, RL = 0.33, β},
 (* Generate a list of k values to find eigenvalues. As δ changes,
 the ending point of the table will increase or decrease,
 otherwise an error occurs. *)
 ks = Table[k, {k, 0.1, 1, 0.001}];
 (* Calculate beta values *)
 β = Table[1 / Sqrt[40 * μ (1 + 1 / δ^2)] / k / α1, {k, ks}];
 (* Find the first ev and store in a list. In the findroot function,
 pick a real and imaginary number close to where ω is. In
  the theory we say that β~ωLH. So we normalize the growth
  rate to the lower hybrid frequency by dividing by β. *)
 ev = List[ω / β[[1]] /. FindRoot[F[ω, First[ks], δ, α1, RL] == 0, {ω, 0.4 + 0.1 i}]];
 Print[StringJoin["Found First Root: ", ToString[Last[ev]]]];
 Print[StringJoin["Computational value: ", ToString[Last[ev] β[[1]]]]];
 Do[ev = Append[ev,  ω / β[[i]] /. FindRoot[F[ω, ks[[i]], δ, α1, RL] == 0,
       {ω, Last[ev] β[[i - 1]]}]], {i, 2, Length[ks], 1}];
 ListLinePlot[{Thread[{ks, Im[ev]}], Thread[{ks, Re[ev]}]},
  AxesOrigin → {0, -1}, Frame → True, PlotRange → {{0, 1.0}, {0, 1}},
  FrameLabel → {{"ω,γ/ω_LH", None}, {"k_y  L_E", None}},
  LabelStyle → {Bold, 14}, PlotStyle → {Directive[Dashed, Black], Black}]]
```

```
Found First Root: 0.427348 + 0.076126 I
Computational value: 0.398129 + 0.0709211 I
```

FindRoot::lstol :

The line search decreased the step size to within tolerance specified by AccuracyGoal and PrecisionGoal but was unable to find a sufficient decrease in the merit function. You may need more than MachinePrecision digits of working precision to meet these tolerances. >>

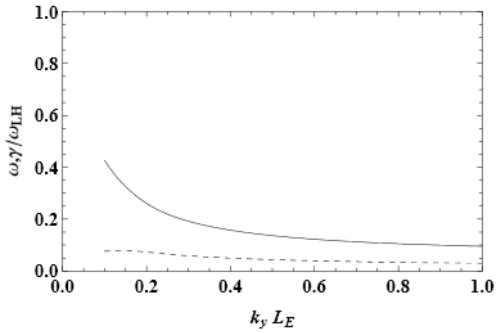

- **As a function of ky $*$ L_E - Normalized Plots**
- **As a function of ky**
- **As a function of λ_y**
- **As a function of δ**
- **As a function of B**
- **As a function of Density**
- **As a function of α_1**
- **As a function of Eo**
- **As a function of R_L**
- **As a function of L_n**

Shooting Code - Electron-Ion Hybrid Theory (k_z)

ALEXIS Parameters

```
Needs["ErrorBarPlots`"]
Needs["PlotLegends`"]

e = 1.602 * 10^-19;
me = 9.109 * 10^-31;
εo = 8.85 * 10^-12;
ne = 6 * 10^14;
Bo = 127.5 / 10000;
Eo = 7 * 100;
LE = 0.4 / 100;
ky = 87;
kz = 14;
ωce = e * Bo / me;
ωpe = Sqrt[e^2 * ne / (me * εo)];
Veo = Eo / Bo;
δ = ωpe / ωce
α1 = Veo / (ωce * LE)
kyLE = ky * LE
kzLE = kz * LE
```

```
0.616352

0.00612105

0.348

0.056
```

```
n[d_] := Bo^2 * εo / me * d^2

B[d_] := 1/d * Sqrt[ne * me / εo]

Efield[a_] := a * e * Bo^2 * LE / me

n[0.2]
```

6.31761×10^{13}

```
dlist = Table[i, {i, 0.3, 0.8, 0.05}];

B[0.2] * 10000
```

392.925

```
alist = Table[i, {i, 0.005, 0.105, 0.01}];

Efield[0.09] / 100
```

102.924

Shooting Code

```
(* First Define a function that integrates from the left defined by -
 L to the right +L, for a given frequency and parameters *)
VE[x_] := Module[{}, Sech[x]^2]
shoot[ω_?NumericQ, ky_?NumericQ, δ_?NumericQ, α1_?NumericQ, kz_?NumericQ] :=
 Module[{μ = 1837, s = 10, β},
  β = 1 / Sqrt[40 * μ * (1 + 1 / δ^2)] / ky / α1;
  NDSolve[{y''[x] == (ky^2 + kz^2 - ((δ^2 / (δ^2 + 1)) / (1 - β^2 / ω^2))
          ((D[D[VE[x], x], x]) / (ω - VE[x])) + (kz^2 / (ky^2 α1^2 * (ω - VE[x])^2)))) y[x],
    y[-s] == 0.1, y'[-s] == ky 0.1}, y, {x, -s, s}][[1]]]

(* Then define a function that numerically evaluates the integrated
 differential equation at the end point and compares it to the
 growing asymptotic solution, this number should be zeroed out *)
F[ω_?NumericQ, ky_?NumericQ, δ_?NumericQ, α1_?NumericQ, kz_?NumericQ] :=
 Module[{s = 10}, y[s] / Exp[ky s] /. shoot[ω, ky, δ, α1, kz]]
```

Eigenfunction

```
(*This module finds a single eigenvalue and plots the eigenfunction *)
Module[{ωFig3, solFig3, μ = 1837, α1 = 0.035, ky = 0.3, δ = 0.50, kz = 1, β},
 (* This is how you would find a single root of F,
 i.e. eigenvalue of the boundary value problem *)
 ωFig3 = ω /. FindRoot[F[ω, ky, δ, α1, kz] == 0, {ω, 0.5 + 0.5 i}];
 β = 1 / Sqrt[40 * μ * (1 + 1 / δ^2)] / ky / α1;
 wwlh = ωFig3 / β;
 Print[
  StringJoin["Eigen value: ", ToString[Re[wwlh]], "+", ToString[Im[wwlh]], "i"]];
 (* And then to get the eigenfunction you call the
  shoot routine again with the root *)
 solFig3 = shoot[ωFig3, ky, δ, α1, kz];
 Plot[{Re[(y[x] / y[0])] /. solFig3, Im[(y[x] / y[0])] /. solFig3}, {x, -10, 10},
  PlotStyle → {Black, Directive[Dashed, Black]}, Frame → True,
  FrameLabel → {"x/L", "ϕ(x)"}, FrameStyle → {Bold, 14}, PlotRange → All]]
```

Frequency and Growth Rates

- **As a function of kz**

```
(* This module calculates the growth rate as a function of kz *)
Module[{μ = 1837, α1 = 0.035, ky = 0.3, ev, δ = 0.55, kzs, β},
 (* Generate a list of k values to find eigenvalues. *)
 kzs = Table[kz, {kz, 0.0001, 0.0067, 0.0001}];
 (* Calculate beta values *)
 β = 1 / Sqrt[40 * μ (1 + 1 / δ^2)] / ky / α1;
 (* Find the first ev and store in a list. In the findroot function,
 pick a real and imaginary number close to where ω is. In
  the theory we say that β~ωLH. So we normalize the growth
  rate to the lower hybrid frequency by dividing by β. *)
 ev = List[ω / β /. FindRoot[F[ω, ky, δ, α1, First[kzs]] == 0, {ω, 0.5 + 0.1 i}]];
 Print[StringJoin["Found First Root: ", ToString[Last[ev]]]];
 Print[StringJoin["Computational value: ", ToString[Last[ev] β]]];
 Do[
  ev = Append[ev,  ω / β /. FindRoot[F[ω, ky, δ, α1, kzs[[i]]] == 0, {ω, Last[ev] β}]],
  {i, 2, Length[kzs], 1}];
 UniformDensitykzTheory = ListLinePlot[
   {Thread[{kzs / 0.004, Re[ev]}], Thread[{kzs / 0.004, Im[ev]}]},
   AxesOrigin → {0, 0}, Frame → True, PlotRange → {{0, 3}, {0, 5}}, FrameLabel →
    {Style["k_z  (m^-1)", 18, Bold], Style["ω,γ/ω_LH", 16, Bold]}, FrameTicksStyle → 14,
   PlotStyle → {Directive[Thick, Black], Directive[Black, Dashed, Thick]},
   PlotLegend → {Style["ω/ω_LH", 16], Style["γ/ω_LH", 16]},
   LegendPosition → {0.365, 0.27}, LegendSize → {0.4, 0.3},
   LegendShadow → 0, LegendBorder → None, ImageSize → 500] (*;
 Export["C:/Users/Ami/Graduate School/Dissertation/Results
    and Conclusions/Uniform Density Plots/Preliminary
    Plots/UniformDensitykzTheory.PNG",Rasterize[UniformDensitykzTheory]]*)]
```

```
Found First Root: 3.17611 + 2.07447 I
Computational value: 0.537769 + 0.351243 I
```

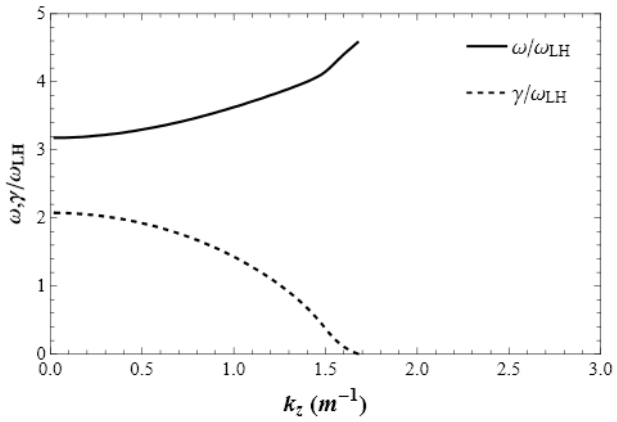
ω/ω_LH
γ/ω_LH
ω,γ/ω_LH
k_z (m^-1)
0
1
2
3
4
5
0.0
0.5
1.0
1.5
2.0
2.5
3.0

■ As a function of λz

```
(* This module calculates the growth rate as a function of λz *)
Module[{μ = 1837, α1 = 0.09, ky = 0.3, ev, δ = 0.55, kzs, β},
 (* Generate a list of k values to find eigenvalues. *)
 kzs = Table[kz, {kz, 0.001, 0.0175, 0.0001}];
 (* Calculate beta values *)
 β = 1 / Sqrt[40 * μ (1 + 1 / δ^2)] / ky / α1;
 (* Find the first ev and store in a list. In the findroot function,
 pick a real and imaginary number close to where ω is. In
  the theory we say that β~ωLH. So we normalize the growth
  rate to the lower hybrid frequency by dividing by β. *)
 ev = List[ω / β /. FindRoot[F[ω, ky, δ, α1, First[kzs]] == 0, {ω, 0.5 + 0.5 i}]];
 Print[StringJoin["Found First Root: ", ToString[Last[ev]]]];
 Print[StringJoin["Computational value: ", ToString[Last[ev] β]]];
 Do[
  ev = Append[ev,  ω / β /. FindRoot[F[ω, ky, δ, α1, kzs[[i]]] == 0, {ω, Last[ev] β}]],
  {i, 2, Length[kzs], 1}];
 UniformDensityWaveLengthTheory =
  ListLinePlot[{Thread[{(2 π) / (kzs / 0.004), Re[ev]}],
    Thread[{(2 π) / (kzs / 0.004), Im[ev]}], {{1.7, 0}, {1.7, 14.5}}},
   AxesOrigin → {0, 0}, Frame → True, PlotRange → {{0, 10}, {0, 12}},
   FrameLabel → {Style["λ_z (m)", 18, Bold], Style["ω,γ/ω_LH", 16, Bold]},
   FrameTicksStyle → 14, PlotStyle → {Directive[Thick, Black],
     Directive[Black, Thick, Dashed], Directive[Dashed, Thick, Red]},
   PlotLegend → {Style["ω/ω_LH", 16], Style["γ/ω_LH", 16], Style["L_ALEXIS", 16]},
   LegendPosition → {0.4, 0.26}, LegendBorder → None,
   LegendSize → {0.4, 0.3}, LegendShadow → 0, ImageSize → 500];
 Export["C:/Users/Ami/Graduate School/Dissertation/Results
    and Conclusions/Uniform Density Plots/Preliminary
    Plots/UniformDensityWaveLengthTheory3.PNG",
  Rasterize[UniformDensityWaveLengthTheory]]]
```

```
Found First Root: 8.00194 + 5.14297 I

Computational value: 0.526891 + 0.338641 I

C:/Users/Ami/Graduate School/Dissertation/Results and Conclusions/Uniform
  Density Plots/Preliminary Plots/UniformDensityWaveLengthTheory3.PNG
```

B.2 LabVIEW system control

B.2.1 HMI (HMI.vi)

Front Panel

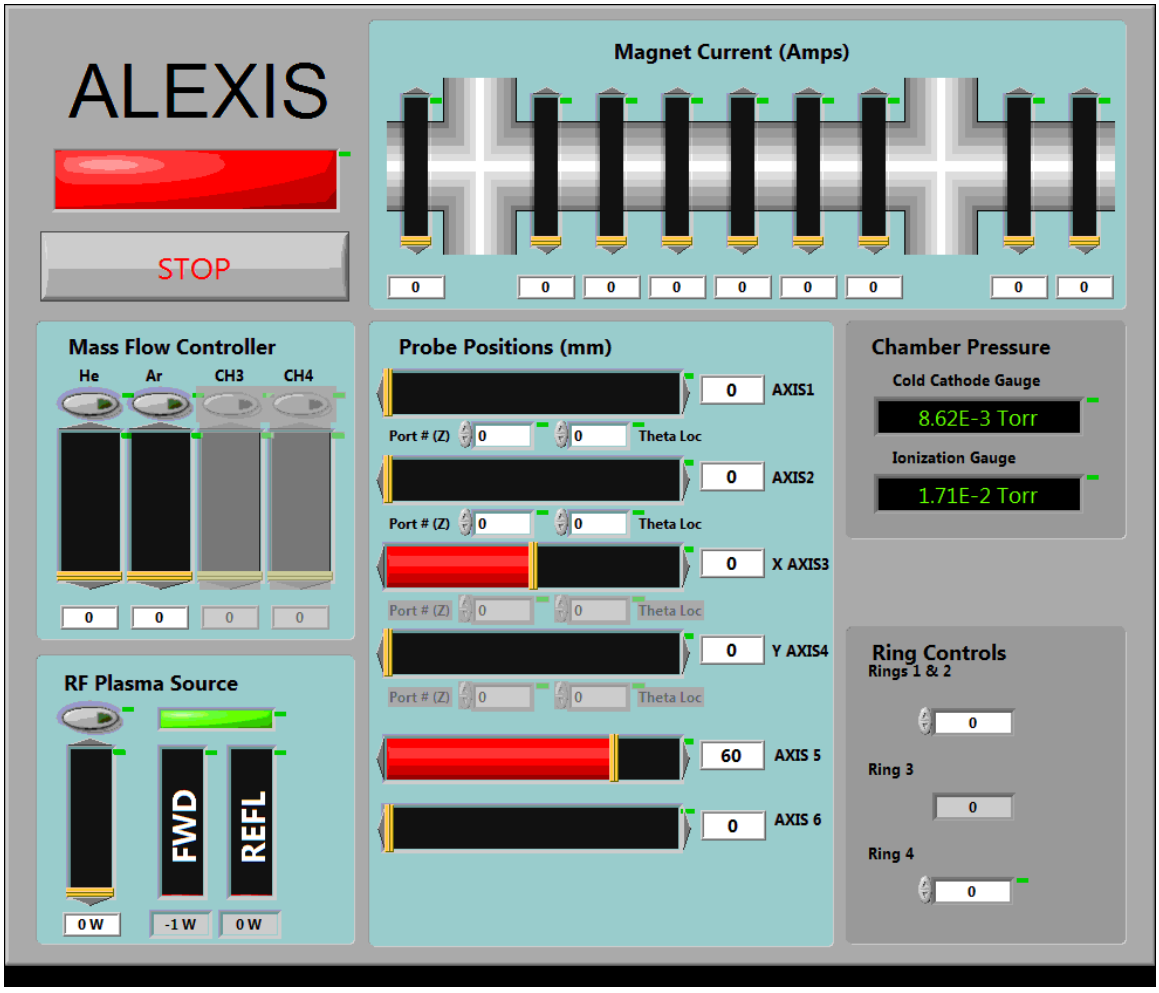

Block Diagram

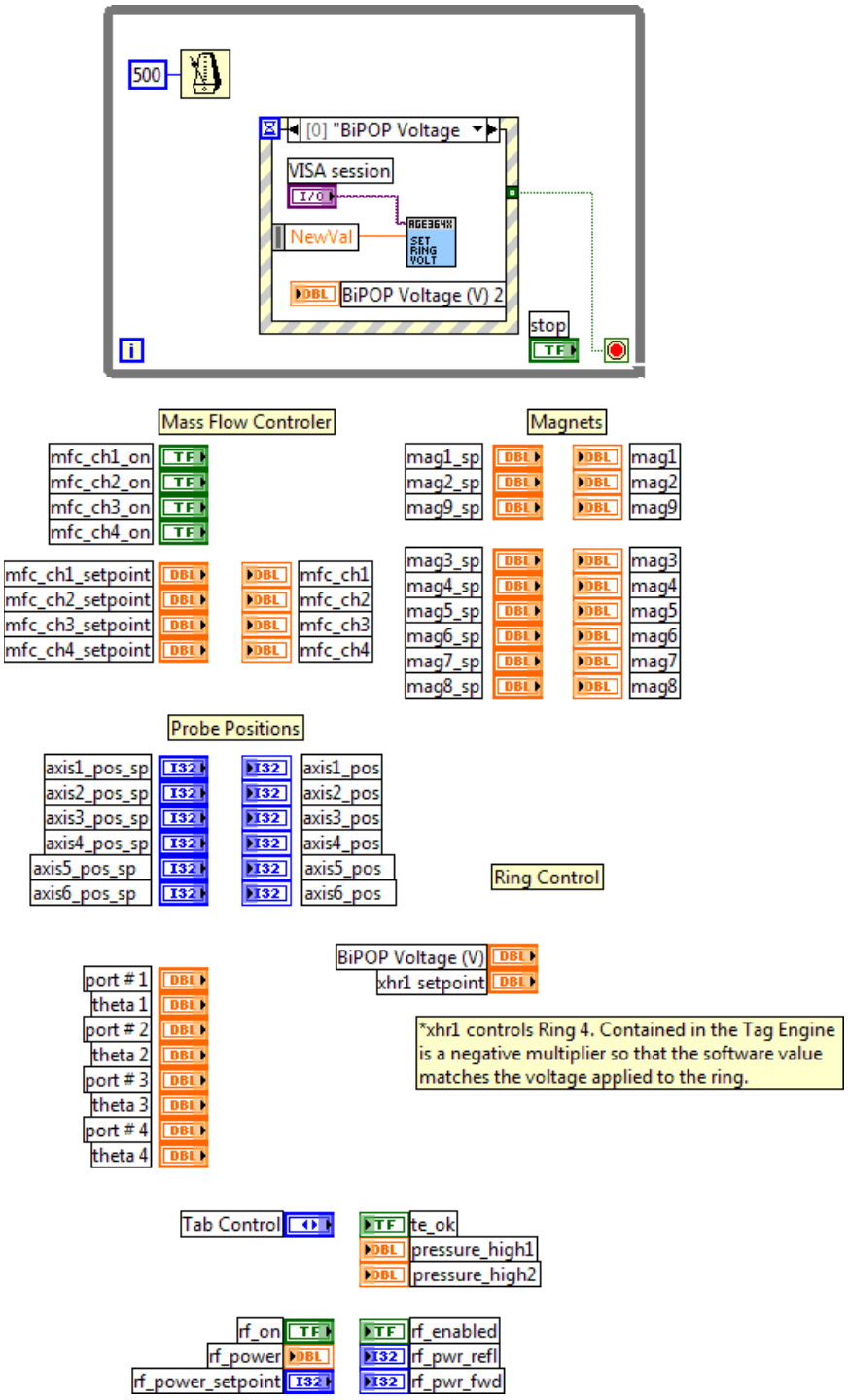

List of SubVIs and Express VIs

set_bipop_voltage.vi
C:\Users\Public\Documents\LabVIEW VI's\alexis_sub_vi's\set_bipop_voltage.vi

B.2.2 Gas control (Gas_Ramp.vi)

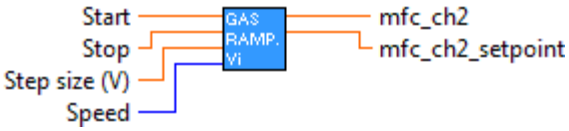

Front Panel

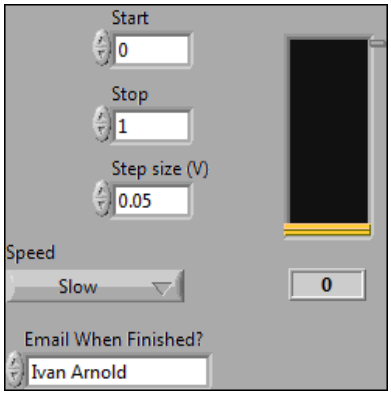

Block Diagram

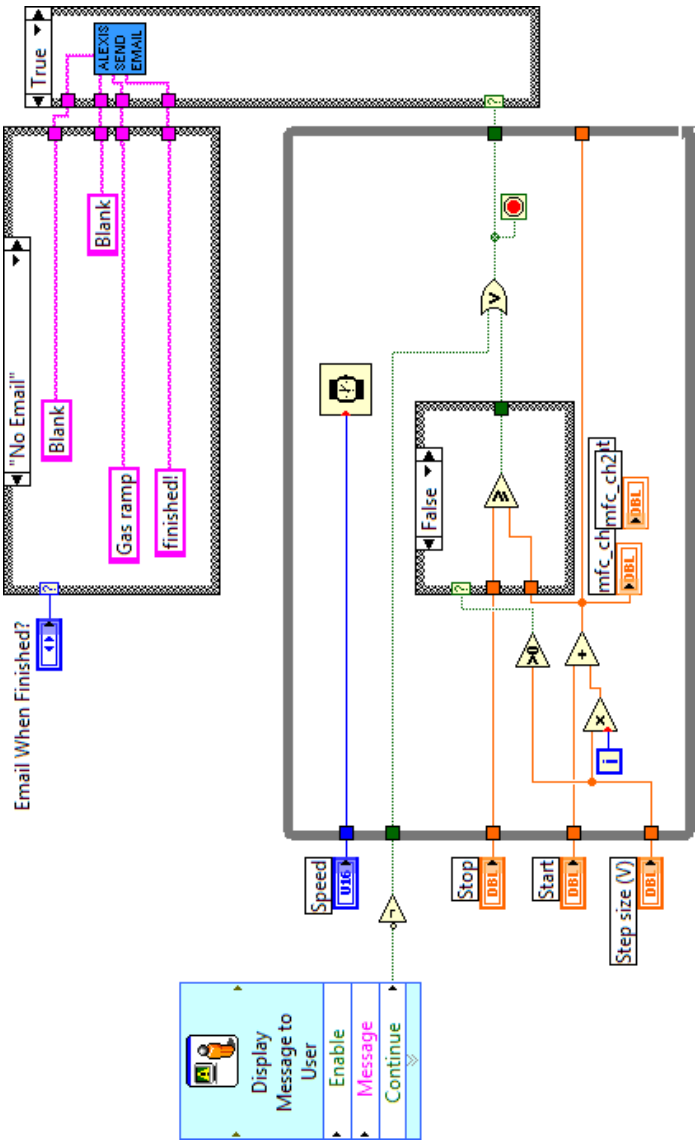

List of SubVIs and Express Vis

Alexis_Gmail_No_Attachments.vi
C:\Users\DuBois\Desktop\alexis_sub_vi's\Alexis_Gmail_No_Attachments.vi

Display Message to User
Display Message to User
Displays a standard dialog box that contains an alert or a message for users.

This Express VI is configured as follows:

Message: Please be sure the MFC is on using the software toggle switch in the HMI.

Have you checked the chilled water?

B.2.3 Filament control (Filament_ramp.vi)

Front Panel

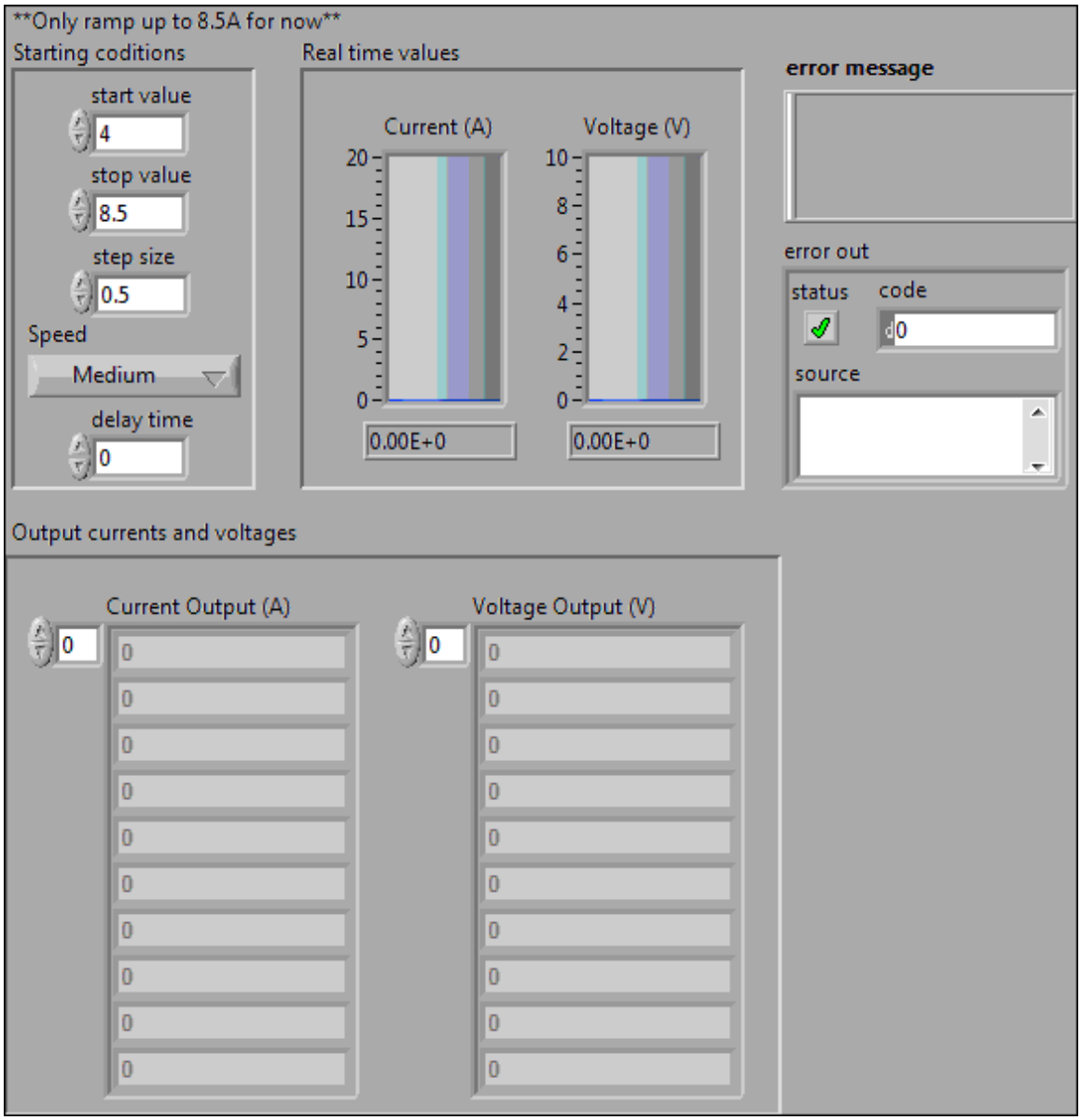

Block Diagram

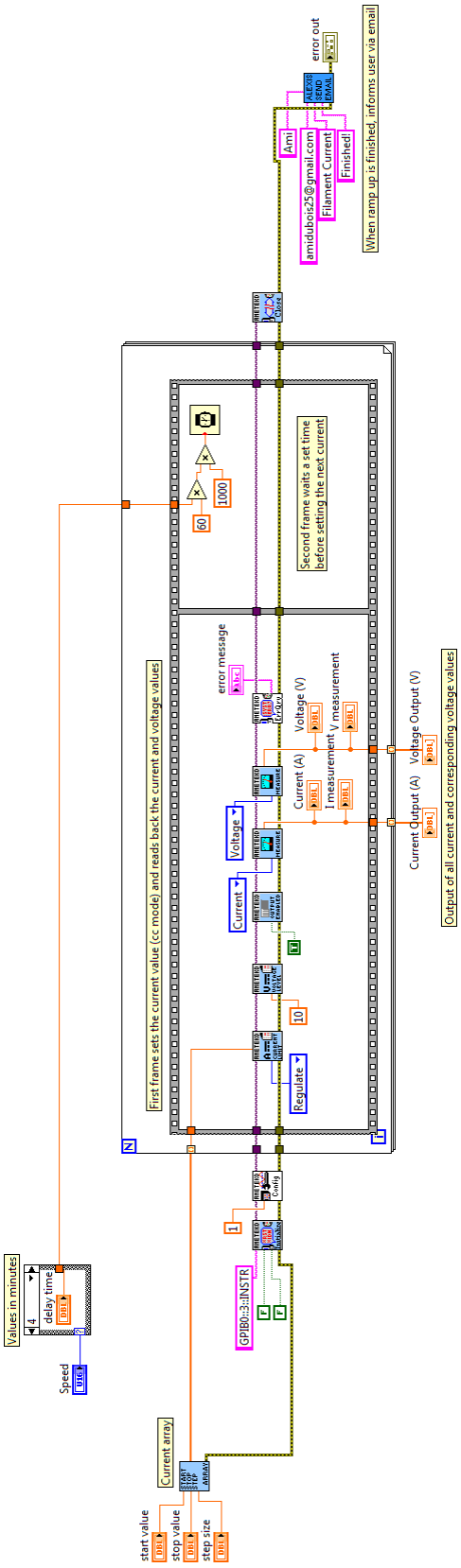

List of SubVIs and Express VIs

AmetekDC Query Error.vi
C:\Program Files (x86)\National Instruments\LabVIEW 2010\instr.lib\AmetekXG20-76\AmetekDC.llb\AmetekDC Query Error.vi

AmetekDC Measure [MSR].vi
C:\Program Files (x86)\National Instruments\LabVIEW 2010\instr.lib\AmetekXG20-76\AmetekDC.llb\AmetekDC Measure [MSR].vi

AmetekDC Configure Output Enabled.vi
C:\Program Files (x86)\National Instruments\LabVIEW 2010\instr.lib\AmetekXG20-76\AmetekDC.llb\AmetekDC Configure Output Enabled.vi

AmetekDC Configure Voltage Level.vi
C:\Program Files (x86)\National Instruments\LabVIEW 2010\instr.lib\AmetekXG20-76\AmetekDC.llb\AmetekDC Configure Voltage Level.vi

AmetekDC Configure Current Limit.vi
C:\Program Files (x86)\National Instruments\LabVIEW 2010\instr.lib\AmetekXG20-76\AmetekDC.llb\AmetekDC Configure Current Limit.vi

Alexis_Gmail_No_Attachments.vi
C:\Users\DuBois\Desktop\alexis_sub_vi's\Alexis_Gmail_No_Attachments.vi

AmetekDC Close.vi
C:\Program Files (x86)\National Instruments\LabVIEW 2010\instr.lib\AmetekXG20-76\AmetekDC.llb\AmetekDC Close.vi

AmetekDC Set Command Time Delay.vi
C:\Program Files (x86)\National Instruments\LabVIEW 2010\instr.lib\AmetekXG20-76\AmetekDC.llb\AmetekDC Set Command Time Delay.vi

AmetekDC Initialize.vi
C:\Program Files (x86)\National Instruments\LabVIEW 2010\instr.lib\AmetekXG20-76\AmetekDC.llb\AmetekDC Initialize.vi

Start Stop Step to Array.vi
C:\Users\DuBois\Desktop\NRL\Start Stop Step to Array.vi

B.3 LabVIEW data acquisition

B.3.1 Langmuir probe (LP frequency radial sweep GFITS Only.vi)

Front Panel

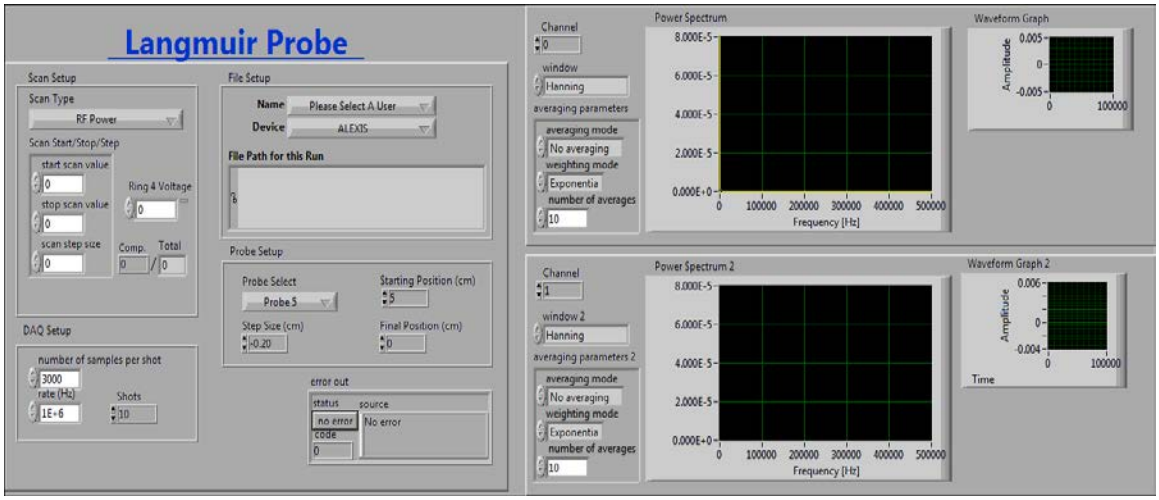

Block Diagram

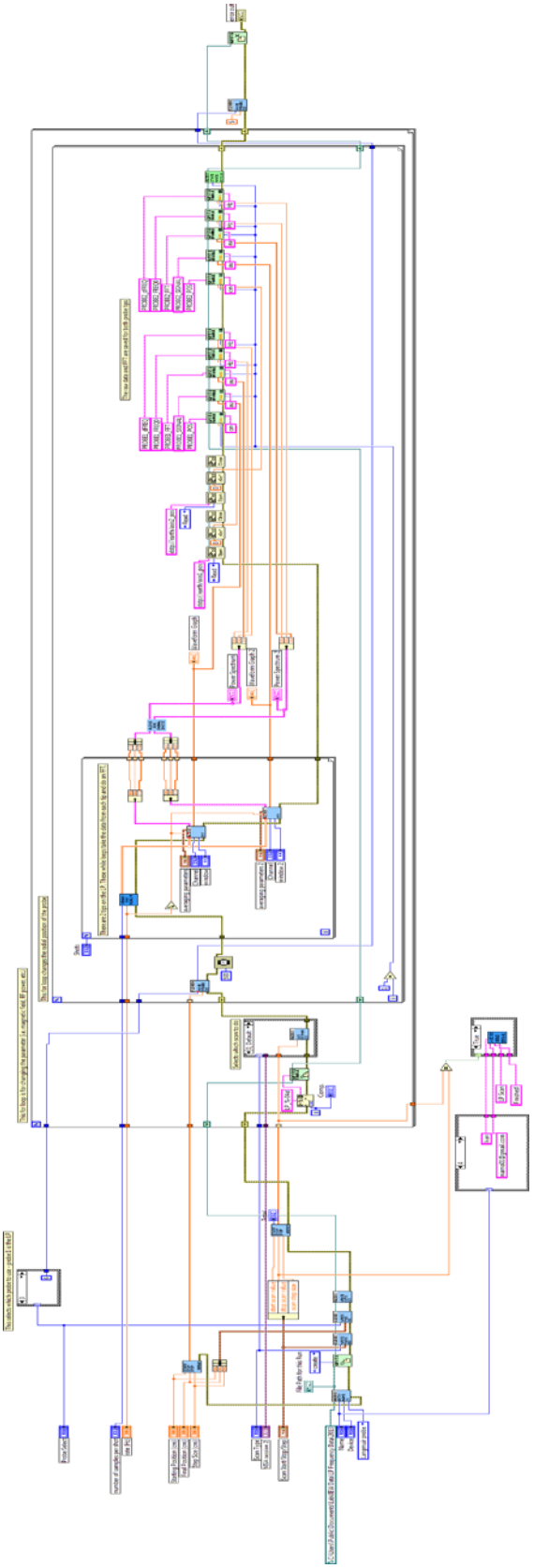

List of SubVIs and Express VIs

set_bipop_voltage.vi
C:\Users\Public\Documents\LabVIEW VI's\alexis_sub_vi's\set_bipop_voltage.vi

Alexis_Gmail_No_Attachments.vi
C:\Users\DuBois\Desktop\alexis_sub_vi's\Alexis_Gmail_No_Attachments.vi

fft_wrapper.vi
C:\Users\DuBois\Desktop\alexis_sub_vi's\fft_wrapper.vi

cDaq9181 read.vi
C:\Users\DuBois\Documents\My Dropbox\Lab Shared - ALEXIS\Ami's ALEXIS VIs\ALEXIS VIs\SubVIs\cDaq9181 read.vi

Machine_state_FITS.vi
C:\Users\DuBois\Desktop\alexis_sub_vi's\Machine_state_FITS.vi

gfitsio-write-column-dbl-scalar_new.vi
C:\Users\DuBois\Desktop\LabVIEW Data - Shortcut.lnk\gfitsio\gfitsio-write-column-dbl-scalar_new.vi

gfitsio-write-column_new.vi
C:\Users\DuBois\Desktop\LabVIEW Data - Shortcut.lnk\gfitsio\gfitsio-write-column_new.vi

gfitsio-write-column-sgl-1d_new.vi
C:\Users\DuBois\Desktop\LabVIEW Data - Shortcut.lnk\gfitsio\gfitsio-write-column-sgl-1d_new.vi

gfitsio-write-column-dbl-1d_new.vi
C:\Users\DuBois\Desktop\LabVIEW Data - Shortcut.lnk\gfitsio\gfitsio-write-column-dbl-1d_new.vi

Avg_Data_Shots.vi
C:\Users\DuBois\Desktop\alexis_sub_vi's\Avg_Data_Shots.vi

Wait with Error IO.vi
C:\Users\DuBois\Desktop\NRL\Wait with Error IO.vi

set_mfc_voltage_ds.vi
C:\Users\DuBois\Desktop\alexis_sub_vi's\set_mfc_voltage_ds.vi

set_out_mag_cur_ds.vi
C:\Users\Public\Documents\LabVIEW VI's\alexis_sub_vi's\set_out_mag_cur_ds.vi

set_in_mag_cur_ds.vi
C:\Users\Public\Documents\LabVIEW VI's\alexis_sub_vi's\set_in_mag_cur_ds.vi

set_rf_power_ds.vi
C:\Users\DuBois\Documents\My Dropbox\Lab Shared - ALEXIS\Ami's ALEXIS VIs\ALEXIS VIs\SubVIs\set_rf_power_ds.vi

gfitsio-open-create-replace-table_new.vi
C:\Users\DuBois\Desktop\LabVIEW Data - Shortcut.lnk\gfitsio\gfitsio-open-create-replace-table_new.vi

gfitsio-close-file_new.vi
C:\Users\DuBois\Desktop\LabVIEW Data - Shortcut.lnk\gfitsio\gfitsio-close-file_new.vi

move_probe_ds.vi
C:\Users\Public\Documents\LabVIEW VI's\alexis_sub_vi's\move_probe_ds.vi

write_fits_keys_ds.vi
C:\Users\Public\Documents\LabVIEW VI's\alexis_sub_vi's\write_fits_keys_ds.vi

write_probe_keys_ds.vi
C:\Users\Public\Documents\LabVIEW VI's\alexis_sub_vi's\write_probe_keys_ds.vi

write_var_keys_ds2.vi
C:\Users\Public\Documents\LabVIEW VI's\alexis_sub_vi's\write_var_keys_ds2.vi

gfitsio-open-create-replace-file_new.vi
C:\Users\DuBois\Desktop\LabVIEW Data - Shortcut.lnk\gfitsio\gfitsio-open-create-replace-file_new.vi

AutoGenerate_Filenames_v3.vi
C:\Users\DuBois\Desktop\alexis_sub_vi's\AutoGenerate_Filenames_v3.vi

Start Stop Step to Array.vi
C:\Users\DuBois\Desktop\NRL\Start Stop Step to Array.vi

B.3.2 Emissive probe (EP_scan_FITS.vi)

Front Panel

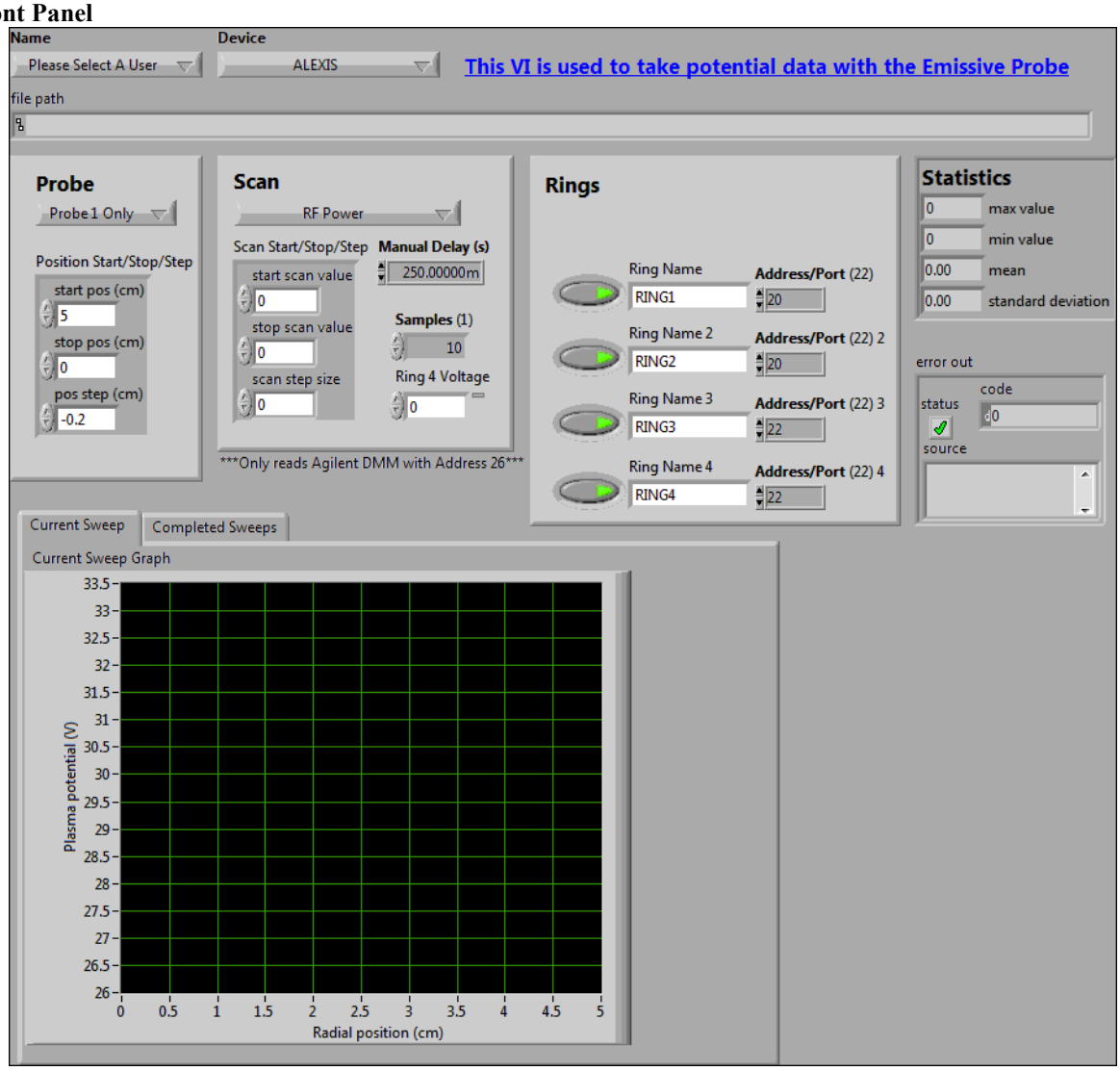

Block Diagram

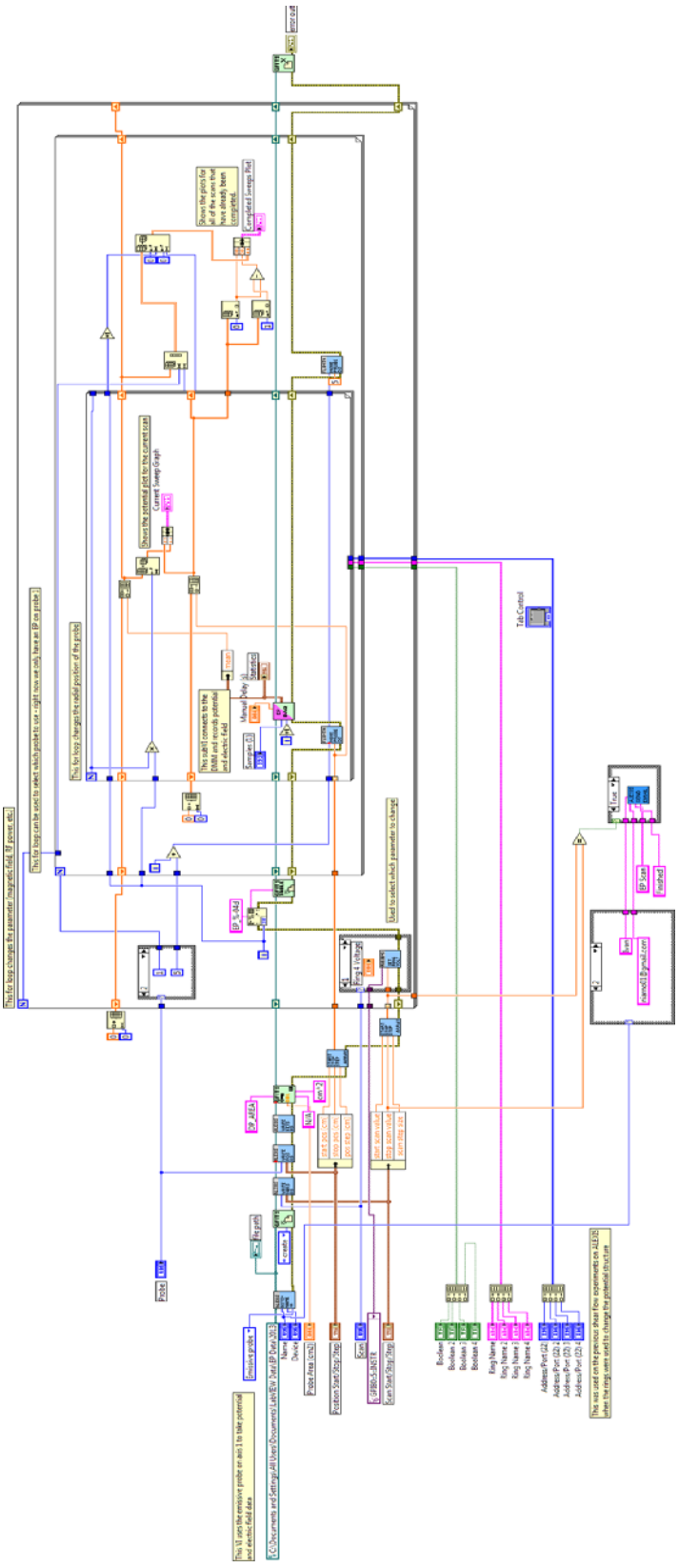

List of SubVIs and Express VIs

set_bipop_voltage.vi
C:\Users\Public\Documents\LabVIEW VI's\alexis_sub_vi's\set_bipop_voltage.vi

Alexis_Gmail_No_Attachments.vi
C:\Users\DuBois\Desktop\alexis_sub_vi's\Alexis_Gmail_No_Attachments.vi

EP-DMM-DAQ.vi
C:\Users\DuBois\Desktop\alexis_sub_vi's\EP-DMM-DAQ.vi

gfitsio-write-key.vi
C:\Users\DuBois\Documents\My Dropbox\Lab Shared - ALEXIS\Ami's ALEXIS VIs\ALEXIS VIs\gfitsio\gfitsio-write-key.vi

gfitsio-write-key-double.vi
C:\Users\DuBois\Documents\My Dropbox\Lab Shared - ALEXIS\Ami's ALEXIS VIs\ALEXIS VIs\gfitsio\gfitsio-write-key-double.vi

move_probe_ds.vi
C:\Users\Public\Documents\LabVIEW VI's\alexis_sub_vi's\move_probe_ds.vi

set_mfc_voltage_ds.vi
C:\Users\DuBois\Desktop\alexis_sub_vi's\set_mfc_voltage_ds.vi

set_out_mag_cur_ds.vi
C:\Users\Public\Documents\LabVIEW VI's\alexis_sub_vi's\set_out_mag_cur_ds.vi

set_in_mag_cur_ds.vi
C:\Users\Public\Documents\LabVIEW VI's\alexis_sub_vi's\set_in_mag_cur_ds.vi

set_rf_power_ds.vi
C:\Users\DuBois\Documents\My Dropbox\Lab Shared - ALEXIS\Ami's ALEXIS VIs\ALEXIS VIs\SubVIs\set_rf_power_ds.vi

gfitsio-open-create-replace-table.vi
C:\Users\DuBois\Desktop\LabVIEW Data - Shortcut.lnk\gfitsio\gfitsio-open-create-replace-table.vi

gfitsio-close-file.vi
C:\Users\DuBois\Desktop\LabVIEW Data - Shortcut.lnk\gfitsio\gfitsio-close-file.vi

Start Stop Step to Array.vi
C:\Users\DuBois\Desktop\NRL\Start Stop Step to Array.vi

write_fits_keys_ds.vi
C:\Users\Public\Documents\LabVIEW VI's\alexis_sub_vi's\write_fits_keys_ds.vi

write_probe_keys_ds.vi
C:\Users\Public\Documents\LabVIEW VI's\alexis_sub_vi's\write_probe_keys_ds.vi

write_var_keys_ds.vi
C:\Users\Public\Documents\LabVIEW VI's\alexis_sub_vi's\write_var_keys_ds.vi

gfitsio-open-create-replace-file.vi
C:\Users\DuBois\Desktop\LabVIEW Data - Shortcut.lnk\gfitsio\gfitsio-open-create-replace-file.vi

AutoGenerate_Filenames_v3.vi
C:\Users\DuBois\Desktop\alexis_sub_vi's\AutoGenerate_Filenames_v3.vi

B.3.3 Double probe (DP_scan_FITS.vi)

Front Panel

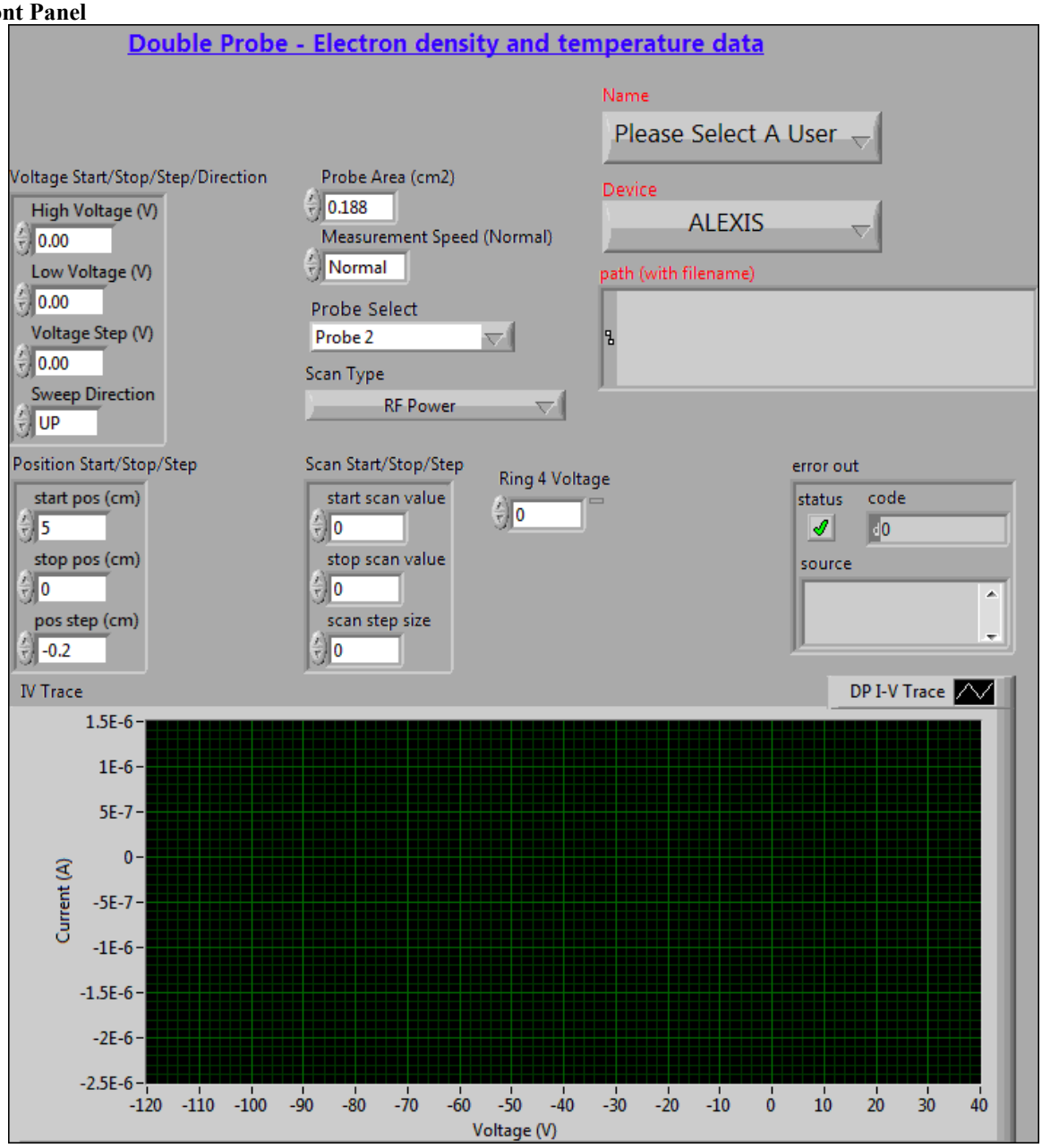

Block Diagram

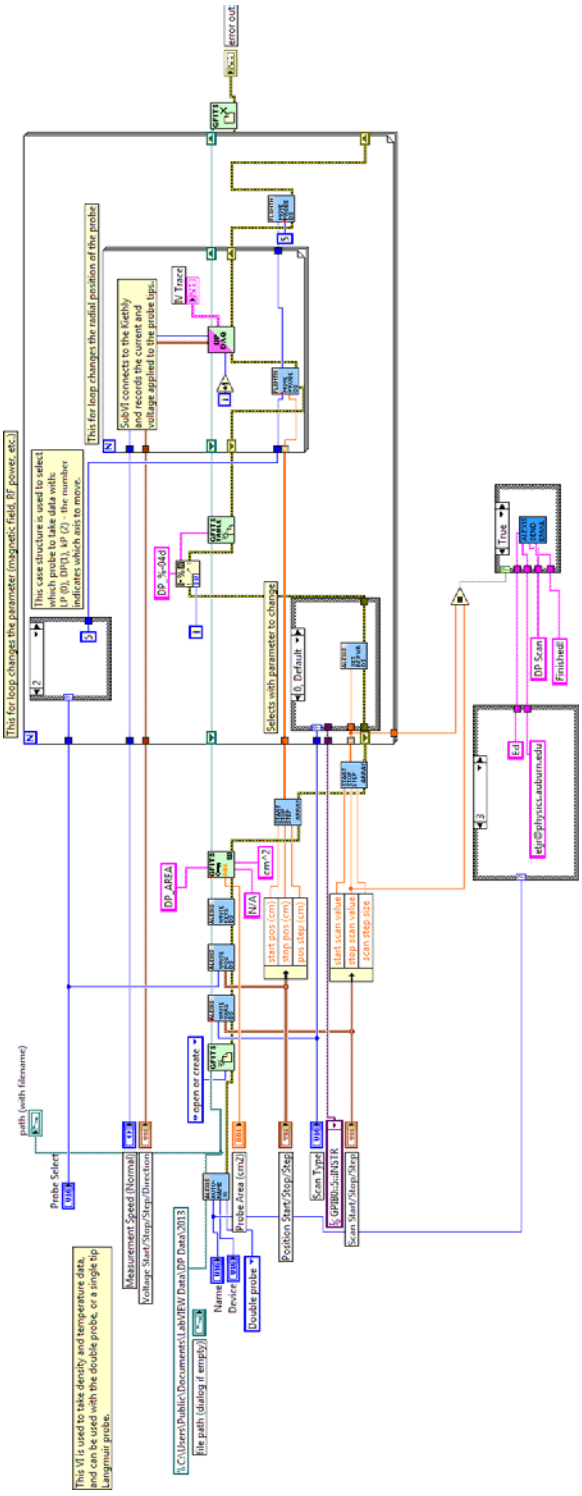

List of SubVIs and Express VIs

set_bipop_voltage.vi
C:\Users\Public\Documents\LabVIEW VI's\alexis_sub_vi's\set_bipop_voltage.vi

Alexis_Gmail_No_Attachments.vi
C:\Users\DuBois\Desktop\alexis_sub_vi's\Alexis_Gmail_No_Attachments.vi

DP-GFITS-daq.vi
C:\Users\DuBois\Desktop\alexis_sub_vi's\DP-GFITS-daq.vi

gfitsio-write-key.vi
C:\Users\DuBois\Documents\My Dropbox\Lab Shared - ALEXIS\Ami's ALEXIS VIs\ALEXIS VIs\gfitsio\gfitsio-write-key.vi

gfitsio-write-key-double.vi
C:\Users\DuBois\Documents\My Dropbox\Lab Shared - ALEXIS\Ami's ALEXIS VIs\ALEXIS VIs\gfitsio\gfitsio-write-key-double.vi

move_probe_ds - Copy.vi
C:\Users\DuBois\Documents\My Dropbox\Lab Shared - ALEXIS\Ami's ALEXIS VIs\ALEXIS VIs\SubVIs\move_probe_ds - Copy.vi

set_mfc_voltage_ds.vi
C:\Users\DuBois\Desktop\alexis_sub_vi's\set_mfc_voltage_ds.vi

set_out_mag_cur_ds.vi
C:\Users\Public\Documents\LabVIEW VI's\alexis_sub_vi's\set_out_mag_cur_ds.vi

set_in_mag_cur_ds.vi
C:\Users\Public\Documents\LabVIEW VI's\alexis_sub_vi's\set_in_mag_cur_ds.vi

set_rf_power_ds.vi
C:\Users\DuBois\Documents\My Dropbox\Lab Shared - ALEXIS\Ami's ALEXIS VIs\ALEXIS VIs\SubVIs\set_rf_power_ds.vi

move_probe_ds.vi
C:\Users\Public\Documents\LabVIEW VI's\alexis_sub_vi's\move_probe_ds.vi

gfitsio-open-create-replace-table.vi
C:\Users\DuBois\Desktop\LabVIEW Data - Shortcut.lnk\gfitsio\gfitsio-open-create-replace-table.vi

gfitsio-close-file.vi
C:\Users\DuBois\Desktop\LabVIEW Data - Shortcut.lnk\gfitsio\gfitsio-close-file.vi

Start Stop Step to Array.vi
C:\Users\DuBois\Desktop\NRL\Start Stop Step to Array.vi

write_fits_keys_ds.vi
C:\Users\Public\Documents\LabVIEW VI's\alexis_sub_vi's\write_fits_keys_ds.vi

write_probe_keys_ds.vi
C:\Users\Public\Documents\LabVIEW VI's\alexis_sub_vi's\write_probe_keys_ds.vi

write_var_keys_ds2.vi
C:\Users\Public\Documents\LabVIEW VI's\alexis_sub_vi's\write_var_keys_ds2.vi

gfitsio-open-create-replace-file.vi
C:\Users\DuBois\Desktop\LabVIEW Data - Shortcut.lnk\gfitsio\gfitsio-open-create-replace-file.vi

AutoGenerate_Filenames_v3.vi
C:\Users\DuBois\Desktop\alexis_sub_vi's\AutoGenerate_Filenames_v3.vi

B.3.4 “k” – probe (kP_ThetaSweepONLY_AVG_StepMotor.vi)

Front Panel

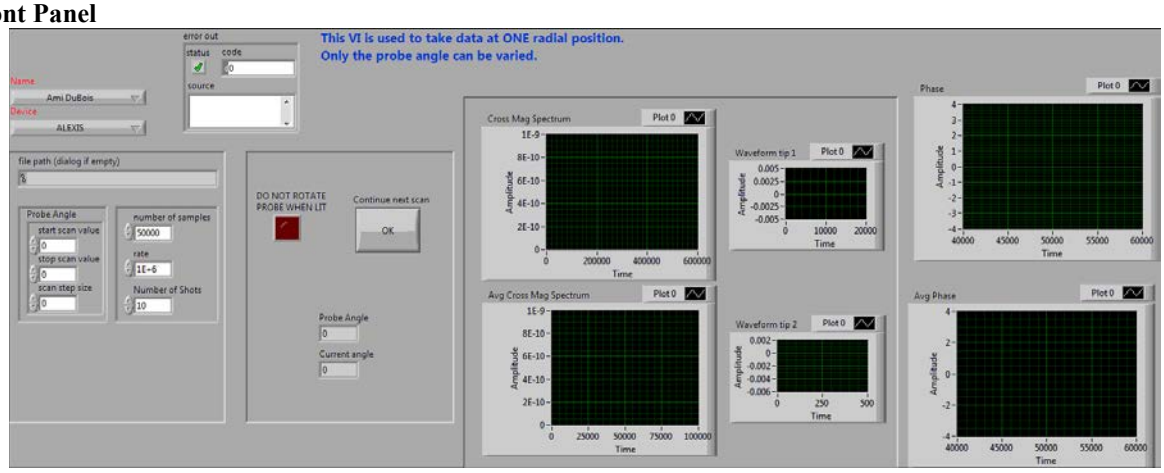

Block Diagram

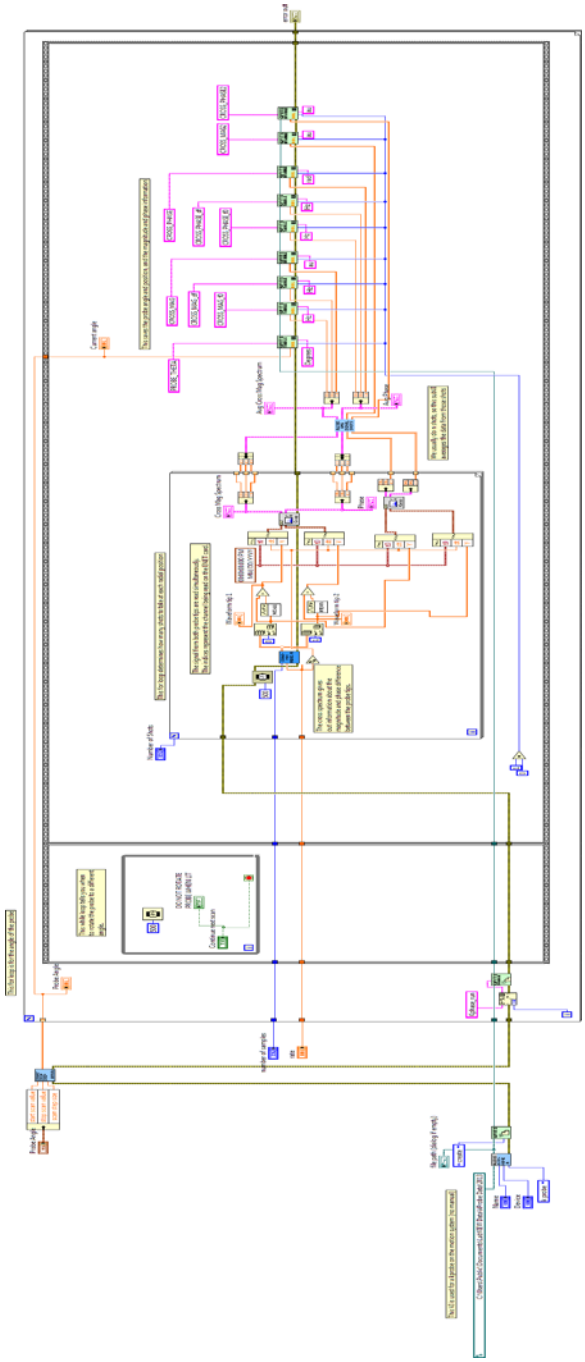

List of SubVIs and Express VIs

NI_MAPro.lvlib:Cross Spectrum (Mag-Phase).vi
C:\Program Files (x86)\National Instruments\LabVIEW 2010\vi.lib\measure\maspectr.llb\Cross Spectrum (Mag-Phase).vi

NI_AALBase.lvlib:Mean.vi
C:\Program Files (x86)\National Instruments\LabVIEW 2010\vi.lib\Analysis\baseanly.llb\Mean.vi

cDaq9181 read.vi
C:\Users\DuBois\Documents\My Dropbox\Lab Shared - ALEXIS\Ami's ALEXIS VIs\ALEXIS VIs\SubVIs\cDaq9181 read.vi

Wait with Error IO.vi
C:\Users\DuBois\Desktop\NRL\Wait with Error IO.vi

gfitsio-write-column-dbl-1d_new.vi
C:\Users\DuBois\Desktop\LabVIEW Data - Shortcut.lnk\gfitsio\gfitsio-write-column-dbl-1d_new.vi

Avg_Data_Shots.vi
C:\Users\DuBois\Desktop\alexis_sub_vi's\Avg_Data_Shots.vi

gfitsio-write-column-dbl-scalar_new.vi
C:\Users\DuBois\Desktop\LabVIEW Data - Shortcut.lnk\gfitsio\gfitsio-write-column-dbl-scalar_new.vi

gfitsio-write-column_new.vi
C:\Users\DuBois\Desktop\LabVIEW Data - Shortcut.lnk\gfitsio\gfitsio-write-column_new.vi

gfitsio-open-create-replace-table_new.vi
C:\Users\DuBois\Desktop\LabVIEW Data - Shortcut.lnk\gfitsio\gfitsio-open-create-replace-table_new.vi

Start Stop Step to Array.vi
C:\Users\DuBois\Desktop\NRL\Start Stop Step to Array.vi

gfitsio-open-create-replace-file_new.vi
C:\Users\DuBois\Desktop\LabVIEW Data - Shortcut.lnk\gfitsio\gfitsio-open-create-replace-file_new.vi

AutoGenerate_Filenames_v3.vi
C:\Users\DuBois\Desktop\alexis_sub_vi's\AutoGenerate_Filenames_v3.vi

B.4 LabVIEW data analysis

B.4.1 Langmuir probe (LP_analysis_2012.vi)

Front Panel

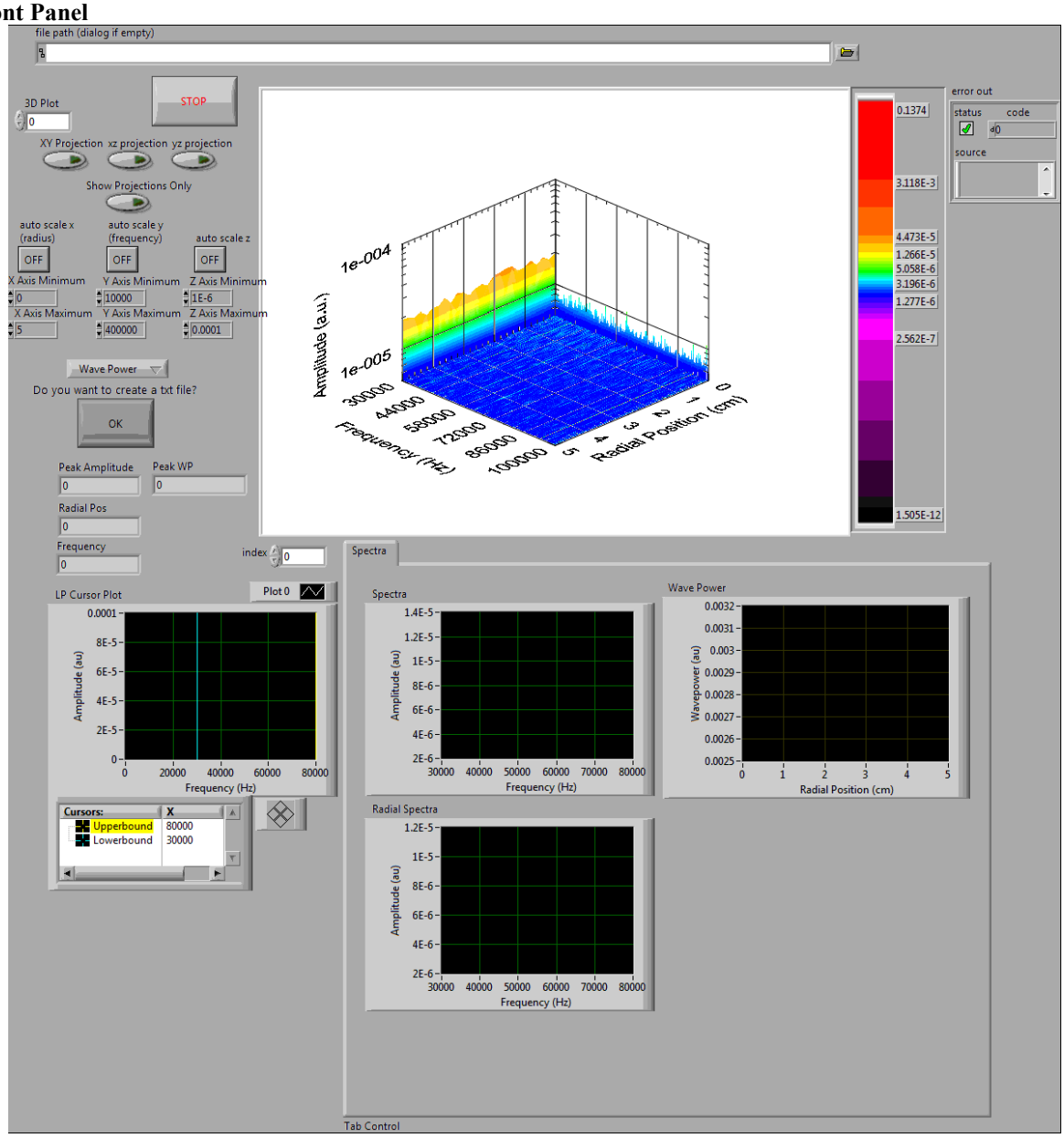

Block Diagram

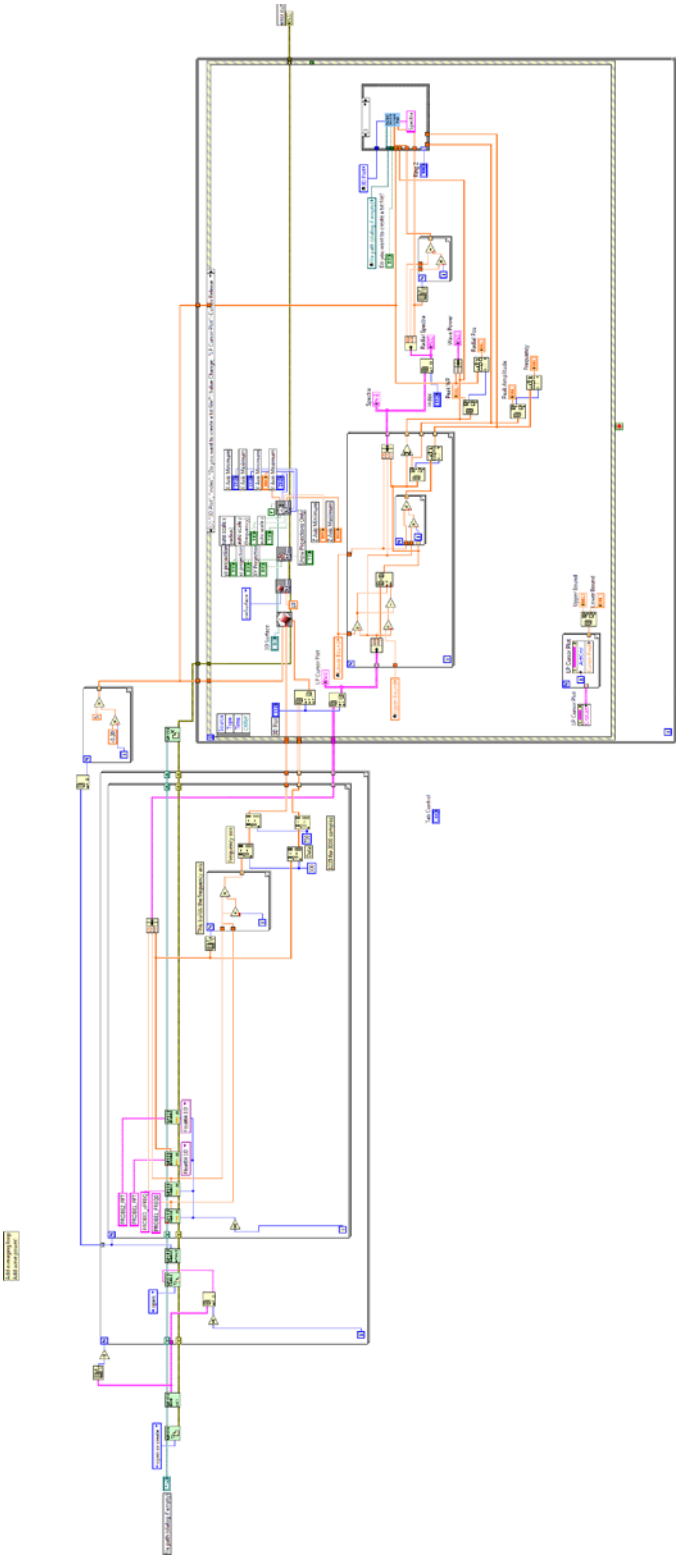

List of SubVIs and Express VIs

gfitsio-open-create-replace-file_new.vi
C:\Users\Ami\Dropbox\Lab Shared - ALEXIS\Ami's ALEXIS VIs\ALEXIS VIs\gfitsio\gfitsio-open-create-replace-file_new.vi

gfitsio-get-hdu-list_new.vi
C:\Users\Ami\Dropbox\Lab Shared - ALEXIS\Ami's ALEXIS VIs\ALEXIS VIs\gfitsio\gfitsio-get-hdu-list_new.vi

gfitsio-close-file_new.vi
C:\Users\Ami\Dropbox\Lab Shared - ALEXIS\Ami's ALEXIS VIs\ALEXIS VIs\gfitsio\gfitsio-close-file_new.vi

gfitsio-open-create-replace-table_new.vi
C:\Users\Ami\Dropbox\Lab Shared - ALEXIS\Ami's ALEXIS VIs\ALEXIS VIs\gfitsio\gfitsio-open-create-replace-table_new.vi

gfitsio-get-num-rows_new.vi
C:\Users\Ami\Dropbox\Lab Shared - ALEXIS\Ami's ALEXIS VIs\ALEXIS VIs\gfitsio\gfitsio-get-num-rows_new.vi

gfitsio-read-column_new.vi
C:\Users\Ami\Dropbox\Lab Shared - ALEXIS\Ami's ALEXIS VIs\ALEXIS VIs\gfitsio\gfitsio-read-column_new.vi

gfitsio-read-column-dbl-1d_new.vi
C:\Users\Ami\Dropbox\Lab Shared - ALEXIS\Ami's ALEXIS VIs\ALEXIS VIs\gfitsio\gfitsio-read-column-dbl-1d_new.vi

create_mathematica_file.vi
C:\Users\Ami\Dropbox\Lab Shared - ALEXIS\Ami's ALEXIS VIs\ALEXIS VIs\SubVIs\create_mathematica_file.vi

NI_3dgraph.lvlib:Axes Properties.vi
C:\Users\Ami\Dropbox\Lab Shared - ALEXIS\Ami's ALEXIS VIs\ALEXIS VIs\SubVIs\Axes Properties.vi

NI_3dgraph.lvlib:Projection Properties.vi
C:\Program Files (x86)\National Instruments\LabVIEW 2010\vi.lib\Platform\3dgraph.llb\Projection Properties.vi

NI_3dgraph.lvlib:Basic Properties.vi
C:\Program Files (x86)\National Instruments\LabVIEW 2010\vi.lib\Platform\3dgraph.llb\Basic Properties.vi

NI_3dgraph.lvlib:3D Surface.vi
C:\Program Files (x86)\National Instruments\LabVIEW 2010\vi.lib\Platform\3dgraph.llb\3D Surface.vi

gfitsio-read-column-sgl-scalar.vi
C:\Users\Ami\Dropbox\Lab Shared - ALEXIS\Ami's ALEXIS VIs\ALEXIS VIs\gfitsio\gfitsio-read-column-sgl-scalar.vi

B.4.2 Emissive probe (EP_analysis.vi)

Front Panel

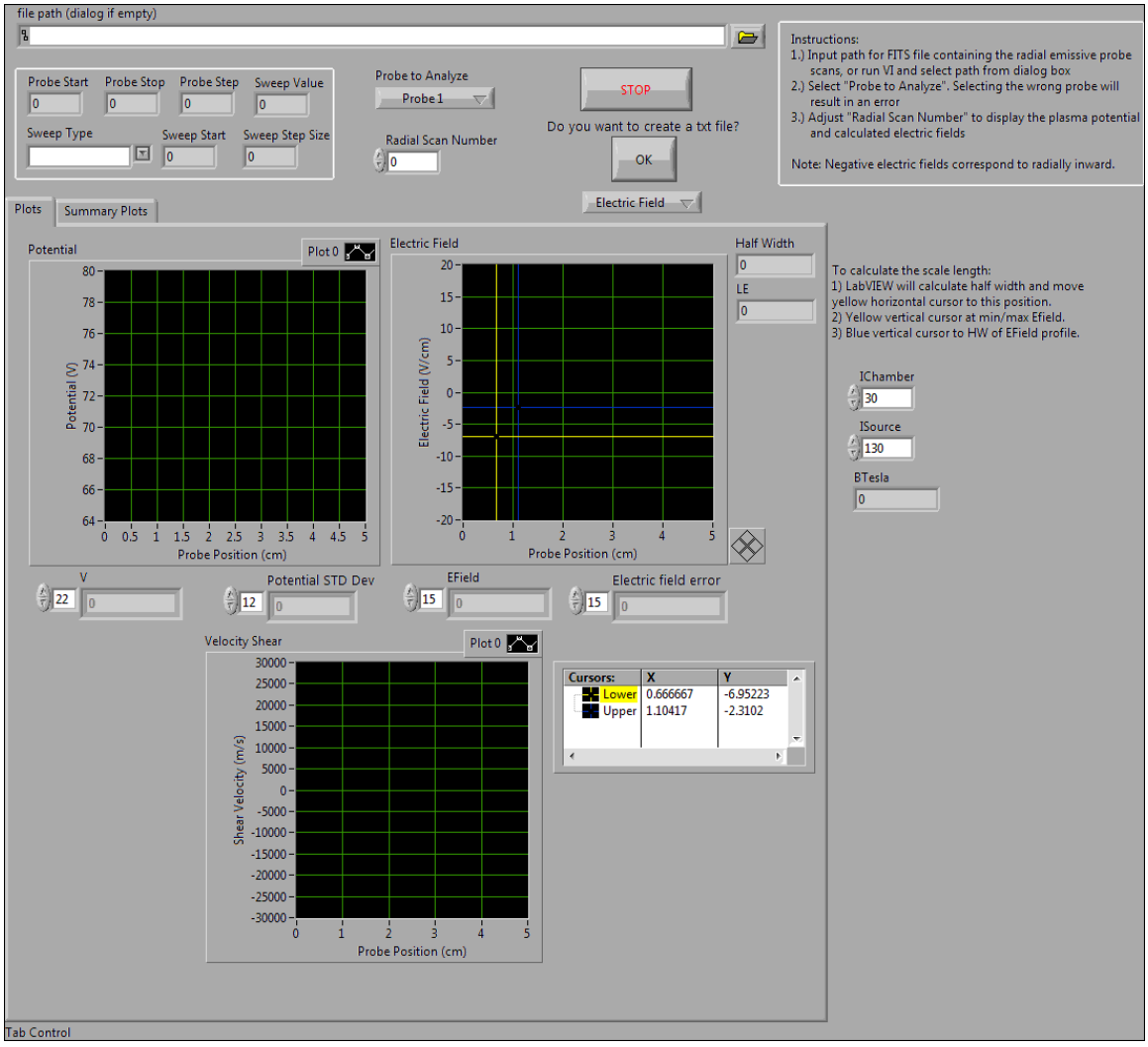

Block Diagram

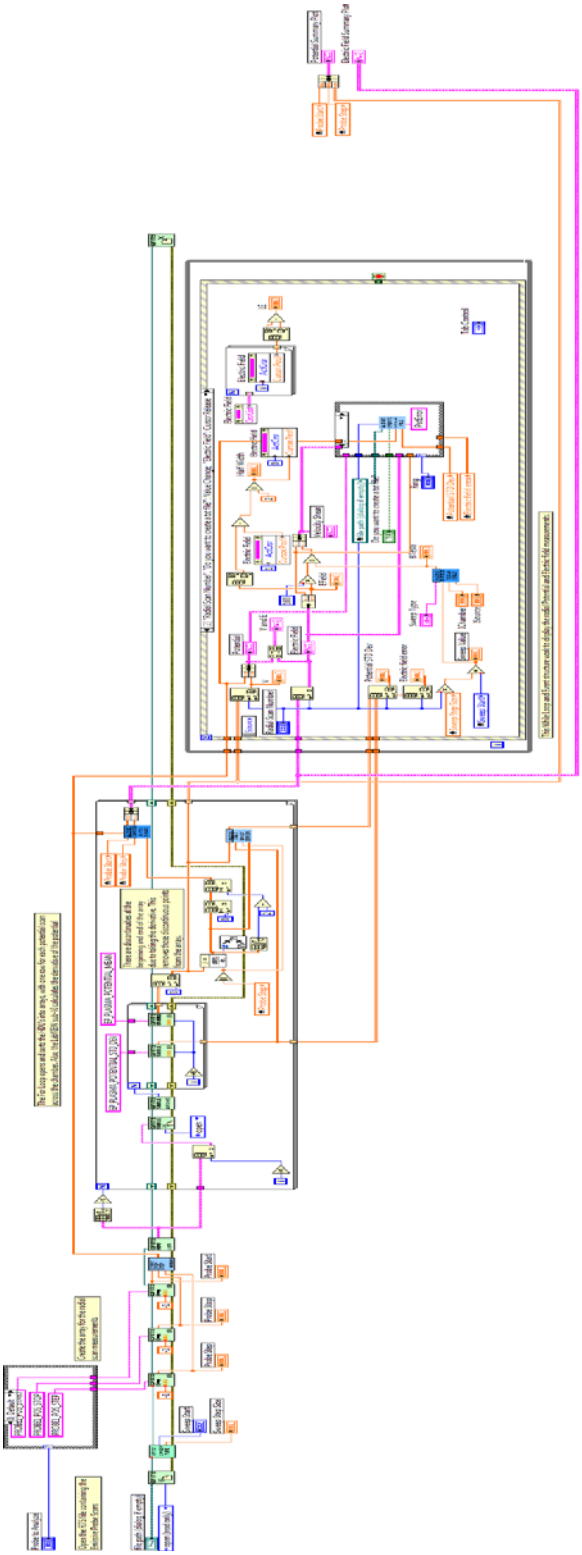

List of SubVIs and Express VIs

create_mathematica_file.vi
C:\Users\Ami\Dropbox\Lab Shared - ALEXIS\Ami's ALEXIS VIs\ALEXIS VIs\SubVIs\create_mathematica_file.vi

Calculate_BField_Tesla.vi
C:\Users\Ami\Dropbox\Lab Shared - ALEXIS\Ami's ALEXIS VIs\ALEXIS VIs\SubVIs\Calculate_BField_Tesla.vi

gfitsio-read-column-dbl-1d.vi
C:\Users\Ami\Dropbox\Lab Shared - ALEXIS\Ami's ALEXIS VIs\ALEXIS VIs\gfitsio\gfitsio-read-column-dbl-1d.vi

Error Cluster From Error Code.vi
C:\Program Files (x86)\National Instruments\LabVIEW 2010\vi.lib\Utility\error.llb\Error Cluster From Error Code.vi

gfitsio-get-num-rows.vi
C:\Users\Ami\Dropbox\Lab Shared - ALEXIS\Ami's ALEXIS VIs\ALEXIS VIs\gfitsio\gfitsio-get-num-rows.vi

gfitsio-read-column-dbl-scalar.vi
C:\Users\Ami\Dropbox\Lab Shared - ALEXIS\Ami's ALEXIS VIs\ALEXIS VIs\gfitsio\gfitsio-read-column-dbl-scalar.vi

gfitsio-read-column.vi
C:\Users\Ami\Dropbox\Lab Shared - ALEXIS\Ami's ALEXIS VIs\ALEXIS VIs\gfitsio\gfitsio-read-column.vi

EField_Convert_RadialPos.vi
C:\Users\Ami\Dropbox\Lab Shared - ALEXIS\Ami's ALEXIS VIs\ALEXIS VIs\SubVIs\EField_Convert_RadialPos.vi

Calculate_derivative_error.vi
C:\Users\Ami\Dropbox\Lab Shared - ALEXIS\Ami's ALEXIS VIs\ALEXIS VIs\SubVIs\Calculate_derivative_error.vi

NI_AALPro.lvlib:Derivative x(t).vi
C:\Program Files (x86)\National Instruments\LabVIEW 2010\vi.lib\Analysis\2dsp.llb\Derivative x(t).vi

gfitsio-open-create-replace-table.vi
C:\Users\Ami\Dropbox\Lab Shared - ALEXIS\Ami's ALEXIS VIs\ALEXIS VIs\gfitsio\gfitsio-open-create-replace-table.vi

gfitsio-get-hdu-list.vi
C:\Users\Ami\Dropbox\Lab Shared - ALEXIS\Ami's ALEXIS VIs\ALEXIS VIs\gfitsio\gfitsio-get-hdu-list.vi

gfitsio-close-file.vi
C:\Users\Ami\Dropbox\Lab Shared - ALEXIS\Ami's ALEXIS VIs\ALEXIS VIs\gfitsio\gfitsio-close-file.vi

Start Stop Step to Array.vi
C:\Users\Ami\Dropbox\Lab Shared - ALEXIS\Ami's ALEXIS VIs\ALEXIS VIs\NRL VIs\Start Stop Step to Array.vi

gfitsio-read-key-double.vi
C:\Users\Ami\Dropbox\Lab Shared - ALEXIS\Ami's ALEXIS VIs\ALEXIS VIs\gfitsio\gfitsio-read-key-double.vi

gfitsio-read-key.vi
C:\Users\Ami\Dropbox\Lab Shared - ALEXIS\Ami's ALEXIS VIs\ALEXIS VIs\gfitsio\gfitsio-read-key.vi

FITS_Sweep_Selector.vi
C:\Users\Ami\Dropbox\Lab Shared - ALEXIS\Ami's ALEXIS VIs\ALEXIS VIs\SubVIs\FITS_Sweep_Selector.vi

gfitsio-open-create-replace-file.vi
C:\Users\Ami\Dropbox\Lab Shared - ALEXIS\Ami's ALEXIS VIs\ALEXIS VIs\gfitsio\gfitsio-open-create-replace-file.vi

B.4.3 Double probe (DP_analysis_Fit_New.vi)

Front Panel

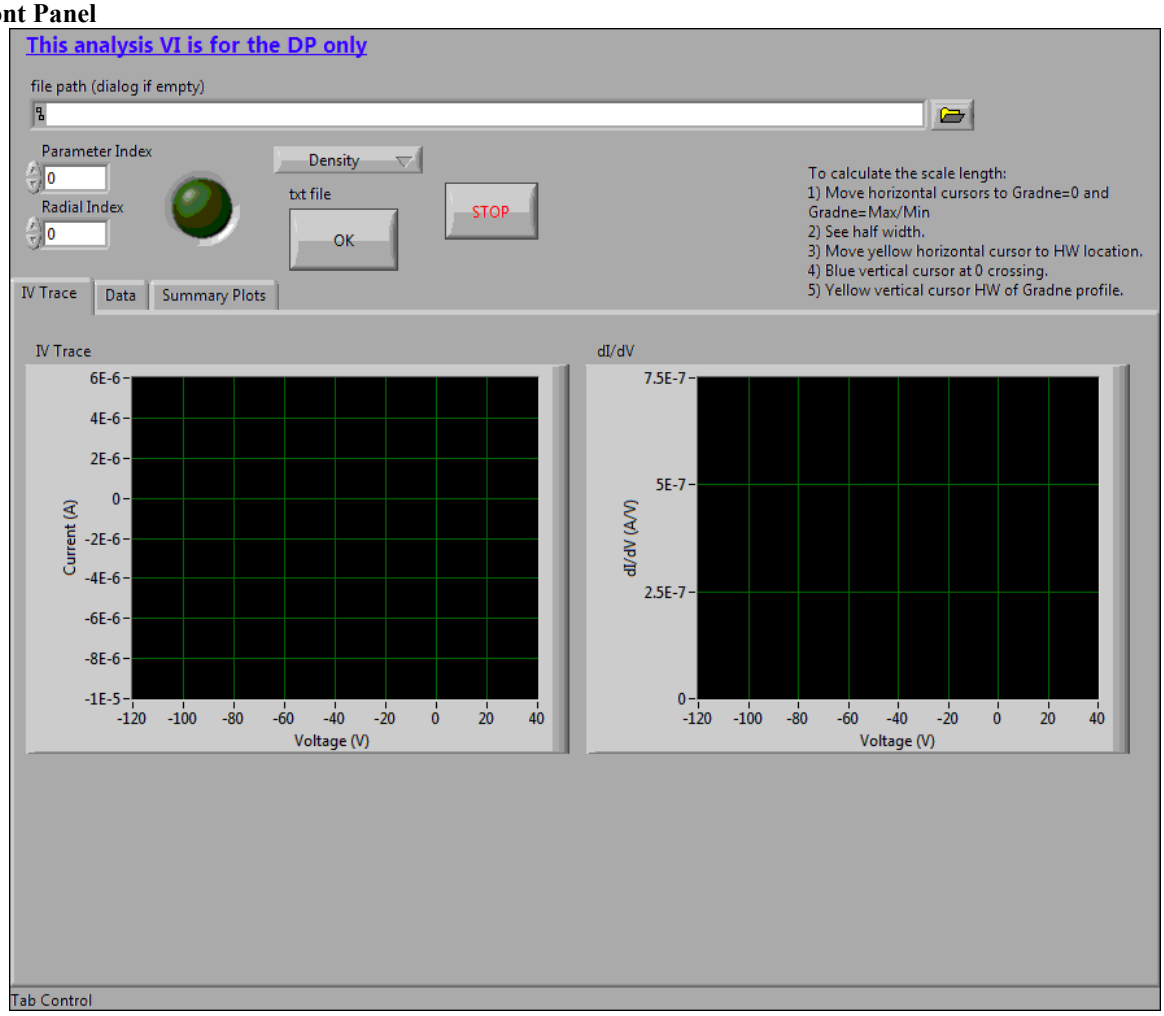

Block Diagram

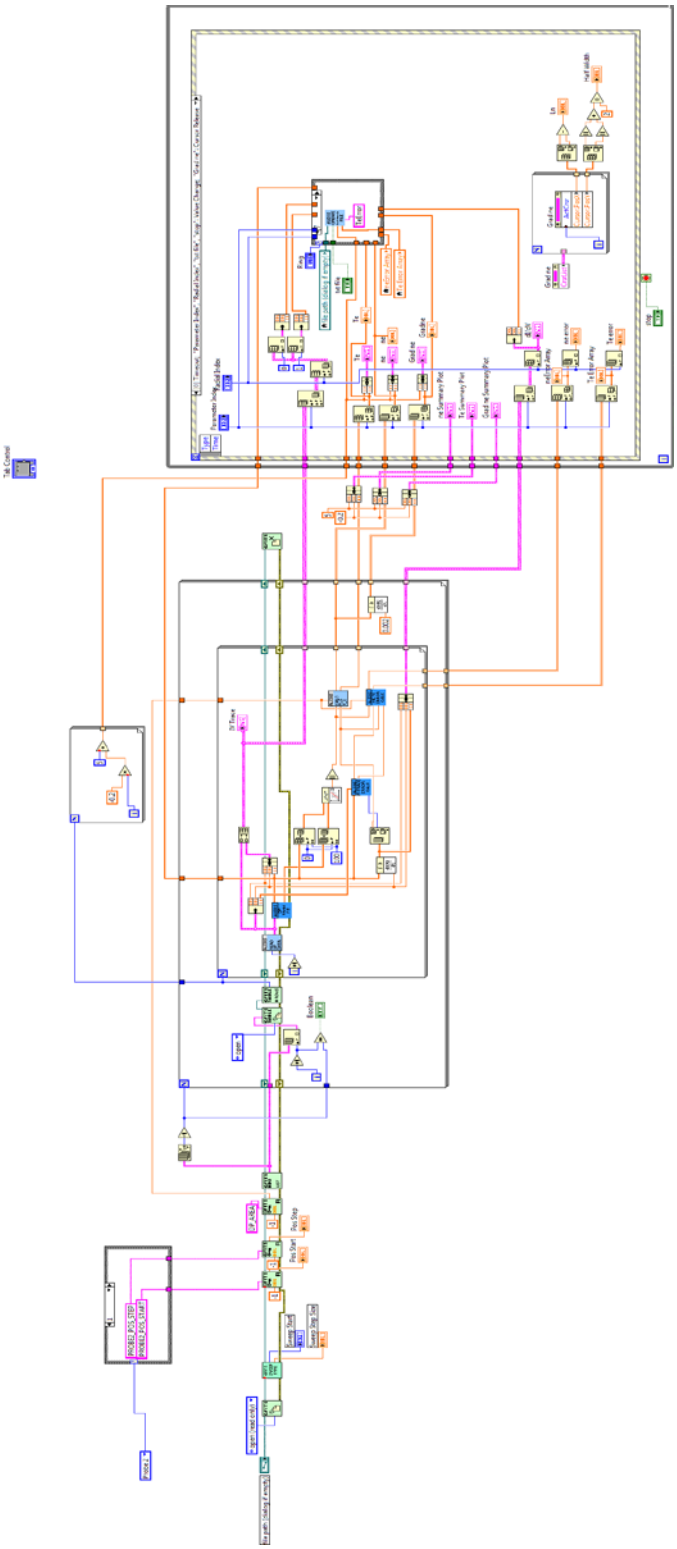

List of SubVIs and Express VIs

create_mathematica_file.vi
C:\Users\Ami\Dropbox\Lab Shared - ALEXIS\Ami's ALEXIS VIs\ALEXIS VIs\SubVIs\create_mathematica_file.vi

DP_calculate_ne_Te.vi
C:\Users\Ami\Dropbox\Lab Shared - ALEXIS\Ami's ALEXIS VIs\ALEXIS VIs\SubVIs\DP_calculate_ne_Te.vi

Calculate_ne_Te_Error.vi
C:\Users\Ami\Dropbox\Lab Shared - ALEXIS\Ami's ALEXIS VIs\ALEXIS VIs\SubVIs\Calculate_ne_Te_Error.vi

NI_AALPro.lvlib:Linear Fit.vi
C:\Program Files (x86)\National Instruments\LabVIEW 2010\vi.lib\Analysis\6fits.llb\Linear Fit.vi

Calculate_IVTrace_Error.vi
C:\Users\Ami\Dropbox\Lab Shared - ALEXIS\Ami's ALEXIS VIs\ALEXIS VIs\SubVIs\Calculate_IVTrace_Error.vi

DP_IVTrace_Fit.vi
C:\Users\Ami\Dropbox\Lab Shared - ALEXIS\Ami's ALEXIS VIs\ALEXIS VIs\SubVIs\DP_IVTrace_Fit.vi

read_dp_data_No_correction.vi
C:\Users\Ami\Dropbox\Lab Shared - ALEXIS\Ami's ALEXIS VIs\ALEXIS VIs\SubVIs\read_dp_data_No_correction.vi

gfitsio-get-num-rows.vi
C:\Users\Ami\Dropbox\Lab Shared - ALEXIS\Ami's ALEXIS VIs\ALEXIS VIs\gfitsio\gfitsio-get-num-rows.vi

NI_AALPro.lvlib:Derivative x(t).vi
C:\Program Files (x86)\National Instruments\LabVIEW 2010\vi.lib\Analysis\2dsp.llb\Derivative x(t).vi

gfitsio-open-create-replace-table.vi
C:\Users\Ami\Dropbox\Lab Shared - ALEXIS\Ami's ALEXIS VIs\ALEXIS VIs\gfitsio\gfitsio-open-create-replace-table.vi

gfitsio-get-hdu-list.vi
C:\Users\Ami\Dropbox\Lab Shared - ALEXIS\Ami's ALEXIS VIs\ALEXIS VIs\gfitsio\gfitsio-get-hdu-list.vi

gfitsio-close-file.vi
C:\Users\Ami\Dropbox\Lab Shared - ALEXIS\Ami's ALEXIS VIs\ALEXIS VIs\gfitsio\gfitsio-close-file.vi

gfitsio-read-key-double.vi
C:\Users\Ami\Dropbox\Lab Shared - ALEXIS\Ami's ALEXIS VIs\ALEXIS VIs\gfitsio\gfitsio-read-key-double.vi

gfitsio-read-key.vi
C:\Users\Ami\Dropbox\Lab Shared - ALEXIS\Ami's ALEXIS VIs\ALEXIS VIs\gfitsio\gfitsio-read-key.vi

FITS_Sweep_Selector.vi
C:\Users\Ami\Dropbox\Lab Shared - ALEXIS\Ami's ALEXIS VIs\ALEXIS VIs\SubVIs\FITS_Sweep_Selector.vi

gfitsio-open-create-replace-file.vi
C:\Users\Ami\Dropbox\Lab Shared - ALEXIS\Ami's ALEXIS VIs\ALEXIS VIs\gfitsio\gfitsio-open-create-replace-file.vi

B.4.4 “k” – probe (kP_LorentzAnalysis_AVG.vi)

Front Panel

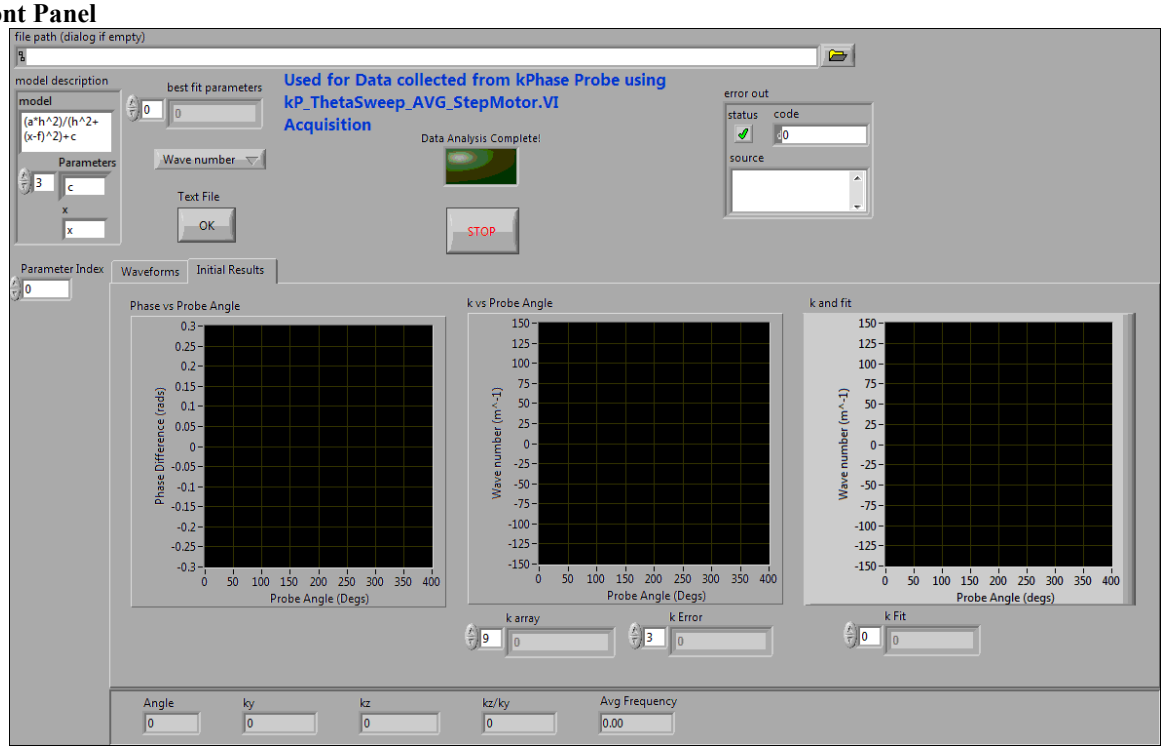

Block Diagram

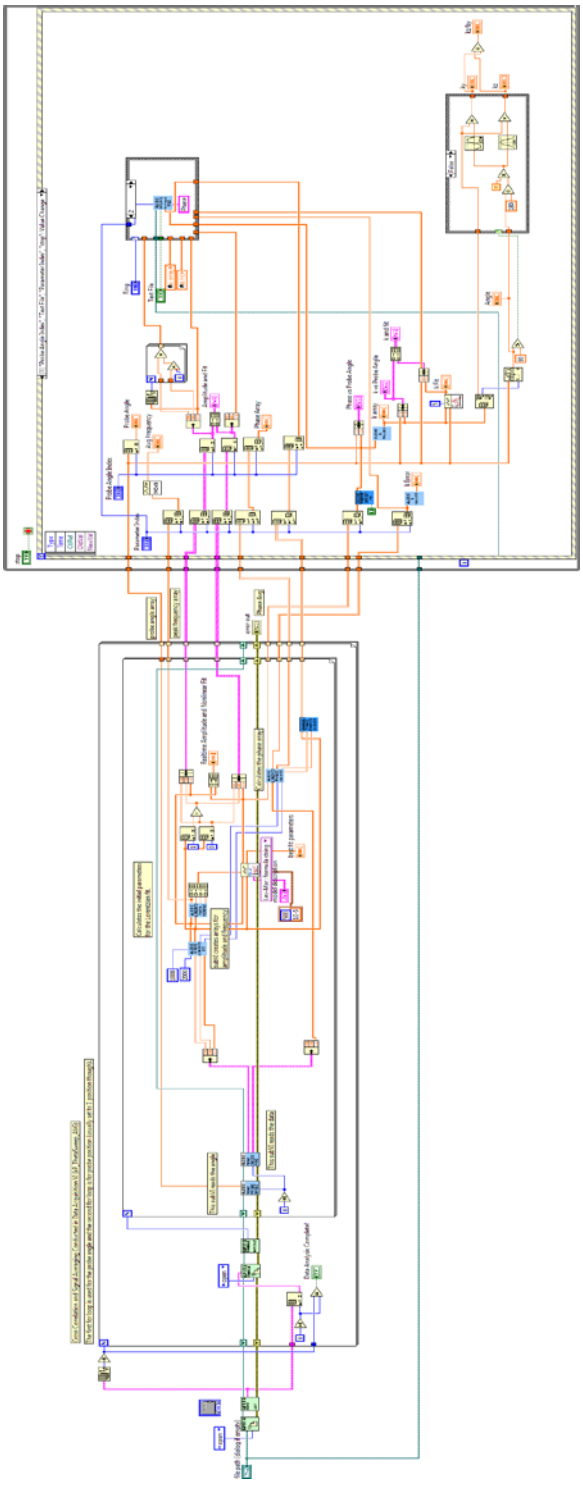

List of SubVIs and Express VIs

create_mathematica_file.vi
C:\Users\Ami\Dropbox\Lab Shared - ALEXIS\Ami's ALEXIS VIs\ALEXIS VIs\SubVIs\create_mathematica_file.vi

NI_AALPro.lvlib:General Polynomial Fit.vi
C:\Program Files (x86)\National Instruments\LabVIEW 2010\vi.lib\Analysis\6fits.llb\General Polynomial Fit.vi

Phase_Offset_Fix.vi
C:\Users\Ami\Dropbox\Lab Shared - ALEXIS\Ami's ALEXIS VIs\ALEXIS VIs\SubVIs\Phase_Offset_Fix.vi

NI_AALBase.lvlib:Mean.vi
C:\Program Files (x86)\National Instruments\LabVIEW 2010\vi.lib\Analysis\baseanly.llb\Mean.vi

calculate_k_values.vi
C:\Users\Ami\Dropbox\Lab Shared - ALEXIS\Ami's ALEXIS VIs\ALEXIS VIs\SubVIs\calculate_k_values.vi

Phase_Frequency_SubArray.vi
C:\Users\Ami\Dropbox\Lab Shared - ALEXIS\Ami's ALEXIS VIs\ALEXIS VIs\SubVIs\Phase_Frequency_SubArray.vi

PhaseValuesSUBVI.vi
C:\Users\Ami\Dropbox\Lab Shared - ALEXIS\Ami's ALEXIS VIs\ALEXIS VIs\SubVIs\PhaseValuesSUBVI.vi

NI_Gmath.lvlib:Nonlinear Curve Fit LM formula string.vi
C:\Program Files (x86)\National Instruments\LabVIEW 2010\vi.lib\gmath\NumericalOptimization\Nonlinear Curve Fit LM formula string.vi

NI_Gmath.lvlib:Nonlinear Curve Fit.vi
C:\Program Files (x86)\National Instruments\LabVIEW 2010\vi.lib\gmath\NumericalOptimization\Nonlinear Curve Fit.vi

LorentzianFitParametersSUBVI.vi
C:\Users\Ami\Dropbox\Lab Shared - ALEXIS\Ami's ALEXIS VIs\ALEXIS VIs\SubVIs\LorentzianFitParametersSUBVI.vi

calculate_Lorentz_x-axis.vi
C:\Users\Ami\Dropbox\Lab Shared - ALEXIS\Ami's ALEXIS VIs\ALEXIS VIs\SubVIs\calculate_Lorentz_x-axis.vi

read_CrossMagPhase.vi
C:\Users\Ami\Dropbox\Lab Shared - ALEXIS\Ami's ALEXIS VIs\ALEXIS VIs\SubVIs\read_CrossMagPhase.vi

gfitsio-get-num-rows_new.vi
C:\Users\Ami\Dropbox\Lab Shared - ALEXIS\Ami's ALEXIS VIs\ALEXIS VIs\gfitsio\gfitsio-get-num-rows_new.vi

read_probe_angle_data.vi
C:\Users\Ami\Dropbox\Lab Shared - ALEXIS\Ami's ALEXIS VIs\ALEXIS VIs\SubVIs\read_probe_angle_data.vi

gfitsio-open-create-replace-table_new.vi
C:\Users\Ami\Dropbox\Lab Shared - ALEXIS\Ami's ALEXIS VIs\ALEXIS VIs\gfitsio\gfitsio-open-create-replace-table_new.vi

gfitsio-get-hdu-list_new.vi
C:\Users\Ami\Dropbox\Lab Shared - ALEXIS\Ami's ALEXIS VIs\ALEXIS VIs\gfitsio\gfitsio-get-hdu-list_new.vi

gfitsio-open-create-replace-file_new.vi
C:\Users\Ami\Dropbox\Lab Shared - ALEXIS\Ami's ALEXIS VIs\ALEXIS VIs\gfitsio\gfitsio-open-create-replace-file_new.vi